A Thesis Submitted for the Degree of PhD at the University of Warwick

http://go.warwick.ac.uk/wrap/77488

Library Declaration and Deposit Agreement

1. STUDENT DETAILS

Please complete the following:

Full name: …………………………………………………………………………………………….

University ID number: ………………………………………………………………………………

2. THESIS DEPOSIT

2.1 Under your registration at the University, you are required to deposit your thesis with the University in BOTH hard copy and in digital format. The digital copy should normally be saved as a single pdf file.

2.2 The hard copy will be housed in the University Library. The digital copy will be deposited in the University's Institutional Repository (WRAP). Unless otherwise indicated (see 2.6 below), this will be made immediately openly accessible on the Internet and will be supplied to the British Library to be made available online via its Electronic Theses Online Service (EThOS) service.
[At present, theses submitted for a Master's degree by Research (MA, MSc, LLM, MS or MMedSci) are not being deposited in WRAP and not being made available via EthOS. This may change in future.]

2.3 In exceptional circumstances, the Chair of the Board of Graduate Studies may grant permission for an embargo to be placed on public access to the thesis **in excess of two years**. This must be applied for when submitting the thesis for examination (further information is available in the *Guide to Examinations for Higher Degrees by Research*.)

2.4 If you are depositing a thesis for a Master's degree by Research, the options below only relate to the hard copy thesis.

2.5 If your thesis contains material protected by third party copyright, you should consult with your department, and if appropriate, deposit an abridged hard and/or digital copy thesis.

2.6 Please tick one of the following options for the availability of your thesis (guidance is available in the *Guide to Examinations for Higher Degrees by Research)***:**

☐ Both the hard and digital copy thesis can be made publicly available immediately

☐ The hard copy thesis can be made publicly available immediately and the digital copy thesis can be made publicly available after a period of two years (*should you subsequently wish to reduce the embargo period please inform the Library*)

☐ Both the hard and digital copy thesis can be made publicly available after a period of two years (*should you subsequently wish to reduce the embargo period please inform the Library*)

☐ Both the hard copy and digital copy thesis can be made publicly available after _______________ (insert time period in excess of two years). **This option requires the prior approval of the Chair of the Board of Graduate Studies (see 2.3 above)**

The University encourages users of the Library to utilise theses as much as possible, and unless indicated below users will be able to photocopy your thesis.

☐ I **do not** wish for my thesis to be photocopied

3. GRANTING OF NON-EXCLUSIVE RIGHTS

Whether I deposit my Work personally or through an assistant or other agent, I agree to the following:

- Rights granted to the University of Warwick and the British Library and the user of the thesis through this agreement are non-exclusive. I retain all rights in the thesis in its present version or future versions. I agree that the institutional repository administrators and the British Library or their agents may, without changing content, digitise and migrate the thesis to any medium or format for the purpose of future preservation and accessibility.

4. DECLARATIONS

I DECLARE THAT:

- I am the author and owner of the copyright in the thesis and/or I have the authority of the authors and owners of the copyright in the thesis to make this agreement. Reproduction of any part of this thesis for teaching or in academic or other forms of publication is subject to the normal limitations on the use of copyrighted materials and to the proper and full acknowledgement of its source.

- The digital version of the thesis I am supplying is either the same version as the final, hard-bound copy submitted in completion of my degree once any minor corrections have been completed, or is an abridged version (see 2.5 above).

- I have exercised reasonable care to ensure that the thesis is original, and does not to the best of my knowledge break any UK law or other Intellectual Property Right, or contain any confidential material.

- I understand that, through the medium of the Internet, files will be available to automated agents, and may be searched and copied by, for example, text mining and plagiarism detection software.

- At such time that my thesis will be made publically available digitally (see 2.6 above), I grant the University of Warwick and the British Library a licence to make available on the Internet the thesis in digitised format through the Institutional Repository and through the British Library via the EThOS service.

- If my thesis does include any substantial subsidiary material owned by third-party copyright holders, I have sought and obtained permission to include it in any version of my thesis available in digital format and that this permission encompasses the rights that I have granted to the University of Warwick and to the British Library.

5. LEGAL INFRINGEMENTS

I understand that neither the University of Warwick nor the British Library have any obligation to take legal action on behalf of myself, or other rights holders, in the event of infringement of intellectual property rights, breach of contract or of any other right, in the thesis.

Please sign this agreement and ensure it is bound into the final hard bound copy of your thesis, which should be submitted to Student Reception, Senate House.

Student's signature: ………………………………………………… Date: …………………………………………………

Polyclonal Architecture of the Mammalian Head

by

John M.J. Lapage

Thesis

Submitted to the University of Warwick

for the degree of

Doctor of Philosophy

School of Life Sciences

September 2015

Dedicated to friends, colleagues and family
for supporting me in getting to this point,
and especially to those who blurred the lines between those groups.

Contents

List of Tables ix

List of Figures x

Acknowledgments xvi

Declarations xvii

Abstract xviii

Chapter 1 General Introduction and Structure of this Thesis 1
- 1.1 Structure 1
- 1.2 A Brief History of Lineage Labelling 3
  - 1.2.1 Manual Labelling 4
  - 1.2.2 Genetic Labelling 4
- 1.3 The Confetti Reporter Construct 5
  - 1.3.1 The Brainbow suite 6
  - 1.3.2 Confetti and its alternatives 7
  - 1.3.3 Applications of Random Genetic Lineage Analysis 7
- 1.4 Description of Confetti Behaviour 10
- 1.5 Deciphering Biological Relevance from Confetti 11
- 1.6 Summary of Confetti Lineage Labelling 15

I The basis of heterodonty, thecodonty and tooth specification 16

Chapter 2 Introduction 17
- 2.1 Proximodistal Specification of the Tooth Row 18
- 2.2 Heterodonty in mammals 20
- 2.3 Modes of tooth attachment 22
- 2.4 Summary 23

Chapter 3 Early distal to proximal migrations are necessary for proximal lower jaw development 24
- 3.1 Methodology 26
  - 3.1.1 Hand2-Cre as a marker for Distal Cells 26

3.1.2 Samples and sections 26
3.1.3 The Founder Effect and Confetti 28
3.2 Results 29
3.2.1 Hand2 cells are distal cells 29
3.2.2 Distal cells are present in the proximal domain 33
3.2.3 The mandibles arise from a small population of cells 33
3.3 Summary - Distal cells invade the proximal territory of the mandible 39

Chapter 4 Clonal architecture of teeth reveals the nature of heterodonty 40
4.1 Introduction 40
4.2 Methods 41
4.3 Results 42
4.3.1 Incisors are comprised of majority distal population and a minority presumptively proximal population 42
4.3.2 Mature molars are comprised of majority presumptively proximal population and a minority distal population 50
4.3.3 The mandible is derived from few distal cells, and is distinct from the alveolar bone 53
4.4 Summary - Heterodonty is underpinned by differing proportions of distal and presumptively proximal cells 55

Chapter 5 The Polyclonal Architecture of the Teeth and Associated Bones Demonstrates the Origins of Thecodonty 57
5.1 Methods 58
5.1.1 Labelling Strategy 58
5.1.2 Choice of PCA as an Analytical Tool 58
5.1.3 Implementation of PCA 60
5.1.4 Representation of Data 61
5.2 Results 62
5.2.1 The molars and associated alveolar bone are developmentally distinct from the mandible and maxilla in Wnt1-Confetti Labelled Tissue 62
5.3 The distal contributions to the molars also show modularity of tooth and alveolar bone, distinct from the mandible 70
5.4 Adjacent molars and alveolar bone arise from the same basal population, but are divergent from one another 83

5.5 Summary - Teeth and alveolar bones are cryptic developmental modules, distinct from the dentary bones 88

Chapter 6 Clonal Architecture of Teeth: A Discussion of Part I 91
6.1 Distal to Proximal Migrations in the Patterning of the Jaws 92
6.2 Distal cells in the specification of molar position 95
6.3 Heterodonty is a dynamical property arising from differential expansions of distal and proximal cells in time 98
6.4 Developmental and Evolutionary Nature of the Thecodont Tooth . . 100
6.5 Conclusions 105

II Global Clonal Architecture of the Mammalian Calvaria 107

Chapter 7 Introduction: A Novel invasive growth mode of dermal bones. 108
7.1 Anatomy of Calvarial Bone 109
7.2 Summary of the Work of Kate Jordan 110
  7.2.1 Following the invasive processes of polyclonal spread with Confetti 111
7.3 The Traditional Model of Sutural Growth 112
  7.3.1 Problems with the Sutural Model of Dermal Bone Development 112
7.4 Summary 113

Chapter 8 Obtaining Single Cell Resolution in Whole Mammalian Calvaria 115
8.1 Methods 116
  8.1.1 Choice of Clearing Method 116
  8.1.2 Microscopy 117
  8.1.3 Initial Processing 118
  8.1.4 Generation of Maps from Stacks 118
  8.1.5 Estimation of Cell Number per Layer 119
8.2 Results 121
  8.2.1 Anatomical Map and Landmarks 121
  8.2.2 The Four Confetti Colours are present in different proportions 121
  8.2.3 Single Cell Maps of Whole Calvaria 130
  8.2.4 Maps of Cell Density in Whole Calvaria 130
8.3 Summary - Maps of Confetti labelled cells within Layers show no evidence of sutural growth 138

Chapter 9 Mapping Horizontal Spreading of Single Presumptive Clones in the layers of Dermal Bone 139

9.1 Introduction 139
9.2 Methods 140
9.3 Results 142
  9.3.1 Early Confetti Labelling is Very Mixed 142
  9.3.2 Watershedding of blur maps reveals cryptic presumptively clonal patches 142
  9.3.3 Example Patch Maps show organisation within the Bone, and a generally homogenous morphology 142
  9.3.4 Patch Density maps reveal differences between layers 154
  9.3.5 Patch area is relatively constant between Layers and Samples, while Cell Density distribution varies across layers. 162
9.4 Summary: Potential Cryptic Modules revealed by mapping Horizontal Presumptive Clonal Spread 165

Chapter 10 Mapping Vertical Invasion between the Layers of the Calvaria 168

10.1 Introduction 168
10.2 Method 169
10.3 Results 173
  10.3.1 Invasion is polyclonal and can occur at specific points 173
  10.3.2 Layer Matching Maps 173
  10.3.3 Nested concentric points are visible across the samples 183
  10.3.4 Colour Matching resolves into lines 183
  10.3.5 The interfrontal bone displays a pattern of nested development 187
10.4 Summary - Invasion between layers appears organised 188

Chapter 11 Expansion and Integration of Polyclones in Three Dimensions 189

11.1 Introduction 189
11.2 Method 190
11.3 Results 191
  11.3.1 The Edge-Centroid Metric reveals correspondences between patches and layer matching, which are confirmed by observation 191
  11.3.2 Invasion between Layers 2 and 3 occurs at the centres of patches in both of these layers 195

11.3.3 Invasion between Layers 1 and 2 occurs mostly at the centres of Layer 1 Patches, and not always at Layer 2 patch centres . 195
11.3.4 Invasion of cells between Layers 1 and 3 occurs mostly through the centres of patches across all three layers. 196
11.3.5 Correspondence of Patch Shapes in different Layers, and of different Reporter Colours 202
11.4 Summary - Invasion between layers is largely organised to patch centres, and part of a three dimensional polyclonal spread 202

Chapter 12 Integrated Three Dimensional Clonal Expansion Predicts Bone Biomineral Thickness Growth 206
12.1 Introduction 206
12.2 Methods 207
12.3 Results 208
12.3.1 Layer 2 Thickness Maps do not support sutural definition of thickness growth 208
12.3.2 More Layer 1 and 2 patches are found in Thicker Bone, compared to Layer 3 212
12.3.3 The relationship between area and thickness suggests synchronous and asynchronous phases of layer maturation 212
12.3.4 Cell Density changes suggest three phases of layer maturation, with synchronous and asynchronous components 216
12.3.5 Preferential layer communication is linked to the thickness of the deposited biomineral 222
12.4 Summary: Clonal Dynamics Change as the Bone Grows Thicker . . 223
12.4.1 A common synchronous phase of layer establishment 223
12.4.2 Layer 1 Patch Maturation 223
12.4.3 Layer 2 Patch Maturation 225
12.4.4 Layer 3 Patch Maturation 225
12.4.5 Relationship between Layer matching and Thickness correlates with patch characteristics 226
12.4.6 Conclusions 226

Chapter 13 Clonal Architecture of Muscle Attachment Regions 229
13.1 Introduction 229
13.2 Methods 230
13.3 Results 233

13.3.1 Muscles attaching to the nasal bone share a common lineage with an island of bone they attach to. 233
13.3.2 Muscles attaching to the frontal bone around the eye share a common lineage with an island of bone they attach to. 237
13.4 Summary: A common progenitor population links bone and muscle . 241

Chapter 14 Polyclonal architecture of the sutures 243

14.1 Introduction 243
14.2 Methods, Regions of Interest and Predictions 244
14.3 Results 246
14.3.1 Sutures exclude bone-resident polyclones, and appear to allow for spreading of polyclones along their extent 246
14.3.2 Vertical polyclonal cellular communication in and around sutures. 249
14.3.3 Distinct polyclonal populations in the nasal and frontal bones are segregated by the polyclonal populations within the frontonasal suture 249
14.3.4 Distinct polyclonal populations in the two nasal bones are segregated by the nasal suture 255
14.3.5 Distinct polyclonal populations are present in the interfrontal and the frontal bones, segregated by apparently normal sutures.259
14.4 Summary - Sutural populations do not give rise to adjacent bones . 263

Chapter 15 Discussion: Cryptic Polyclonal Modularity Underpins Cranial Dermal Bone Development 266

15.1 Patch-like structures in human skulls 266
15.1.1 Wormian bones as evidence for the patch-based model 267
15.1.2 Craniolacunae explained in the patch model 269
15.1.3 The Patch model gives new insight into the evolution of micromery and macromery 269
15.1.4 Summary 270
15.2 Comparative Anatomy of the Interfrontal Bone 273
15.2.1 The interfrontal bone is a phenotypic trait in mice and rats . 273
15.2.2 Homologues of the interfrontal bone within birds 274
15.2.3 The interfrontal bone in amphibians 274
15.2.4 The interfrontal bone in lungfish 278
15.2.5 The interfrontal bone in humans 278
15.2.6 Summary of Comparative Anatomy 279

15.3 Reflections upon methodology 279
15.4 Summary of Novel Findings 280

Chapter 16 Concluding Remarks: Common Themes in the Polyclonal Architecture of the Jaw, Teeth and Calvaria 282

Appendix A Technical Information, Methods and Materials 284

A.1 Animal Work 284
  A.1.1 Husbandry 284
  A.1.2 Generation of Wnt1-Cre x Gt(ROSA)26Sor$^{tm1(CAG-Brainbow2.1)Cle}$/J Mice 284
  A.1.3 Generation of Hand2-Cre x Gt(ROSA)26Sor$^{tm1(CAG-Brainbow2.1)Cle}$/J Mice 284
A.2 Dissection 285
  A.2.1 Processing of Whole Calvaria 285
  A.2.2 Processing Samples for Sectioning 286
A.3 Simulating the founder effect in Confetti 286
A.4 Extending Stitching within ImageJ/FIJI 287
A.5 Principal Components Analysis as a means for interpreting Confetti data 288
  A.5.1 Pre-analysis steps 289
  A.5.2 Regional quantification of colour proportions 290
  A.5.3 Normalisation 293
  A.5.4 Implementation of the PCA 294
  A.5.5 Generation of a PCA Map 294
A.6 Imaging, processing and segmentation of calvarial images 294
  A.6.1 Automation of imaging 294
  A.6.2 Stitching of stacks 298
  A.6.3 Pre-Analysis processing 299
  A.6.4 Delamination segmentation 300
A.7 Flattening and Blurring 305
  A.7.1 Colour encoding procedure 305
  A.7.2 Normalisation of Blur Maps 307
  A.7.3 Trimming of Samples 307
A.8 Watershed analysis reveals single colour patches 310
  A.8.1 Quantifying features within watershed patches 311
  A.8.2 Tabulation and Plotting 312
A.9 Comparing colours in multi-dimensional space 313

  - A.9.1 Elaborations upon the Colour Distance principle. 314
  - A.9.2 Summary and generation of invasion maps 316
  - A.9.3 Comparing Colour Similarity and Bone Thickness 316
- A.10 Solutions 316
  - A.10.1 Mowiol 316
  - A.10.2 4% Paraformaldehyde 317

List of Tables

1.1 Multi-fluorescence lineage labelling constructs for use in *Mus musculus* 8

A.1 Details of Mice Used 285
A.2 Metrics for encoding colour similarity 315

List of Figures

1.1 The Confetti construct and its recombination behaviour. 12
1.2 Confetti reveals dynamics of initiation and growth 13
1.3 Developmental derivation and independence revealed by Confetti . . 14

3.1 Origin of Figures 3.7 and 3.8 27
3.2 The Founder Effect gives predictive power to the number of initiating cells 30
3.3 Proportion of the four Confetti labelling colours in a Wnt1-Cre/Confetti calvarium 31
3.4 The Founder Effect is useful even in the presence of very imbalanced labelling 32
3.5 Hand2-Confetti Expression in the distal branchial arches at E10.5 . . 34
3.6 Detail: Hand2-Confetti Expression in the distal branchial arches at E10.5 35
3.7 Distal cells invade the proximal territory by E14.5 36
3.8 Distal cells form the initial population of the molar mesenchyme . . 37

4.1 Sections used in this chapter 41
4.2 Distal populations form the majority of E16.5 Incisors 43
4.3 Presumptively proximal cells within the Incisor 44
4.4 Cryptic Polyclonal Boundaries within the distal populations of incisors 45
4.5 Distal cells form the majority of the second molar at E16.5 46
4.6 Polyclonal expansions of distal cells within the lower molars. 47
4.7 Polyclonal expansions of distal cells within the lower molars. 48
4.8 Cryptic Polyclonal Boundaries around the developing molar 51
4.9 Adjacent first and second molars have similar Confetti populations, but a large difference in the number of unlabelled cells 52
4.10 Reassembled lower dentition of the animal depicted in Figure 4.1A . 54

5.1 Sections used in this chapter 59
5.2 Sagittal section of an E18.5 first lower molar and mandible in a Wnt1-Confetti Mouse 63

5.3 PCA Map of the sample shown in Figure 5.2, demonstrating independence of the alveolar bone, odontoblasts and periodontal ligament of a first modal from the mandible. 64
5.4 PCA plots for Figure 5.3, demonstrating independence of the alveolar bone, odontoblasts and periodontal ligament of a first modal from the mandible 65
5.5 Sagittal section of an E18.5 third lower molar and mandible in a Wnt1-Confetti Mouse 66
5.6 PCA Map of the sample shown in Figure 5.5, demonstrating independence of the alveolar bone, odontoblasts and periodontal ligament of a third modal from the mandible. 67
5.7 PCA plots for Figure 5.6, demonstrating independence of the alveolar bone, odontoblasts and periodontal ligament of a third modal from the mandible. 68
5.8 Sagittal section of an E18.5 upper second molar and maxilla in a Wnt1-Confetti Mouse 71
5.9 PCA Map of the sample shown in Figure 5.8, demonstrating independence of the alveolar bone, odontoblasts and periodontal ligament of an upper second modal from the maxilla. 72
5.10 PCA plots for Figure 5.9 demonstrating independence of the alveolar bone, odontoblasts and periodontal ligament of an upper second modal from the maxilla. 73
5.11 Sagittal section of an E16.5 lower first molar and mandible in a Hand2-Confetti Mouse 75
5.12 PCA Map of the sample shown in Figure 5.11, demonstrating independence of the distal contributions in the alveolar bone, odontoblasts and periodontal ligament of a first modal from the mandible. 76
5.13 PCA plots for Figure 5.12, demonstrating independence of the distal contributions in the alveolar bone, odontoblasts and periodontal ligament of a first modal from the mandible. 77
5.14 Coronal section of an E16.5 lower first molar and mandible in a Hand2-Confetti Mouse. 78
5.15 PCA Map of the sample shown in Figure 5.14, demonstrating independence of the distal contributions in the alveolar bone, odontoblasts and periodontal ligament of a first modal from the mandible. 79

5.16 PCA plots for Figure 5.15, demonstrating independence of the distal contributions in the alveolar bone, odontoblasts and periodontal ligament of a first modal from the mandible. 80
5.17 Clonal heterogeneity in the incisor at P0 81
5.18 Alveolar bone adjacent to the incisor likely arises from the odontoblast population 84
5.19 Sagittal section of E18.5 upper first and second molars with maxilla in a Wnt1-Confetti Mouse. 85
5.20 PCA Map of the sample shown in Figure 5.14, demonstrating both similarities and differences between the two teeth modules, which are also segregated from the maxilla 86
5.21 PCA plots for Figure 5.20, demonstrating both similarities and differences between the two teeth modules, which are also segregated from the maxilla 87
5.22 Barplots of variance explained by each principal component in each Figure of this Chapter 90

6.1 Cell Lineage Tree of the Morphogenetic Field Model 93
6.2 Cell Lineage Tree of the Invasionary Model 94
6.3 Model of polyclonal compartmentation within the tooth 95
6.4 Model of Tooth Position Specification in the Absence of Long Range Signalling 97
6.5 Differential Distal and Proximal expansion defines the teeth 99
6.6 The proportion of distal cells may be sufficient to impart tooth type 101
6.7 Cryptic polyclonal architecture underpins thecodonty 103

8.1 Estimated Proportions of Confetti Colours 120
8.2 Bones within each sample 122
8.3 Flattened Cell Map Of Sample A, Layer 1 123
8.4 Flattened Cell Map Of Sample A, Layer 2 124
8.5 Flattened Cell Map Of Sample A, Layer 3 125
8.6 Flattened Cell Map Of Sample B, Layer 1 127
8.7 Flattened Cell Map Of Sample B, Layer 2 128
8.8 Flattened Cell Map Of Sample B, Layer 3 129
8.9 Blur Map Of Sample A, Layer 1 131
8.10 Blur Map Of Sample A, Layer 2 132
8.11 Blur Map Of Sample A, Layer 3 133
8.12 Blur Map Of Sample B, Layer 1 135

8.13 Blur Map Of Sample B, Layer 2 136
8.14 Blur Map Of Sample B, Layer 3 137

9.1 Conceptual basis of lateral spread leading to cell density loss 141
9.2 Wnt1 Confetti Labelling of the frontal bone at E14.5 143
9.3 Example of Patch Segmentation 145
9.4 Yellow Patches In Layer 1 of Sample A 147
9.5 Yellow Patches In Layer 2 of Sample A 148
9.6 Yellow Patches In Layer 3 of Sample A 149
9.7 Yellow Patches In Layer 1 of Sample B 151
9.8 Yellow Patches In Layer 2 of Sample B 152
9.9 Yellow Patches In Layer 3 of Sample B 153
9.10 Density of Patches in Layer 1 of Sample A 155
9.11 Density of Patches in Layer 2 of Sample A 156
9.12 Density of Patches in Layer 3 of Sample A 157
9.13 Density of Patches in Layer 1 of Sample B 159
9.14 Density of Patches in Layer 2 of Sample B 160
9.15 Density of Patches in Layer 3 of Sample B 161
9.16 Patch Area is broadly consistent across all Layers and Samples . . . 163
9.17 Layer 3 has very few dense patches, Layer 2 has more, and Layer 1 has the most 164
9.18 *Drepanaspis* sp. have patch like bony tiles between large plates. . . . 166
9.19 The extreme Wormian bone condition in Osteogenesis Imperfecta . . 167

10.1 Similar polyclonal combinations can be encoded as an image intensity in a Layer Matching Map 170
10.2 The Principle of ‘Colour Distance’ 172
10.3 Colour Encoding of Layer Matching 173
10.4 Sagittal section of an E18.5 Wnt1-Confetti frontal bone reveals vertically nested polyclonal invasions 174
10.5 Individual nested polyclonal invasions in Wnt1-Confetti 175
10.6 Non-Density Encoded Colour Matching of Sample A 177
10.7 Density Encoded Colour Matching of Sample A 178
10.8 Non-Density Encoded Colour Matching of Sample B 180
10.9 Density Encoded Colour Matching of Sample B 181
10.10 Examples of Roundel Patterning 184
10.11 Examples of Linear Patterning 185
10.12 Organised Layer matching in the Interfrontal Bones 186

11.1 Diagram of Edge Centroid Metric Results 190
11.2 Region of Sample A for Edge-Centroid result verification 192
11.3 Edge Centroid Results for Sample A 193
11.4 Edge Centroid Results for Sample B 194
11.5 Correspondence of Patches to Colour Matching between Layers 2 and 3197
11.6 Correspondence of Patches to Colour Matching between Layers 1 and 2198
11.7 Correspondence of Patches to Colour Matching between Layers 1 and 3200
11.8 Patches of different layers share geometry when linked by vertical invasion 203
11.9 Patches of different label colours share geometry 204

12.1 Thickness Map of Layer 2 in Sample A 209
12.2 Thickness Map of Layer 2 in Sample A 210
12.3 The Average L2 Patch Thickness of Layers 1 and 2 is greater than that of Layer 3 213
12.4 Sample A: Patch area shares a similar relationship with underlying Layer 2 thickness across all three layers 214
12.5 Sample B: Patch area shares a similar relationship with underlying Layer 2 thickness across all three layers 215
12.6 Sample A: Cell Density is related to Layer 2 thickness across Layers 2 and 3. 217
12.7 Sample B: Cell Density is related to Layer 2 thickness across Layers 2 and 3. 218
12.8 Sample A: Cell Density has no strong relationship with Patch Area across the three layers. 219
12.9 Sample B: Cell Density has no strong relationship with Patch Area across the three layers. 220
12.10Colour Similarity Between Layers Plotted Against Layer 2 Thickness 221
12.11Three broad phases of invasion between layers 224
12.12Layer invasion and patch dynamics are linked processes 228

13.1 Current Model of Enthesis Structure 231
13.2 Colour Scale of Layer 2 Thickness 231
13.3 Muscle Attachment Regions investigated 232
13.4 Sample A Muscle Attachment Region on Right Nasal Bone in Detail 234
13.5 Sample B Muscle Attachment Region on Left Nasal Bone in Detail . 235
13.6 Sample A Muscle Attachment Region Close To Left Eye in Detail . . 238

13.7 Sample B Muscle Attachment Region Medial to Right Eye Socket in Detail 239
13.8 Schematic of Neural Crest Mediated Muscle Attachment 242

14.1 Regions selected for PCA Analaysis 245
14.2 Predictions of sutural clonal architecture based on a traditional model of sutural growth 245
14.3 Anatomical location of Figure 14.4 within Sample B. 246
14.4 Cellular and Patch characteristics of sutures 247
14.5 Layer colour similarity at sutures 250
14.6 Visualisation of the PCA across the left frontonasal suture 252
14.7 Plots of Principal Component Analysis across the frontonasal suture 253
14.8 Visualisation of the PCA across the nasal suture 256
14.9 Plots of Principal Component Analysis across the nasal suture . . . 257
14.10 Visualisation of the PCA across the interfrontal bone 260
14.11 Plots of Principal Component Analysis across the interfrontal bone . 261
14.12 Barplots of variance explained by each principal component in each Figure of this Chapter 265

15.1 The extreme Wormian bone condition in Osteogenesis Imperfecta . . 268
15.2 Filamentous remnants of bone in craniolacunia is reminiscent of patch boundaries 271
15.3 Patch-like architecture in the garfish *Belone belone* 272
15.4 The interfrontal bone in ratite birds and neoaves 275
15.5 The composite ethmoid of the Ostrich, *Struthio camelus* 276
15.6 The tumescent casque of the hornbill *Ceratogymna elata* is likely homologous to the interfrontal bone. 277

A.1 Optimisation of scanning depth 297
A.2 Delamination plugin interface 303
A.3 Encoding of a 2D Colour Map 308
A.4 Encoding of a 2D Colour Map (Continued) 309

Acknowledgments

I would like to first and foremost thank my supervisor Professor Georgy Koentges, without whose guidance, insight and persistent faith, my work would not have been possible. In keeping with the tradition of my predecessor, I offer the words of another great teacher: οὐ γὰρ ὡς ἀγγεῖον ὁ νοῦς ἀποπληρώσεως ἀλλ᾽ ὑπεκκαύματος μόνον ὥσπερ ὕλη δεῖται ὁρμὴν ἐμποιοῦντος εὑρετικὴν καὶ ὄρεξιν ἐπὶ τὴν ἀλήτηειαν.

I would like to thank the rest of my lab group past and present, and particularly Sophia Gibbs, whom first brought the Confetti mice into the lab, Dr. Xintao Zhang for all of her training and assistance, and Frankie Dunn for her efforts in the early stages of this project.

Like any project, this was underpinned by an under-appreciated and often unseen team of support staff, whom are necessary for the functioning of a Department. As well as generally thanking all of them, I would like to give special thanks to Dr. Sam Dixon and Dr. Ian Bagley of the BSU for their assistance with the project, and to the imaging suite manager Mr. Ian Hands-Portman for tolerating and even encouraging my wanton abuse of both the microscopes and the scheduling system.

Finally I would like to thank all those who have supported me outside of science, both friends and family. I owe particular thanks to my father for providing me with accommodation during the write-up, and to my mother for providing me with cakes during the same period.

Declarations

I, John M.J. Lapage, confirm that the work presented in this thesis is my own and is submitted in its entirety in fulfilment of the degree of Doctor of Philosophy in Biology at the University of Warwick. No material included herein has been submitted for any other degree. I further confirm that information included in this thesis that derives from other sources is clearly indicated.

Abstract

While much of modern developmental biology has focussed upon molecularly defined cell populations, relatively little is understood about how clonal groups within these broad cell populations organise complex tissues. In this thesis, I explore the clonal architecture of the jaws and teeth, and of the dermal bones of the calvaria, revealing cryptic modules as novel developmental features in both. I combine Confetti multi-colour genetic lineage labelling with novel analytical techniques in order to map clonal populations in 3D and provide quantitative parameters for clonal expansions.

Tooth identity within the mandible is thought to be encoded by the an initial proximodistal position within the branchial arch, which implies that cells do not undergo migration. I observe distal Hand2-Cre labelled cells in the proximal territory, which necessitates migration. These distal cells give rise to the mandible, alveolar bone and a small proportion of odontoblasts, while unlabelled proximal cells were found in the distal territory of the incisors in different proportions. The clonal composition of teeth and jaw bones is dissected by novel analysis of mixed cell populations. I find odontogenic and alveolar bone populations to share a common lineage, comprising a cryptic developmental unit distinct from the mandible, a feature that I can also verify in another transgenic for the upper jaw. I also find that the initial tooth composition radically changes in ontogenetic time. Starting from similar compositions of distal and proximal cells I find that in incisors the distal population expands while the proximal wanes, while in molars the opposite occurs. This is the first evidence for a temporally changing cell population structure underlying the well defined heterodonty between incisors and molars and allows a reinterpretation of early tooth specification events.

The dermal bones of the calvaria are thought to grow in thickness by static osteoblasts depositing matrix appositionally and growth is supposed to occur exclusively at sutures. Whole calvaria single-cell clonal lineage analysis of cranial neural crest cells with Wnt1-Cre and Confetti labelling reveals an extensively dynamic program of invasive growth distributed throughout all parts of the dermal bone. Cryptic clonal modules grow laterally, with invasion through and into the bone primarily organised around the centres of these ‘patches’. The process of bone maturation is revealed to consist of a series of invasions between the three layers of the bone, with the innermost compacta layer driving initial thickness growth by invasion into the middle spongy layer, and the outermost (dermis-adjacent) compacta layer driving later growth. Conversely there is no evidence to suggest that the sutures are principal generative regions, as they do not share a common clonal lineage with adjacent bone. I also investigate muscle attachment regions and find that the same clones traverse tissue boundaries from bone into muscle connective tissues, thus a clonal model predicated on joint ‘attachment point precursor cells’ can now explain patterns of skeletomuscular connectivity previously found at the population level by my supervisor. A novel generative model of bone growth from cryptic clonal patch modules is proposed, allowing us for the first time to understand thickness growth and the evolutionary transition from a micromeric to a macromeric dermal bone condition, events first visible in crown gnathostomes (placoderms).

Chapter 1

General Introduction and Structure of this Thesis

1.1 Structure

This thesis explores the role of Neural Crest cells in two different regions of the mammalian head. The polyclonal architecture is discussed: the manner by which individual dividing groups of cells interact and cooperate to form structures.

Part 1 focuses on teeth and jaws. Following an introduction to the key concepts in Chapter 2, Chapter 3 inspects the validity of the widely held model by which tooth positions and types are specified. I demonstrate that cells which are traditionally thought to be confined to the distal end of the mandible and the incisors in fact contribute to the proximally located molars as well. I show that the basic tenet of current models is incorrect: *i.e.* that proximodistal gradient-based patterning on a stable cell population landscape is wrong. My approach discovers widespread dynamic migration processes hitherto unknown such that early distal cells are to be found proximally and vice versa

In Chapter 4 I demonstrate in more mature teeth the divergent polyclonal dynamics of incisors and molars. I propose a model of differential polyclonal expansions of distal versus proximal cells in incisors versus molars as a potential structural basis of tooth heterodonty. I furthermore reveal curious cryptic boundaries within the teeth and associated bones. In Chapter 5, I use a novel tool to resolve polyclonal boundaries in order to study the interrelationship between genetically labelled odontoblasts and adjacent periodontal ligament and alveolar bone. I map polyclonal commonalities which sheds light onto a hitherto unknown modular nature of teeth and periodontal structures separate from the adjacent jaw bones. Chapter 6 discusses and summarises the findings in a novel model of tooth development based upon migration of cells, polyclonal expansion and developmental modularity rather than long-range signalling.

Part II of this thesis explores the polyclonal architecture of the dermal bones of the head, particularly the frontal and nasal bones. Previous work by Kate Jordan in the Koentges lab (unpubl) that I was involved in had revealed a novel mechanism by which dermal bones grow. She identified that within the three-layer architecture of the dermal bone, the middle Layer 2 expands from the centre, necessitating invasion from the outer layers. To test the validity and scope of this invasive mechanism I attempted to establish the very first polyclonal maps of dermal bones at single cell resolution.

Chapter 8 describes the method by which two lineage labelled samples were generated and imaged as three dimensional whole mounts, at single cell resolution. These samples are then segmented into the layers of the skulls by novel tools, and prepared into maps that preserve the key three dimensional data but in a more easily manipulable two dimensional format. Broad structures are observed and discussed.

Horizontal spread of individual clones is explored in Chapter 9. Individual putatively clonal 'patch' regions are identified that recapitulate both disease state and important aspects of evolutionarily ancient micromeric conditions. These are shown to be remarkably consistent regardless of layer and position within layer, suggesting a decoupling of two previously aligned phenomena. Chapter 10 explores vertical invasion of cells through an entirely novel method of analysis that explores mixed populations in a different manner to that employed in previous Chapters. Local maxima and minima of interlayer migration are identified and discussed.

Chapter 11 integrates horizontal polyclonal spread and vertical invasion, seeks to explore the spatial relationship between layers in communication with one another and how cells spread within a single layer. Invasion between layers is found to spatially correspond to centres of horizontal spread in putatively clonal patches within those layers. Chapter 12 integrates the different independent strands of inquiry within the whole mount samples into one model of development, using biomineral thickness growth as a common unifying axis. This demonstrates polyclonal patches integrated across the layers of the skull represent developmental modules within large dermal bones.

Chapters 13 and 14 focus on polyclonal organisation in two higher-order structures.

Chapter 13 explores muscle attachment regions, and demonstrates that bone, tendon and muscle in muscle attachment regions all arise from the same small cellular population, which is distinct from the bone to which the muscle is attaching. In Chapter 14 the sutural model of growth is explored further, and shown to be unsupportable in light of the polyclonal patterning around sutures. An alternative model of suture formation is discussed, wherein cells from the bone give rise to the sutures, and there is only a small degree of migration between sutures and bones.

Chapter 15 discusses the findings of Part II as a novel model of dermal bone development based upon cryptic polyclonal patch modules. This implies a potential novel approach to understanding conditions such as craniosynostosis, as well as demonstrating the persistence of ancient micromeric structures in extant macromeric bones.

The Appendix consists of the methods and materials, but also includes detailed descriptions of the bespoke software developed to tackle the novel problems of this work. Though these approaches were created in response to specific problems, where possible the applications are designed in a generalised fashion, and can be applied to similar studies in other tissues, and with other experimental setups.

This thesis employs widely available technology in novel ways with new analytical approaches and tools, ultimately leading to a complete redefinition of how the teeth, jaw and calvaria develop.

1.2 A Brief History of Lineage Labelling

'Polyclonal Architecture' describes the divisional relationships of groups of cells within a structure, and how these individual lineages interact to form structures. If one knows which cells are more closely related to one another in divisional history and ontogenic time, inferences can be made about which anatomical structures are developmentally (and thus evolutionarily) related to one another, how individual structures are initiated and about cellular dynamics in unobserved timepoints. In order to accomplish this, a technique must be employed that encodes lineage information *in vivo*. This technique, which employs random time-controlled lineage labelling, is common to all parts of this thesis, and is discussed below in the context of other historical approaches.

1.2.1 Manual Labelling

Lineage analysis in large model organisms rely on a panoply of manually-directed labelling techniques, including the use of dyes [Bronner-Fraser and Fraser, 1988; Clarke, 1999], injector of reporter mRNA, photo-switchable markers [Nowotschin and Hadjantonakis, 2009] and particularly the generation of traceable chimeras [Rawles, 1947; Le Douarin and Teillet, 1974; Le Douarin and Jotereau, 1975; Lance-Jones and Lagenaur, 1987; Selleck and Bronner-Fraser, 1995; Stern et al., 1998] to answer the same question: what do the cells of this structure become at a later time point?

These techniques are obviously limited by the accessibility of the tissue. Furthermore they rely heavily on the *a priori* understanding of the tissue: if one is studying the development of a limb, these techniques can be used to observe how the cells of the limb bud adopt their fates, but not to detect the presence of cells from outside the limb bud invading the structure during development. The experimentalist must decide both what to label, and where to look for it later, creating a dependence on prior assumptions. It is also often very difficult to identify specific cell types at early stages

1.2.2 Genetic Labelling

Cre-lox recombinase [Sternberg and Hamilton, 1981; Sauer and Henderson, 1988], coupled with the growing advances in transgenic manipulation of mice has allowed for experimenters to access organisms on a different level: that of the specifying genes. A single tissue-specific Cre line can form the basis of many experiments when crossed with reporter cassettes revealing localisation of expression, or with lines containing excisable genes, allowing for tissue-specific chimeric mutation.

The nature of reporters has also changed. Early genetic labelling approaches used single colour reporters requiring fixation and chromogenic reactions, such as Beta-Galactosidase [MacGregor et al., 1991]. While many key discoveries were made using this system, which some groups use to this day, it is limited by the requirement for a development protocol in order to observe a colour. A genetically encoded fluorescent marker had to be found: not only would this allow for specific localisation within cells without the need for further protocols, but also the labels could be observed in live cells, and in three dimensions thanks to developments in confocal laser scanning microscopy [Shotton, 1989].

This label came in the form of Green Fluorescent Protein (GFP) [Shimomura et al., 1962; Prasher et al., 1992; Chalfie et al., 1994], a protein of the jellyfish *Aequorea victoria.* This small protein has largely defined the last 20 years of cell biology, as it allows not only genetic labelling in live organisms but also can be attached as a domain to many proteins, giving insight into their function and locations.Heim et al. [1995] demonstrated that mutations within the sequence could modify and improve the characteristics of GFP, which lead to the generation of a spectrum of GFP derivatives. In addition novel fluorescent proteins have been derived from diverse biological sources and themselves modified to produce useful biological labelling tools, reviewed in Kremers et al. [2011].

The analytical downside of marker-based lineage labelling is that it commonly produces large and inscrutable labelled populations. Biology is not so kind that each cell has a distinctive gene that can be exploited for research, and some cell types are defined by combinatorial identities and thus are more difficult to label. This limitation can be circumvented by labelling random groups of genetically definable cells within a population, and analysing the resulting patterns. The Brainbow suite of reporters, originally developed to dissect circuitry in the CNS, is one of the most well-known of these strategies, relying on multiple Lox paired recombination sites to give random colouring.

1.3 The Confetti Reporter Construct

This thesis relies heavily upon the Confetti reporter construct as described in Snippert et al. [2010] and displayed within Figure 1.1A. This construct consists of the Brainbow 2.1 construct [Livet et al., 2007] downstream of a strong CAGGS promoter and preceded by an additional loxP-flanked PGK-Neo^r-pA cassette, which acts as a non-fluorescent transcriptional roadblock. The composite construct is inserted in the Rosa26 (R26R) locus. In brief, this construct gives constitutive and near-ubiquitous transcription of the PGK-Neo^r protein until Cre-mediated recombination, through multiple excisions and inversions, selects one of four fluorescent proteins. The reasons for selecting this construct and a more full description of its behaviour are described in this section.

1.3.1 The Brainbow suite

At the time of our selection of Confetti by my colleague Sophia Gibbs, the first two generations of Brainbow reporters were available, with the third generation being published shortly afterwards. The core suite of tools known as Brainbow were designed with neuroscience experiments in mind. Standard Brainbow experiments use ubiquitously expressed Cre, with the Thy1 promoter used to drive expression in a small number of neurons. This elegant design has allowed for great insight into neural circuits, but has limited the flexibility and transferability of the reporter for developmental investigations as the Thy1 promoter is specific to neurons. Thus Brainbow-derived experiments in other tissues such as bone must use reporters with alternative promoters swapped in.

The core Brainbow suite has three distinct generations, outlined in table 1.1, all of which use the same Thy1 regulatory region. Brainbow 1 and 1.1 both follow the same design principle and utilise two and three pairs of non-complementary Lox recombination target sites respectively. Any recombination will remove one site from the other pairs, thus ensuring that only one excision may occur.

The second generation consists of a prototype, Brainbow 2.0, and a commercially available derivative Brainbow 2.1. Brainbow 2.0 consists simply of a pair of opposing LoxP sites flanking a GFP and a reversed YFP. Upon recombination this cassette inverts to bring the YFP under regulatory control, silencing the GFP. Further inversions may occur. 2.1 expands upon this idea by adding a second identical cassette downstream, containing a CFP and an RFP. 2.1 can also undergo excisions, leaving only one cassette.

The third generation of Brainbow returns to the design principle of the first generation, but with some valuable novelties. Further work was done to select the fluorescent proteins for 3.0, with the selection of three proteins from originating from different species which can be identified independently by antibodies. This means that labelling can be recovered after bleaching or quenching of the fluorophores. The proteins also have superior spectral separation compared to those in the first generation. Brainbow 3.1 added a further improvement shared with Confetti, and added an additional non-fluorescent protein that is constitutively expressed. This is a non-fluorescent mutant of YFP called ∅NFPnls, which can also be identified by antibody. This is likely a superior alternative to Confetti's PGK-Neo^r, as ∅NFPnls is likely to have similar dynamics within the cell as the true fluorescent proteins when overexpressed. Brainbow 3.2 further improved upon this concept by adding

CMV-Woodchuck elements to the ends of each coding region, which prevent RNA degradation and thus increase protein yield per transcript.

1.3.2 Confetti and its alternatives

A small number of constructs have been created which dispense with the Brainbow Thy1 promoter in favour of ubiquitous expression of the reporter, with selectivity coming from the choice of Cre promoter. This generalises the approach to almost any tissue. At the time this project was instigated there were two available: R26-Rainbow [Rinkevich et al., 2011], and Confetti [Snippert et al., 2010]. R26-Rainbow mimics Brainbow 1.1, giving constitutive expression of one colour (in this case GFP) which is randomly replaced by one of three colours after a single excision. Confetti contains the Brainbow 2.1 cassette downstream of an additional non-fluorescent neomycin gene, resulting in four possible colours from a series of excisions.

Confetti was the obvious choice of the easily available lines. The lack of fluorescent background does mean sacrificing an internal control, but eases an already burdensome imaging regime. Furthermore the four colours allow for the best single-colour resolution, while multi-colour combinatorial labelling in a single cell would again require redesign of the reporter.

1.3.3 Applications of Random Genetic Lineage Analysis

A previously mentioned, Brainbow was originally designed for use in deciphering neural circuitry: labelling individual cells and their processes in a manner that would allow for observation of fine circuitry [Livet et al., 2007]. This neuroscientific pedigree is borne out in the continued use of the brain-specific Thy1 promoter with a ubiquitous Cre, rather than a more common developmental biology arrangement of a ubiquitous reporter construct and a tissue-specific Cre line. Confetti was developed from Brainbow 2 in order to generalise its utility to many developmental problems.

Another attempt to use a randomised multi-colour reporter in a more general developmental biology context was in *Drosophila*. Hampel et al. [2011] reported the generation and use of 'Drosophila Brainbow', which represented a Brainbow-1-based fluorescent cassette under the control of the commonly used UAS promoter, allowing for spatial targeting with any of the thousands of tissue-specific Gal4-expressing lines available. At effectively the same time another group prepared and demonstrated a Brainbow-2-based reporter in *Drosophila*, which they termed 'Flybow'

Table 1.1: Multi-fluorescence lineage labelling constructs for use in *Mus musculus*

Designation	Reference	Transcription Control	Constituitive Protein	Selectable Proteins
Brainbow 1.0	Livet et al. [2007]	Thy1	dTomato (RFP)	mCerulean (CFP), mYFP^{A206K}
Brainbow 1.1	Livet et al. [2007]	Thy1	Kusabira-Orange OFP	mCerulean (CFP), mYFP^{A206K} mCherry (RFP)
Brainbow 2.0[a]	Livet et al. [2007]	Thy1	mCerulean (CFP)	mCerulean (CFP), tdimer2 (RFP)
Brainbow 2.1	Livet et al. [2007]	Thy1	hrGFPII	mCerulean (CFP), hrGFPII, mYFP^{A206K}, tdimer2 (RFP)
Brainbow 3.0[b]	Cai et al. [2013]	Thy1	mOrange2	eGFP, mKate2 (Far-RFP)
Brainbow 3.1 and 3.2[c]	Cai et al. [2013]	Thy1	∅NFPnls[d]	mOrange2, eGFP, mKate2 (Far-RFP)
R26-Rainbow	Yanai et al. [2013]	R26R-CAGGS	EGFP	mCerulean (CFP), mOrange, mCherry (RFP)
Confetti[e]	Snippert et al. [2010]	R26R-CAGGS	PGK-Neo^{r}	mCerulean (CFP), hrGFPII, mYFP^{A206K}, tdimer2 (RFP)

[a] Not commercially available - published prototype for 2.1

[b] Not commercially available - published prototype for 3.1

[c] Differs from 3.1 only in that CMV-Woodchuck elements are appended to each protein.

[d] Non-fluorescent protein derived from *Phialidium* YFP

[e] Derived from Brainbow 2.1

[Hadjieconomou et al., 2011].

It is no great surprise that Drosophilists were eager to attempt this approach, as not only does the fruit fly represent a very tractable model organism, but also other types of randomly initiated genetic mosaic analysis has long been an element of the field. The Mosaic Analysis with A Repressible Cell Marker (MARCM) technique developed by [Lee and Luo, 2001] labels one daughter lineage in a random assortment of active cell divisions at the time of induction. This was further extended to detectably label both daughter lineages by [Griffin et al., 2009] and the 'Twin Spot Generator' which built upon an earlier reporter developed by Luo for use in mice [Zong et al., 2005]. Using these single-lineage techniques experimentalists could analyse many animals and build up a map of all of the distinct lineages which had diverged from the point of induction, and their fates [Cachero et al., 2010]. In effect, the applications of Brainbow-like approaches in *Drosophila* built upon this paradigm of selecting out presumptively clonal lineages.

The majority of mammalian experiments using Brainbow or Confetti rely upon expression of an inducible CreER, which is intended to catalyse recombination only in the presence of Tamoxifen [Hayashi and McMahon, 2002]. This allows for temporal control of recombination, at the expense of making full degeneration unlikely if the expression window is short, leading to significant unlabelled populations. The studies for which Confetti was first designed [Snippert et al., 2010; Schepers et al., 2012] utilised CreER under the control of appropriate tissue specific drivers, and made very fine observations about the nature of intestinal crypts and the stem cells which populate them. However as there was no mixture of expanding clones, both studies made reasonable interpretations of simple cohesive patterns, similar to Figure 1.2A, thus creating a limitation upon how confident one could be in suggesting that a patch of cells was indeed monoclonal.

Despite the obvious wealth of knowledge that this sort of labelling promises, most applications of random lineage labelling rely entirely on reasonably valid but ultimately subjective interpretations of simple patterns, without considering quantitative means of interpreting more complex mixed populations, in a polyclonal or perhaps more descriptively a 'metaclonal' fashion. A number of methods for interpreting mixed polyclonal populations are presented in this thesis, and will be discussed within the appropriate Chapters where they are employed. The remainder of this chapter will explore the behaviour of the Confetti construct, which must be well understood in order to properly interpret its outputs.

1.4 Description of Confetti Behaviour

Unlike the majority of the Brainbow variants which rely upon non-complementary pairs of Lox recombination target sites, Confetti relies upon five complementary LoxP sites, any of which can in theory interact with any other. Furthermore, some interactions will occur between sites that have inverse orientation to one other, leading to inversion rather than excision. This means that successive rounds of recombination can re-arrange the locus. This behaviour is depicted in Figure 1.1B.

This random reassortment leads to 52 functionally distinct conformations, excluding inversions of the non-coding region between the two colour cassettes. These can be grouped into five sets with distinct recombination behaviour. While excision is not an absolute certainty in any individual recombination reaction, it is irreversible unlike inversion. After a number of recombinations one can be assured that the majority of cells will have recombined such that they possess a 'degenerate' form consisting one of the two colour cassettes, depicted outlined by a purple dashed line within Figure 1.1B. At this point, further recombination will simply invert the colour cassette.

A key characteristic that must be noted is that unlike other Brainbow variants, the colour expressed can be lost or altered through subsequent recombination. In fact, due to persistence of the fluorescent protein, dual-colour cells can be observed when a fully degenerate form is continuing to recombine frequently. This phenomenon is not important when one can be sure that Cre activity has ceased through regulatory control or use of an inducible recombinase, but when Cre can be known to persist, the possibility of further inversions of the locus must be considered within any interpretation of the data.

If one assumes that all possible recombinations are equally likely, the proportions of colours obtained will be skewed slightly in the favour of the red and cyan cassette. This is because the asymmetry of the construct means that from the original state, there are two possible excisions which could remove the green and yellow cassette, and only one which may remove the red and cyan cassette. One would further assume that within these pairings, an equal probability of green to yellow and red to cyan would be achieved after an arbitrary number of recombinations. This is however not observed. GFP is reliably less observed than all other colours, a feature observed by [Snippert et al., 2010], who further report that yellow:red:cyan were observed in equal proportions in their experiments. As shown later, using the estimates of cell counts employed in this thesis the proportions are approximately 70% Yellow, 20%

Cyan, 10% Red and less than 1% Green (from Figure 8.1).

1.5 Deciphering Biological Relevance from Confetti

While Confetti produces undeniably beautiful samples, one must also be able to interpret relevant information from these collections of colours. Key observations within this thesis includes arguments around polyclonality against monoclonality, static against dynamic cell populations, and developmental derivation against independence. It is important to note that all patterns can only be interpreted with reference to the stage at which they were labelled. The definitions of 'polyclonal' and 'monoclonal' only apply to divisions that occur after labelling.

On a simple level, it is easy to recognise a presumptively monoclonal region, or a simple polyclonal region (Figures 1.2A and B respectively). However attempts to derive information solely from the presence of adjacent colours fall into a common trap of assuming that regions of adjacent common cell label colour must arise from a common progenitor, when really the probability of independent selection of the same colour is relatively high. Regions with no apparent organisation (Figure 1.2C) can occur as a result of several different processes. Newly labelled populations take on such a randomised pattern, so this could represent a region that has not undergone division since labelling. Alternatively this could represent a polyclonal population much like in Figure 1.2B that has simply undergone mixing. Notably, it is relatively unlikely that two small progenitor populations will independently adopt the same abundances of the different labels, so relative mixtures of the different colours can be informative.

Interpretation of patterns across large groups of cells can be very insightful. Figure 1.3 represents a hypothetical situation where each tooth derives from single cells. Bilateral labelling as in 1.3A would suggest developmental derivation, with each tooth on either side either deriving from the same population or each tooth giving rise to the next. An alternative would be the arrangement shown in 1.3B, where there is no overall pattern, demonstrating developmental independence of each tooth.

It should be noted that such observations must be considered with respect to both anatomical features and the timing of labelling. Defining a 'region' for consideration is traditionally a subjective exercise. A clear border between polyclonally discrete regions running through a known anatomical feature such as a bone might represent a conserved cryptic development boundary, revealing two parts of a structure as

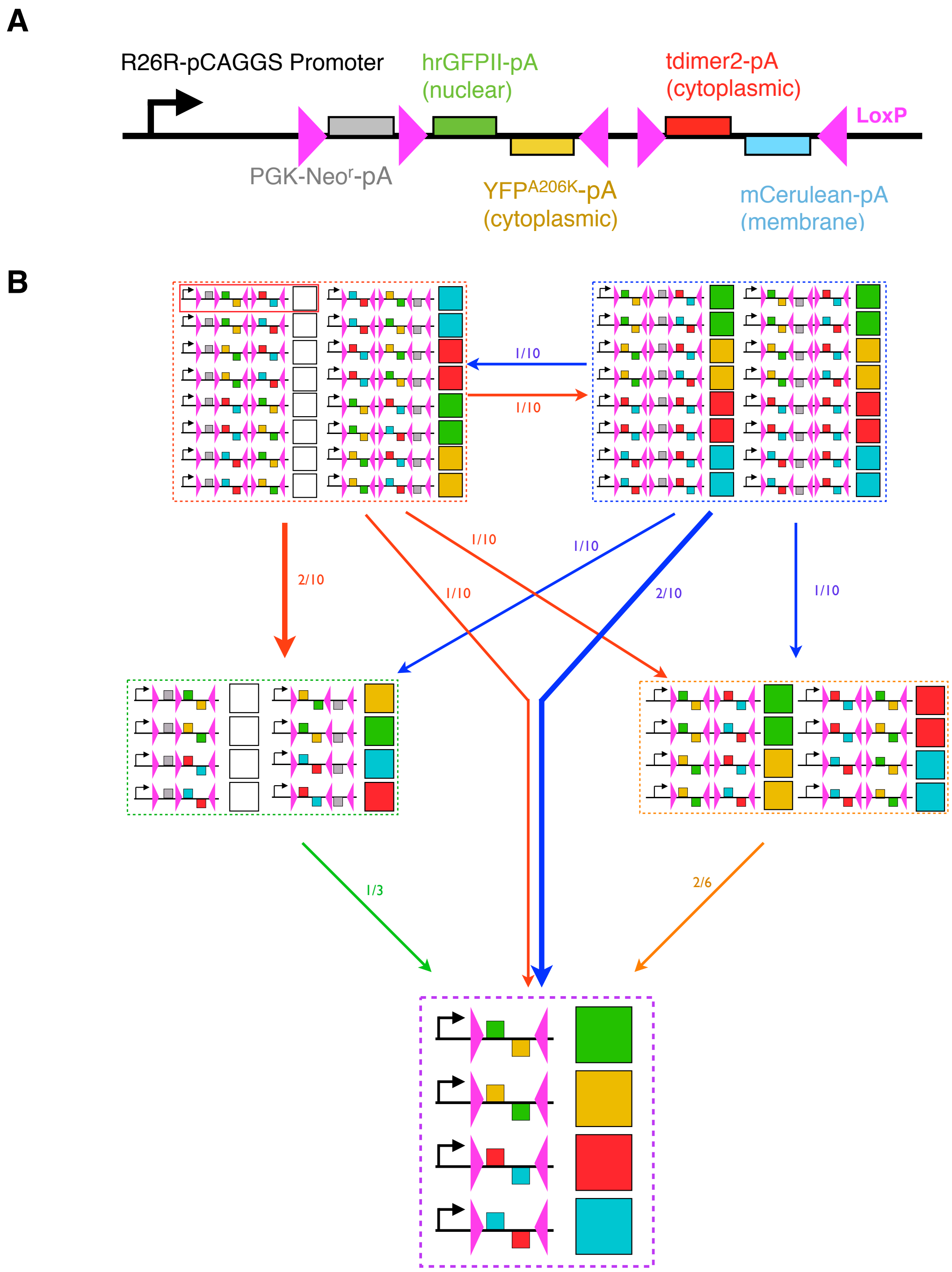

Figure 1.1: The Confetti construct and its recombination behaviour. A: Diagram of the Confetti reporter, with protein-coding regions marked as boxes and LoxP sites as magenta triangles. **B:** The original Confetti construct is marked with an unbroken red outline. Colour output is denoted within the squares to the right of each form. Arrows denote possible conformation changes and their probabilities as a proportion of the possible recombinations that may occur. Residual recombinations will give a different conformation within the same set.

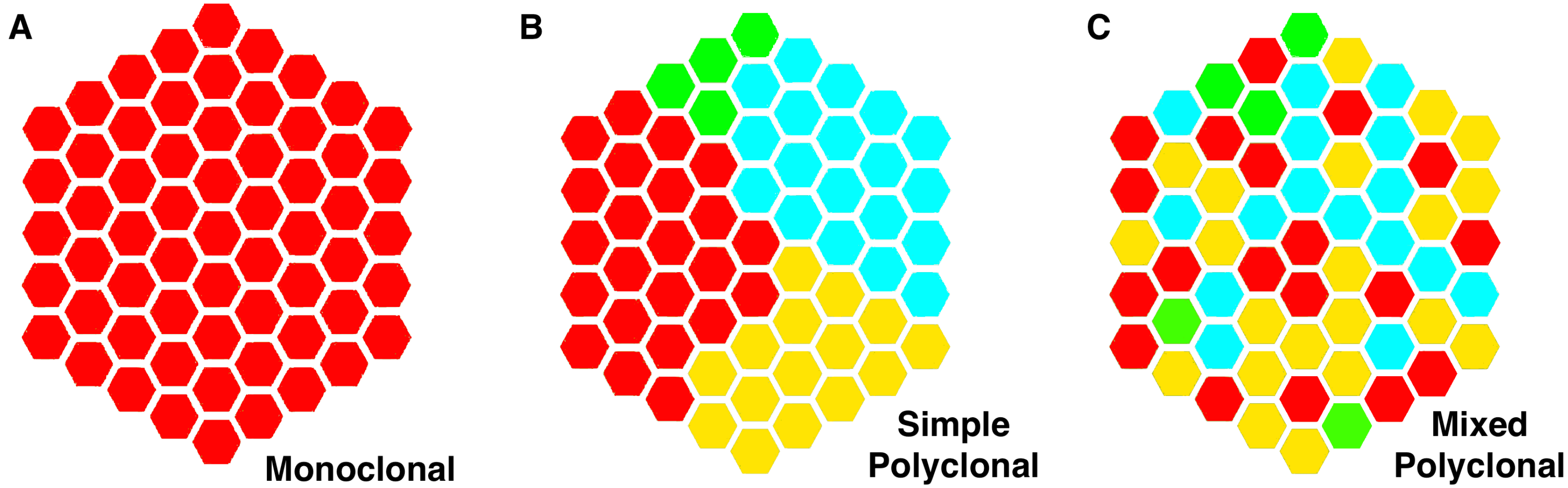

Figure 1.2: Confetti reveals dynamics of initiation and growth. Hexagons represent cells expressing one of the four Confetti colours. **A:** A group of cells derived from a single cell will share the same colour. However, the presumption of monoclonality in this instance is very likely inaccurate **B:** A group of cells derived from a few cells that do not undergo mixing will appear as contiguous groups of colour. While it can be assumed that groups of different colours are of independent origins, within these groups monoclonality cannot be safely assumed. **C:** A newly labelled population will appear entirely mixed, but the same arrangement can come about by mixing of a polyclonal population. No useful interpretation of monoclonality can be made from such patterns. However the relatively abundances of different labelled populations are unlikely to be independently replicated in two different progenitor populations, which can be informative.

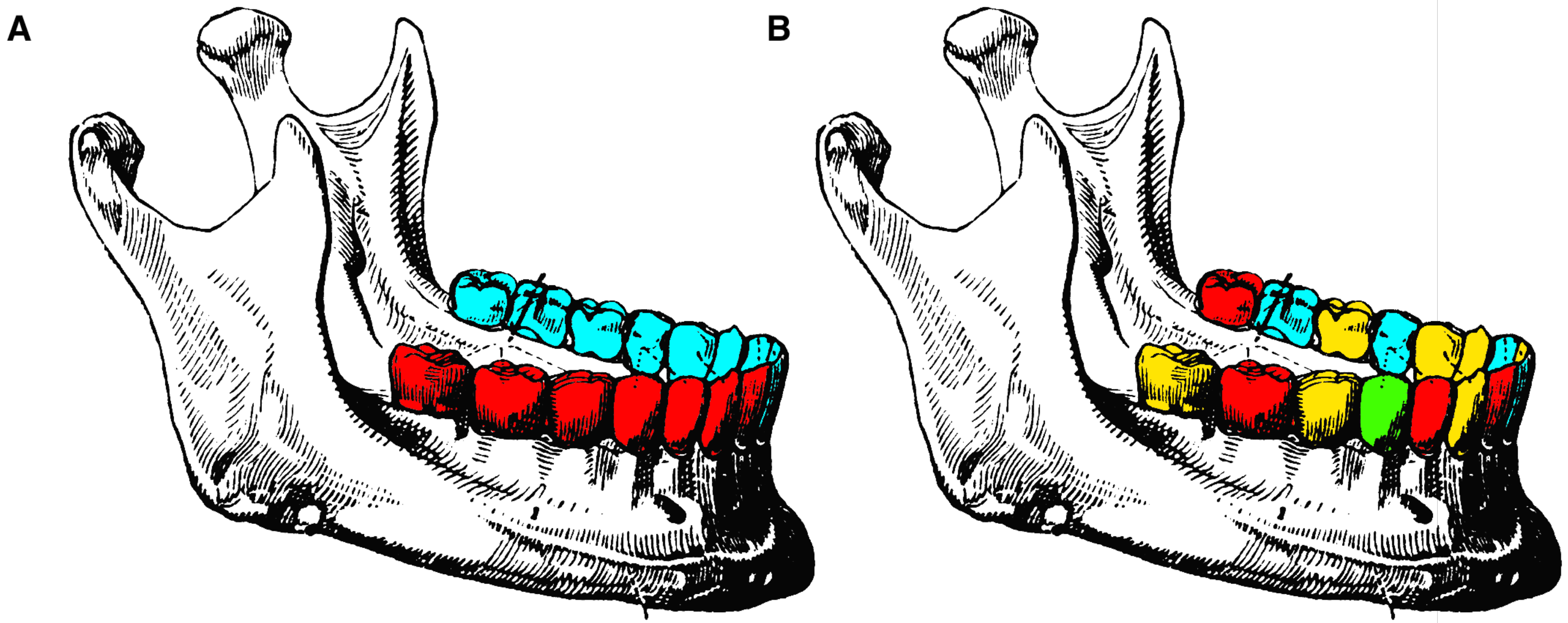

Figure 1.3: Developmental derivation and independence revealed by Confetti. Both examples assume a hypothetical situation where each tooth is monoclonal. **A:** Continuous colour along both tooth rows would suggest that the left and right rows of teeth were each derived from one clone each. **B:** Conversely, random colouring would suggest that each tooth is developmentally independent.

developmentally modular units. Conversely, development boundaries that seem to ignore known anatomical boundaries, such as finding that a bone is polyclonally similar to an attached muscle, could reveal unknown developmental relationships and cryptic compartments similar to what Kontges and Lumsden [1996] discovered with rhombomerically defined attachment regions of musculature in the avian head skeleton.

Novel analytical techniques capable of deriving information from polyclonally mixed populations are key to elevating Random Genetic Lineage Labelling from the a narrow set of applications to which it is currently applied, and into the realm of universally useful techniques. It has already been shown to be serviceable in several species, and can enhance the output of existing expression control systems. It is simply a matter of making sense of what is being reported when the cells do not behave in a cohesive manner. Techniques for accomplishing just this aim are presented in this thesis.

1.6 Summary of Confetti Lineage Labelling

Random lineage labelling allows for the dissection of populations that cannot be discriminated by exploitation of promoters alone. Confetti represents the best general mammalian lineage reporter cassette available, allowing for four-colour reporting of any Cre activity. However, most experiments use such labelling strategies to either extricate individual cells, or label contiguous unmixed patches. In this thesis many mixed populations are observed, which requires an entirely different analytical approach. The software designed to tackle these problems are introduced in each Chapter and discussed in-depth in the Appendix. The use of Confetti and possible improvements is discussed in Chapter 15. Animals used in this thesis are detailed in Table A.1, as well as in each section where appropriate.

Part I

The basis of heterodonty, thecodonty and tooth specification

Chapter 2

Introduction

Teeth are an ancient part of craniofacial anatomy. Tooth position and morphology is tightly controlled within species, and yet there is a vast variety of shapes, sizes and strategies. This introduction will cover key differences in tooth biology, and discuss the two principal theories of tooth formation.

The canonical mammalian condition is to have up to four types of teeth in the same row and affixed by a ligament into a bony cup in the jaw. Many but not all clades have two sets of teeth, one for infant stages of life and one adult set, but some such as rodents have continuously growing incisors and a few unrelated clades continuously replace lost teeth, such as kangaroos, elephants, manatees and crocodiles. While there are secondary losses of specific teeth and in extreme cases total loss of teeth such as in anteaters and pangolins, mammals largely have the same organisation underpinning their remarkably varied dentition. Despite their importance and accessibility, surprisingly little is known about how teeth are specified with respects to their position, type, and developmental timing. The current dominant model and its less popular alternative are discussed here, in relation to these biological questions.

The second big issue of great evolutionary significance is that of the origins of teeth and dermal bones. Early comparative anatomy has sought to link the modular units of teeth and dermal bones in the concept of odontodes. Each tooth in primitive vertebrates is associated with a bone of attachment, a basic dermal bone. Many times in evolution teeth/denticles and the underlying dermal bone were decoupled from each other, leading either to loss of dermal bones and retention of teeth and denticles such as in sharks, or loss of denticles with retention of dermal bone such as found in the tetrapod skeleton. Within the jaws proper teeth have lost many times independently in evolution [Louchart and Viriot, 2011], suggesting that there is some kind of modularity and shared lineage between teeth and its associated alveolar bone. The exact relationship between teeth, alveolar bones and the underlying dermal bones has never been investigated at the polyclonal level.

Both these evolutionary and developmental questions have been previously unaccessible. Multi-colour lineage labelling tools like Confetti have unlocked the gate on this avenue of enquiry, though novel software tools and methods of analysis were required to allow us to open that gate and lay bare the polyclonal architecture of the teeth and jaw.

2.1 Proximodistal Specification of the Tooth Row

The first observable event in the development of the tooth is an invagination of the dental epithelium [Jernvall and Thesleff, 2012]. The control of position in these invaginations is highly controlled, as the resulting teeth need to grow cooperatively with their neighbours, and also often require good correspondence with teeth in the other jaw.

Denticles and teeth are modular units, emerging from developmental 'odontodes', the regions of unique, point like epithelio-mesenchymal interactions [Fraser et al., 2010]. Despite their serial nature there is regional diversity, on denticles at the outside of the body or within the tooth row. It is widely held that the tooth row and the process of specifying tooth position and identity is governed by long-range signalling events within branchial arches. Inside these arches, cell populations are considered to be 'stable' components of a morphogenetic field that are being subjected to gradient sources of signals, such as Bone Morphogenic Proteins, Fibroblast Growth Factors and Sonic Hedgehog [Vainio et al., 1993; Tissier-Seta et al., 1995; Tucker et al., 1998; McCollum and Sharpe, 2001; Tucker and Sharpe, 2004; Townsend et al., 2009].

The key tenet of this model is the stability of the underlying mesenchymal cell population: if the spatial organisation at an early patterning stage directly translates into the spatial position and cell fate of the mesenchyme then the cells must not migrate our of their fate-defined positions. This is similar to the developmental patterning processes of the developing spinal cord [Yamada et al., 1991; Tanabe and Jessell, 1996; Jessell, 2000] or the fly imaginal disk [Wolpert et al., 2015]. Thus differential deployment of signalling molecules along particular axes is responsible for the regional diversity of the emerging mesenchymal cell populations. In the mouse this leads to a distinct incisor-forming distal territory, segregated from a proximal molar-forming territory.

Another key problem with this model is revealed by Barron et al. [2011]. Hand2 is one molecular marker of the distal, presumptively incisor-bearing region of the jaw, and is co-expressed with the distal marker Msx1 [Thomas et al., 1998; Ruest et al., 2003; Ryll, 2010]. Knock-out of this gene in the jaw ought to affect distal structures, namely the end of the mandible and the incisor. However, quite the opposite is observed: the proximal territory consisting of the mandible and the molar-forming regions are entirely abrogated, while the distal territory (incisor and associated bones) do indeed develop, albeit abnormally. The necessity for a distal gene in development of the proximal territory suggests that the static tooth specification proposed by the morphogenetic field model might not be accurate, or at least that a long-range signalling process is required to explain a phenotype in proximal molars when Hand2 is only expressed distally in nonmolar progenitor tissues.

The progress zone model outlined by Osborn [1978] and further discussed by Atchley and Hall [1991], represents an almost entirely forgotten alternative to the morphogenetic field model. This was developed on the basis of observing alligator dentition patterns and the emergence of tooth rows. It requires a migrating population which specifies tooth position and type by deposition of clones as seed-like inducers of new teeth. Osborn favoured a molecular signalling mechanism wherein one tooth bud would suppress the formation of any other buds within a certain range of the tooth, much like bud inhibition in plants. However, a clock-specified deposition of tooth buds would also be conceptually possible, similar to the progress zone model of somite specification [Maroto and Pourquié, 2001]. This would imply some form of shared lineage between adjacent teeth, the nature of which would depend on the number of cells migrating and dental mesenchymes and/or epithelia. A distal to proximal migration of cells would explain the observations of Barron et al. [2011], as lack of this necessary migration could lead to the observed suppression of the proximal territory. Lumsden [1979] also provides evidence for a model requiring migration, as explants of presumptive first molar tissue were capable of forming multiple molars.

We wished to test this central component of the widely accepted morphogenetic model by investigating in how far the distal population of branchial arch mesenchyme stays distal during development of the tooth row. In the morphogenetic field model, no migration of cells is necessary or predicted, and furthermore no particular polyclonal patterns are predicted: the tooth may form from the same tissue as the bone dependent on which molecular signals are received. Observation of distal cells in proximal structures such as the molars would completely undermine the fundamental requirement of morphogenetic stability in the widely accepted model. Furthermore, if such a migration does exist then Confetti labelling will allow us to observe any potential relationship between migratory cells, and thus test Osborn's progress zone model. This shall be first investigated in the next Chapter, and discussed in Chapter 6.

2.2 Heterodonty in mammals

Heterodonty describes the condition wherein several different types of teeth develop, such as incisors and molars, as opposed to homodonty, wherein all teeth have the same morphology. Heterodonty has evolved several times independently in evolution [Gregory, 1920; Jernvall and Thesleff, 2012].

Osteichthyans have an inner and an outer tooth row in upper and lower jaws [Janvier, 1996]. At the base of sarcopterygians in animals like Onychodus [Long, 1991] centrally located tooth-whorls are phenotypically different from other teeth in the same row. Moreover in tetrapods the teeth of the inner tooth arcade are bigger than those of the outer one, leading to significantly sized fangs at specific locations [Clack, 2012]. However further on in the tetrapod crown group homodonty is prevalent as it is in extant amphibians. the initial amniote heterodonty was lost again several times independently, within the archosaurs and also within the synapsids and mammals. As a case in point, in many cetaceans teeth have become secondarily homodont again, however tooth shapes or lengths can still vary along the tooth row [Armfield et al., 2013]. Total tooth loss or 'edentulism' is also independently found in many mammals, including pangolins and anteaters [Meredith et al., 2013].

Heterodonty within the same tooth row is found to be a widespread feature among mammals. It is considered to be a historical left-over of heterodonty in the amniote stem group, from the so-called cotylosaurians as the first tetrapods with heterodonty, occlusion and alveolar bones [LeBlanc and Reisz, 2013]. In this group for the first time incisiform and molariform tooth types can be distinguished within the same tooth row. Curiously no gene mutation or misexpression of genes has so far led to respecification of tooth types in non-mammalian amniotes. Mammalian heterodonty is well reviewed by Stock et al. [1997].

There are two key questions regarding heterodonty that remain unresolved: how each tooth bud fate is specified and the process by which a tooth bud adopts its distinct morphology. As outlined above it is broadly assumed that the epithelium is responsible for tooth initiation, but Kollar and Baird [1969] classically demonstrated that *in vitro* tooth germs comprising heterologous mixes of incisor and molar epithelium and mesenchyme will always adopt the tooth type of the mesenchyme, demonstrating its primacy in heterodont specification.

The only experiments potentially pertinent to either question were those by Tucker [Tucker et al., 1998] where implantation of noggin beads in the distal territory led to a 'molarization' of distal teeth. As noggin is a direct inhibitor of distal BMP signalling this was used so far as the one (and strongest) piece of evidence for gradient based acquisition of regional identity. Interestingly, noggin also affects neural crest migration [Sela-Donenfeld and Kalcheim, 1999] but because migrations were so far not traceable, this potential alternative explanation of disrupted migration rather than disrupted local signalling was disregarded.

The opposite transformation of molar into incisor was never accomplished. Currently it is believed that changes in signalling on the basis of a stable cell population map are responsible for the morphological changes in tooth shape later on. The progress zone model on the other hand could explain this by molariform teeth arising from mixed proximal and migratory distal populations, while incisors arise from the distal population that do not migrate. In any case, the exact place of tooth induction and elaboration has never been mapped experimentally onto the proximodistal branchial arch map as defined by distal or proximal expression patterns. It should be noted that no reliable proximal marker has been identified, and that it is perhaps better defined as the absence of distal markers.

The second question regarding morphogenesis of teeth is a more complex issue than specification of tooth type. This involves the coordination of many hundreds of cells as well as orchestration with adjacent teeth, bone and the opposite jaw. Recently this process has been very excitingly explored through computational modelling of tooth development [Salazar-Ciudad et al., 2010; Harjunmaa et al., 2014], which can recapitulate even very complex tooth morphologies based on three genetic components and seven physical characteristics of the tissue. However, no *in vivo* cellular differential has been observed between the incisors and the molars that might explain why different tooth morphologies arise, particularly with respect to non-identical teeth of the same type.

The strong prediction of proximodistal stability in the morphogenetic field model allow me to easily test this hypothesis simply by observing whether polyclonal populations within the different tooth types behave differently. Mixed distal and proximal populations have never before been observed within the teeth, but if they are present then differential expansion of the two populations may provide a foundation for the development of heterodonty in the absence of long-range signalling. This shall be addressed in Chapter 4, and discussed in Chapter 6.

2.3 Modes of tooth attachment

'Thecodont' comes from the Latin 'socket-tooth' and describes animals such as mammals which possess teeth that are embedded in sockets within the dentary bone, and which are attached by ligaments rather than ankylosed to the bone. This is distinct from the acrodonty and pleurodonty of squamates where the teeth are ankylosed to the surface of the jaw bones, either directly onto the apex of the jaw or to the lingual side of the bone respectively.

The ontogenesis of the thecodont structure remains an unresolved question. The assumption is that the alveolar bone forms from the existing dentary bone, and the ligament represents the demarkation line between the developmental units of the tooth and the jaw. Interestingly, thecodonty, the embedding of teeth within specialised sockets buried in the jaw bones is a novel feature of the first tetrapods that also display heterodont dentition [LeBlanc and Reisz, 2013]. In how far are the processes leading to the formation of the alveolar casing of each tooth related to its composition and shape? Is there a basic pattern found in all teeth with regards to the lineages inside and surrounding a given tooth? The answer to this question can shed light onto the old question where dermal bones come from in the first place.

In traditional literature [De Beer et al., 1971] it was thought that odontodes induce dermal bones and therefore that the bone of attachment found at the base of each placoid scale in chondrichthyans is actually the basic unit of dermal bone formation and by a process of accretion those bones could fuse together to larger bones, a so called transition from micromery to macromery of bones as articulated in the past literature [Janvier, 1996]. Clearly there have been many cases in evolutionary history where dermal bone formation and bone of attachment/tooth/denticle formation were decoupled. For example in sharks - derived from dermal bone carrying ancestors (similar to placoderms or acanthodians) the dermal bone armour is almost completely lost (except for the so-called 'Bone of Attachment' underneath each placoid scale), while there are many cases in amniote tetrapods where teeth are lost along with their respective alveolar caskets while dermal bones develop nevertheless, birds being one of the most prominent examples. Interestingly, in clinical edentulism, the alveolar bone caskets are also lost, which at least suggests developmental dependency and at most suggests that the tooth and bony casket represent a polyclonal module of development [Imirzalioglu et al., 2002; Bani et al., 2010].

If we could understand whether or not there are shared lineages between odontoblasts and adjacent alveolar bones on one hand and what the lineage relationships are between that alveolar bone and the remainder of the surrounding dental bone, then we can start to address this old question with the resolution required. Using Confetti lineage labelling we can both explore the ontogeny of the structures of murine teeth and assess the implications of the morphogenic field model. Quite simply, one can examine which structures are most similar to one another in colour population. This however requires novel tools to assess mixtures of cellular populations in a previously unaddressed manner. This thesis will address this question in Chapter 5.

2.4 Summary

There is a widely accepted model of tooth development that posits molecular signalling as the exclusive architects of the jaw. This predicts an isolation of distal and proximal populations, and a lack of complex polyclonal architecture. Another largely forgotten model suggests that teeth are specified by invasion, which predicts that the supposedly stable mesenchymal cellular map would in fact be disrupted, with cells of multiple territories being found in the teeth.

These assumptions can be relatively easily tested by labelling either population. In this thesis, the distal population is labelled through use of the Confetti reporter [Snippert et al., 2010], as explored in the previous section. This reveals not only a distal to proximal invasion as the principal developmental architect of the tooth row, but also previously unknown cryptic polyclonal boundaries that reveal the polyclonal modularity of odontoblasts, periodontal ligaments and alveolar bones.

Chapter 3

Early distal to proximal migrations are necessary for proximal lower jaw development

The development of an animal is an astoundingly complex operation. It is not the case that each part of the body simply grows in situ from the right part of a blastomere: there are invasions, convolutions, invaginations and migrations that must be performed to bring the right cells to the correct positions. The convolutions of development are in part due to ancestry: evolution can shape tissue into astoundingly derived features far removed from the ancestral forms, but the developmental route to these forms will often follow an initial ancestral pattern before diverging. A classic example of this would be the formation of tissue into pharyngeal arches. In fish, these become the gills, while in humans they represent a sort of 'staging ground' in which the populations that become the jaw, thyroid, bones of the inner ear and other facial structures are patterned towards their roles. Some structures form directly from these arches, while others require migration into a new position. The recapitulation of the intermediate gill-like morphology is not conceivably the only means by which this specification could take place, but this demonstrates that evolution operates by elaboration, rather than by overhaul.

Conventional wisdom and widely accepted models would suggest that the patterning of the mandibular arch defines the foundations of cell identity in the jaw, upon which elaborated patterns are applied [Stock et al., 1997; Tucker et al., 1998]. The key difference encoded in the arch is proximal and distal tissue, which are destined to become molar-bearing jaw and incisor-bearing jaw respectively. Later events then specify tooth position, with the distal-proximal identity giving rise to tooth type. Molecular patterning supposedly gives spatial axes to a generally capable mesenchyme, with combined signals specifying tooth positions, in a so-called morphogenetic field. This is an elegant concept, but one which has never truly been proven.

The implicit stability of morphogenetic compartments in the jaw is easily testable through Confetti labelling of distal cells. If these cells are found in supposedly proximal territories then the morphogenetic field model is wrong. The patterns and distributions of different colours within the Confetti-labelled population then allows for interpretation of how this invasion might have occurred, including numbers of cells and modularity of development.

The proximodistal Dlx code, namely Dlx5 and 6, are essential components of specifying this axis [Tucker and Sharpe, 2004]. Hand2 has been found to be upstream of these [Ruest et al., 2003; Thomas et al., 1998]. Interestingly this distal expression of Hand2, found in murine branchial arches, is incredibly old and is traceable into the most basal vertebrates to date, namely lampreys. Cerny et al. [2010] showed that distal Hand2 expression is found even in lampreys, thus this proximodistal code preceded the emergence of teeth or denticles. This code can also be found well preserved in sharks [Gillis et al., 2013].

Despite the remarkably conserved proximodistal branchial arch axis across all vertebrates, the exact fates of distal and proximal components in terms of teeth have only been mapped in a rather cursory fashion by using a R26-LacZ marker [Ruest et al., 2003], but without insight into the polyclonal architecture. This prevents the detection of proximodistal clonal expansions and does not allow us to detect potentially shared lineages between the inside and outside of a tooth or the relationship between alveolar bone and surrounding dermal bones in the distal area.

In this Chapter we shall observe distal cells that invade the proximal territory in a time course. The involvement of these cells in early bell stage molars will be demonstrated, undermining the key assumptions of cell population stability in the morphogenetic field model. In subsequent chapters these populations shall be examined at different time points, and their role in forming teeth, dermal bone, alveolar bone and the periodontal ligament investigated.

3.1 Methodology

3.1.1 Hand2-Cre as a marker for Distal Cells

The Hand2-Cre line was used to label distal cells [Ruest et al., 2003]. Examples of its labelling are given, and a more thorough analysis of its role in distal-proximal patterning can be found in Ryll [2010]. Briefly, at early stages (E9-E12.5) it is expressed in the distal regions of branchial arches 1, 2, 3 and 4 as well as in limb buts (E9.5-E10) and the ventricles of the heart. I have made the reasonable assumption that the mammalian face does not derive from neither the limb nor the heart. There is later expression in calvarial dermal bones (E14-E16). At a similar stage, Abe et al. [2002] revealed that expression in the lower tooth row was confined to the incisor, and excluded from the molars. At 18.5 cells there is very little expression in the teeth and mandible, as revealed by in-situ, and active expression is confined to the tongue and submandibular gland, implying that cells labelled by Hand2-Cre in these structures derive from cells which were labelled earlier [Ruest et al., 2003]. However at P0.5 there is some sparse late expression in the Molar [Abe et al., 2002].

The expression pattern of Hand2 lead us to examine the stages of jaw develpment at which expression was less prevalent, thus increasing the reliability of our chosen Confetti reporter [Snippert et al., 2010] as a stable marker for lineage. The cross Hand2-Cre x
Gt(ROSA)26Sor$^{tm1(CAG-Brainbow2.1)Cle}$/J is referred to as Hand2-Confetti throughout this and subsequent chapters. Animal husbandry is described in Appendix A.1, and sample preparation in Appendix A.2.

3.1.2 Samples and sections

Figures 3.5 and 3.6 are of the same sample: an E10.5 embryo which was bisected along its dorsal edge and flattened out. Figures 3.7 and 3.8 are adjacent coronal sections of an E14.5 embryo, depicted in Figure 3.1.

Using Confetti and novel quantitative approaches, deep developmental analysis can be made from only one sample. One novel quantitative approach that we took was to consider how presence of only a few colours in a large group of cells can be used to infer the size of the original labelled population that gave rise to that group, known as the Founder Effect.

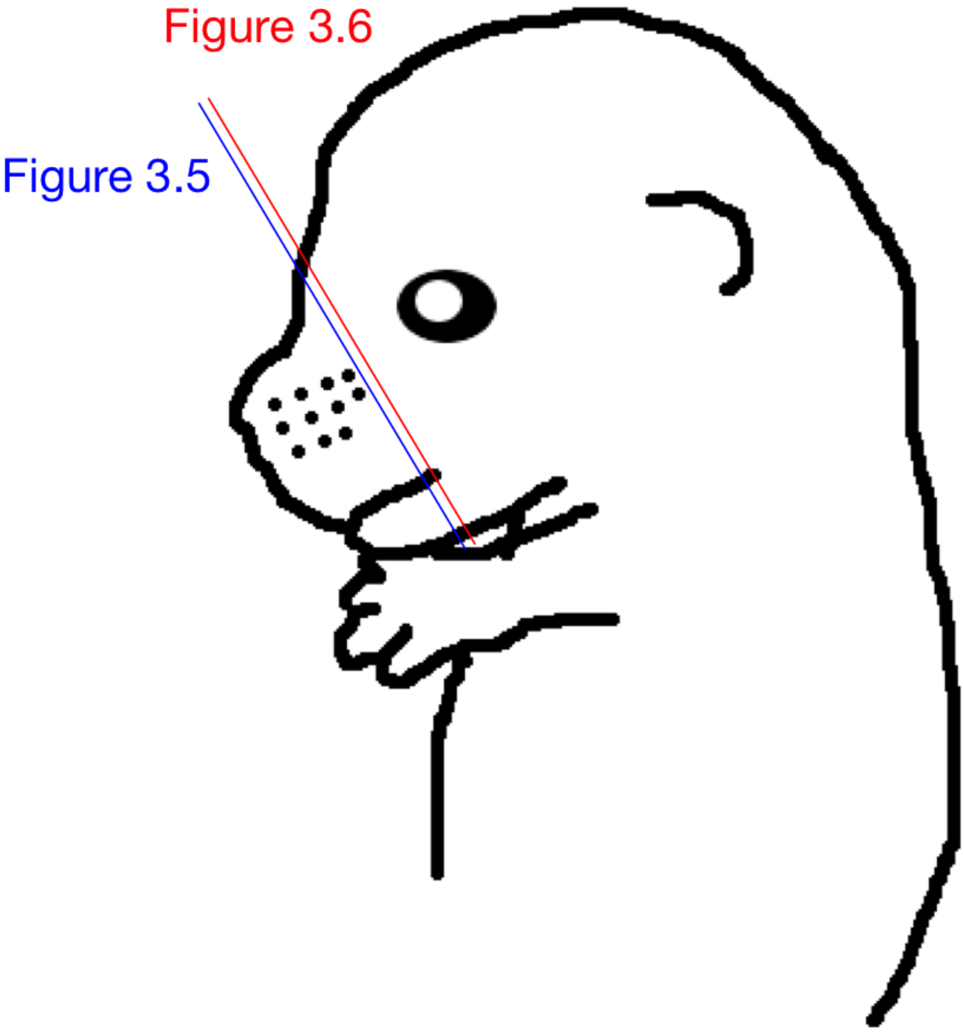

Figure 3.1: Origin of Figures 3.7 and 3.8 Both figures are adjacent coronal sections of the same E14.5 Hand2-Confetti embryo.

3.1.3 The Founder Effect and Confetti

The founder effect describes a phenomenon in population genetics, wherein an allele that is rare within a population can become common in a new population derived from it due to colonisation by a very small number of individuals. This process is believed to be at the root of many aspects of human variation [Ramachandran et al., 2005]. In a more abstract sense it refers to the fact that a small sample of a larger population may not capture the variation of that sample. The inference from this is that if one can compare the variation present in the whole sample to the variation present in a small derived sample, one can estimate the size of the population bottleneck that gave rise to the devised group.

The founder effect can also be used to interpret random lineage labelling. A simple mathematical model was used to calculate the probabilities of each labelling outcome, detailed in Appendix A.3. Based upon the number of different colours present in a certain area, an inference can be made about the number of cells that initially contributed to that region. This is explored in Figure 3.2. Assuming equal probability of each of the four colours, the probability of having a single-colour region arising from anything greater than 3 cells is effectively negligible. A two colour region arising from anything greater than 10 cells is also highly unlikely, and above 20 cells one can effectively assume that all four colours would be present.

Snippert et al. [2010] observed that within their experimental system, the Red, Yellow and Cyan reporters were present in almost equal proportions, while the GFP reporter was effectively absent. Part II of this thesis quantifies over 1.8 million Confetti labelled cells, the proportions of which are shown in detail in Figure 8.1, and also summarised in Figure 3.3. Yellow cells were very abundant at 70% of all cells, with red and cyan cells cumulatively accounting for 29% of cells and GFP only 1%. This suggests that the behaviour of Confetti under a short burst of inducible Cre under the control of the Lgr5 promoter, as performed by Snippert et al. [2010], behaves quite differently to a longer period of Cre activity as we performed. However, regardless of whether there is a lower degree of variability arising from reporter behaviour or due to multiple population bottlenecks, the Founder effect remains highly predictive. Even if the chance of a single colour arising is 90%, or your founder population is drawn from a group that is 90% homogenous, one can predict that the derived group comes from fewer than 50 founder cells, as shown in Figure 3.4.

The simple Monte Carlo simulation of populations based on the observed proportions from Part II reveals that the presence of anything less than all four colours highly constrains the probable size of the founder population for that structure (Fig 3.2B). Single colour regions are unlikely to arise from anything greater than approximately 12 cells. Regions with only two colours are most likely to have arisen from approximately 5-10 cells, and are very unlikely to have arisen from greater than 30 original cells. 3 colour regions are very likely, though this apparent loss of discrimination becomes diagnostic in another sense: the observation of any green cells indicates initiation by a relatively large population.

In summary, the presence of fewer than four colours within a structure can be used to estimate the size of the labelled population that originally contributed to that structure through simple probabilistic interpretation.

3.2 Results

3.2.1 Hand2 cells are distal cells

Hand2-Confetti expression is found in the distal territory of the first and second branchial arches at e10-5 (Figure 3.5). This labelling is found in all mesenchymal cells in the distal branchial arches (Figure 3.6). We and others [Ruest et al., 2003; Ryll, 2010] have previously checked if the Hand2 transgene is expressed again later in early stages of tooth development, this is not the case. Based on this observation and the time points we will be studying, it will be clear that all cells labelled in Hand2-Confetti mice are the sole progeny of initially distal cells. From this point on, cells labelled in the Hand2-Confetti cross will be referred to as distal cells.

It should also be noted that there are no apparently unlabelled cells in the distal territory - where apparent voids are observed, this is actually membrane-labelled cyan cells. A problem that was noted by Snippert et al. [2010] and Schepers et al. [2012] was the probability of the Confetti construct adopting a partially degenerated and non-fluorescent conformation. Irreversible excisions will eventually remove the non-fluorescent Neomycin reporter, so the probability of this decreases over the time that Cre is present. Thus we can say with some degree of cautious confidence that unlabelled cells are of the proximal territory. This assumption does not preclude the possibility that there may be an unrecognised intermediate population between the Proximal and Distal. As always, one must be careful not to over-interpret the absence of data as an informative variable, and these cells can only be considered

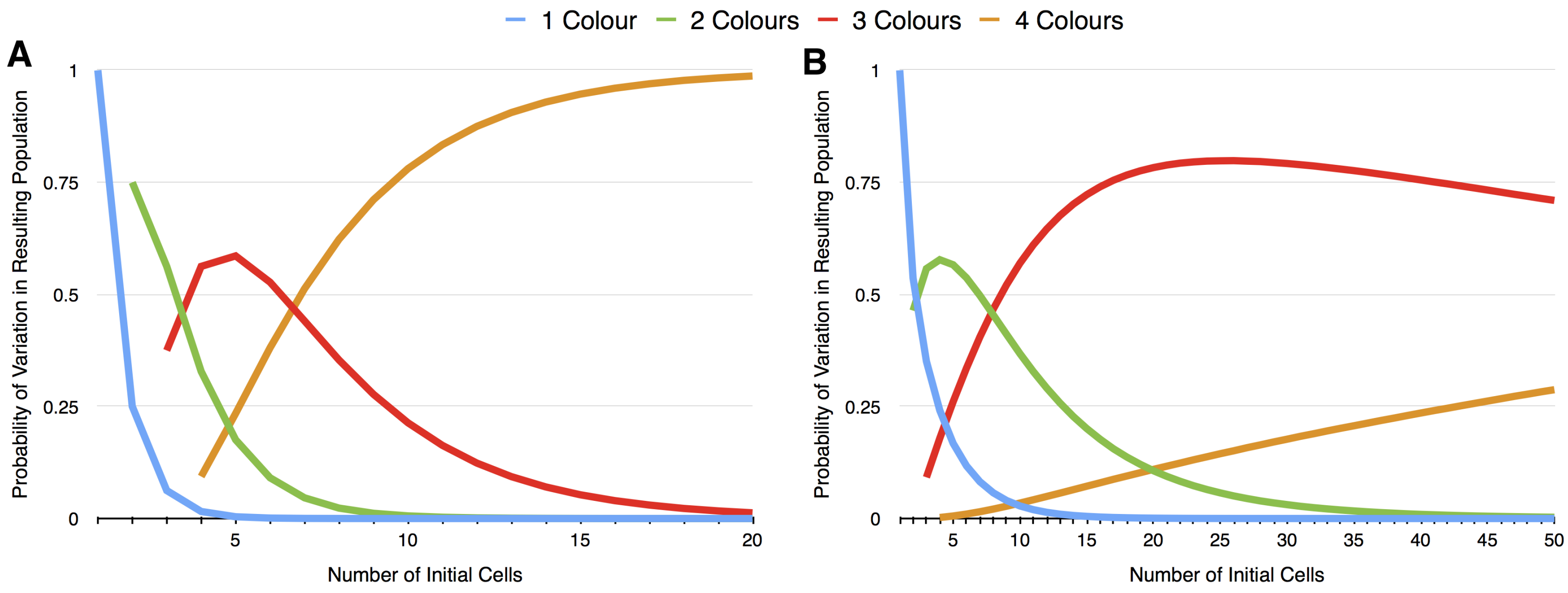

Figure 3.2: The Founder Effect gives predictive power to the number of initiating cells
A: Probability of obtaining a specific number of colours from a different number of initial cells assuming equal probability of each Confetti Colour. **B:** As before, but using the observed proportions detailed in Figure 8.1. Method discussed in Appendix A.3.

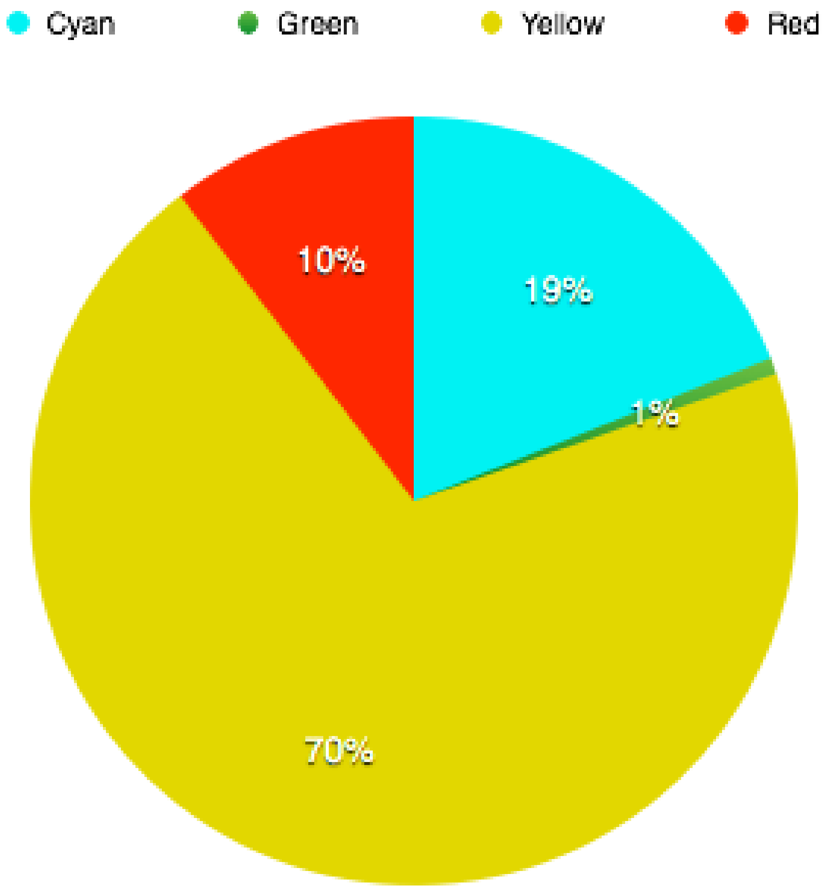

Figure 3.3: Proportion of the four Confetti labelling colours in a Wnt1-Cre/Confetti calvarium. As observed over an estimated 1.8 million cells in Part II. Derived from Figure 8.1.

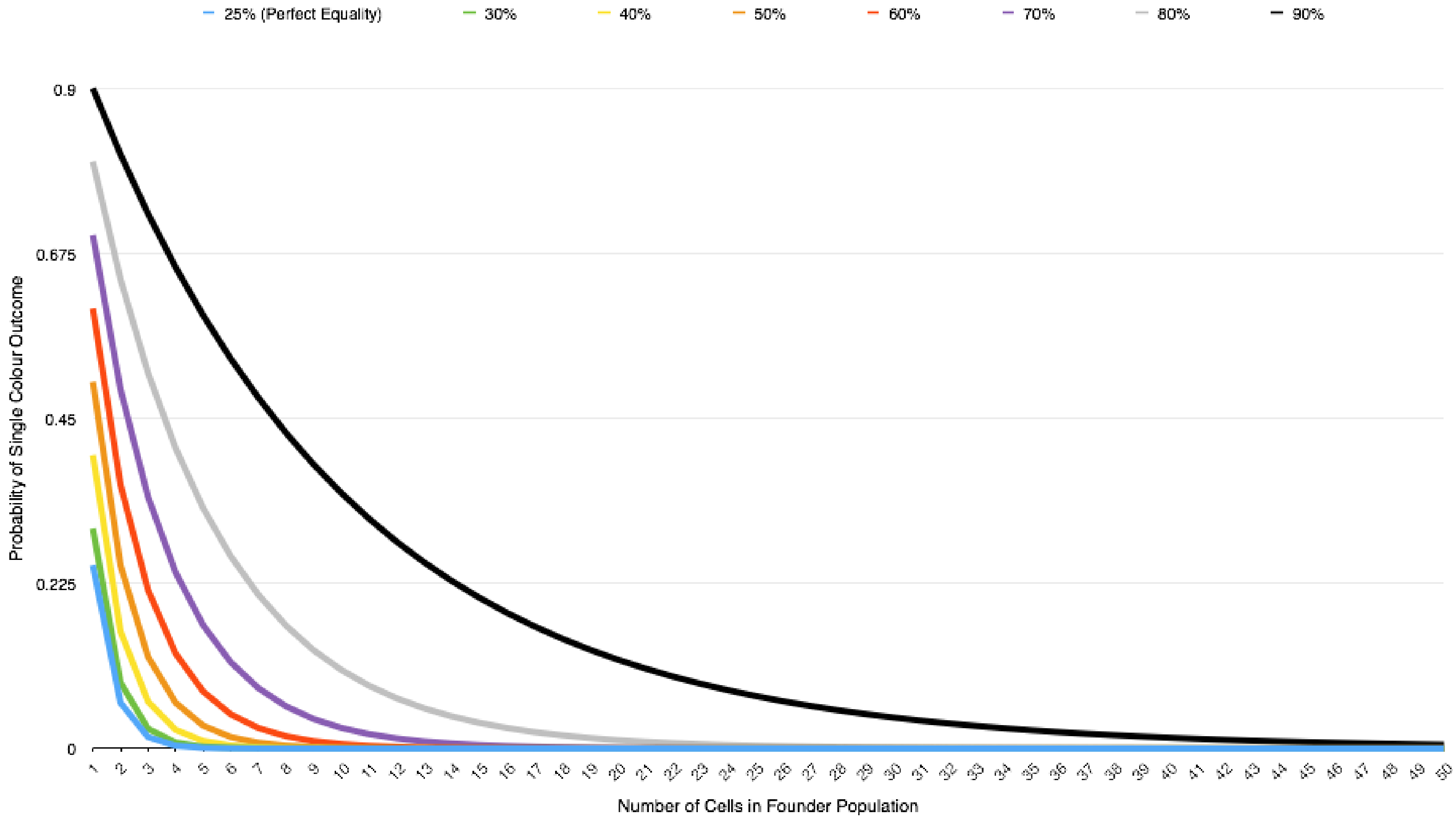

Figure 3.4: The Founder Effect is useful even in the presence of very imbalanced labelling. Probability of achieving homogenous labelling of one colour depending on the proportion of that colour's presence in the original population (different lines) and the size of the founder population diverging from the original population (x axis). Even if the original population is 90% homogenous, there is effectively a negligible probability of a homogenous group deriving from it unless the diverging group consists of fewer than 50 cells.

presumptively proximal.

There are clearly some distal cells along the margin, but have no labelled neighbours. Morphogenetic fields classically rely on sharp boundaries to prevent ambiguous developmental encoding. This is the first piece of evidence that perhaps distal and proximal cells in fact to not conform to tightly isolated anatomical regions.

3.2.2 Distal cells are present in the proximal domain

The morphogenetic field model [Tucker and Sharpe, 2004] would predict an absence of distal cells in the molar-bearing region. Figure 3.7 shows a coronal section from this region, on the level of the first molar buds at embryonic day 14.5 There are an abundance of distal cells, demonstrating that the distal populations migrate into the proximal territory. Startlingly, each tooth is comprised of a mixture of distal and presumptively proximal cells, in complete contrast to the presumed stability of the morphogenetic field model.

At E14.5 the molar buds are surrounded by Hand2 cells, which also represent the initial invaginating cells of the nascent cap to the exclusion of presumptively proximal cells (Figures 3.7 and 3.8). The organisation of the colours encompassing the buds would suggest migration rather than novel labelling, as there are no double-labelled cells visible which would suggest recent activation of the label, and there is a suggestive concentric lamination around the bud that suggests linear spreading of putatively polyclonal populations rather than coincidental labelling in line with the fly-paper model of early tooth formation [Mammoto et al., 2011; Rodeck and Whittle, 2009, p.16]. The orientation of cells is suggestive of a medial-lateral axis of migration, though directionality cannot be inferred at this stage.

3.2.3 The mandibles arise from a small population of cells

The jaws on either side of the face are differently coloured, with the presumptive left jaw being entirely yellow and the right displaying red and cyan cells. This lack of diversity is a critical: the only reasonable explanation for the homogeny within the presumptive mandibles is that the entire structure grows from only a few distal cells. The models presented in section 3.1.3 can be used to estimate that the mandibles must have diverged from the rest of the surrounding heterogenous mesenchyme very early in development, and thus derived from a small population of cells that has been segregated from mixing with other populations over the course

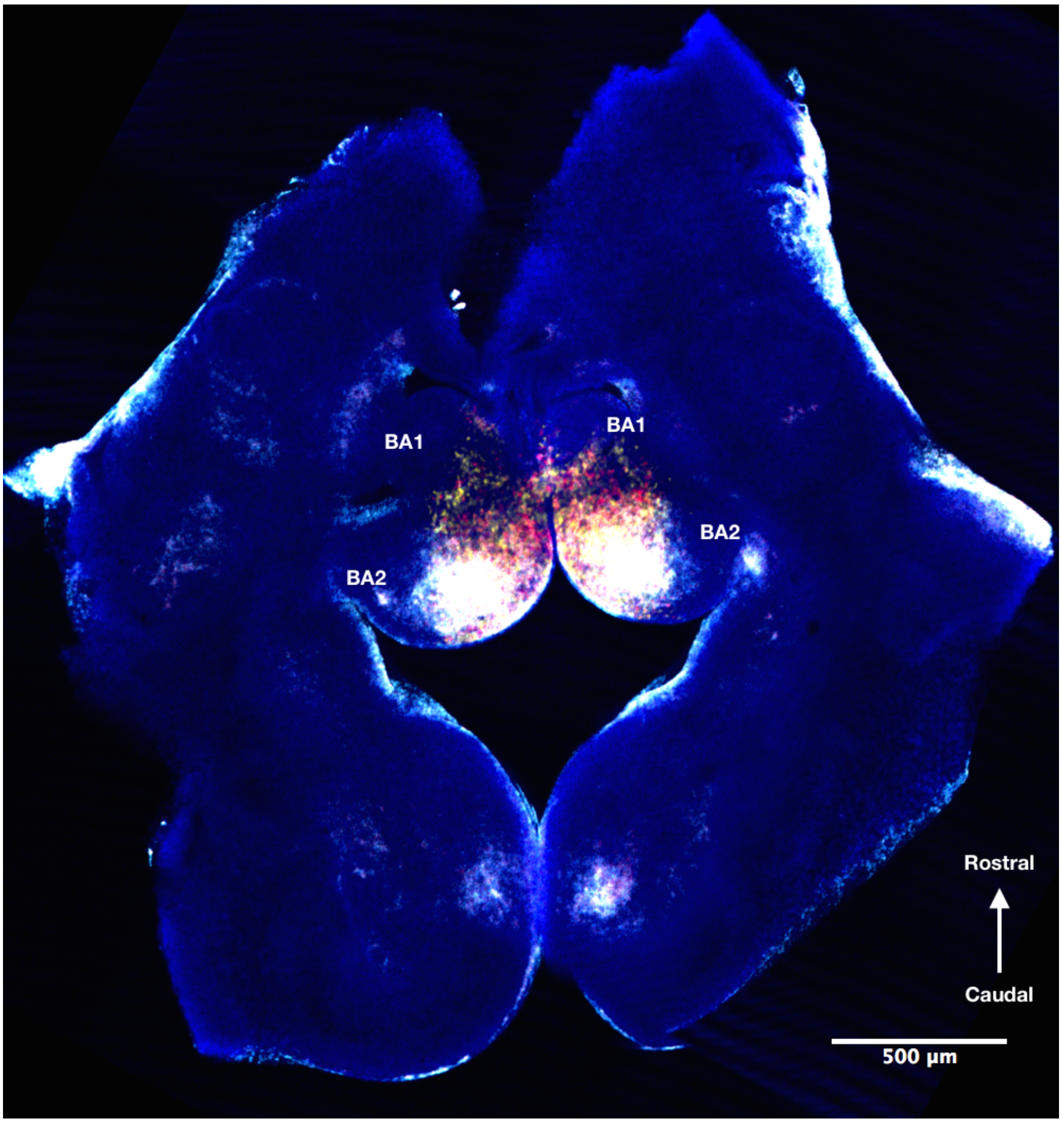

Figure 3.5: Hand2-Confetti Expression in the distal branchial arches at E10.5. At embryonic day 10.5, confetti expression in the Hand2-Cre x Confetti mouse is found in the mesenchyme of first and second branchial arches, exclusively at the distal ends. Branchial arches shown in detail in Figure 3.6. *BA1* - First Branchial Arch (Mandibular), *BA2* - Second Branchial Arch (Hyoid)

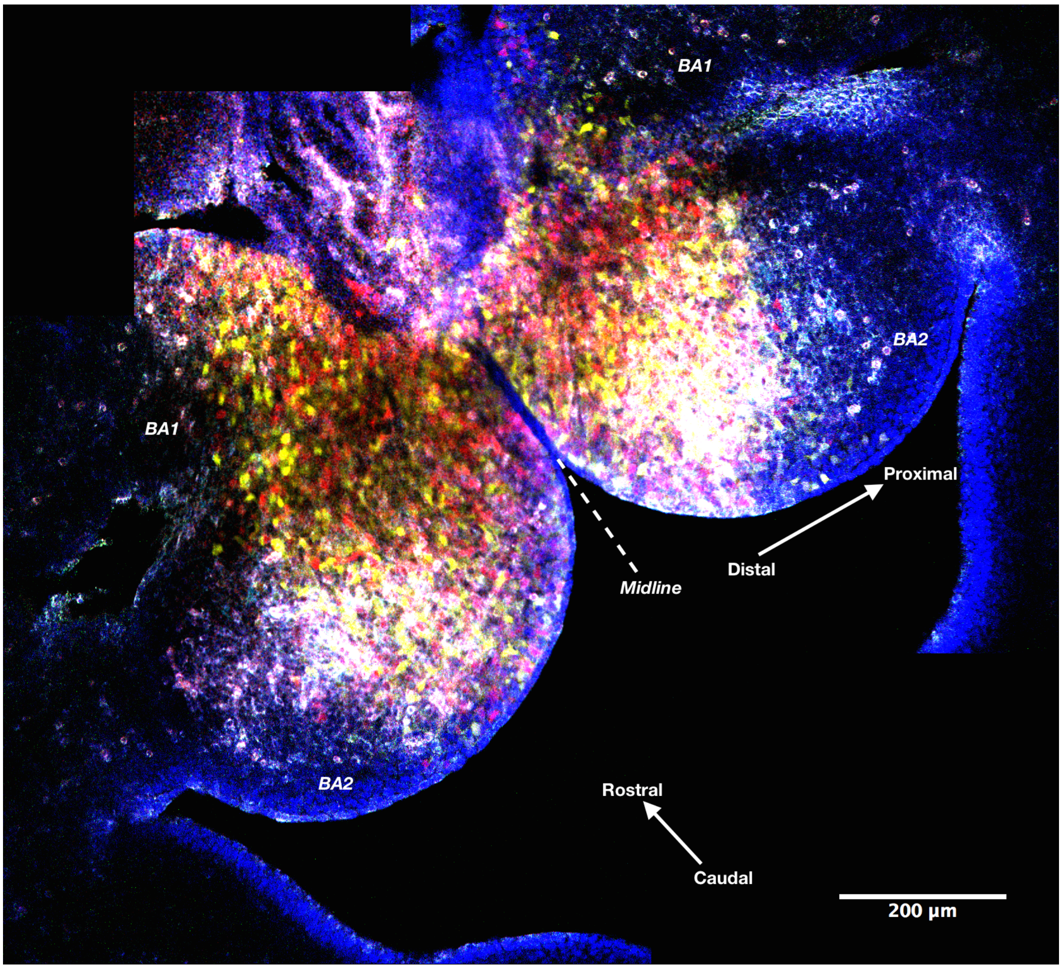

Figure 3.6: Detail: Hand2-Confetti Expression in the distal branchial arches at E10.5. At embryonic day 10-5, confetti expression in the Hand2-Cre x Confetti mouse is found in the mesenchyme of first and second branchial arches, exclusively at the distal ends. Apparent labelling outside of the distal ends is autofluorescence or reflection within the whole mount. *BA1* - First Branchial Arch (Mandibular), *BA2* - Second Branchial Arch (Hyoid).

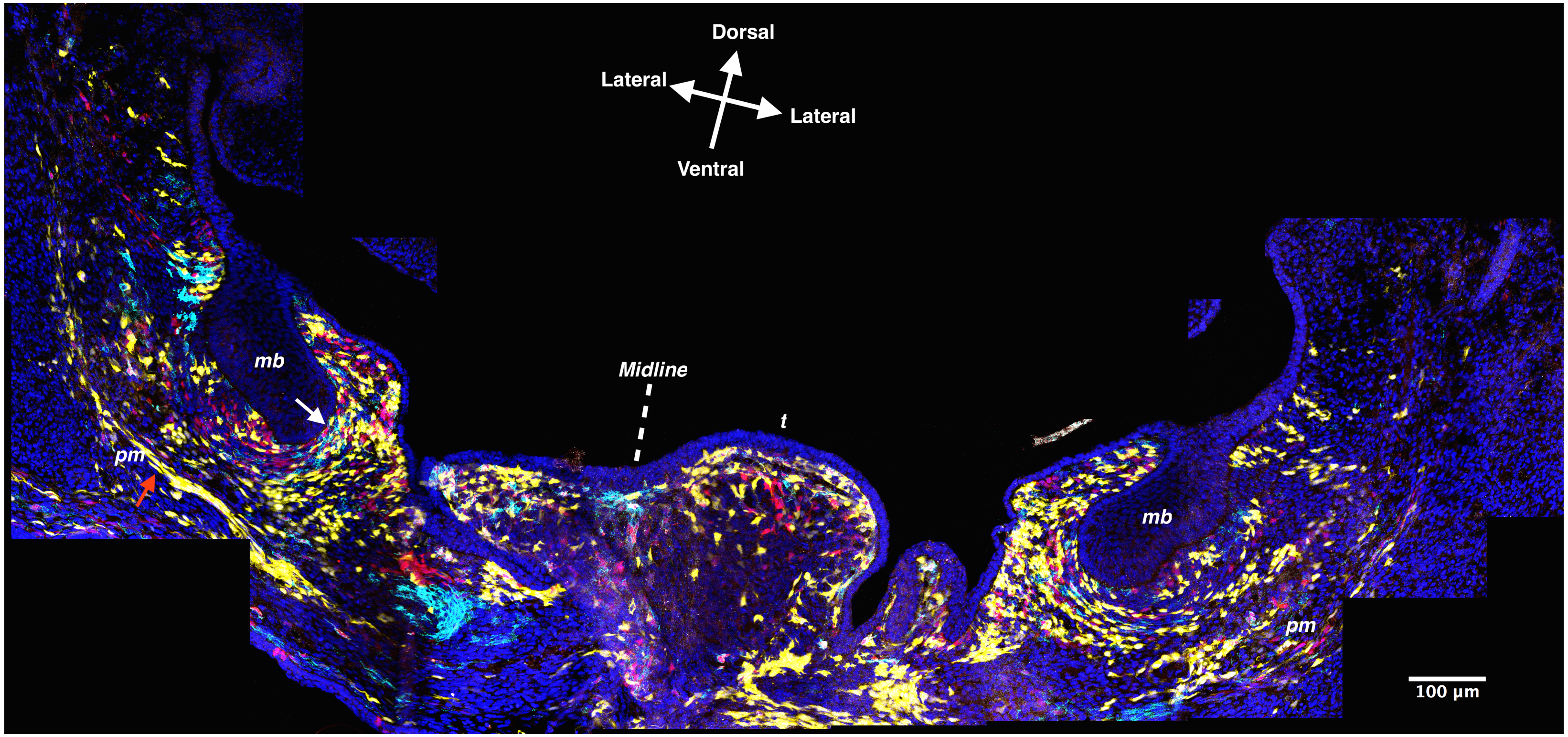

Figure 3.7: Distal cells invade the proximal territory by E14.5 By embryonic day 14.5 distal cells have invaded the supposed proximal molariform territory. This coronal section demonstrates an abundance of distal confetti-labelled cells in the tongue, molar buds and presumptive mandible. Note that within the molar on the left of the image, red and cyan cells are more dense in a layer immediately adjacent to the bud, while yellow cells dominate slightly further away (white arrow). Cells are oriented parallel to the curved surface of the bud, suggesting either circumnavigating migration or active participation in invagination. The presumptive mandible (red arrow) appears entirely yellow labelled, suggesting establishment from very few cells, and a lack of relationship to the multicoloured tooth. *mb* - molar bud, *pm* - presumptive mandible, *t* - tongue.

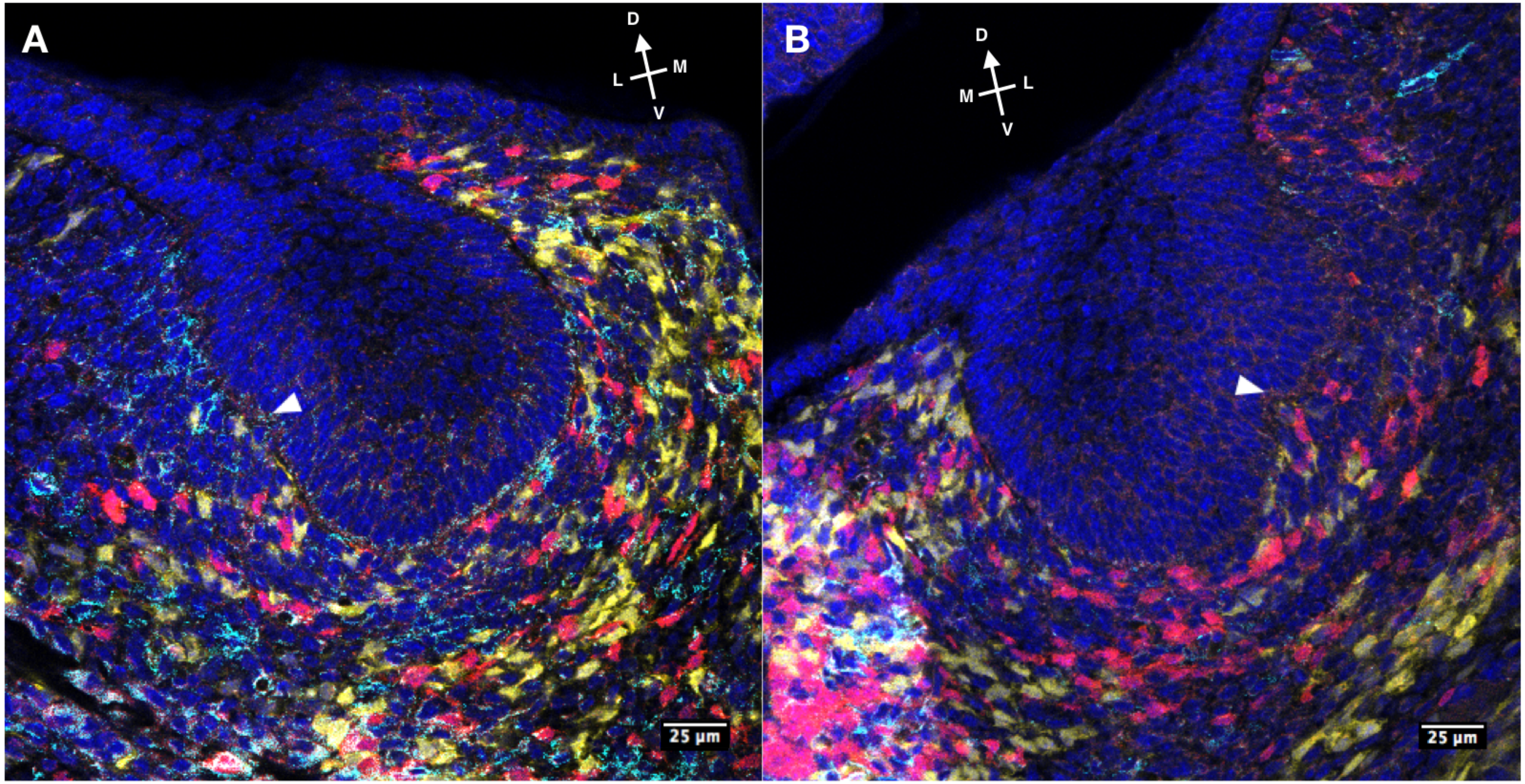

Figure 3.8: Distal cells form the initial population of the molar mesenchyme. Coronal sections of the Left (**A**) and Right (**B**) first molars of a Hand2-Confetti mouse at Embryonic Day 14.5, or Late Bud/Early Bell stage. The mesenchyme involved in enveloping the tooth bud from the dental epithelium is largely labelled under Hand2-Confetti. It is this same population which is also initiating invasion under the presumptive primary enamel knot (white arrows). Adjacent section to Figure 3.7.

of many cell divisions. It is likely based on the probability of observing either one or two constitutent colours, regardless of the mixture of the original population, that fewer than 20 cells give rise to the whole mandible.

Conversely the odontogenic population demonstrates at least three colours. This does not imply secondary activation, as this was ruled out by both Ruest et al. [2003] and Ryll [2010], and there is an apparent laminar arrangement of labelling around the tooth buds. However, this does imply a larger migrating population, more than 50 cells (Figure 3.2).

3.3 Summary - Distal cells invade the proximal territory of the mandible

Hand2 labels distal cells in the mandibular arch (Figures 3.5 and 3.6). Based on the presence of distal cells in the proximal molar-bearing territory of the mandible (Figures 3.7 and 3.8), the chief tenet of the morphogenetic field model must be discarded. The mesenchyme surrounding the molar buds is almost entirely of distal origin, and clearly involved both in the active invagination of the dental epithelium and in the initial invasion underneath the enamel knot (Figure 3.8).

Furthermore the distoproximal migrations can be divided into an osteogenic mandibular migration and a putatively odontogenic buccal migration. This is based upon the unique insights of Confetti labelling: one can attach probabilities to a single cell adopting a specific colour, therefore the probability of a population adopting a specific outcome is calculable. Any population of cells in a developed animal arises from a progenitor population, and based on the mix of colours within that structure, a 'most probable' population size can be estimated. The mandible itself can be formed of only one colour, but can also have some diversity. This suggests a very small population which diverges from the rest of the distal population very early in dvelopment (Figures 3.2). The buccal odontogenic population has mixed identity, so likely has an initiating population of greater than 50 cells.

My observation of a distoproximal migration or a polyclonal expansion of the distal Hand2-Confetti labelled population into the proximal domain is very interesting as it might reflect a generic branchial arch migratory mechanism. Cerny has previously found migration from the distal mandibular arch into the proximal/maxillary territory in axolotl [Cerny et al., 2004]. In a similar vein work tracking Hand2-labelled cells in branchial arches of zebrafish have provided similar evidence for proximal migration [Iklé et al., 2012]. In our case we see a similar scenario for both dermal bone formation as well as migration of odontogenic precursors. Thus it is possible that despite coordination of the two a common mechanism is used by both populations.

The presence of any distal population migrating into proximal territory strongly suggests that Osborn's progress zone model of tooth formation applied to a novel distal-to-proximal migration is a better explanation for early tooth specifying events than the morphogenetic field model. At the very least, the presence of these cells utterly undermines the assumption of morphogenetic stability that underpins the morphogenetic field theory.

Chapter 4

Clonal architecture of teeth reveals the nature of heterodonty

4.1 Introduction

In the last chapter it was demonstrated that distal cells invade the proximal territory and appear to be the initiating population of teeth. In observing this, a different major question arises: if both incisors and molars are specified from distal populations, by which mechanism do they subsequently diverge to form different tooth types?

It was recognised already by Ruch [Schmitt et al., 1999] that at the early placodal or bud stage there is no evidence for heterodonty to be found. The first differences become obvious at the (late) bell stage. Given that we have lineage information from Confetti we therefore examined in a time course the development of these polyclonal structures. If there is no discernible difference between incisors and molars with respect to this population then the molecular identities that were previously identified in the morphogenetic field model may provide full explanation for heterodonty. If however there is a cell origin distinction between the two classes of teeth, these molecular addresses must be either irrelevant to heterodonty, or intermediates in a process that requires population differences.

Once again Confetti labelling provides the answers to this questions. Using the same approach as the last chapter, later tooth stages can be examined for any sign of divergence in cell dynamics of the putative odontogenic distal mesenchyme in different tooth types. We can compare the early bud stage presented in the last chapter with the heterochronic early bell (second molar) and late bell stages (first molar) in E16.5 animals to reveal the developmental course of odontoblasts.

4.2 Methods

As in the previous chapter, the animal husbandry is described in section A.1, and sample preparation in Appendix A.2. The cryosections used in this chapter come from two E16.5 animals and are detailed in Figure 4.1.

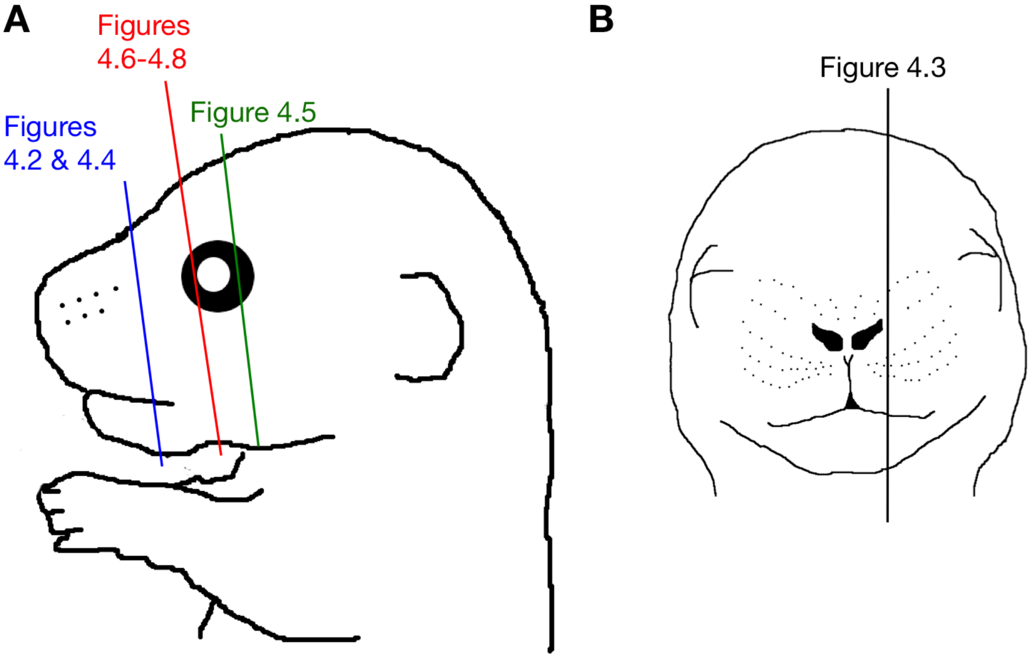

Figure 4.1: Sections used in this chapter. Both the animal that all coronal sections come from (**A**) and the animal from which the sagittal section was used (**B**) were E16.5 embryos.

4.3 Results

4.3.1 Incisors are comprised of majority distal population and a minority presumptively proximal population

At E16.5 the incisors are almost entirely labelled as distal cells (Figure 4.2), though there is very surprisingly a small population of unlabelled presumptively proximal cells (Figure 4.3). At the root of the tooth unlabelled cells are very numerous indeed (Figure 4.3). This could suggest a reciprocal proximal-to-distal migration, though one would have to be able to independently label proximal cells in order to prove this. More curiously, a cryptic polyclonal boundary can be observed running at an angle through the incisors (Figure 4.4). Remarkably, large portions territories are defined with a symmetrical line of division running through the teeth, though not parallel to major body axes. The dominance of distinct colours, such as yellow in the top-right incisor territory of Figure 4.4 suggests that only a small portion of the randomly labelled branchial arches eventually contribute to the incisor. The extent of these large coloured territories suggests that the incisor itself forms from only a few cells within the distal population that expand greatly.

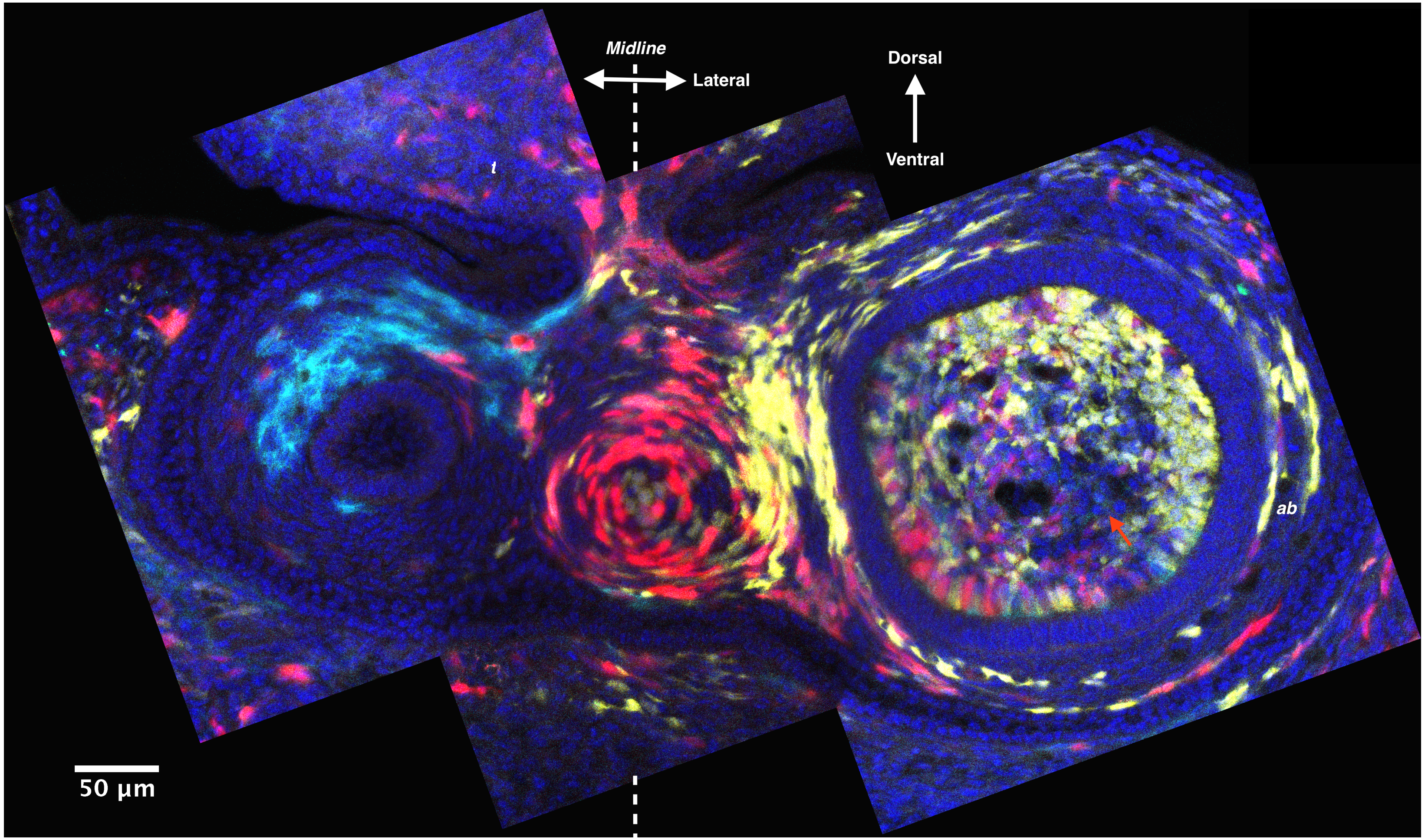

Figure 4.2: **Distal populations form the majority of E16.5 Incisors** Due to the oblique coronal section, the left side of the image is slightly behind the incisor, while the right side of the image runs directly through the incisor. The incisors are predominantly labelled distal cells, but there are also a number of unlabelled presumptively proximal cells (red arrow). *ab* - alveolar bone, *t* - tongue.

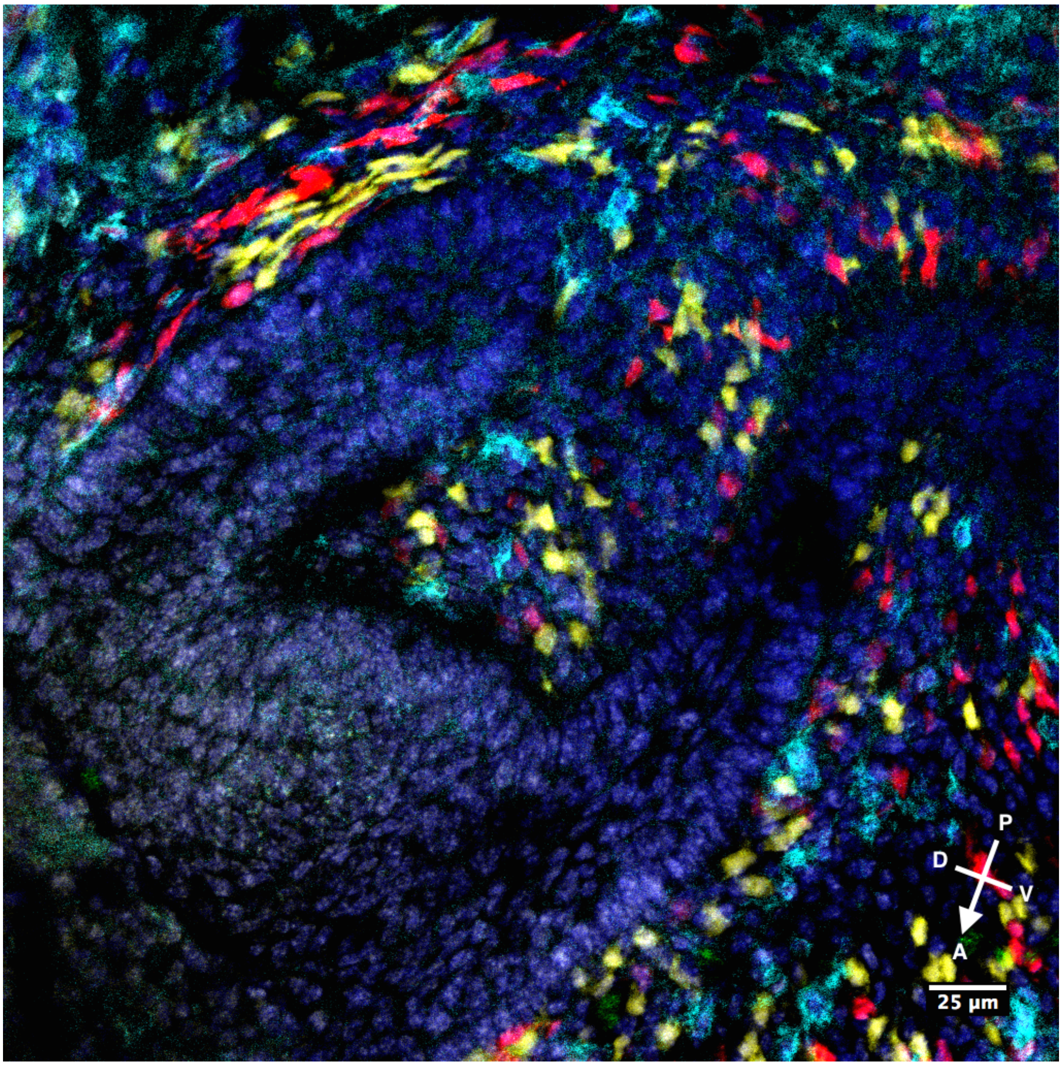

Figure 4.3: Presumptively proximal cells within the Incisor. Sagittal section through the edge of the root of the lower incisor. There are many unlabelled presumptively proximal cells present alongside a very randomly mixed distally labelled population. This demonstrates that while distal cells migrate proximally, there may also be proximal cells invading distal territory.

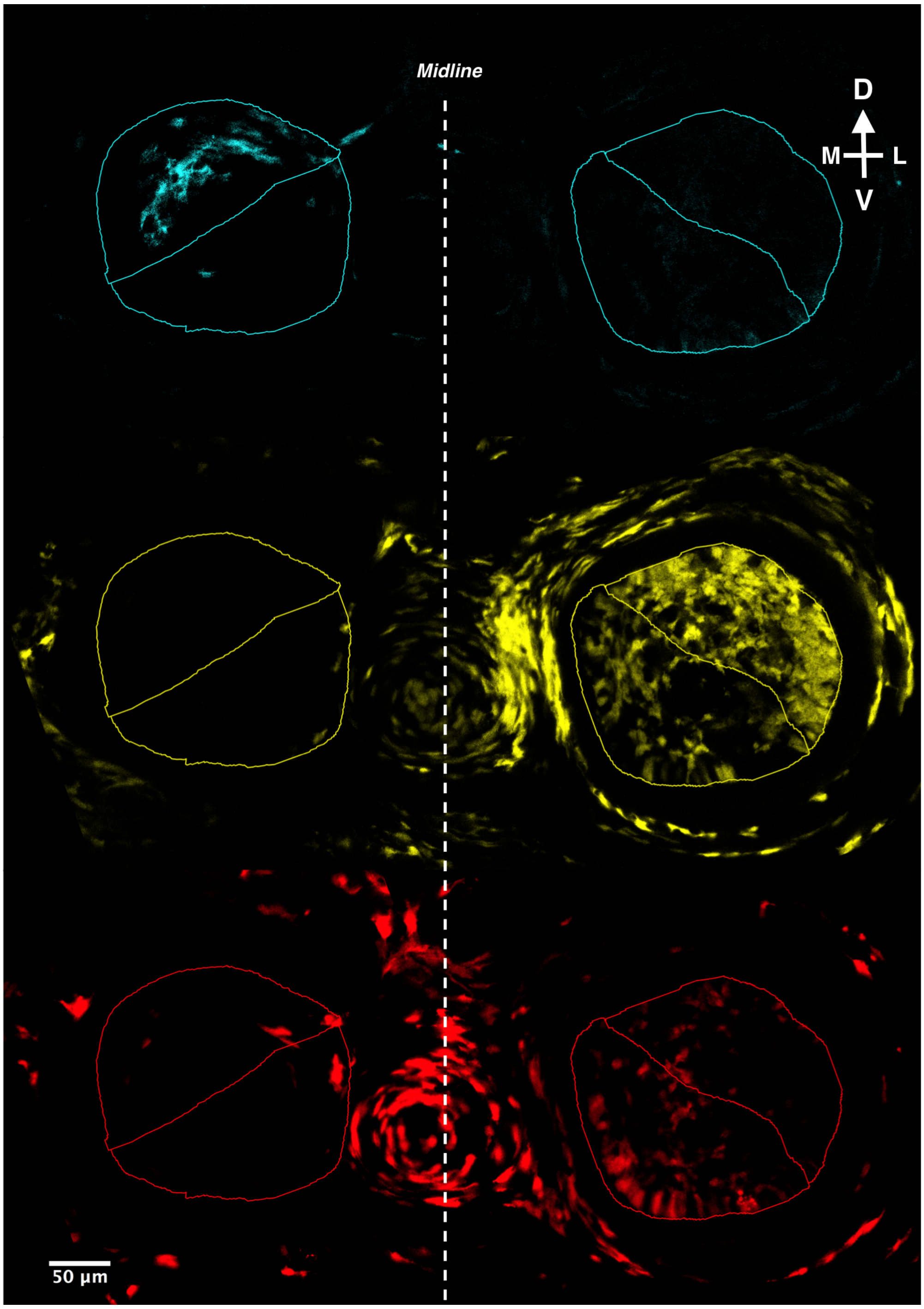

Figure 4.4: Cryptic Polyclonal Boundaries within the distal populations of incisors. Individual Confetti channels show segregation into broad buccal and external domains in the incisors shown in Figure 4.2. These do not appear to be entirely segregated, but this compartmentation defines the majority of the cells in either half of the tooth. Green cells not shown, as there is only one in the sample.

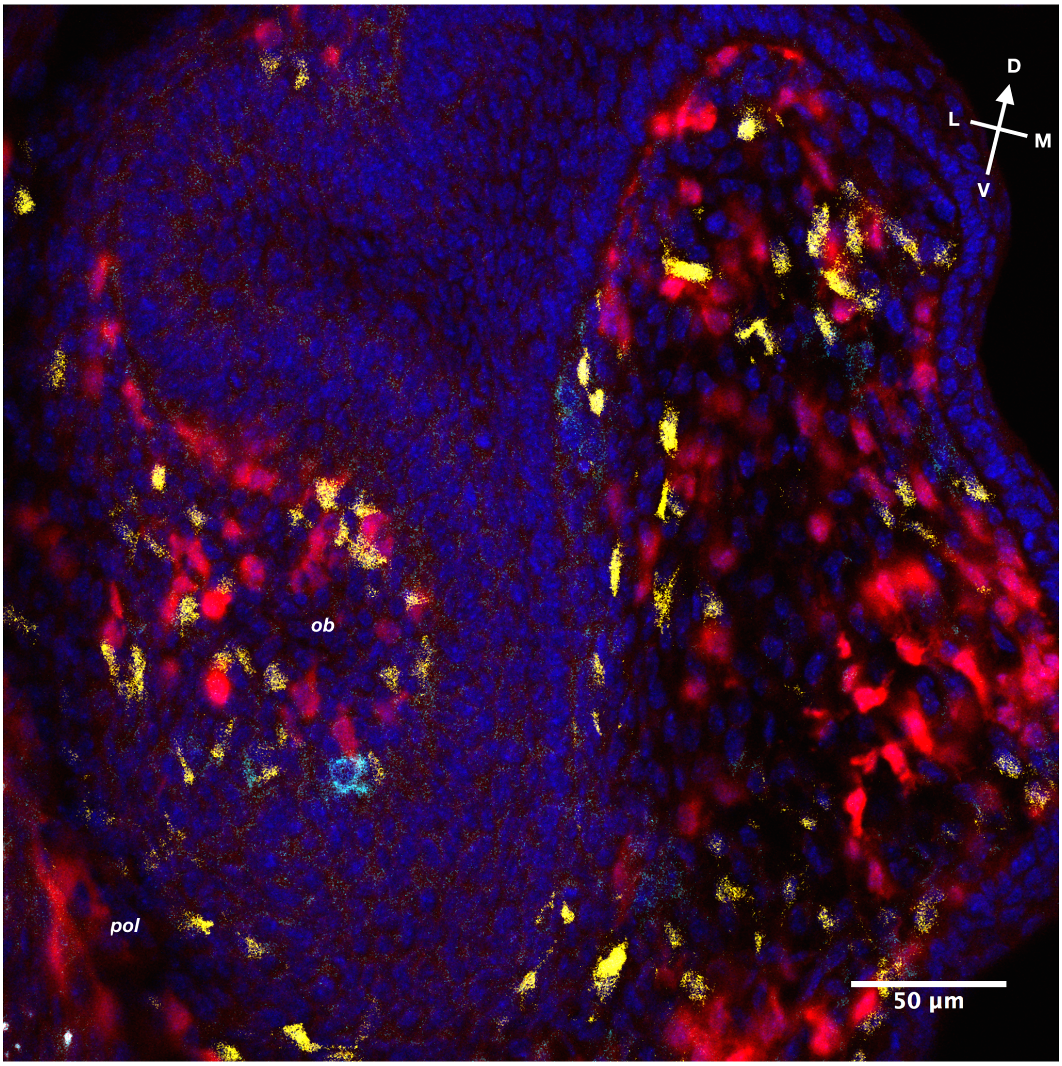

Figure 4.5: Distal cells form the majority of the second molar at E16.5. Coronal section of the second molar at embryonic day 16.5. At this cap stage, the majority of cells within the developing tooth are from the distal population, though there are some unlabelled cells that have invaded also. This tooth is adjacent in the jaw to the one shown in Figure 4.8. *pol* - periodontal ligament, *ob* - odontoblasts

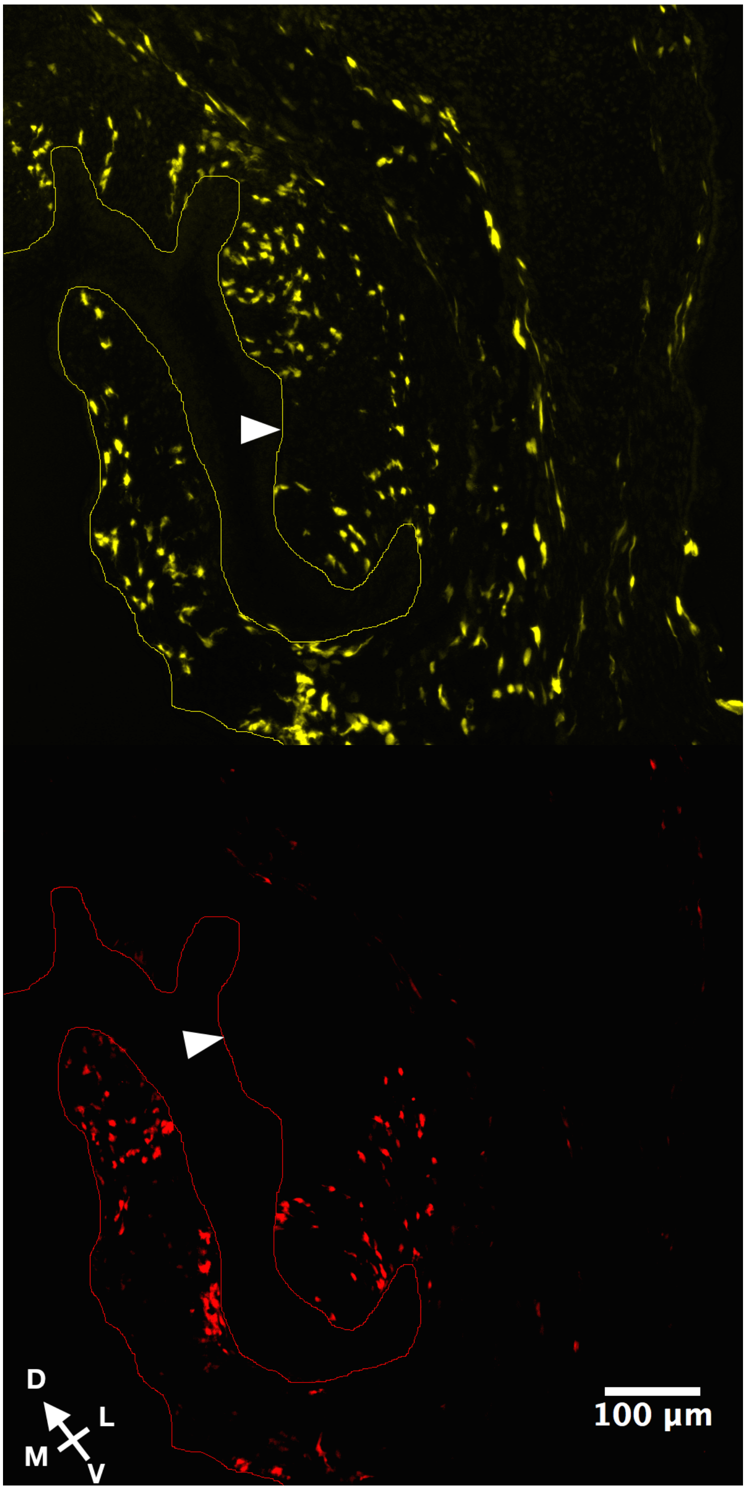

Figure 4.6: Polyclonal expansions of distal cells within the lower first molar. *Continued overleaf in Figure 4.7*

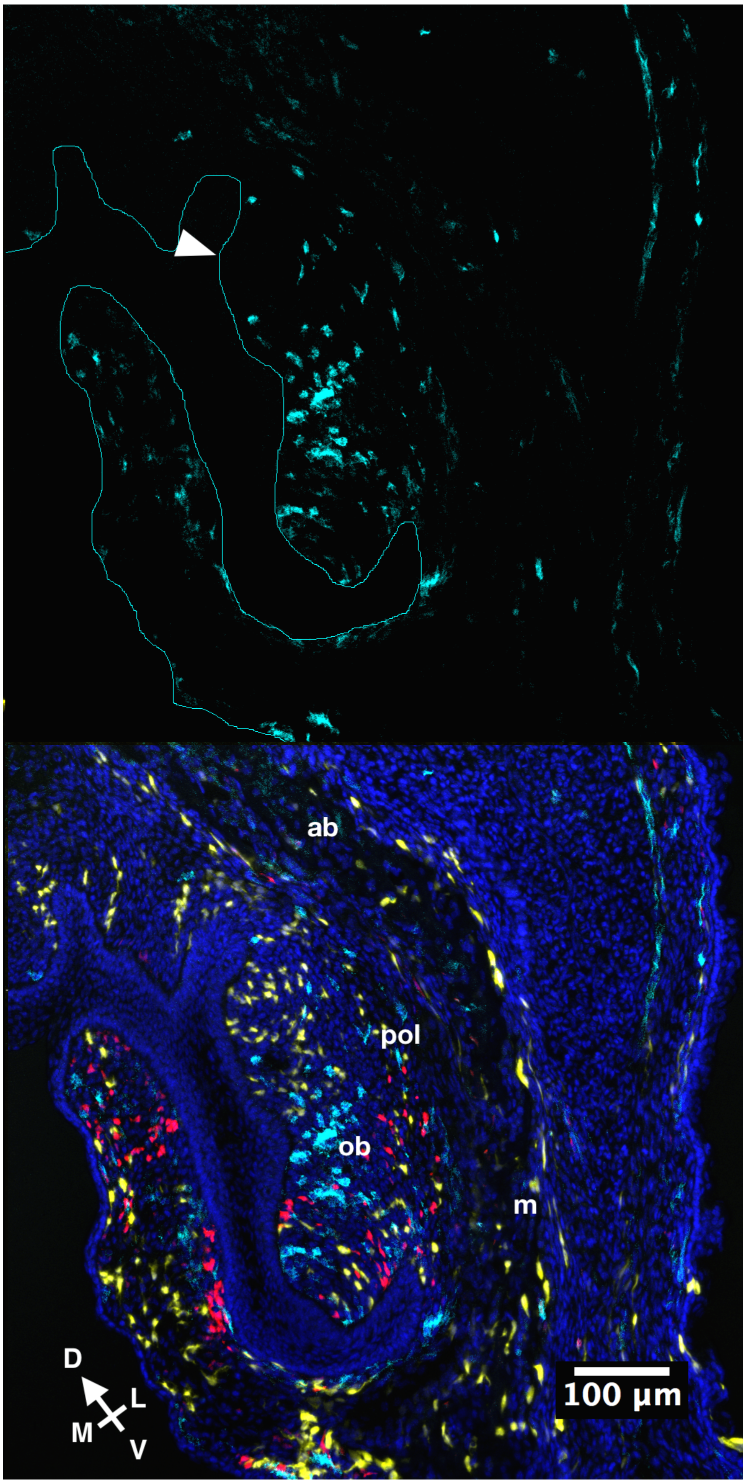

Figure 4.7: Polyclonal expansions of distal cells within the lower first molar. *Continued from Figure 4.6, caption overleaf.*

Figures 4.6 and 4.7: Polyclonal expansions of distal cells within the lower first molar. Coronal section of lower first molar at embryonic day 16.5. This molar is relatively well mixed, bearing three colours and revealing compartments within the tooth. Each cell colour has voids within parts of the tooth (white arrows). This implies some degree of developmental independence between the two cusps of this molar. *m* - mandible, *ab* - alveolar bone, *pol* - periodontal ligament, *ob* - odontoblasts.

4.3.2 Mature molars are comprised of majority presumptively proximal population and a minority distal population

By E16.5, adjacent lower molars are at different stages of development, revealing two more phases of distal cell involvement in molar development. In the E16.5 second molar, distal cells are observed to represent the majority of cells within the tooth, though with several proximal cells also invading (Figure 4.5). In the same sample, the adjacent first molar has a majority of unlabelled cells (Figure 4.8). As these teeth are adjacent in the same tooth row, their constituent cells reveal dynamics of this developmental axis. Their respective numbers of cells are presented in Figure 4.9.

Cell counts reveal differential expansion of distal and presumptively proximal cells, as well as shared lineage of distal cells in the molars

Two key aspects of the tooth row are revealed by this data. First, there is a far greater abundance of unlabelled proximal cells within the first molar, compared to the less developed second molar. If we were to assume that the first molar had identical proportions to the second molar when it was at the same developmental stage, then there has been a doubling of the distal population, but an eight-fold increase in the unlabelled population. This indicates a differential expansion of the two populations either by cell division or further immigration of unlabelled cells to the tooth.

A second aspect is the similarity of the two populations. Both have a significant yellow population, and a noticeable red population, with the second molar including also a few cyan cells. It should be noted that as these are sections, they represent only a small sample of the total cells of the tooth. None the less given the distorting influence of the founder effect, this would imply that the two adjacent teeth have formed from reasonably similar populations. This suggests that the distal populations contribute to adjacent teeth by budding from a single migratory population, rather than several populations being specified independently and migrating into position.

Because Figures 4.2, 4.5, 4.7 and 4.8 are from the same animal (Figure 4.1A) we can assemble these to aid in interpretation of the lower dentition (Figure 4.10). There is no apparent link between the distal contributions to the incisors and the molars, suggesting that the two tooth types are specified by two different populations. As

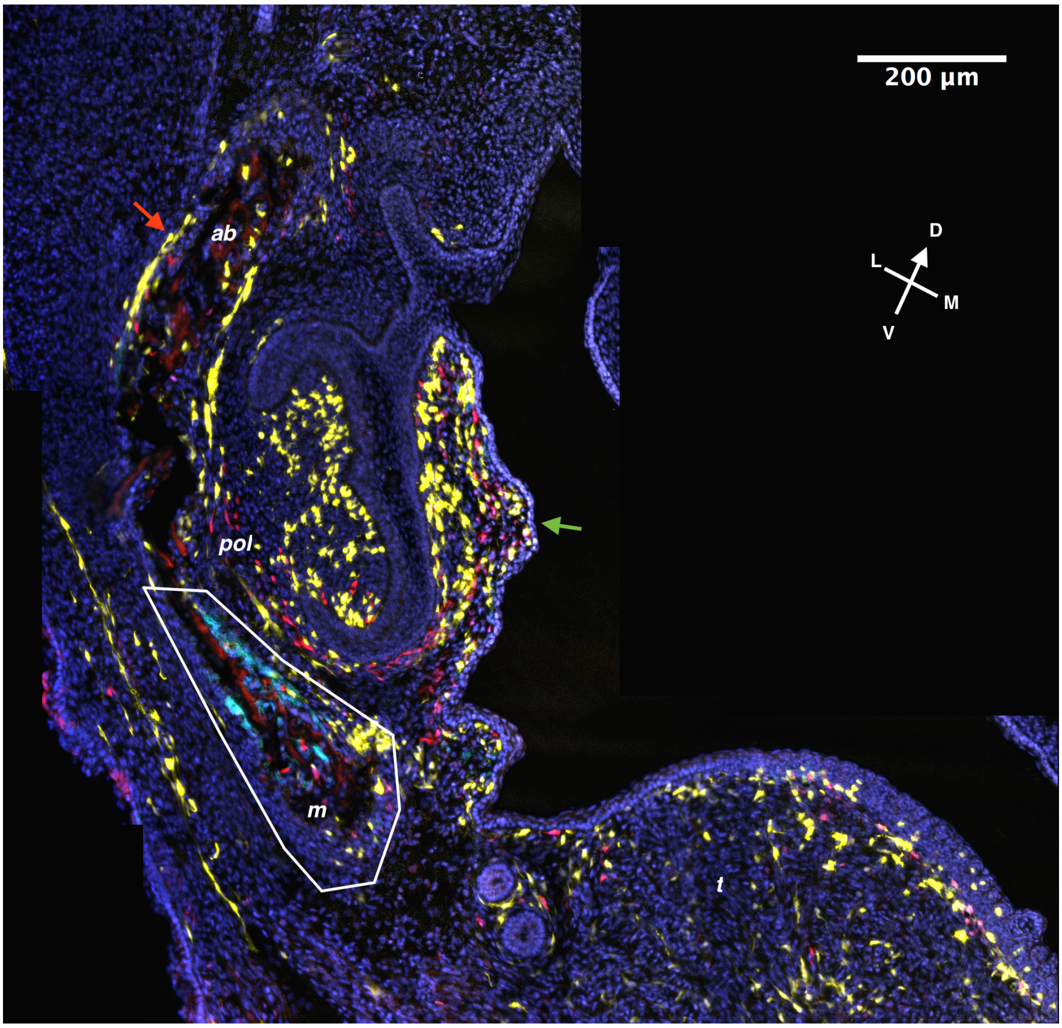

Figure 4.8: Cryptic Polyclonal Boundaries around the developing molar. Stitched coronal section. At embryonic day 16.5, a cryptic polyclonal boundary can be observed in the distal populations of the jaw. The yellow and red populated tooth bears none of the cyan cells that are present the mandible (white box), though do bear similarity to both the mesenchyme surrounding the tooth (green arrow), and the alveolar bone positioned laterally to it (red arrow). This tooth is adjacent in the jaw to the one shown in Figure 4.5 and opposite in the mouth to the molar shown in 4.6 and 4.7. *t* - tongue, *m* - mandible, *ab* - alveolar bone, *pol* - periodontal ligament.

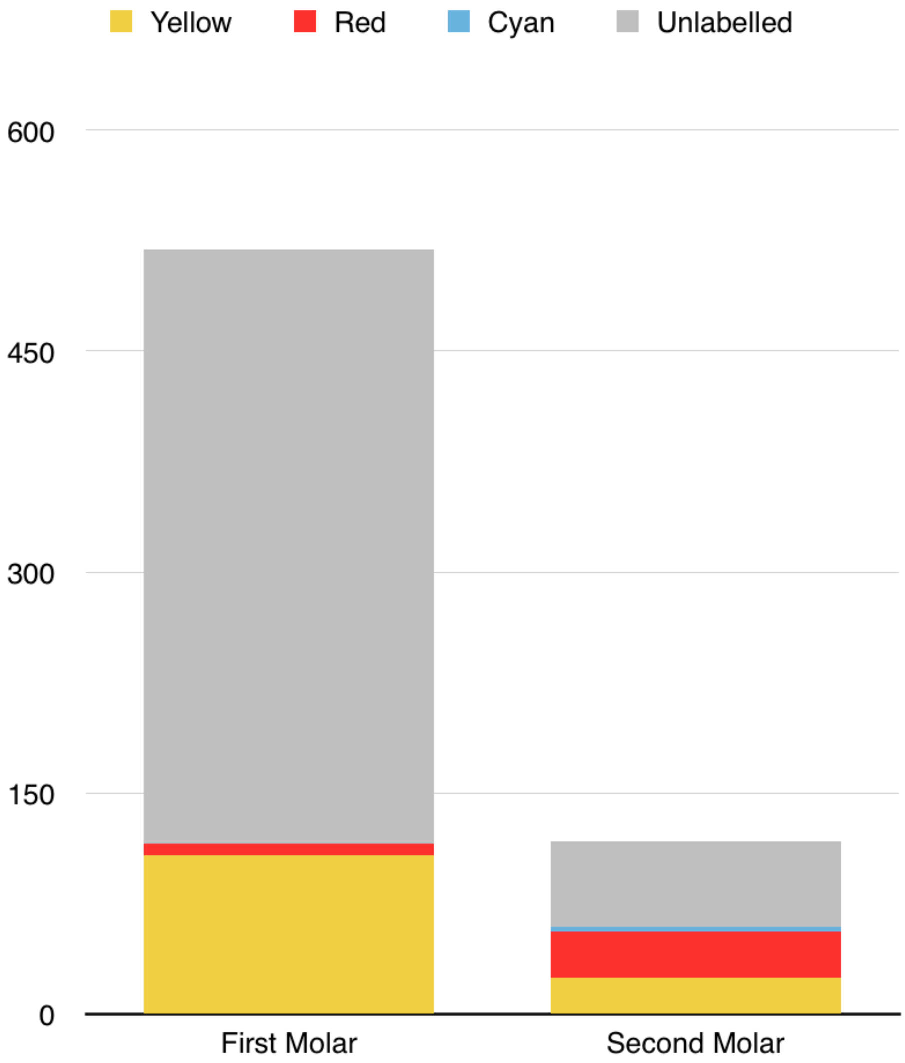

Figure 4.9: Adjacent first and second molars have similar Confetti populations, but a large difference in the number of unlabelled cells. Counts of Confetti labelled distal cells and unlabelled presumptively proximal cells in an adjacent first molar (Figure 4.8) and second molar (Figure 4.5). The first molar has twice as many labelled distal cells as the less-developed second molar, but eight times as many unlabelled cells, suggesting differential expansion of the two populations. Both distal populations have been subjected to the founder effect, but are still relatively similar, consisting mostly of red and yellow cells, suggesting that they arose from the same original migratory population.

expected, there is no lineage similarity across the midline, suggesting that each side of the jaw specifies its own teeth. However, we can suggest that adjacent molars of the same row do potentially share a common lineage, a possibility that can be explored further in the next Chapter.

Differences of cell mixture underpin heterodonty

This demonstrates a fundamental distinction between the two tooth types: within incisors distal cells dominate with a minor presumptively proximal component, and within molars a majority of presumptively proximal cells with a minor distal component. Notably at early stages, both are predominantly distal. Therefore the critical distinction between the incisors and molars are cell division dynamics which affect the final mixture of labelled and unlabelled cells within each.

The first molar on the opposite side of the mouth to Figure 4.8 is shown in Figures 4.6 and 4.7. It is apparent that there is a spatial segregation of the tooth into overlapping polyclonal regions. This suggests that there is some expansion of distal cells during the establishment of the cap-stage tooth. The fact that the other teeth observed are not as remarkably mixed suggests that it is a very small population of cells which starts the initial invasion, leading to founder effects in the resulting architecture of the tooth. Based on this polyclonal modularity, and the observation of two and three colour teeth, the model of Chapter 3.1.3 would suggest that the initial distal contribution to the tooth is fewer than 10 cells.

4.3.3 The mandible is derived from few distal cells, and is distinct from the alveolar bone

The previously proposed distinction between the odontogenic and mandibular migratory populations is still evident in these Figures. More astonishingly, the alveolar bone appears to not only be developmentally independent from the mandible, but furthermore appears to match the tooth-forming population (Figure 4.8, red arrow). There are two possible explanations for this: the alveolar bone may arise from a third migratory population distinct from either tooth or mandible, or the alveolar bone and odontogenic population are developmentally linked. This hypothesis must be tested across a number of teeth, and is the subject of the next chapter.

More critically here though, the suggestion that the putative mandible derives from a small distal population is further vindicated. This section of mandible is entirely red

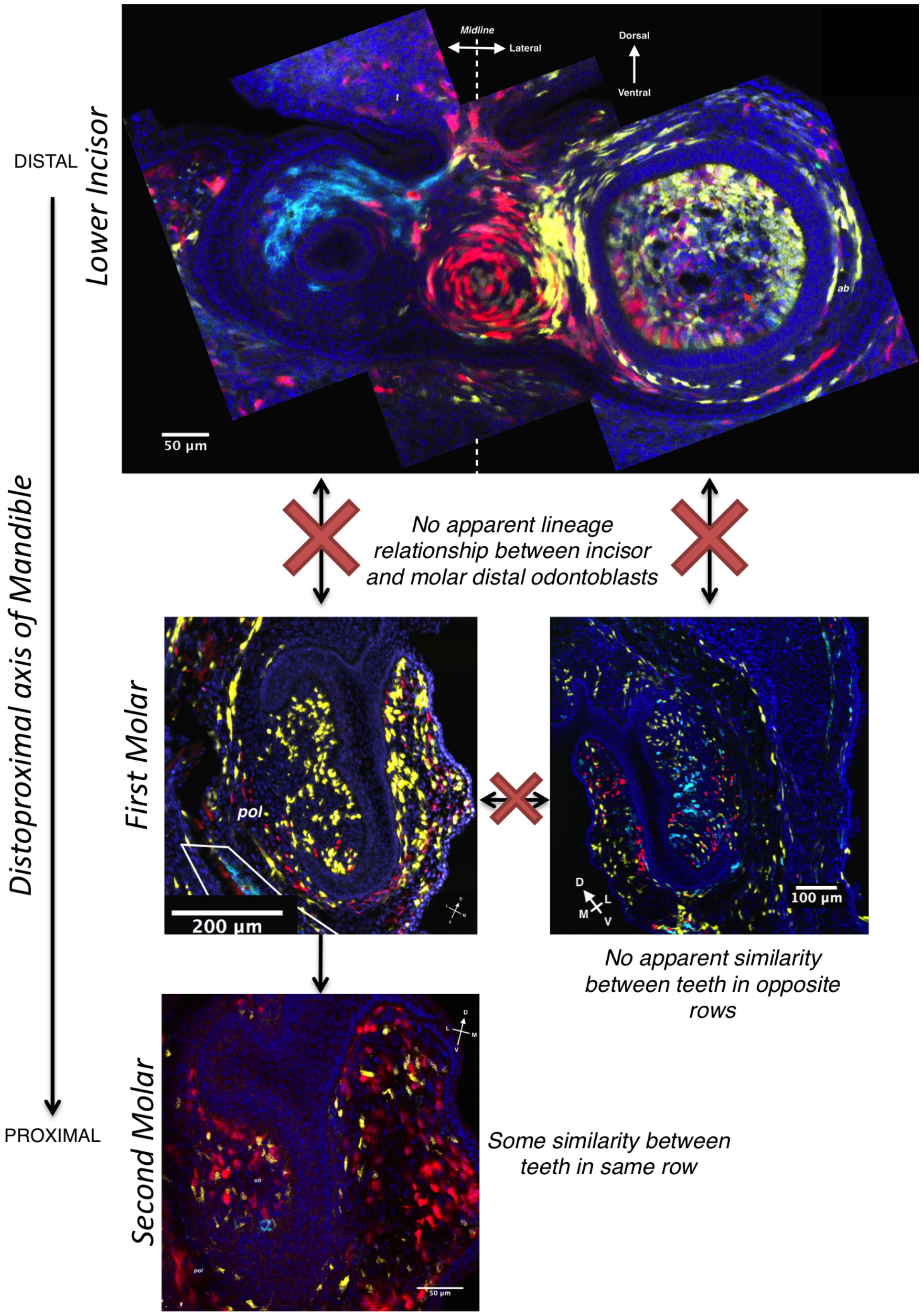

Figure 4.10: Reassembled lower dentition of the animal depicted in Figure 4.1A The lower incisors (From Figure 4.2) bear no apparent lineage relationship with either the first right molar (from Figure 4.8, nor the first left molar (from Figure 4.7. The right second molar (From Figure 4.5) however does bear some potential lineage relationship to the first molar on the same side, suggesting that both are generated from the same proximally migrating distal population.

and cyan, with no yellow cells. This further indicates that even at a well developed E16.5 stage, the mandible is still entirely derived from the descendants of a small (<10 cells) distal population.

4.4 Summary - Heterodonty is underpinned by differing proportions of distal and presumptively proximal cells

While the previous chapter demonstrated that molars form from a distal population of cells that migrate into proximal territory, this chapter demonstrates that the two tooth types develop very differently. Within the incisors, distal cells proliferate, and while there is a population of presumptively proximal cells, it appears to be small (Figures 4.2 and 4.3). In the molars, a small group of distal cells clearly have an important role in initiating the tooth and initially are dominant (Figure 4.5). These grow quiescent after a few divisions and are gradually diluted out by presumptively proximal cells (Figures 4.8 and 4.7).

The observation of a cellular differential between incisors and molars suggests that it is the proportion of distal cells which ultimately determines tooth type. Tucker et al. [1998] demonstrated that BMP4 signalling is required for the presumptive incisor bud to adopt an incisor morphology. This suggests that the distal cells each produce a quantity of BMP4, with the size of the population thus determining the ultimate tooth morphology.

The observation of similar polyclonal composition between adjacent teeth (Figures 4.9 and 4.10) suggests that the larger odontogenic migration of distal cells proceeds in the proximal direction, producing bud populations that populate the jaw. The alternative mechanism to this would be if each distal contribution to the molars were specified while still in the distal territory, before migration into position. While this latter unsupported model would still require tooth positions to be specified prior to migration, the proposed successive budding is effectively supportive of the progress zone model of Osborne, and thus does not necessitate *a priori* tooth positions.

There are a few readily apparently cryptic boundaries within the observed populations. The cryptic boundary running through the incisor is intriguing, but if it has any real developmental significance it is currently inscrutable. The cryptic boundaries between the mandible and the alveolar bone are potentially very important.

The segregated migrations discussed in the previous chapter did not necessarily predict an origin for the alveolar bone. Nonetheless, it would appear that there is not only a distinction between mandible and alveolar bone, but also a potential relationship between odontoblast and alveolar bone lineages. This is contrary to the assumption that the alveolar bone is an extension of the mandible. This relationship however cannot be explored by simple observation, as it is difficult to intuit mixed relationships: for example, is the tooth more similar to the region that is more medial or that which is more lateral to it? This requires a quantitative approach, discussed in the next Chapter.

In summary, distal cells have been observed in molar development, exhibiting differential expansion from a small invading population. This is in contrast to the distal majority of the incisors, which still surprisingly have a small presumptively proximal component. Thus distal and likely proximal contributions do indeed align with the two tooth types of this heterodont dentition. This strongly implies a role for distal and proximal cells in defining tooth type, which shall be discussed in Chapter 6.

Chapter 5

The Polyclonal Architecture of the Teeth and Associated Bones Demonstrates the Origins of Thecodonty

As found in the last chapter, there is an apparent polyclonal architecture to the tooth and surrounding bone that would contradict the widely accepted model of tooth development. According to the morphogenic field model, the teeth, alveolar bone and mandible or maxilla should have no distinct pattern of polyclonal architecture and all form from patterning of a uniform mesenchymal population. However, Confetti labelling of the distal population suggests an association between the alveolar bone and the tooth, forming a unit distinct from the underlying mandible or maxilla.

This has fundamental implications for the nature of thecodonty. It has been long assumed that thecodonty represents the engulfment of the tooth root by the dentary bone. If this were true, given the model of distal invasion proposed in the previous chapter, the only possible polyclonal boundary would be between the tooth and alveolar bone, which itself would have no distinction from the mandible or maxilla. The fact that the association appears to be between tooth and alveolar bone suggests that perhaps these tissues have an ontogenic link distinct from the mandible and maxilla.

This is difficult to interpret accurately from simple imaging. Confetti cells do not necessarily expand in a static fashion, and mixing or migration of cells is common in development. As a result, mixed populations inhabit most parts of the Figures in the last chapter. This information is however still valuable: two sufficiently mixed populations dividing homogeneously in isolation will still retain closer proportions than a third population of more distant relation. In order to properly explore these distinctions, the definition of distal and proximal is less important, and all cells can be considered in either jaw. This is accomplished by labelling all neural crest cells with Wnt1-Confetti.

In order to explore polyclonal relationships in and around the teeth, a method was required that would aid perception of different mixes of confetti-labelled cells. This tool should reveal the boundaries between different mixtures of cells, and thus the boundaries between different polyclonally defined regions. This is accomplished utilising Principal Components Analysis (PCA) in a novel fashion as an image analysis tool. While PCA has been used in image analysis many times before, it would appear this is the first application for analysing mixtures of randomly labelled cells.

5.1 Methods

5.1.1 Labelling Strategy

As well as the distal population, it is useful to label all cells. This is accomplished by using the Wnt1-Cre transgene, raising Wnt1-Confetti mice that label all cranial neural crest cells. This cross is described in Chapter A.1. Wnt1-Confetti serves as an independent testing ground for the observations made using Hand2-Confetti and allows me to extend my findings to regions not derived from a distal population, namely the teeth in the upper jaw. Animal husbandry is described in Appendix A.1, and sample preparation in Appendix A.2. Sections and animals used are detailed in Figure 5.1.

5.1.2 Choice of PCA as an Analytical Tool

PCA operates by taking into account many different variables across different samples, treating these variables as axes of a multi-dimensional space, identifying the direction in which variance is greatest and re-orienting the data along this new axis, the first ‘principal component’. Further principal components are then identified as axes perpendicular to this, again maximising variance of the data along each axis. Each data point has a new coordinate position within this principal component space, encoding many different original variables into a few summary composite variables that best describe the data. The use of PCA is common in machine vision applications for its ability to integrate large amounts of disparate information into

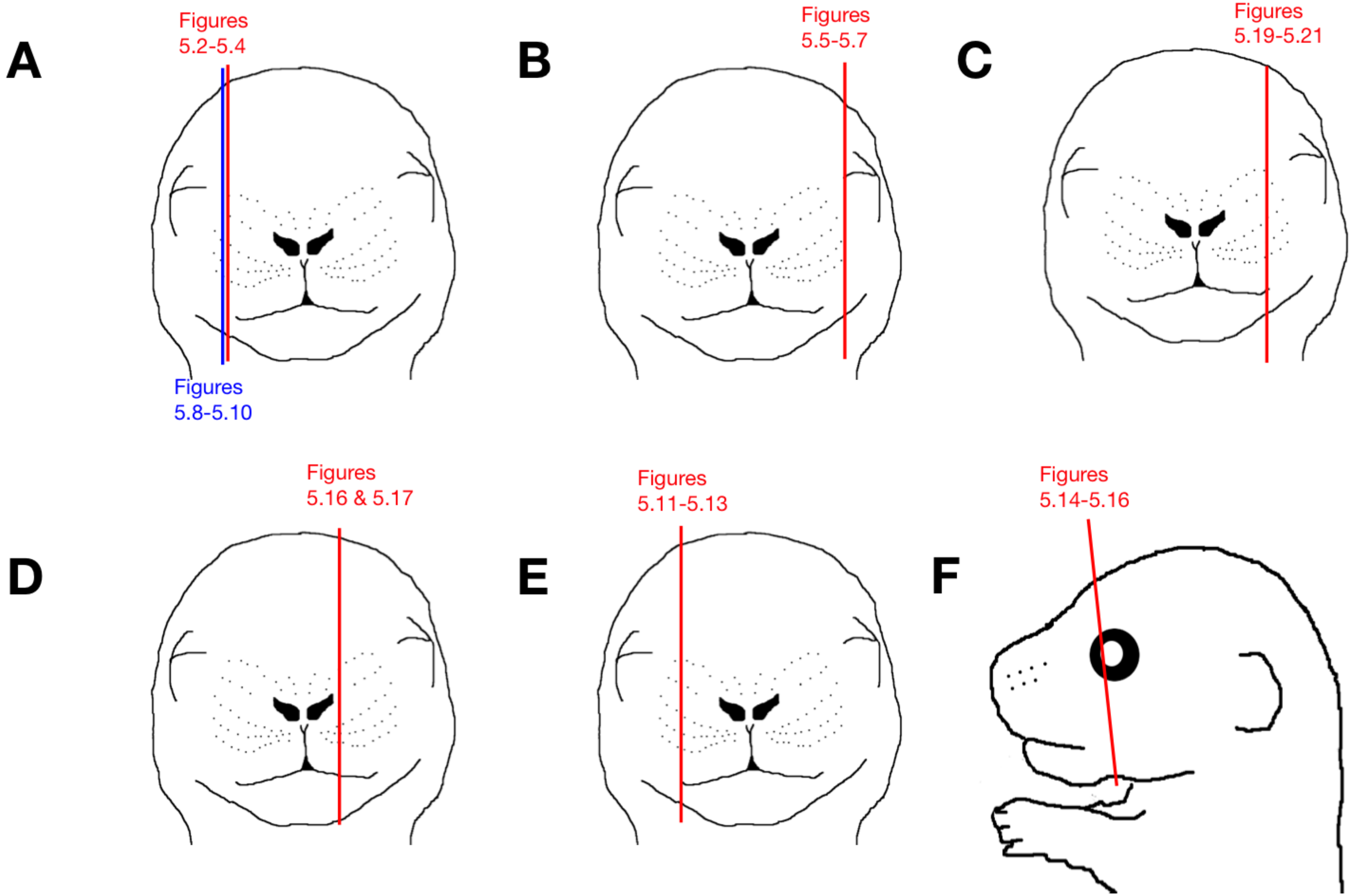

Figure 5.1: Sections used in this chapter. **A-C** are E18.5 Wnt1-Confetti, **D** is a P0 Wnt1-Confetti and **E and F** are both E16.5 Hand2-Confettis.

simple manipulable metrics [Davies, 2004], as well as for various application in biology, from morphometric analysis of skulls to [Bhullar et al., 2012] classification of the chemical characteristics of olfactants [Carey et al., 2010].

The value of using PCA with Confetti is that each colour may be treated as a variable, with the resulting principal components representing mixtures of these colours. This means that a territory that grows out of an initial population that was for example 20% red and 80% yellow will occupy a different position in principal component space to one which is 50% yellow and 50% cyan. Simply put, the complexity of four-colour mixtures can be condensed into summary statistics that encode mixtures.

This elevates our capacity to analyse randomly labelled lineage populations that are far removed from their period of labelling from the simple observation of possibly erroneous monoclones, to a far more discriminatory and valuable interpretation of polyclonal mixtures.

5.1.3 Implementation of PCA

A plugin for ImageJ/FIJI was developed that allowed for Principal Components Analysis of images based on volume of tissue of each colour and its mixture. The full discussion of this methodology is found in section A.5. In brief, for each pixel within regions of interest a sample is taken encompassing all pixels within a certain radius, weighted as a Gaussian blur, giving a multi-colour mixture identity. This identity is mostly defined by the material closest to the pixel being examined, with more distant pixels having ever decreasing weight upon the identity. These identities represent the mixture of labelled cells which comprise the population around that pixel. These are then subjected to PCA, revealing the distinct mixtures that comprise the sample. Different regions within the actual image can be explored within PCA space through a number of different readouts.

The key user-defined variable for this analysis is the σ (sigma) of the blur. This defines the width of the 'search area' around each pixel, and in effect determines how many cells contribute to each mixture. For each of these analyses a σ of $50\mu m$ was used. In a two-dimensional sample, this means that 66% of the identity of the mixture was determined by up to approximately 30 cells, and 95% by up to approximately 125 cells. As distal cells are relatively diffuse, the actual number of cells involved in each mixture is lower.

5.1.4 Representation of Data

Classically the data from PCA is displayed in dot plots, wherein a random sample of points can be shown within PCA space. This however removes information about the original anatomical locations of each point. To counter this, during the preparation phase several regions of interest can be specified, shown in following figures as coloured outlines. These have no impact upon the analysis itself but serve as an index to highlight populations within PCA space. Each row of the results from the PCA analysis represents a single pixel from the original image, and contains its position within the principal component space in columns. The regional index occupies a further column that can then be used to identify the anatomical feature that this pixel originally came from. These indices can then be used to segregate and label points within the dot plot in different colours.

Regional indices are useful for labelling an *a priori* structure, such as identifying teeth distinctly from bone, but they do not allow for any sort of *post-hoc* analysis. In order to do this, the principal component identities of each sample must be mapped back into their original positions within the image. To our knowledge, this is an entirely novel data representation developed for this thesis, which we call a 'PCA Map'.

This is an elegant representation of the data in a human-friendly fashion. Each mixture identity is re-encoded as a colour based on its position within Principal Component Space. Different mixtures will appear as different RGB colours in the PCA Map, with the intensity of red representing position in Principal Component 1, green representing Principal Component 2 and blue representing Principal Component 3. This helps to contextualise the findings of the PCA in a spatial manner, where usually they are only represented in an abstract sense. This also allows for interpretation of boundaries between differently encoded regions in a *post-hoc* fashion, rather than simply attempting to confirm an *a priori* division, as interfaces between distinct mixtures will appear as boundaries of colour.

The mapping of biological information onto a relevant map is not itself a novel concept. Cavalli-Sforza famously mapped genetic allele information onto geographical maps of Europe [Cavalli-Sforza, 1997], and it is becoming common practice in morphogenetic analysis to map information about changes or difference back onto a representation of the analysed structure [Nguyen et al., 2013]. To our knowledge, this is the first time that any metric of polyclonal mixed lineage information has been encoded directly into a map of anatomical structures.

Finally, a bar chart is produced that demonstrates the reliability of the PCA and how much variance is captured by each principal component. This is necessary to validate the interpretation of the PCA. The first two principal components typically account for more than 80% of all variance, and are sufficient to highlight key differences: encoding more as colours is also conceptually difficult given that there are only three primary colours. The variance bar charts for each analysis are all presented in Figure 5.22 at the end of this chapter.

5.2 Results

5.2.1 The molars and associated alveolar bone are developmentally distinct from the mandible and maxilla in Wnt1-Confetti Labelled Tissue

As the Wnt1-Confetti line labels the entirety of the jaw mesenchyme, it is very useful for detecting large scale polyclonal differences distinct from the invasive patterns explored with Hand2-Confetti. Figures 5.2 and 5.5 show a first and third molar respectively in two different E18.5 Wnt1-Confetti individuals. Both represent a large number of highly mixed cells, and it is impossible to interpret samples with any degree of confidence purely by use of subjective or simple methods, necessitating the use of PCA.

The PCA maps in Figures 5.3 and 5.6 reflect the mixture differences across either sample. Both show distinctive change in PCA encoding along a sharp line where the alveolar bone meets the mesenchyme. In both this is a transition from Red (High value in PC1) to Blue (Low value in PC1, High Value in PC3). Note that while this change in PCA encoding runs very close to the anatomical regions we manually defined (coloured lines in Figs 5.2 and 5.5, black lines in Figs. 5.3 and 5.6), the analysis did not have access to this regional information. The correspondence of the change in PCA encoding to our anatomical definitions demonstrates that a true biological boundary between distinct and isolated populations runs along this anatomical boundary.

Figure 5.3 shows striking similarity between the odontoblasts, periodontal ligament and the alveolar bone - all are labelled with the same red or yellow encoding, denoting a high value in PC1. This implies that they are from the same polyclonal population, which excludes the mandible. The yellow encoding in the odontoblasts

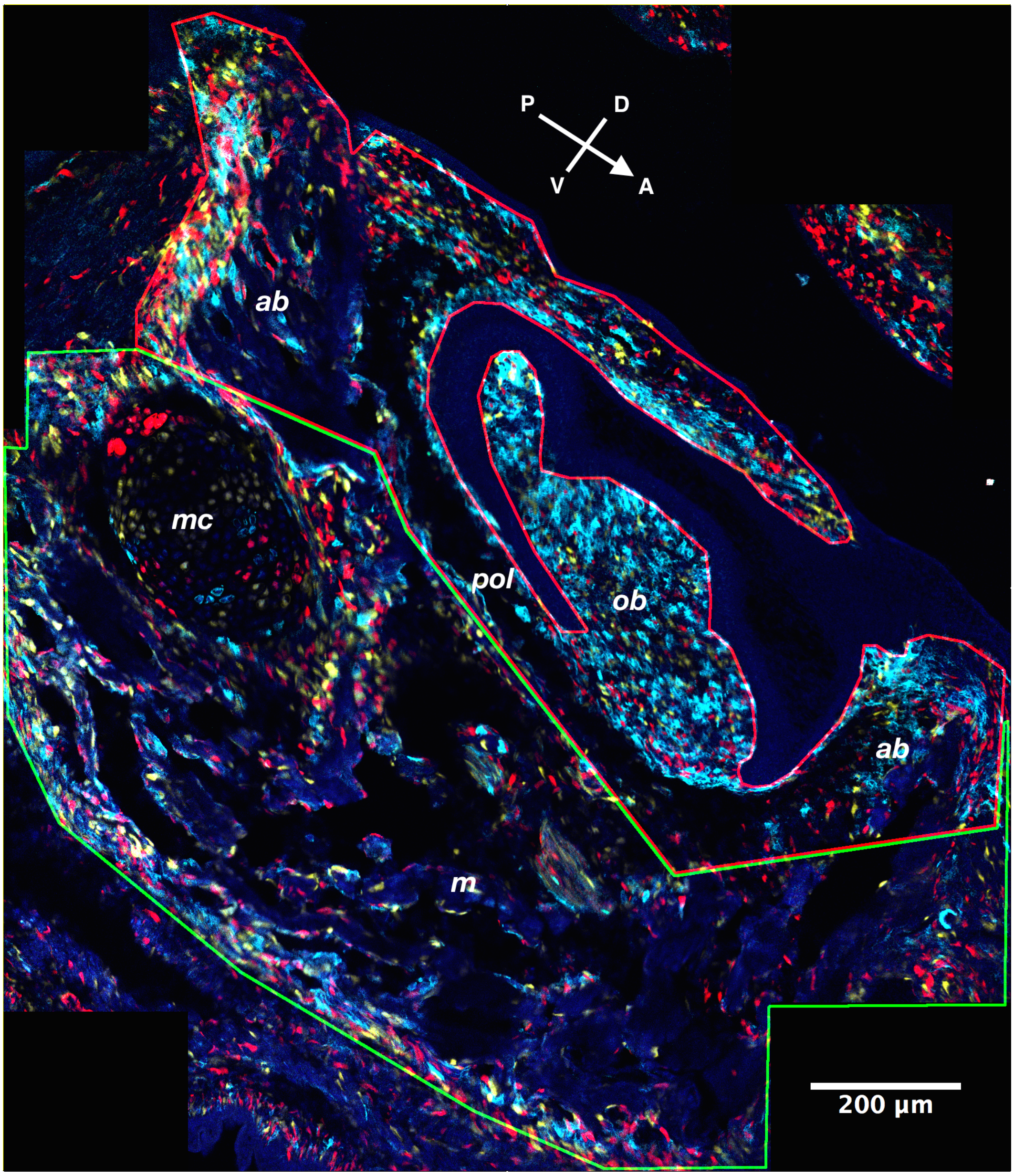

Figure 5.2: Sagittal section of an E18.5 molar and mandible in a Wnt1-Confetti Mouse. Lines show the PCA regions for subsequent related figures. This mandible is very well developed, and the tooth and alveolar bones are likewise very mature. Meckel's cartilage is visible to the left (posterior) edge of the image, demonstrating a mix of contiguous colours in patches, indicative of proliferation without mixing, unlike the rest of the section. Superficially it would appear that the tooth is far more dense with cyan cells than the mandible, which is more mixed and red-dominated. *m* - mandible, *mc* - Meckel's Cartilage, *ob* - odontoblasts, *pol* - periodontal ligament, *ab* - alveolar bone.

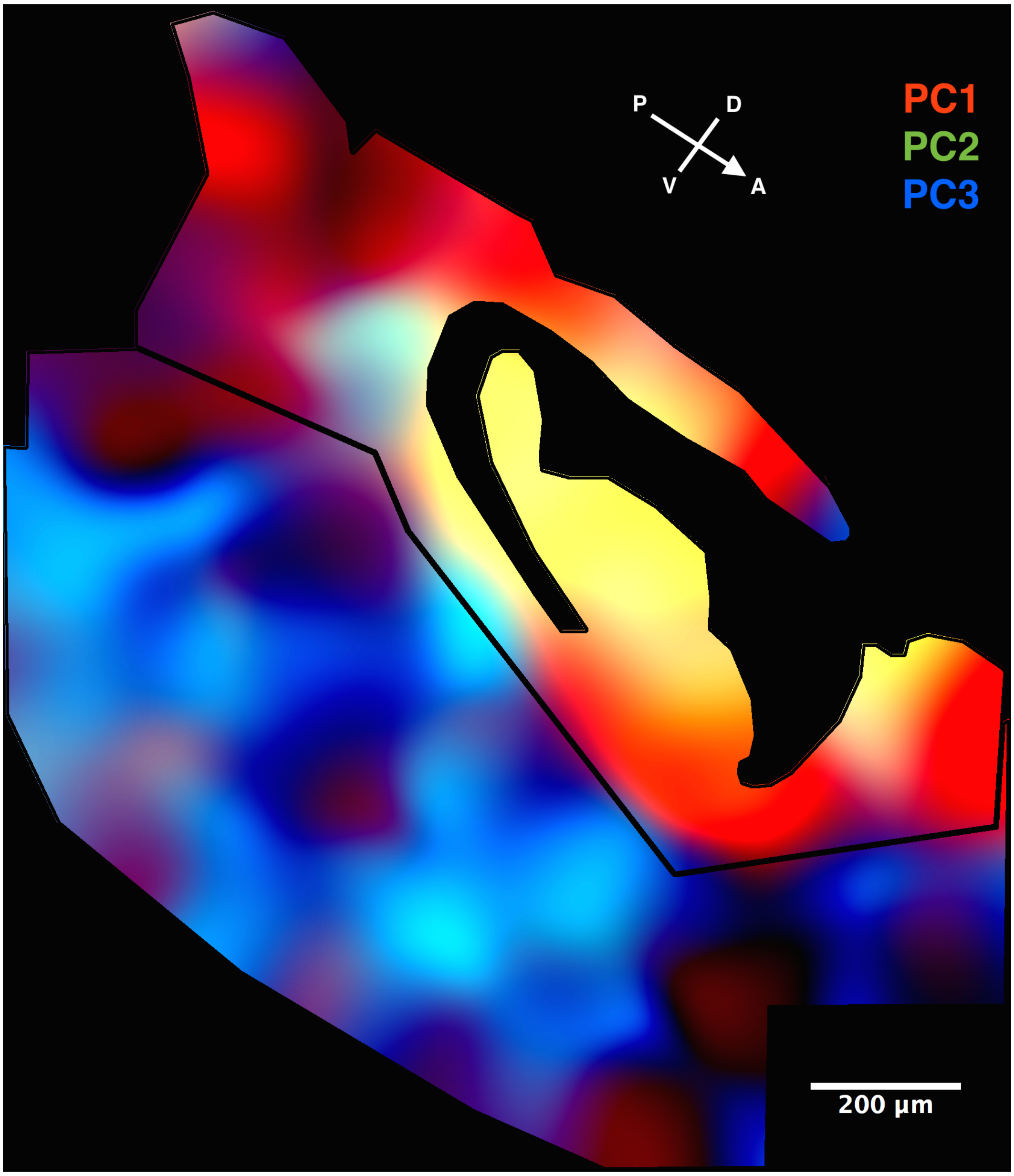

Figure 5.3: PCA Map of the sample shown in Figure 5.2, demonstrating independence of the alveolar bone, odontoblasts and periodontal ligament of a first modal from the mandible. The molar and alveolar bones are clearly distinct from the mandible. Principal Component 1 (red) delineates these two compartments, in a manner that mostly follows the manually defined anatomical compartments (black lines). Also notable is the lack of distinction between the mandible and Meckel's cartilage, demonstrating their shared origins.

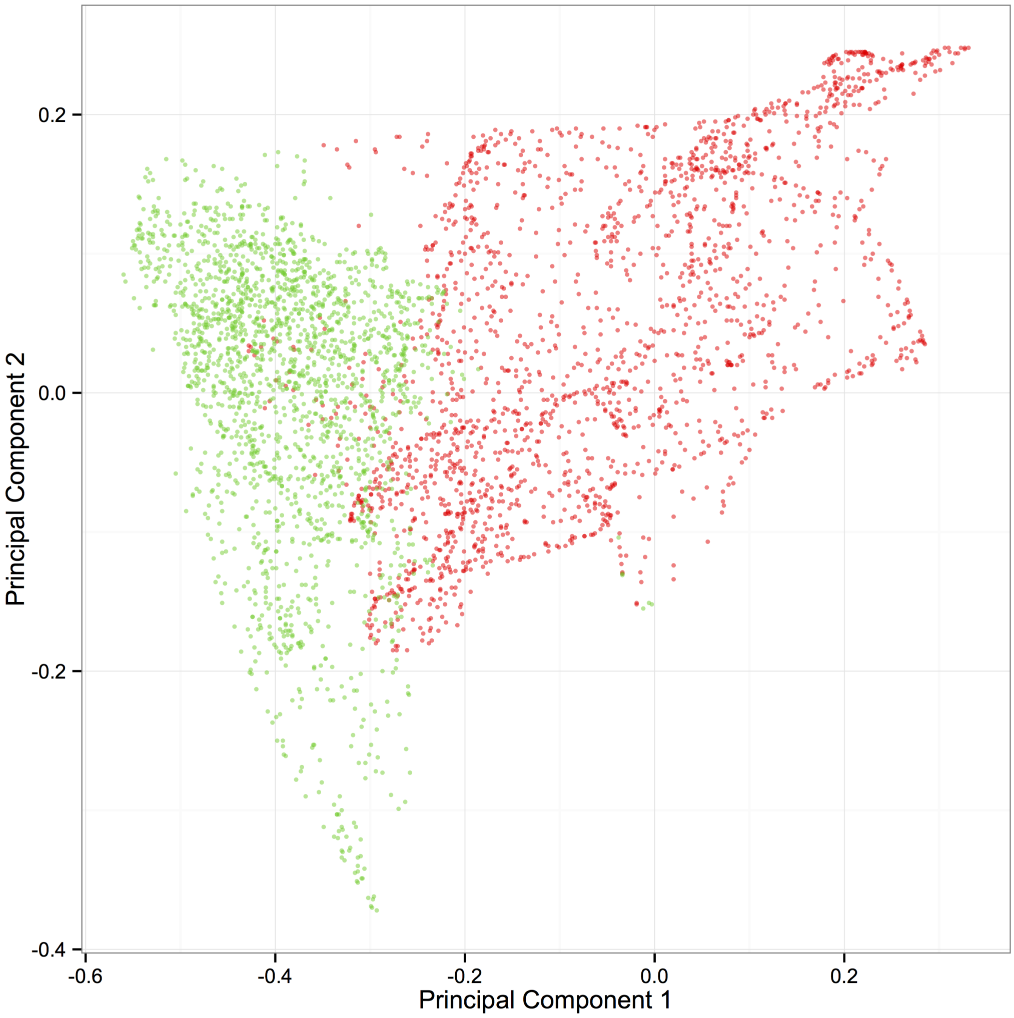

Figure 5.4: PCA plot for Figure 5.3, demonstrating independence of the alveolar bone, odontoblasts and periodontal ligament of a first modal from the mandible Shows 2000 random pixels from the two regions outlined in 5.2 mapped into PCA space using the same colour code: red for tooth, periodontal ligament and alveolar bone, and green for mandible. These clearly segregate with respect to the first principal component. The second component reveals within-compartment variance for both, suggesting the range of variance inherent in two segregated populations of comparable size and proliferation dynamics. This demonstrates that the two compartments are indeed distinct and developmentally segregated.

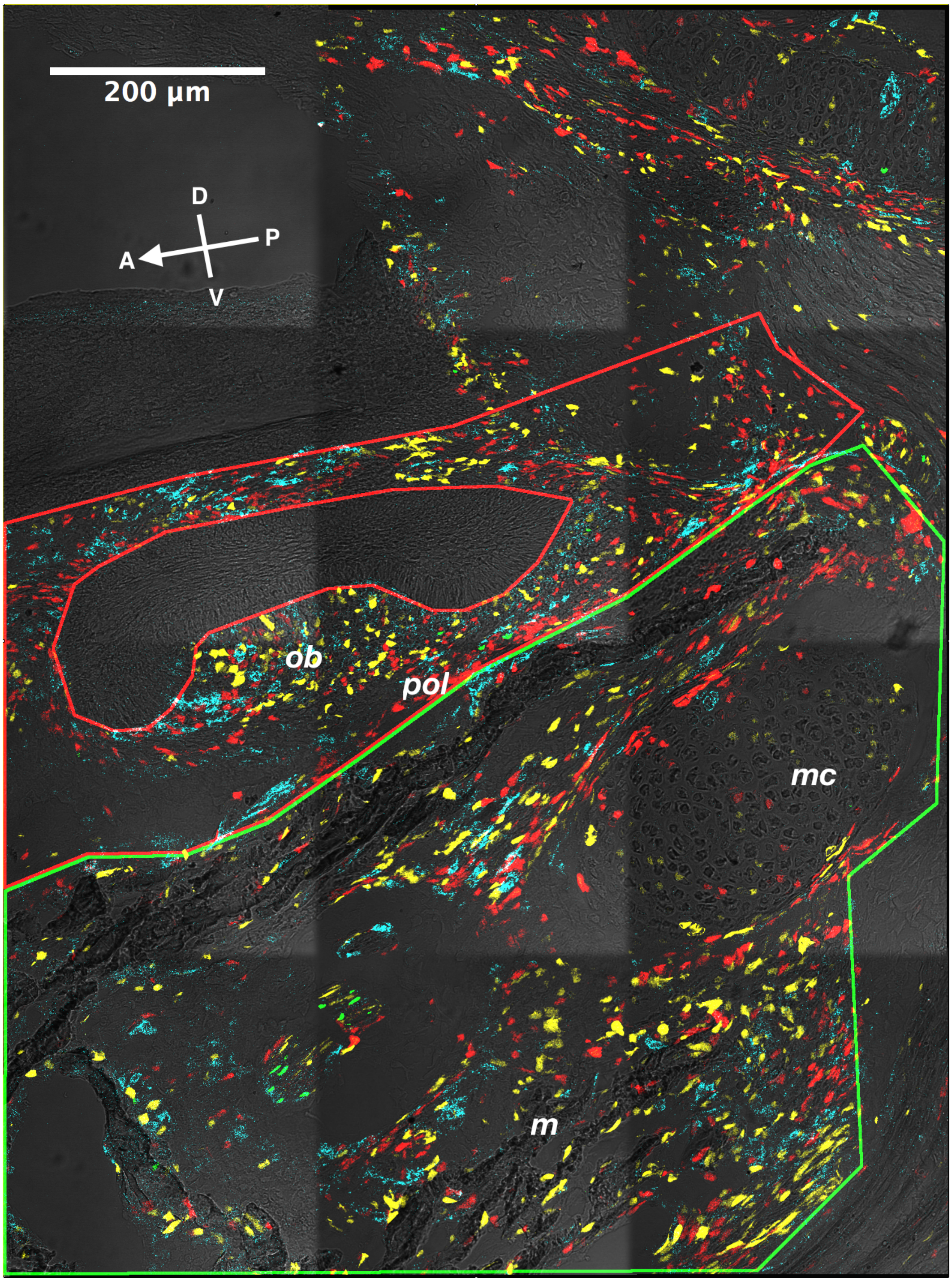

Figure 5.5: Sagittal section of an E18.5 third molar and mandible in a Wnt1-Confetti Mouse. Lines show the PCA regions for subsequent related figures: red denoting the buccal mesenchyme (periodontal ligament, odontoblasts and nascent alveolar bone) and green denoting the mandible. The posterior section of this mandible is very well developed around Meckel's cartilage. This tooth is far less developed than that of Figure 5.2. *m* - mandible, *mc* - Meckel's Cartilage, *ob* - odontoblasts, *pol* - periodontal ligament.

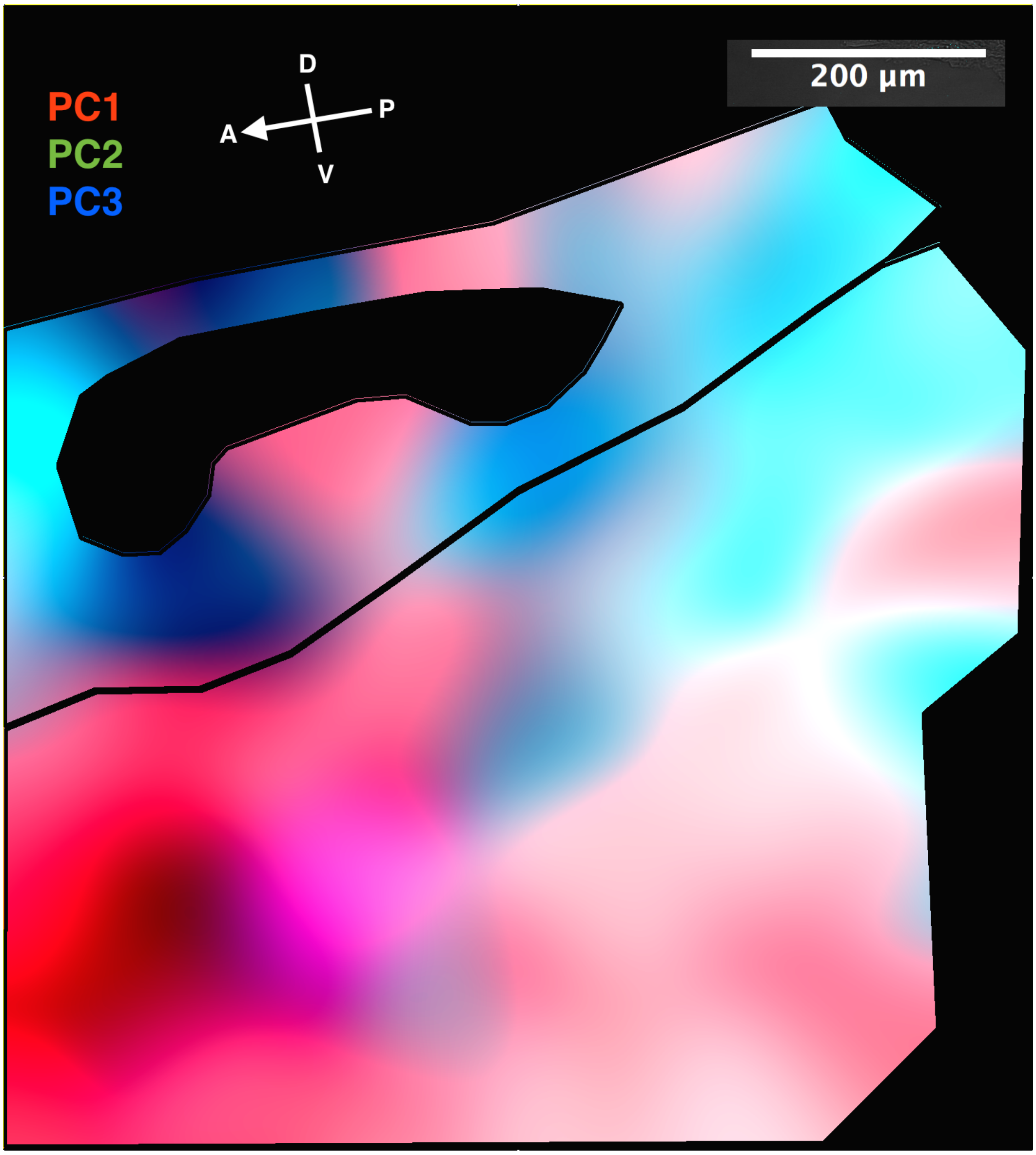

Figure 5.6: PCA Map of the sample shown in Figure 5.5, demonstrating independence of the alveolar bone, odontoblasts and periodontal ligament of a third modal from the mandible.. While less cleanly delineated than the previous example, there is still a reasonably clear distinction between the tissue above the bone and the mandible itself. The PC1-high identity in red is present in the mandible and in small patches within the buccal tissue, though this can occur as a coincidence. Regardless, a cryptic boundary is well supported.

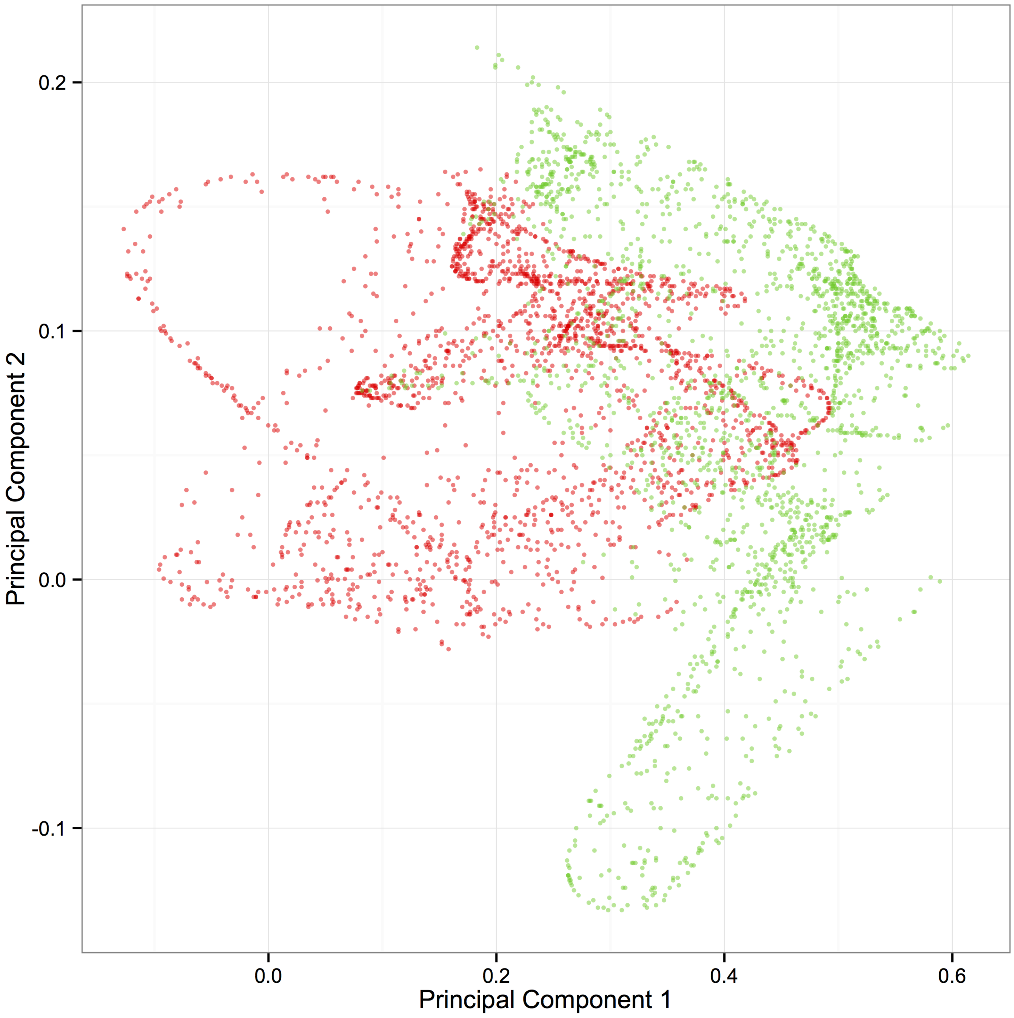

Figure 5.7: PCA plot for Figure 5.6, demonstrating independence of the alveolar bone, odontoblasts and periodontal ligament of a third modal from the mandible. Shows 2000 random pixels from the two regions outlined in 5.5 mapped into PCA space using the same colour code: red for alveolar bone, odontoblasts and periodontal ligament, and green for mandible. This shows similar trends as in Figure 5.4, with the same conclusions: the alveolar bone, periodontal ligament and odontoblasts are distinct and developmentally segregated from the mandible. The two compartments are slightly more mixed at their interface, suggesting a greater similarity than in the previous example, though this can be coincidental.

and anterior alveolar bone shows that while that most of the variance in this image comes from the distinction between the mandible and the buccal mesenchyme (teeth, alveolar bone and periodontal ligaments), there is also a slight distinction between the tooth itself and the alveolar bone posterior to it, likely due to a founder effect in generation of the tooth. This further suggests that the alveolar bone anterior to it may arise from this modified founder population, and consist of cells that emigrate back out from the tooth bell in an anterior (and thus lateral) direction.

The distinction between alveolar bone and buccal mesenchyme can also be seen in Figures 5.5 and 5.6. This represents a tooth further back in the row, and there is still a clear boundary within the PCA map close to the anatomical boundary of mandible and periodontal ligament. There is a greater similarity between the mandibular population and the odontoblasts within this sample. There is no visible contiguity between the mandibular population and the odontoblastic population, so the similarity is likely a coincidental expansion of the very prevalent yellow cells within the odontoblasts.

The plots shown in Figures 5.4 and 5.7 demonstrate that in both there are strong differences between the mandible itself and the population that comprises the alveolar bone and the odontoblasts. In both, the colours of the points correspond to the outlined territories of Figures 5.2 and 5.5 respectively, denoting that this data point was drawn from those anatomical regions: green denoting mandible and red denoting alveolar bone and tooth.

In Figure5.4 the two anatomical regions segregate along an apparently vertical interface, showing complete separation in the first Principal Component. This means that the greatest source of variance anywhere within the image is contained within the difference between the mandibular population and the alveolar/odontogenic population. The conclusion from this is that the alveolar bone and odontoblastic lineages form independently from the mandible. The overlap between these two groups of points within the plots comes from the fact that this is comparing an *a priori* anatomical definition to the actual lineage boundaries of the sample, so there is some encroachment of the actual cellular territories across our artificially defined boundaries.

Figure 5.7 corroborates this point to a degree, though there is a greater overlap between the two populations. Though the populations within the tooth bell and the mandible are more similar than seen in the previous example, this can arise coincidentally, and the anatomical interface between the mandible and the alveolar bone/periodontal ligament still represented an interface between two different lineages, as evidenced by Figure 5.6. The fact that the plot does not demonstrate this difference as adequately as the line is a testament to the utility of mapping analytical data back onto anatomical diagrams. One could of course perform the analysis and then identify contiguous regions of similar PCA encoding, which would by definition create cleanly segregated PCA Plots. However, the approach employed in this chapter better represents the relationship between my *a priori* anatomical interpretation, and the 'true' biological compartmentation.

This distinction of dentary bone contrasted with a joint tooth-alveolar bone-periodontal ligament compartment is also present in the upper molars when compared to the maxilla (Figure 5.8). Once again the same polyclonal identity links the tooth, periodontal ligament and associated alveolar bone, all of which are distinct from the maxilla (Figure 5.9). This also extends to the alveolar bone on the oral side of the tooth. These distinctions segregate strongly within the first two principal components (Figure 5.10). This demonstrates the generality of this lineage boundary across both jaws, and suggests that whatever process shapes the lower jaw also shapes the upper jaw. Therefore the teeth of the upper jaw likely form from a distal to proximal migratory population as in the Hand2-labelled lower jaw, even though this cannot be labelled directly. It cannot be inferred that the maxilla forms from an early small distal to proximal migration as demonstrated in the mandible in the last chapter, only that the teeth have a similar compartmentation from the underlying dentary bone.

5.3 The distal contributions to the molars also show modularity of tooth and alveolar bone, distinct from the mandible

In the last section it was noted that the alveolar bone appears to be produced from the same population as the odontoblasts. This bone is also labelled in Hand2-Confetti as coming from the distal population of the mandible (Figure 5.11). It is worth noting that the mandible is far more densely populated with labelled distal cells relative to the teeth and alveolar bone which have significant unlabelled and thus presumptively proximal constituents, further suggesting that the two structures form by different processes. These two populations do not segregate cleanly in PCA space, but do have quite obvious compartmentation in the PCA map, particularly

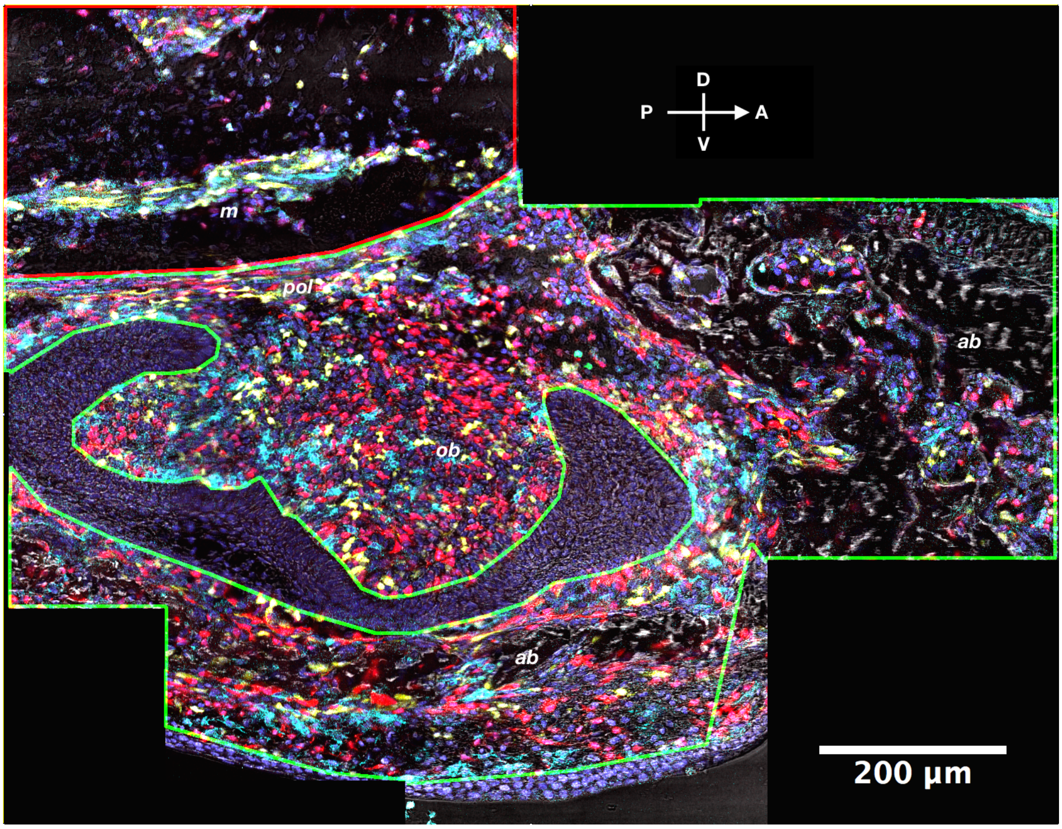

Figure 5.8: Sagittal section of an E18.5 upper second molar and maxilla in a Wnt1-Confetti Mouse. This region shows very well developed alveolar bone, both on the oral side of the tooth (bottom of the image) and to the posterior (right side of the image). The maxilla is visible outlined in red. There is an apparent colour discontinuity, with the teeth and alveolar bone containing far more red cells than the maxilla. *m* - maxilla, *ob* - odontoblasts, *pol* - periodontal ligament, *ab* - alveolar bone.

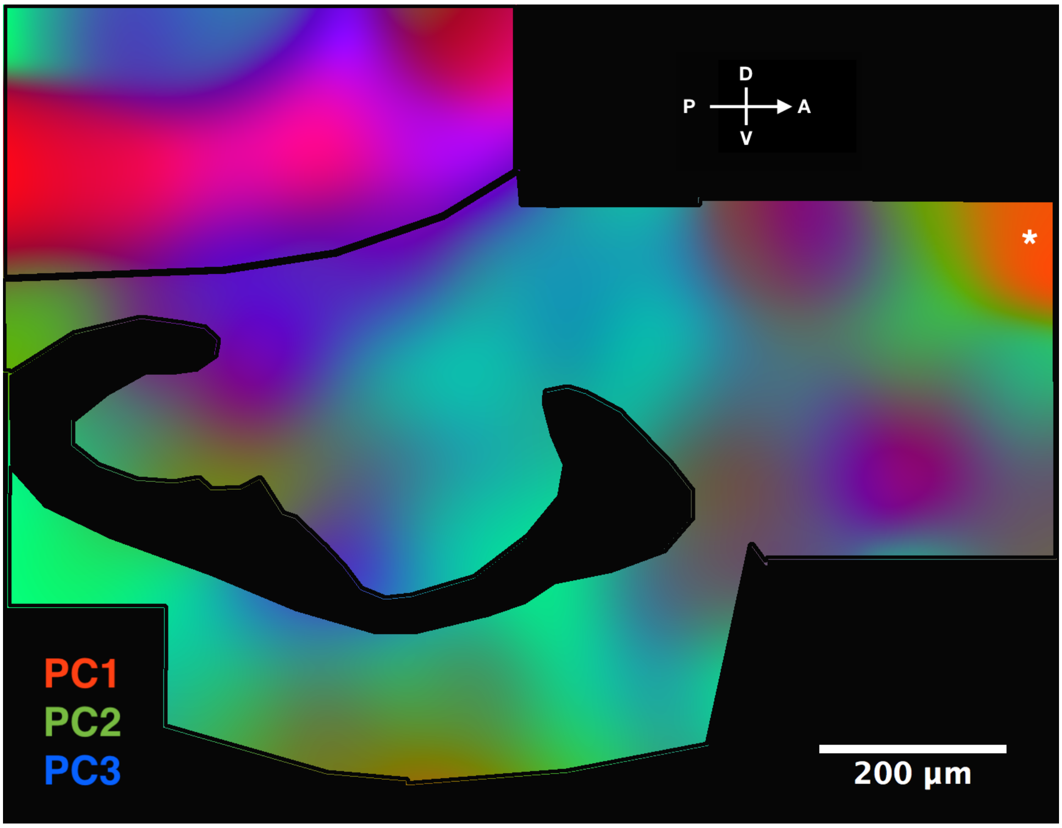

Figure 5.9: PCA Map of the sample shown in Figure 5.8 demonstrating independence of the alveolar bone, odontoblasts and periodontal ligament of an upper second modal from the maxilla. The maxilla is clearly very distinct from the rest of the sample, represented as a strong red stripe within PC1. One mixture is encoded as a turquoise colour, which corresponds to the odontoblasts, oral-side alveolar bone and adjacent alveolar bone. The very posterior edge of the adjacent alveolar bone has a distinct orange encoding (asterisk), suggesting perhaps a different polyclonal territory associated with an adjacent tooth.

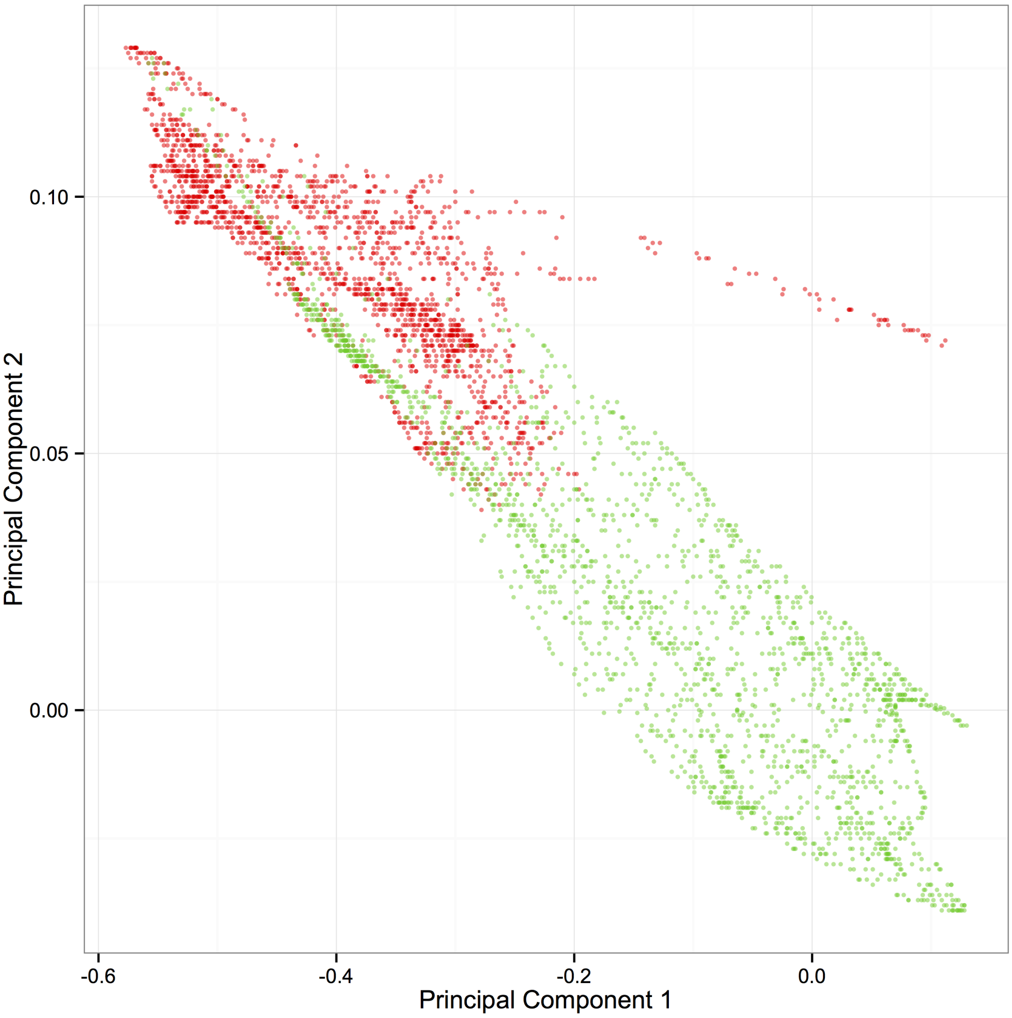

Figure 5.10: PCA plot for Figure 5.9 demonstrating independence of the alveolar bone, odontoblasts and periodontal ligament of an upper second modal from the maxilla. Shows 2000 random pixels from the two regions outlined in 5.8 mapped into PCA space using the same colour code: red for maxilla, and green for tooth, alveolar bone and periodontal ligament. The compartments explored in the upper molar (Fig. 5.5) show the same segregation of maxilla from alveolar bone and tooth populations. The two compartments do not segregate so well within PC1 alone, but do across the first two principal components. The presence of similar compartmentation in the upper jaw suggests that the same distal to proximal migrations are occurring in odontogenesis in both jaws, even though the upper distal population cannot be observed with Hand2 labelling.

in the second principal component (Figure 5.13).

This pattern is borne out in a coronal view 5.14. Here it is clear that the mandible is distinct from the developing alveolar bone and tooth (red outline). Within the PCA map three populations are visible: the mandible, alveolar bone and tooth (Figure 5.15). It would appear that the tooth population and alveolar bone are intimately linked, as they are quite confined within the first principal component space (Figure 5.16), and the blue colour encoded within the alveolar bone also appears on the buccal side of the tooth. However, the closer relationship between the tooth and medial/buccal mesenchyme would suggest that a lateral-to-medial axis of migration creates this pattern.

This process is implicated in formation of alveolar bone around the incisor. Figure 5.17 represents a sagittal section through a P0 incisor, showing complex mixtures of cells throughout the odontoblasts. At the posterior edge (Figure 5.18) very rare green labelled populations are visible extending around the end of the invaginated epithelium and into the bone. Fewer than 5% of clones appear to adopt this colour, so the likelihood of coincidental green labelling is less than 0.25%. This is better explained by either a common lineage origin of odontoblasts and alveolar bone, or alternatively a migration from the tooth giving rise to the alveolar bone, which is supported by the highly suggestive arrangement of cells in that Figure.

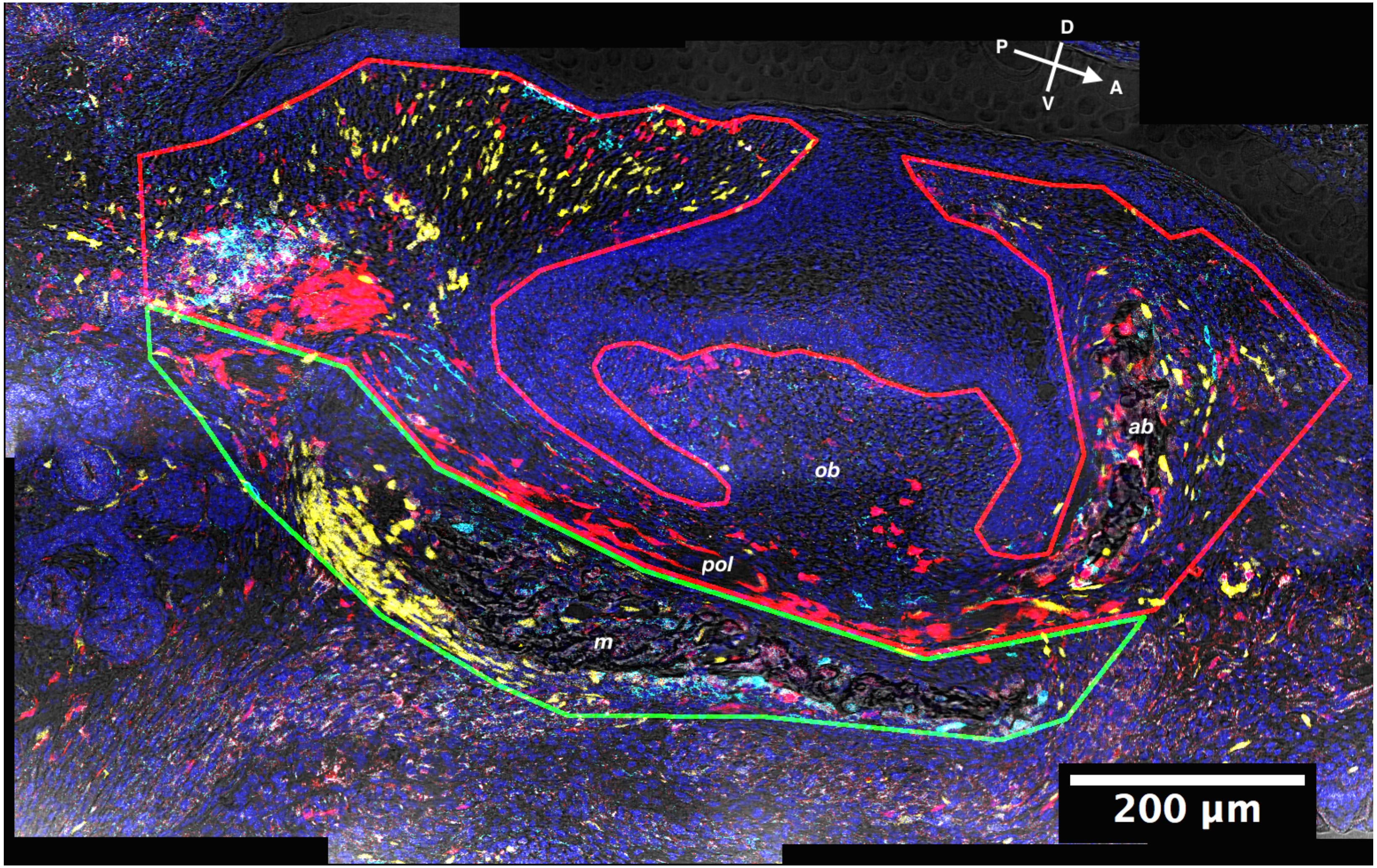

Figure 5.11: Sagittal section of an E16.5 lower first molar and mandible in a Hand2-Confetti Mouse. A clearly red-and-cyan dominated tooth appears to have an association with a population spreading to the anterior (right) of the bone, originating from a knot at the posterior apex of the mandible (green boundary). This association extends into alveolar bone anterior to the tooth (right side of the image). *m* - mandible, *ob* - odontoblasts, *pol* - periodontal ligament, *ab* - alveolar bone.

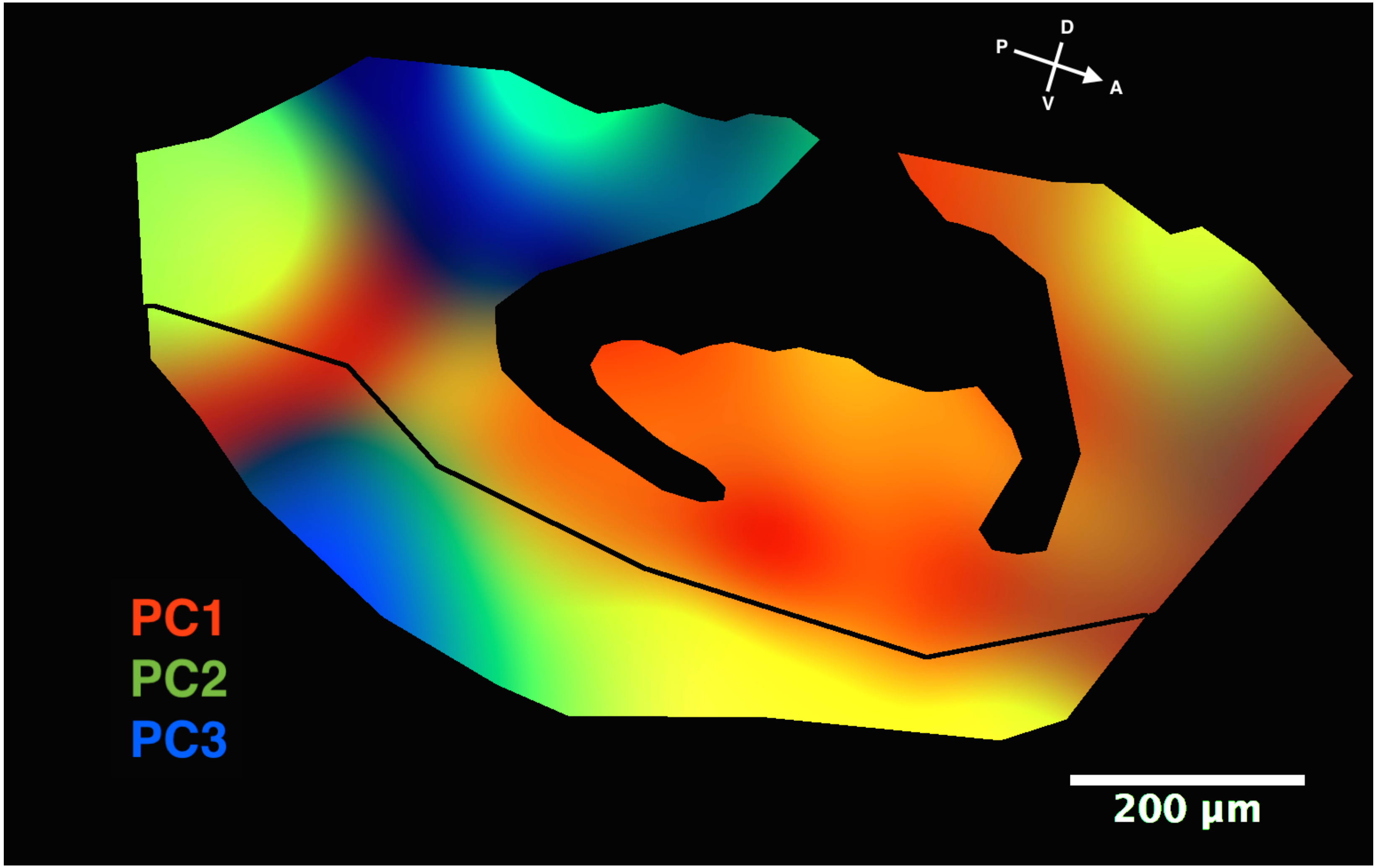

Figure 5.12: PCA Map of the sample shown in Figure 5.11, demonstrating independence of the distal contributions in the alveolar bone, odontoblasts and periodontal ligament of a first modal from the mandible.. The black annotation line appears to follow a clear boundary between A PC1 red/orange region and a PC2/3 green and blue dominated region, which is the mandible. The territory of the population that defines the tooth also extends into the alveolar bone which is anterior (right) to the tooth, and extends under the tooth to the posterior. Interestingly the mesenchyme to the posterior (left) of the tooth appears to have the same origin as the more posterior part of the mandible. Due to the curvature of the jaw, both this mesenchyme and that portion of the jaw are also more lateral and dorsal than the anterior end.

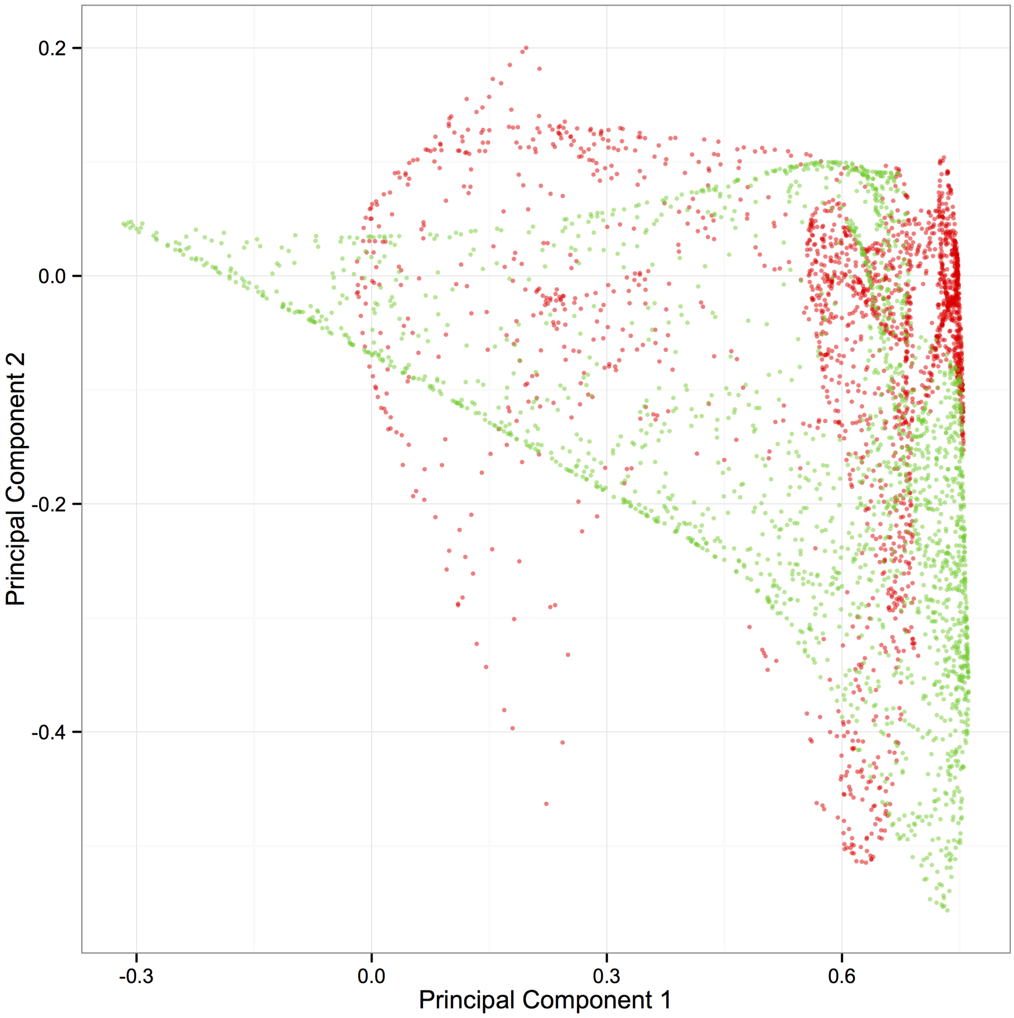

Figure 5.13: PCA plot for Figure 5.12, demonstrating independence of the distal contributions in the alveolar bone, odontoblasts and periodontal ligament of a first modal from the mandible. Shows 2000 random pixels from the two regions outlined in 5.11 mapped into PCA space using the same colour code: red for X and green for Y. While the two populations are not occupying exactly the same space, they are not well segregated. This is due to the presence of several populations within the two regions, demonstrating that the predicted boundaries, while valid, were not exhaustive.

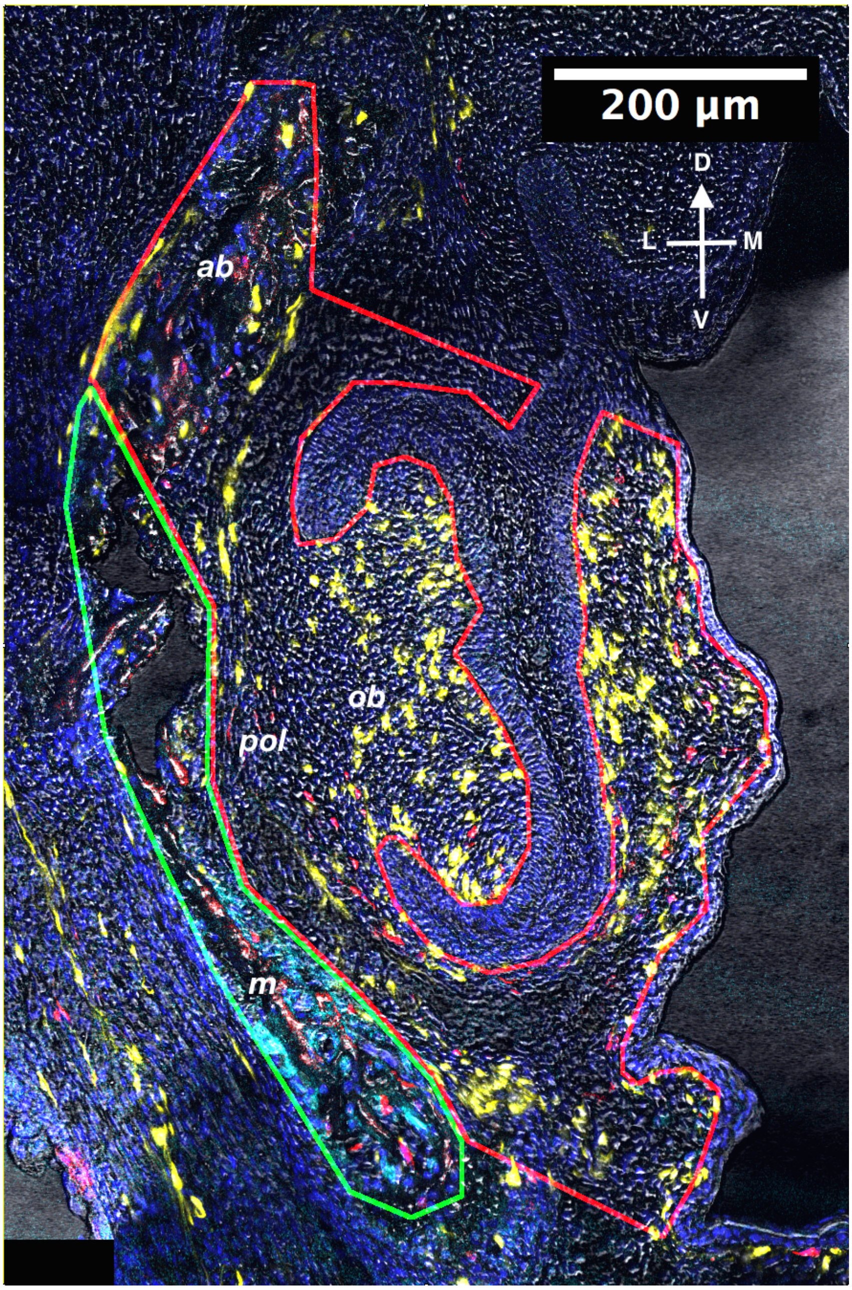

Figure 5.14: Coronal section of an E16.5 lower first molar and mandible in a Hand2-Confetti Mouse. This represents the same tooth shown in Figure 4.8 at a higher resolution. The cryptic polyclonal boundary discussed previously is represented in the annotation boundaries, with the cyan-and-red dominated mandible outlined in green, and the alveolar bone grouped with the tooth. Visually this is the reasonable interpretation and it would appear that there are two compartments defined by presence or absence of yellow and cyan cells. *m* - mandible, *ob* - odontoblasts, *pol* - periodontal ligament, *ab* - alveolar bone.

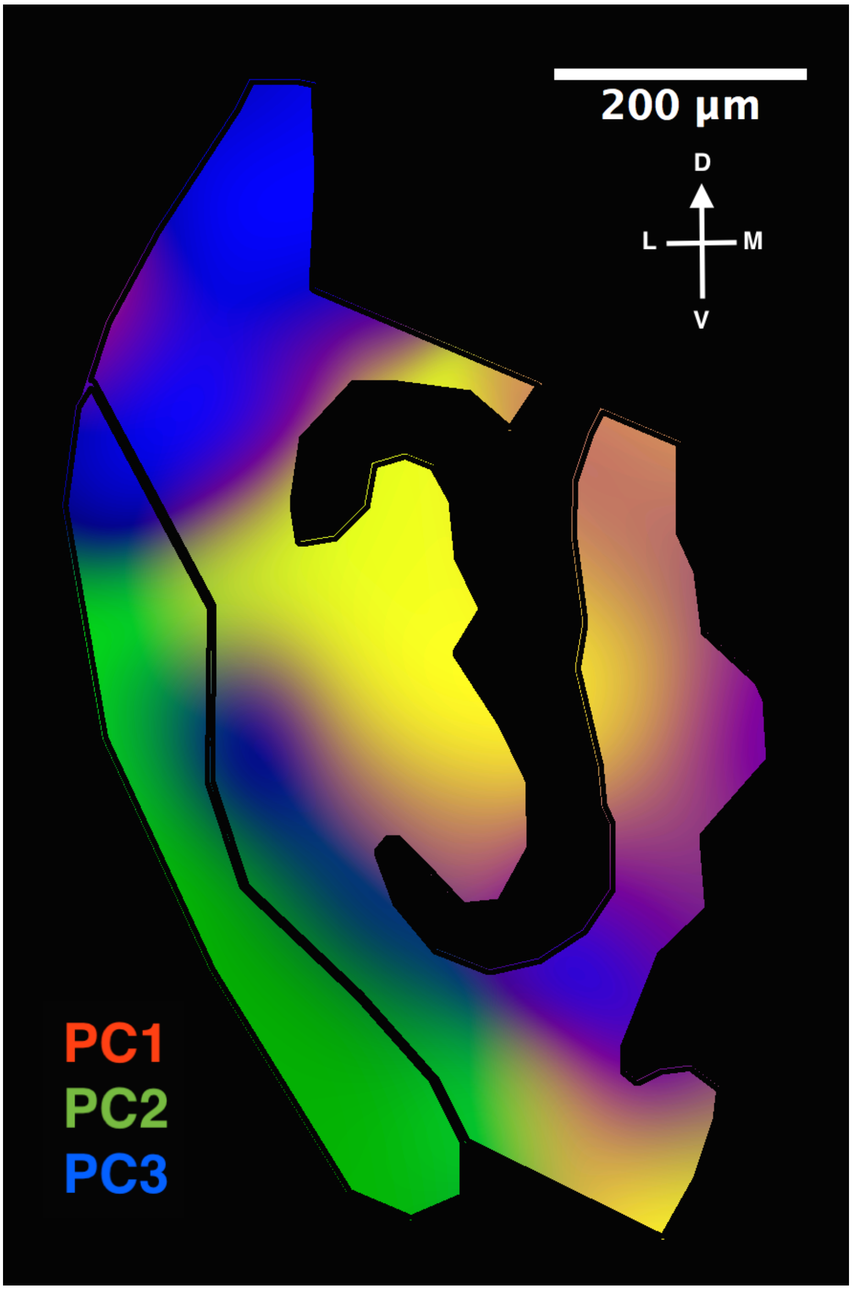

Figure 5.15: PCA Map of the sample shown in Figure 5.14, demonstrating independence of the distal contributions in the alveolar bone, odontoblasts and periodontal ligament of a first modal from the mandible. Contrary to the conclusion reached by simple visual interpretation, PCA reveals three compartments: the ventral aspect of the mandible highlighted in green, the tooth, attachment region and surrounding mesenchyme in yellow, and a third blue-highlighted population representing the dorsal aspect of the mandible and the mesenchyme directly ventral to the tooth.

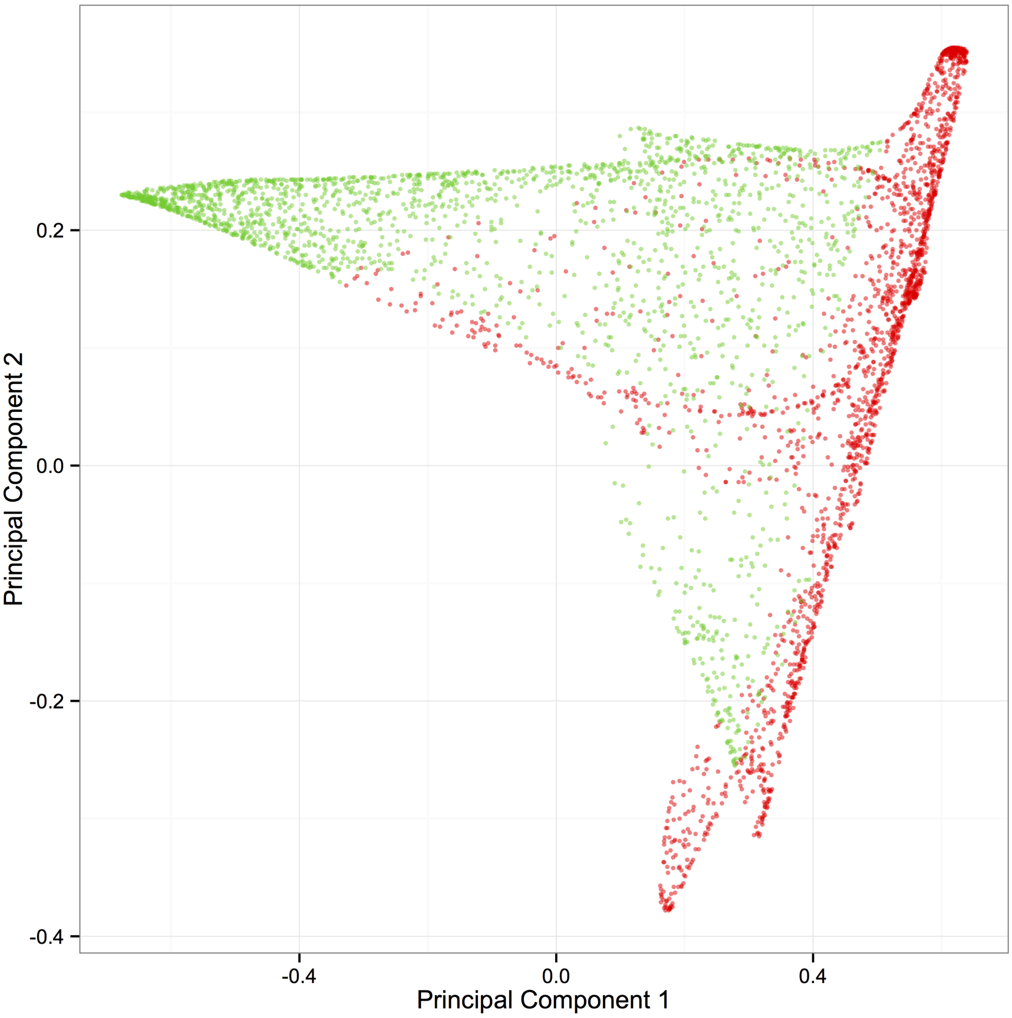

Figure 5.16: PCA plot for Figure 5.15, demonstrating independence of the distal contributions in the alveolar bone, odontoblasts and periodontal ligament of a first modal from the mandible. Shows 2000 random pixels from the two regions outlined in 5.14 mapped into PCA space using the same colour code: red for X and green for Y. These two regions are relatively well segregated, showing that the ventral aspect of the mandible is distinct from the tooth and dorsal mandible.

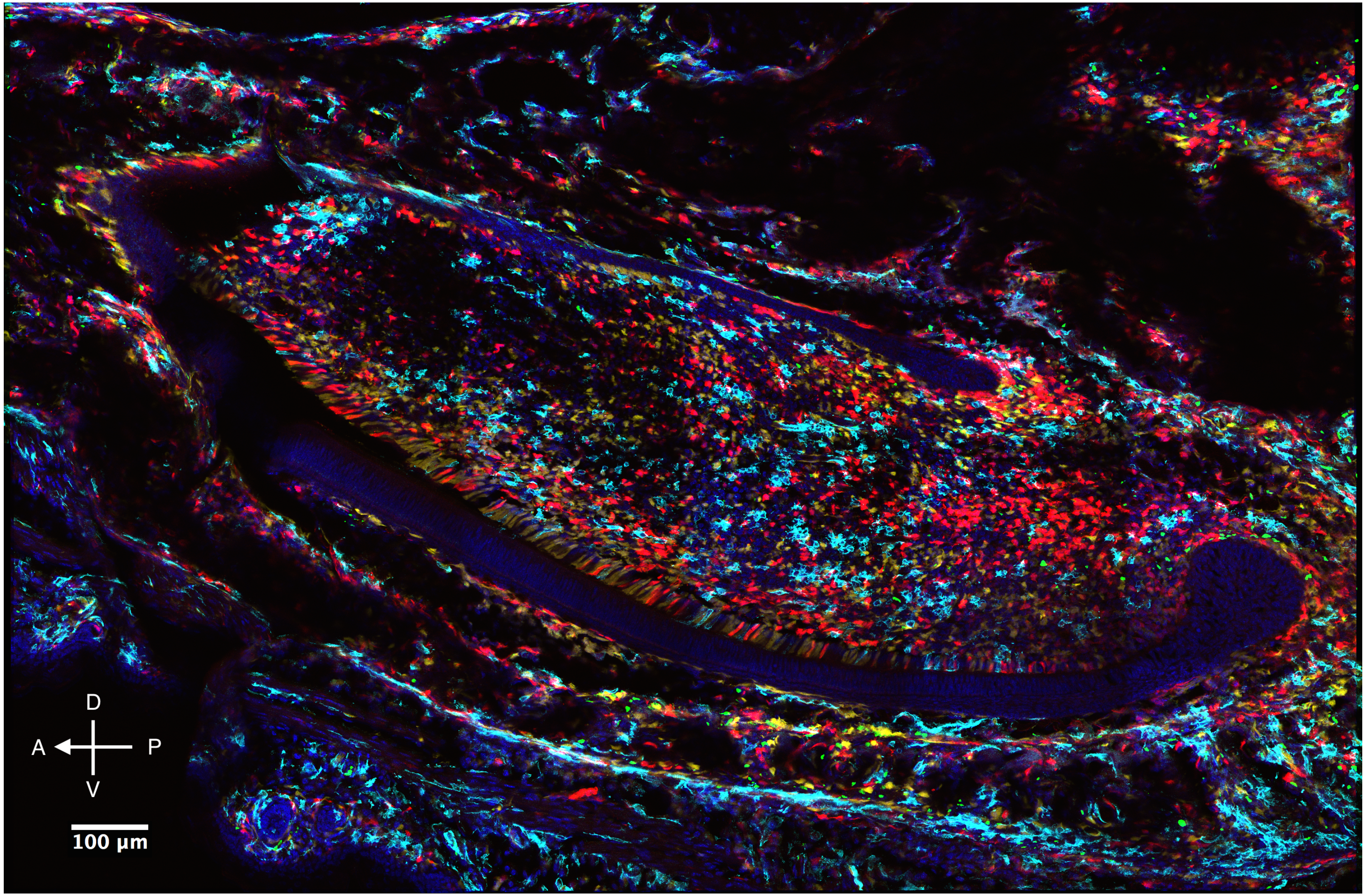

Figure 5.17: Clonal heterogeneity in the incisor at P0 - *Caption Overleaf*

Figure 5.17: Clonal heterogeneity in the incisor at P0 This sagittal section of a lower incisor in a newborn shows significant mixing of the labelled neural crest cells in a Wnt1-Confetti mouse. There are likely regions of single clonal expansion, as evidenced by the large territory of red-labelled cells towards the posterior.

5.4 Adjacent molars and alveolar bone arise from the same basal population, but are divergent from one another

Lumsden has previously shown that single molar buds explanted can lead to several molars later on, a piece of evidence used at the time for a progress zone model of tooth mesenchyme, which for unclear reasons fell from fashion and was largely forgotten. The abandonment of this model is partly due to the difficulty of obtaining clonal resolution at the single cell level. This became now a testable proposition using polyclonal analysis of Confetti: If adjacent molars share a common mesenchyme, that should be visible in our PCA analyses.

Figure 5.19 shows a sagittal section through two adjacent molars, in the upper jaw of a Wnt1-Confetti E18.5 mouse, including associated alveolar bones and periodontal ligament. The polyclonal architecture in this region is very complex and mixed, due to the advanced stage of development and resulting polyclonal variety (Figure 5.20). The distinction between the two teeth and their alveolar bones is demonstrated far more clearly within the plots of Figure 5.21. The distinction between the two teeth and the maxilla is contained within Principal Component 2, while Principal Component 1 shows both the variance across the maxilla and the distinction between the two overlapping tooth compartments. This suggests that the two teeth arise from a common lineage but diverge through isolated elaboration.

In conclusion, the teeth most likely arise as buds from a single migratory population, rather than being patterned from entirely distinct regions of mesenchyme as previously thought.

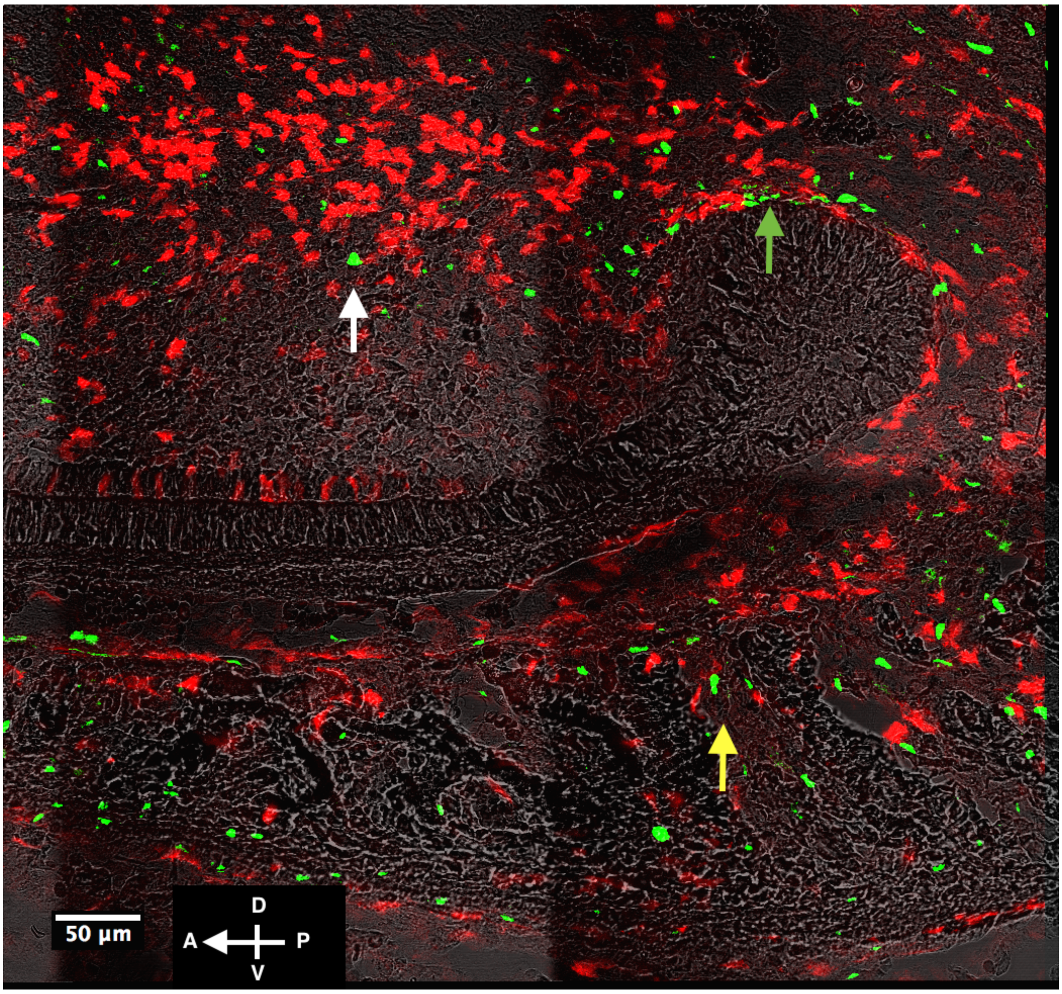

Figure 5.18: Alveolar bone adjacent to the incisor likely arises from the odontoblast population Taken from the posterior dorsal edge of the tooth shown in Figure 5.17. Only red, green and bright field channels shown. Green labelling is unlikely, thus the green population is assumed to be monoclonal. These cells can be found within the tooth (white arrow), encompassing the end of the invaginated epithelium (green arrow) and within the alveolar bone (yellow arrow). They appear to be part of a migratory stream, based upon the orientation and morphology of the red-labelled cells. This implies that the alveolar bone is populated by cells that migrate out from the incisor bud.

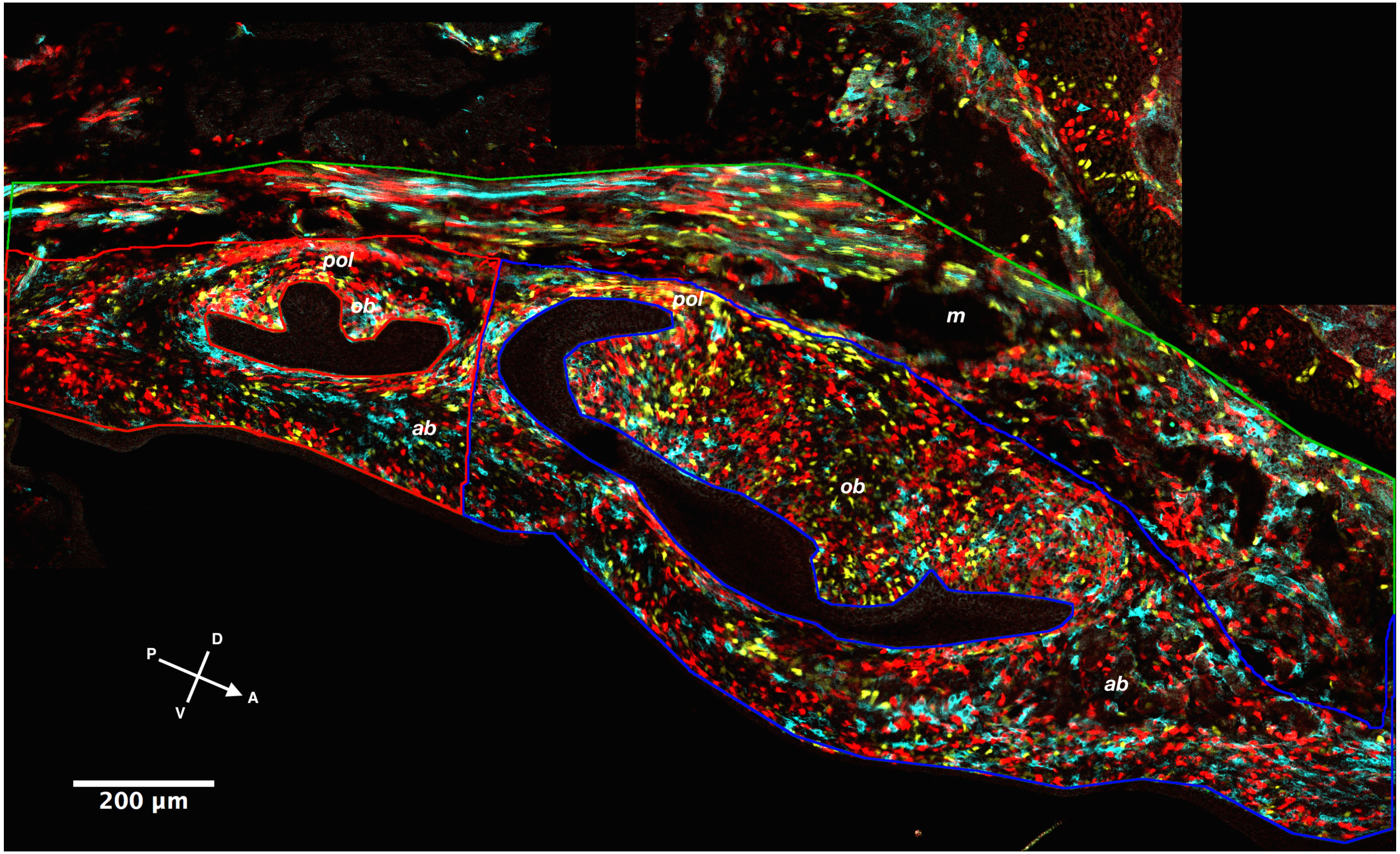

Figure 5.19: Sagittal section of E18.5 upper first and second molars with maxilla in a Wnt1-Confetti Mouse. This large region represents two adjacent upper molars in a Wnt1-Confetti mouse. Both molars (red and blue) are densely populated with labelled cells as is the maxilla (green outline). The key questions are whether the two teeth are distinct from one another, and if there is a clear polyclonal boundary between the two where it falls. There is no clear relationship between the two teeth as both are very heterogenous, populous and complex. This necessitates use of PCA to answer these questions

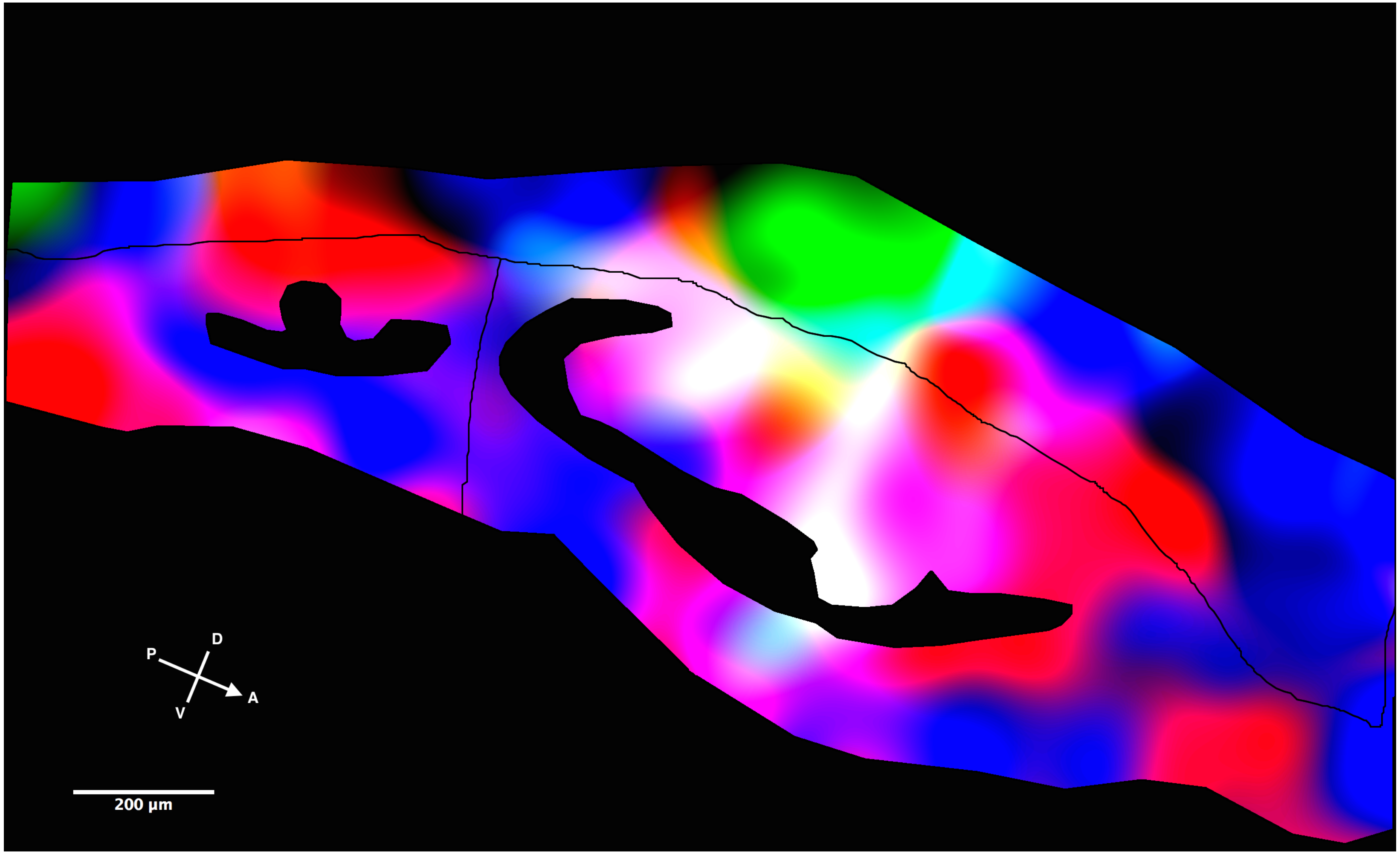

Figure 5.20: PCA Map of the sample shown in Figure 5.14, demonstrating both similarities and differences between the two teeth modules, which are also segregated from the maxilla. Contrary to the conclusion reached by simple visual interpretation, PCA reveals three compartments: the ventral aspect of the mandible highlighted in green, the tooth, attachment region and surrounding mesenchyme in yellow, and a third blue-highlighted population representing the dorsal aspect of the mandible and the mesenchyme directly ventral to the tooth.

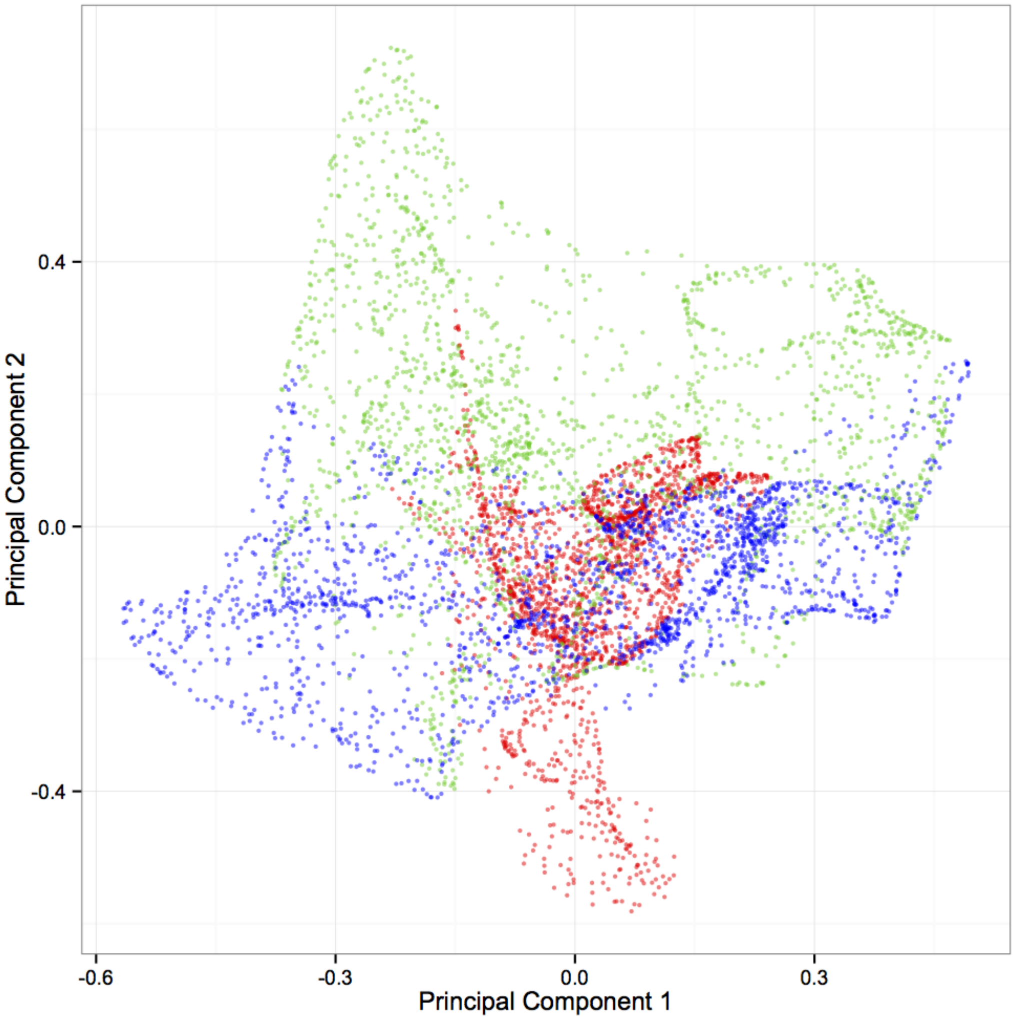

Figure 5.21: PCA plot for Figure 5.20, demonstrating both similarities and differences between the two teeth modules, which are also segregated from the maxilla. Shows 2000 random pixels from the three regions outlined in 5.19 mapped into PCA space using the same colour code: red for X, green for Y and blue for Z. The two teeth, with their associated alveolar bone and periodontal ligament (red and blue) are distinct from the maxilla (green). The two teeth overlap, but also explore different spaces, suggesting that they come from a common origin and have diverged.

5.5 Summary - Teeth and alveolar bones are cryptic developmental modules, distinct from the dentary bones

Based on the polyclonal mixtures within the mandible or maxilla, associated alveolar bones and teeth contained within them, we must at a minimum observe that the alveolar bone is not derived from the associated principle jaw bone. This is evidenced by a consistent boundary in the cell mixture encodings revealed by PCA across all of the PCA analyses presented. This implies that the alveolar bone, periodontal ligament and odontoblasts form from a single population that is segregated from the dentary bone (maxilla or mandible) early on. These two populations are also distinct within the distal migratory population (Figures 5.15 and 5.20), further corroborating the idea that the mandible forms from a distinct migration segregated from the buccal mesenchyme.

The observation of a developmental modularity linking alveolar bone, odontoblasts and periodontal ligament entirely disagrees with the widely accepted model that the alveolar bone is merely a projection of the dentary bone. Clinical evidence corroborates this model: In anodontia, wherein tooth development is abrogated, alveolar bone is said to 'atrophy' [Imirzalioglu et al., 2002; Bani et al., 2010]. The model proposed here would suggest that the alveolar bone is also lost, as it is intrinsically linked with the tooth. More excitingly, the cryptic modularity of the tooth and casket provides a far better basis for the independence of each tooth in maturation time, allowing for the coordination of individual loss and eruption of deciduous teeth.

Figures 5.19 and 5.20 demonstrate weak similarity between adjacent molars in the upper jaw, with the alveolar bone appearing more similar than the odontoblasts. As Figure 4.9 demonstrated, distal populations in adjacent teeth derive from the same lineage, and distal cells have been observed to contribute greatly (and perhaps to the exclusion of proximal cells) in alveolar bone (Figures 5.11 and 5.14). This suggests that the migratory population buds off colonising groups which share lineage, while the rest of the encorporated presumptively proximal cells have no particular lineage relationship that would be shared between adjacent molars.

In conclusion, the best explanation for the phenomena observed is that teeth are not entirely independent organs on their own, but have a close association to their ensconcing alveolar bone and periodontal ligaments which seamlessly ankyloses to the underlying bone. This cryptic modularity is the basis of thecodonty, and corresponds far better with dynamics of tooth development than the traditional explanation of the alveolar bone passively accommodating the teeth.

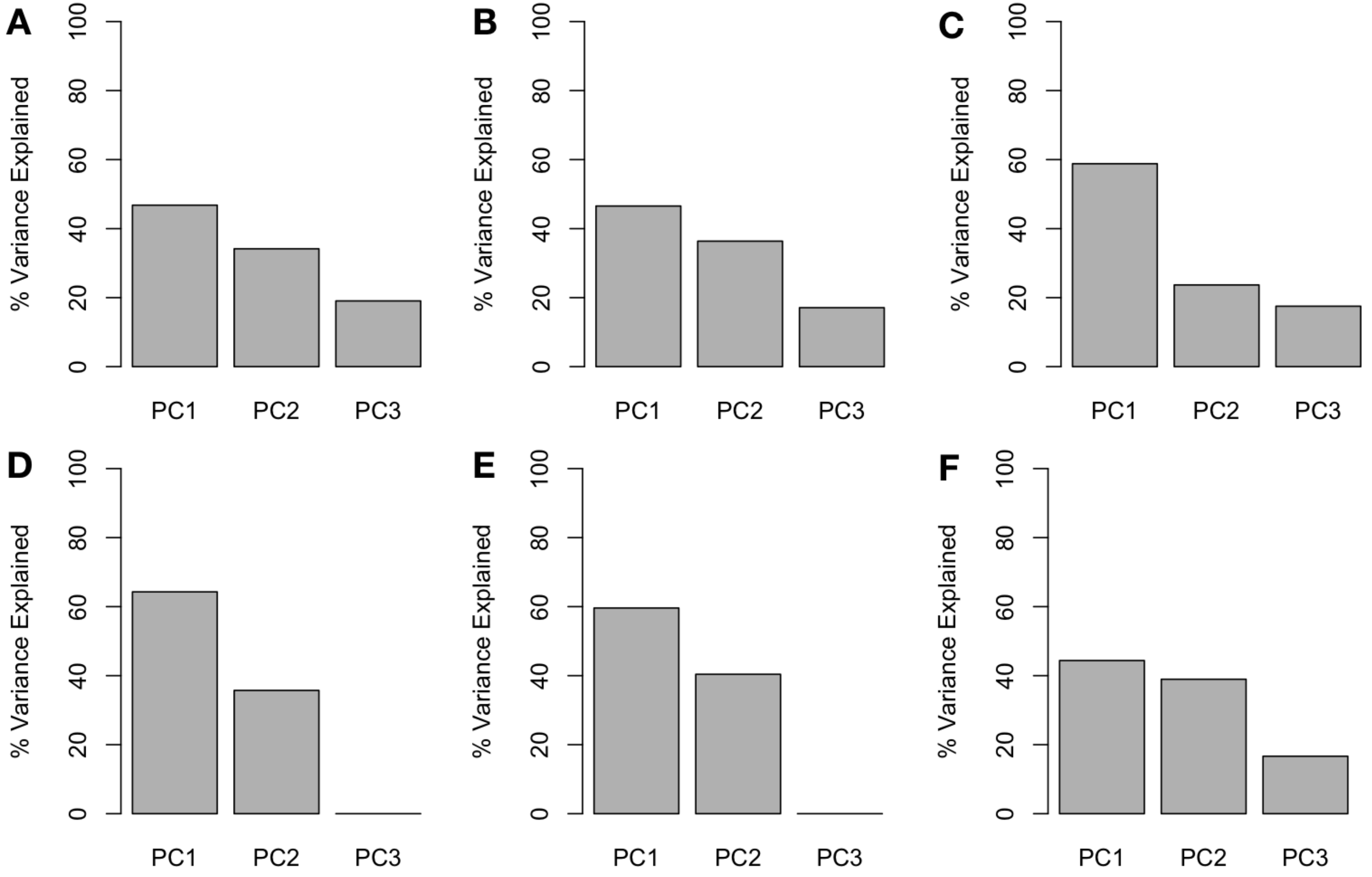

Figure 5.22: Barplots of variance explained by each principal component in each Figure of this Chapter Each bar represents the total variance within the image that is captured by the first three principal components. **A:** Figures 5.2 & 5.3, **B:** Figures 5.5 & 5.6, **C:** Figures 5.8 & 5.9, **D:** Figures 5.11 & 5.12, **E:** Figures 5.14 & 5.15, **F:** Figures 5.19 & 5.20. In each the first two principal components account for over 80% of total variance, validating the analyses. The lack of a significant third column in both Hand2 analyses (**D & E**) is due to the absence of green cells in either sample, and thus the use of only three variables.

Chapter 6

Clonal Architecture of Teeth: A Discussion of Part I

In the introduction to this Part, three features of the canonical mammalian dentition were described: how teeth come to be in certain positions, how teeth come to adopt certain different morphologies and how teeth integrate into the jaw. The morphogenetic field model comfortably explained the first two as a product of signalling gradients and territories, and the question of cellular origins thecodonty was widely regarded as a simple expression of the plasticity of bone morphology in evolution.

All three of these comfortable answers must be discarded in the face of the evidence of the past three chapters. Mesenchymes of the developing tooth row display a remarkable degree of dynamism with disto-proximal migration, mixing of cell populations, clonal expansions in time and space and the discovery of common progenitors of teeth and their adjacent tissues, periodontal ligament and alveolar bone. A new model is required that can account for the polyclonal architecture of the invasive distal population that clearly gives rise to both incisors and molars. Our observations have a number of significant implications for models of tooth induction, composition, the emergence of heterodonty and the modular nature of teeth. This work also represents the first time that complex developmental characteristics have been inferred from the interpretation of mixed lineage populations in a quantitative manner.

6.1 Distal to Proximal Migrations in the Patterning of the Jaws

The most shocking and far-reaching finding within this study is the observation of distal cells in the proximal jaw, as evidenced by the many Hand2-labelled cells in every observed lower jaw molar. Even in the absence of the information that Confetti labelling provides, this thoroughly undermines the assumed stability of cell populations that underpins the morphogenetic field model.

What Confetti allows us to do is dissect the distal populations into at least two distinct migrations. Based on the colour dissimilarity between mandible and the other structures of the jaw, as observed in Figures 3.7 and 4.8, there are most likely two migrations. The relative homogeneity of the mandible suggests that it has a very small progenitor population, while the buccal mesenchyme that gives rise to the alveolar bone, periodontal ligament and odontoblasts is more diverse in its Confetti colours, suggesting a larger progenitor population (Figure 3.2). This furthermore implies that the mandibular migration occurs earlier, when the animal consists of fewer cells. Based on the observation of Lumsden [1988] that mandibular mesenchyme only obtains its odotongenic potential between E10 and E11, the buccal population must be specified in this time period.

The molar row arises from a successive budding of the second larger proximally migrating distal population. This is evidenced by the similarity of composition in adjacent molars, demonstrated in Section 4.9 and Figure 5.21. Each bud creates both the tooth, periodontal ligament and the alveolar bone in which it sits, inferred from the common lineage of the three structures as discussed in the last chapter. This is equally true of the incisor (Figures 5.17 and 5.18).

The morphogenetic field model posits the lineage relationships that are depicted in Figure 6.1: an basal division with no later mixture. While the polyclonal architecture of the proximal population has yet to be elucidated, a distal lineage map can be constructed for this new model, represented in Figure 6.2. Depicting the two invasions of proximal territory, and the successive budding of the tooth row. These distal to proximal migrations are novel observations that are neither predicted nor necessary in the morphogenetic field model, and are in fact antithetical to it as they violate the presumed stability of the morphogenetic field map.

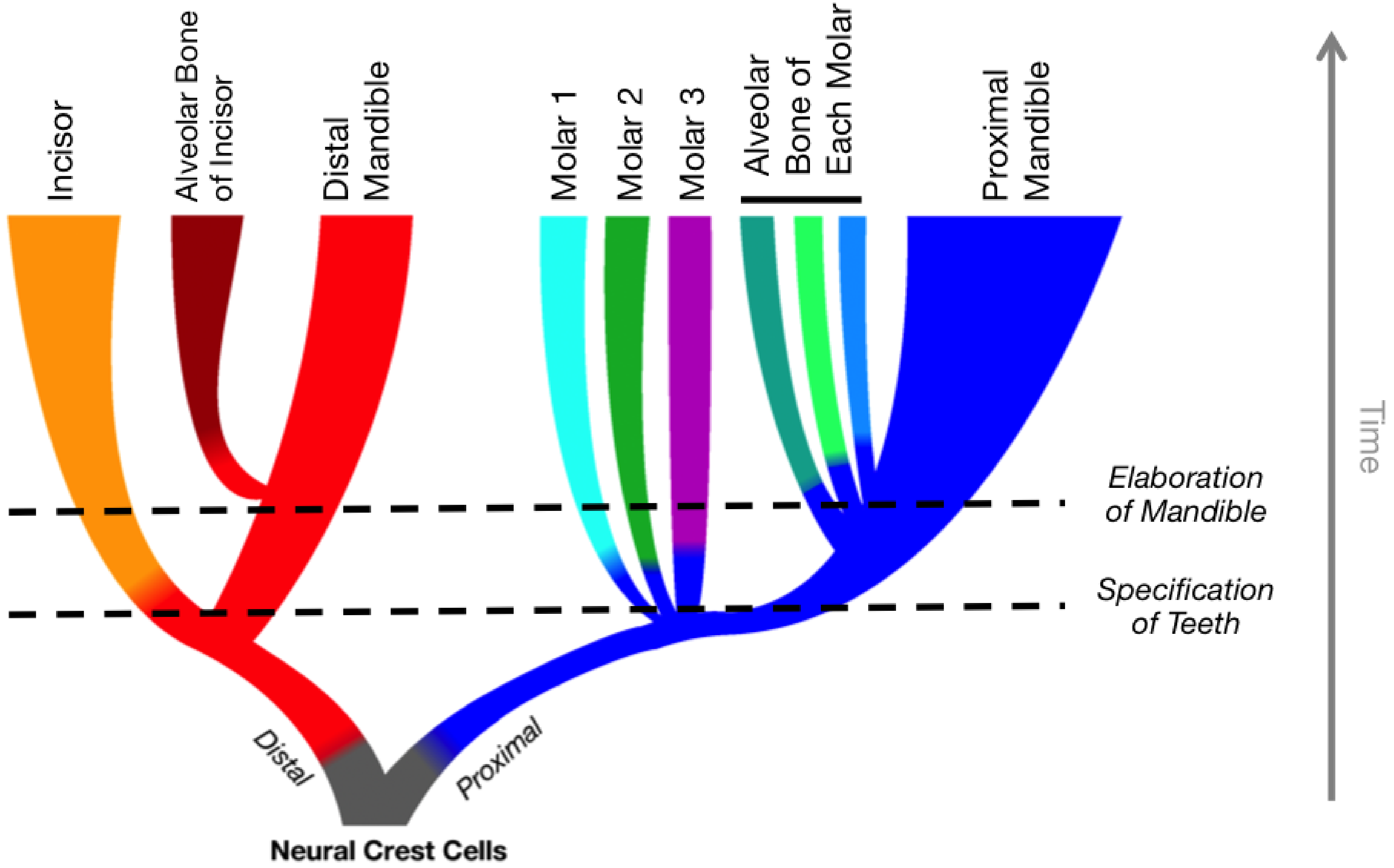

Figure 6.1: Cell Lineage Tree of the Morphogenetic Field Model. Following an initial specification of the mandibular arch into proximal and distal populations, teeth are specified from the respective mesenchymes, without any particular relationship between each tooth bud. Later the osteogenic population which give rise to the mandible elaborates to form the alveolar bone around each tooth.

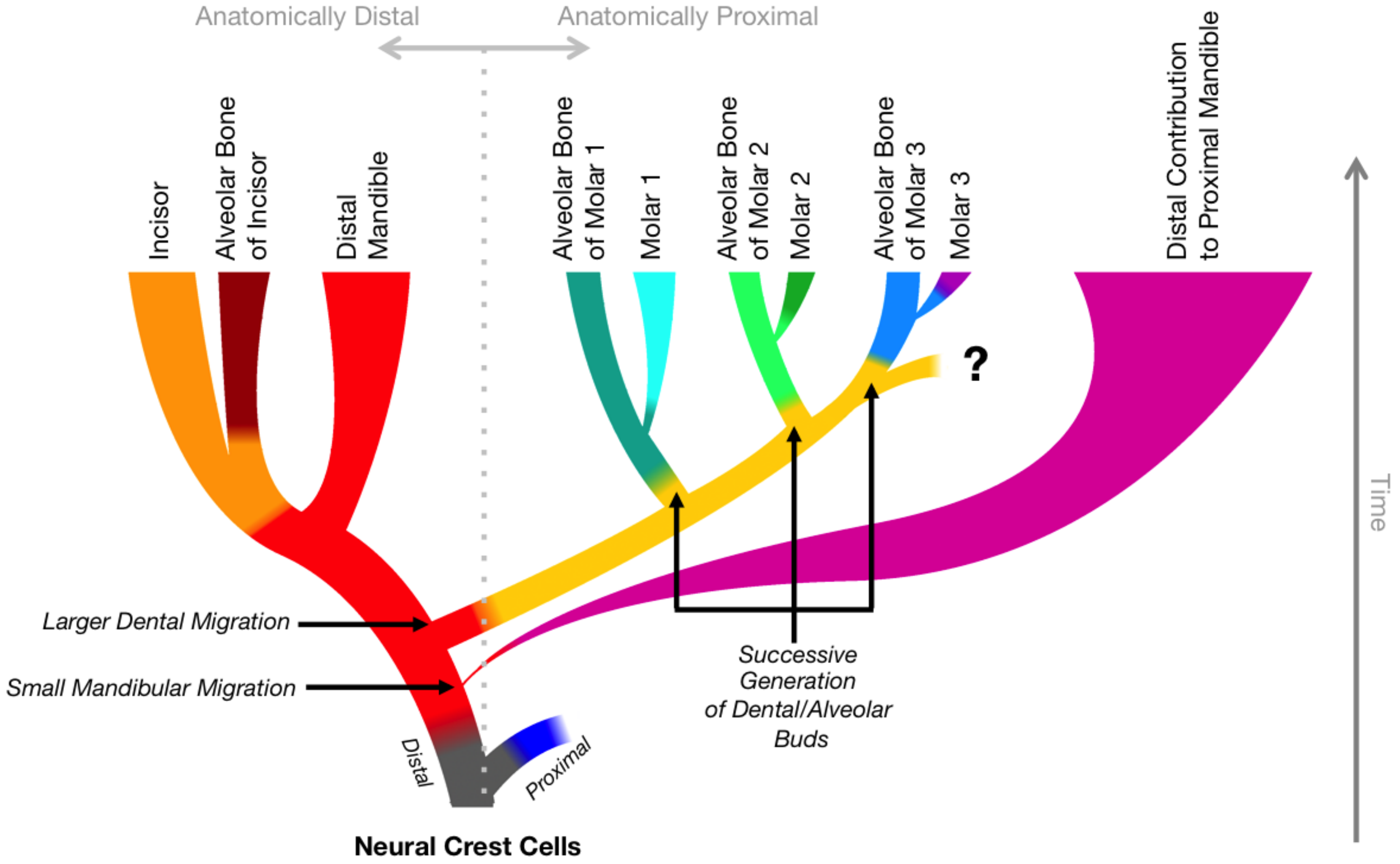

Figure 6.2: Cell Lineage Tree of the Invasionary Model]. Following an initial distal and proximal specification, there are two proximal migrations of distal cells: one initial migration of a small group of cells gives rise to the majority of the mandible, and a later larger migration gives rise to the teeth and alveolar bone. Note the position of alveolar bone as a closely related population to the distal contributions of the tooth. Periodontal ligaments are not represented, as their position within the successive tooth bud populations is currently unknown.

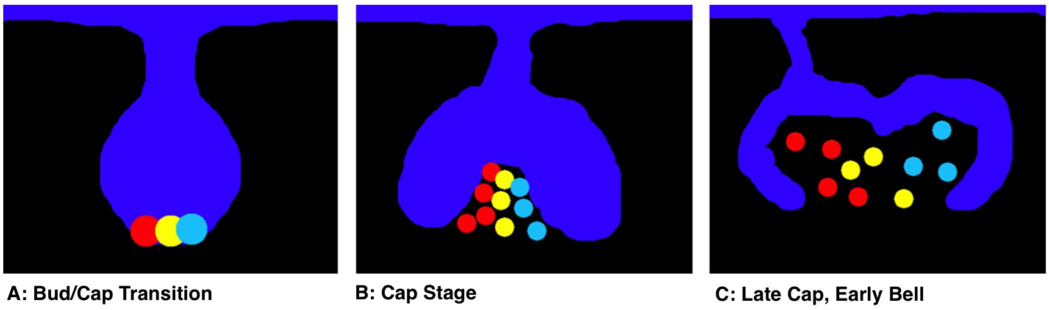

A: Bud/Cap Transition

B: Cap Stage

C: Late Cap, Early Bell

Figure 6.3: Model of polyclonal compartmentation within the tooth. A: At the start of the cap phase, a small number of distal labelled cells form the primary enamel knot. **B:** These cells expand in situ. Some other mesenchyme also enters the developing cap. There is little mixing within the teeth, so the two sides of the tooth remain clonally distinct. **C:** Proliferation within the distal cells ceases. Expansion of the tooth is driven by invasion of unlabelled mesenchyme. The labelled cells spread out, retaining their original pattern of invasion and expansion and giving the appearance of clonal segregation.

6.2 Distal cells in the specification of molar position

Mandibular cells migrating from the distal end of the mandible into the proximal territory appear to represent the majority of the mesenchyme around the nascent tooth buds, as well as forming the majority of the initial population of the molar odontoblasts. The top jaw appears to recapitulate the trends of the bottom jaw when all neural crest cells are labelled, implying that similar processes occur there. This shows that there is no stability to the original morphogentic landscape of the jaws, and renders models built upon the assumption of stability very hard to defend.

The time course of initiation and growth within the molars can be easily intuited from the nascent first molars in Figures 3.7 and 3.8, the intermediate second molar observed in Figure 4.5 and the more mature molars shown in Figures 4.6, 4.7 and 4.8. It is clear that a small population of distal cells invades and divides a number of times. Meanwhile a number of presumptively proximal cells are also incorporated into the tooth but, and either by division or further invasion dilute out the distal population. This results in the overlapping polyclonal modularity of the distal populations in the molar. This process is summarised in Figure 6.3.

It is not clear how teeth positions are chosen. This may still be reliant on epidermal signalling, with the migratory cells undergoing chemotactic homing. This is however, unnecessary. Osborn's model of inhibitory zones is likewise a possibility, though not the most parsimonious. No long range signalling is necessary. This process may simply be organised by a progressive distal-proximal interface, with cells at the juncture being committed towards a certain tooth. This interaction must render the presumptively proximal cells insensitive to further initiating interactions, requiring further distal cells to continue proximal migration through the committed proximal mesenchyme into new territory. This is summarised in Figure 6.4. It is furthermore conceivable that there is a migrating ectodermal/endodermal placodal population [Fraser et al., 2010] coincides with the migrating distal/proximal boundary in the mesenchymal cell population boundary, and it is this which is involved in initiating the tooth proper.

This is the most parsimonious explanation for specification of teeth, and has a further potential intrinsic regulatory property: if the overall size of the tooth is dependent on the initial population that is committed to it, then the distance of migration necessary will likewise be longer, and the gap between tooth buds will inherently be linked to the size of the teeth.

The migration of cells from the distal population labelled in Hand2-Confetti has been shown to most likely proceed from the crest of the mandible towards the mouth, in a lateral-to-medial direction, as discussed in the previous chapter with reference to Figures 5.3 and 5.12. In the mouse this appears to merely give rise to the mesenchyme and alveolar bone. However, in many mammal this would be the site of deciduous tooth development, and more broadly in evolution the successional lamina of tooth replacement is found medial to the mature teeth [Huysseune, 2006; Handrigan and Richman, 2010]. As discussed previously, these distal cells initiate molar development, and the observed lateral to medial migration of these cells is consistent with the successional initiation of teeth on the medial side.

In conclusion, the distal to proximal migration provides a hypothetical mechanical basis for the specification of tooth row position without requiring long range signalling. This possibility will be important to consider in future attempts to understand tooth positional specification. However, the most important consequence of this model is that it places distal cells at the root of tooth specification, and thus begs the question of how they are involved in generation of heterodonty, discussed in the next section.

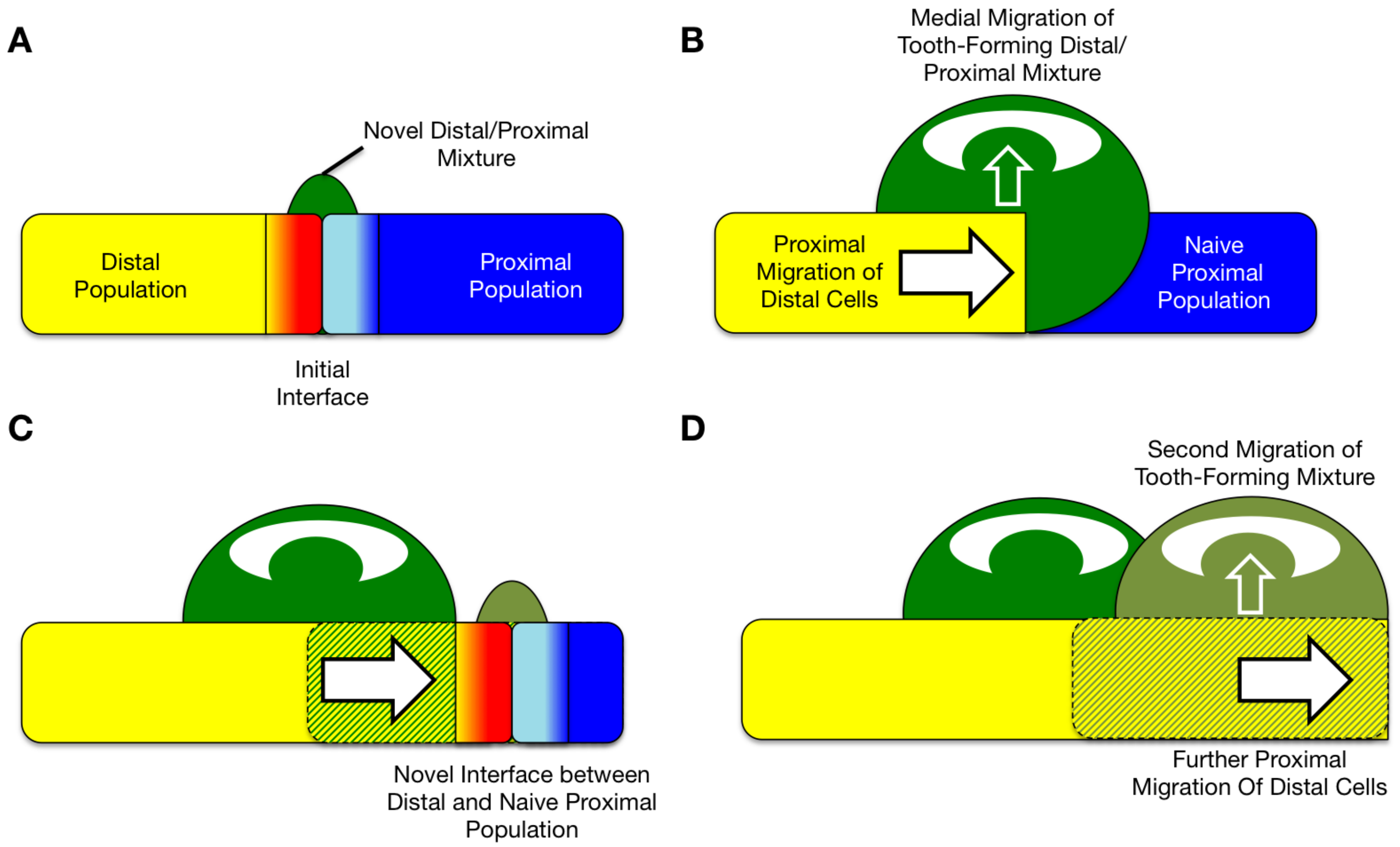

Figure 6.4: Model of Tooth Position Specification in the Absence of Long Range Signalling. A: After initial definition of distal (yellow) and proximal (blue) territories there is a single layer of interface (red and light blue). These populations mix and migrate laterally (green). **B:** The mixed population give rise to a tooth and associated alveolar bone. The distal population is no longer in contact with the naive proximal population, and migrates through the novel mixed population. **C:** Having migrated through the mixed territory (striped region), another interface between naive distal and proximal cells is formed, proximally to the first tooth. **D:** This process can repeat iteratively, and gives rise to tooth-and-bone compartments with similar but different polyclonal identities (different shades of green).

6.3 Heterodonty is a dynamical property arising from differential expansions of distal and proximal cells in time

The principle difference between the well developed incisors and first molars at E16.5 is that the incisors are dominated by distal cells with a presumptively proximal minority (Figure 4.3) and the first molars are dominated by presumptively proximal cells with a distal minority (Figure 4.8). This late abundance of unlabelled cells is surprising, as at E14.5 the first molar is surrounded by labelled distal cells (Figures 3.7 and 3.8), and at E16.5 less developed second molar in the same tooth row is more dominated by distal cells (Figures 4.5 and 4.9). This change in the dominant population implies differential expansion of the two populations within the different teeth: in incisors the distal cells divide many times, giving rise to large polyclonal territories, and in molars the distal cells divide only a few times, implying that presumptively proximal cells are dividing preferentially to bulk out the tooth. This is summarised in Figure 6.5. This fundamental difference of constituent mixtures provides a possible foundation for the generation of heterodonty.

The key finding in this is that heterodonty is not a passive readout of the initial molecular landscape of the morphogenetic field. Rather, it comes about via a dynamic process of migration and differential expansion at particular points along the tooth row. This is a step wise sequence where initial polyclonal distributions are different from later ones and it is the emerging difference in time that makes up the qualitative feature of heterodonty. This can explain why despite the remarkable similarity of early branchial gene expression patterns see across vertebrates, some have teeth and others do not. It was not conceived by previous models that teeth might be fundamentally different in their polyclonal composition and that this composition changes in time.

The growth models of Salazar-Ciudad et al. [2010] and Harjunmaa et al. [2014] posit a larger role for the dental epithelium in shaping the tooth, while it is known from the experiments of Kollar and Baird [1969] that it is the mesenchyme which specifies tooth identity. This implies signalling from the mesenchyme shapes the behaviour of epithelium. The experiments of Tucker et al. [1998] demonstrated that inhibition of BMP signalling in an incisor results in a molariform morphology. From this it was concluded that BMP signalling mediates the morphogenetic field. This evidence can be easily subsumed by our model by proposing that BMP signalling

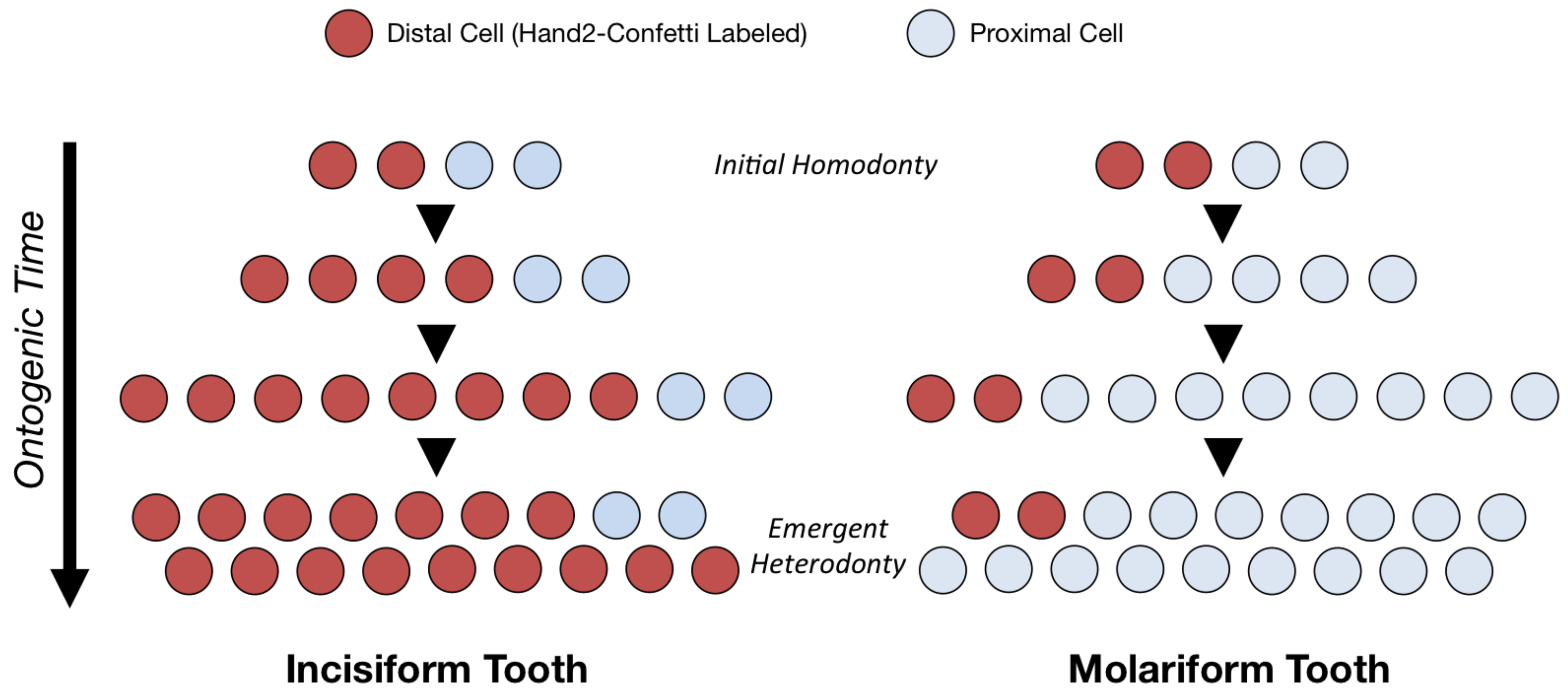

Figure 6.5: Differential Distal and Proximal expansion defines the teeth. Both incisiform (left) and molariform (right) teeth may at one stage of development possess the same proportion of distal (red) and proximal (light blue) cells. This represents an initially homodont condition However, by preferential expansion of one cellular population by divisions (black arrows), two very distinctly different mixed populations can be obtained, leading to an emergent heterodonty.

by distal cells causes changes to the dynamics of the dental epithelium which shapes teeth morphology. The different proportion of distal cells within either tooth results in a differential of BMP signalling and thus distinct morphologies. This model is outlined in Figure 6.6.

This proposal may not simply describe a binary difference in tooth morphology, but also differences between species along a continuum. Part of the basis for diversity in dentition could be the relative abundance of mixtures of cells. A prediction arising from this would be that closely related species with distinct molar morphologies may differ in the number of distal cells contributing to each tooth, or the level of BMP expression in the molar-resident distal cells.

The observation that incisors revert to a molariform morphology in the absence of BMP signalling suggests that this is the default course for tooth development, with incisors representing a derived elaboration. The observation that incisors develop reasonably normally in the absence of Hand2 would suggest that this gene is related to the migratory behaviour of the cells, and not necessarily directly involved in the expression of signalling to the epithelium. Hand2 is widely known to be responsible for coordinated 'sheet migration of cells in the heart and other tissues [Yamagishi et al., 2001; Hendershot et al., 2007, 2008; Barron et al., 2011], and a very ancient property of Hand2 is traceable to the coordination of hand2 positive progenitor cells in heart morphogenesis in bilaterians, shared feature with insects [Cripps and Olson, 2002].

The observation of tooth-and-casket developmental modularity presents another exciting possibility for the development and evolution of heterodonty. Based on current fossil evidence, it seems likely that both thecodonty and heterodonty co-evolved within Cotylosaurs [Gregory, 1920; LeBlanc and Reisz, 2013]. This implies that the alveolar bone is necessary for mammalian heterodonty and thus involved in supporting complex tooth morphologies, an implication that is far better supported by a model that links tooth and alveolar bone development rather than positing the bone as a passively reactive environment that merely accommodates the teeth.

6.4 Developmental and Evolutionary Nature of the Thecodont Tooth

Based on the observed polyclonal relationships in both the lower and the upper jaws, we are forced to accept that the alveolar bone in which the teeth reside is

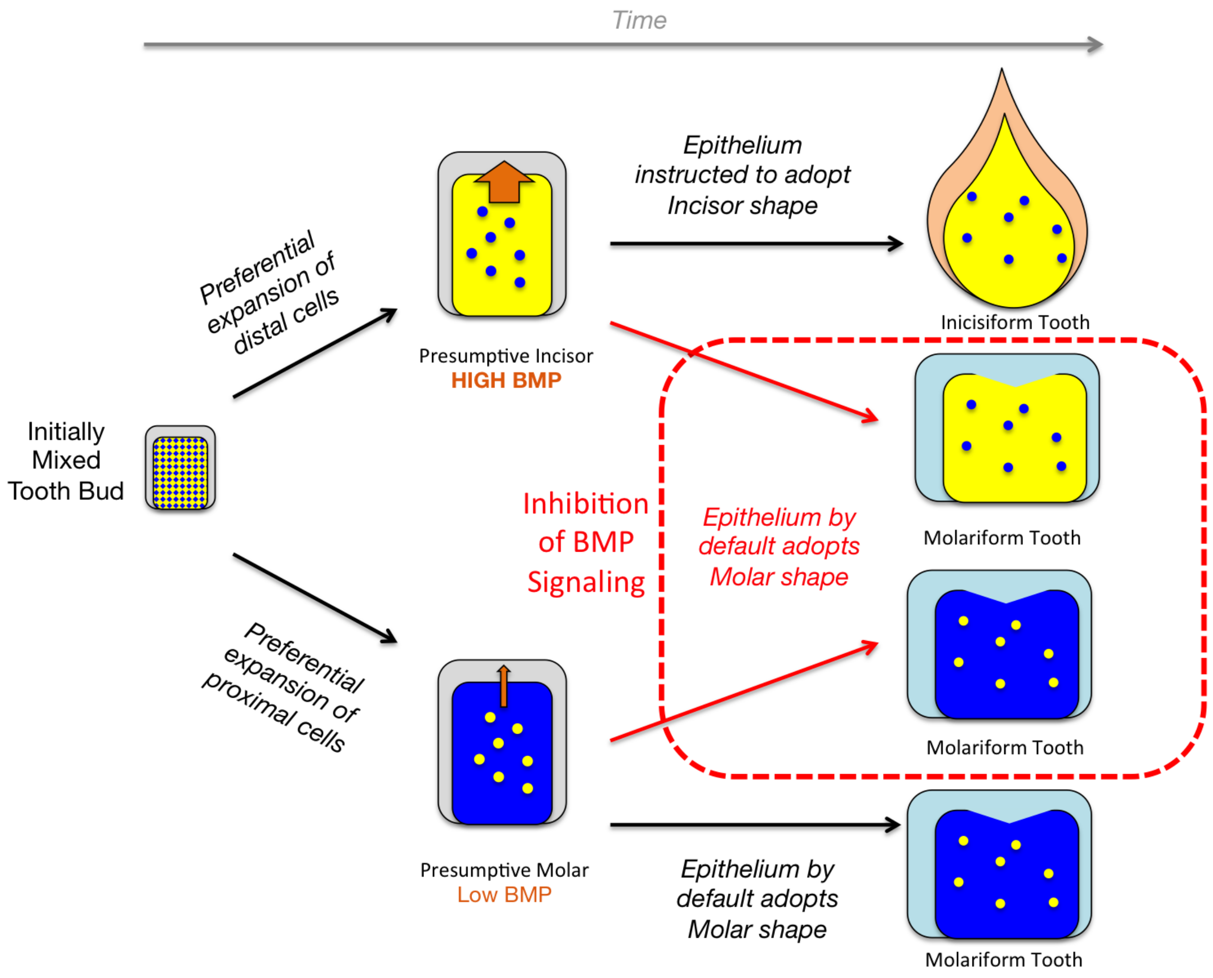

Figure 6.6: The proportion of distal cells may be sufficient to impart tooth type. The process described in Figure 6.5 allows two differently mixed tooth germs to arise: a proximally dominated (blue) presumptive molar, and a distally dominated (yellow) presumptive incisor. Distal cells may be responsible for BMP-mediated signalling to the dental epithelium, which likely mediates the overall morphology of the tooth. In the presence of this signalling an incisiform tooth can be produced. In the absence of this signalling, either due to a low number of distal cells, or as a result of experimental interference, the tooth defaults to a molariform morphology.

not developmentally derived from the maxilla and mandible, as demonstrated by the figures of Section 5.2.1. Furthermore, there are apparently close and consistent relationships between the teeth and the alveolar bone which encapsulates them and physically links them to the dentary bone. The unexpected relationship between the alveolar bone caskets surrounding the molars and the odontoblasts themselves suggests that thecodonty does not represent the engulfment of tooth roots in a more elaborate dentary bone, but rather the deeper cryptic ankylosing of tooth-and-casket developmental units directly onto an underlying jaw.

The relationship between odontoblasts, periodontal ligament and the adjacent alveolar bone might be a reflection of the well-established fundamental relationship between teeth/denticles and their respective bone of attachment [Smith and Coates, 1998], with the difference that in the thecodont condition the tooth sits deep inside and not just on top of the dermal bone socket. The distinction between this model of tooth-in-casket modularity compared to the current concept of independent teeth arising from a stable mesenchyme is summarised in Figure 6.7. This possibility has a number of very interesting consequences that resolve several longstanding issues in tooth development.

First is the highly likely ontogeny of this cryptic alveolar bone to the bone of attachment in chondrichthyes. Dermal bone loss in chondrichthyes is secondary [Janvier, 1996; Giles et al., 2015], and thus the tooth condition of extant sharks for example is one of retention of the bony rudiment of the tooth, but loss of the underlying bone. The opposite is true in edentulist clades such as birds, sloths and anteaters that have evolved from thecodont antecedents: the teeth and bony caskets are lost, but the mandible and maxilla are retained [Meredith et al., 2013; Louchart and Viriot, 2011; Davit-Béal et al., 2009]. The ability to atavistically revive teeth is also retained in birds [Harris et al., 2006]. This suggests a dissociable modularity that is not addressed in traditional models. The developmental segregation of the maxilla and mandible from the teeth and bony caskets permits a dissociability in historical time.

Secondly, the specification of discrete units for each tooth also explains another characteristic unaddressed by older models: dissociability in developmental time, most often referred to as sequence heterochrony [Smith, 2002]. Teeth have an eruption sequence that in some animals such as humans could involve many years of difference between individual eruptions. Each eruption relies upon a complex series of molecular interactions across the alveolar bone, reviewed in Wise et al. [2002]. Considering each tooth and casket as a discrete unit suggests that each can de-

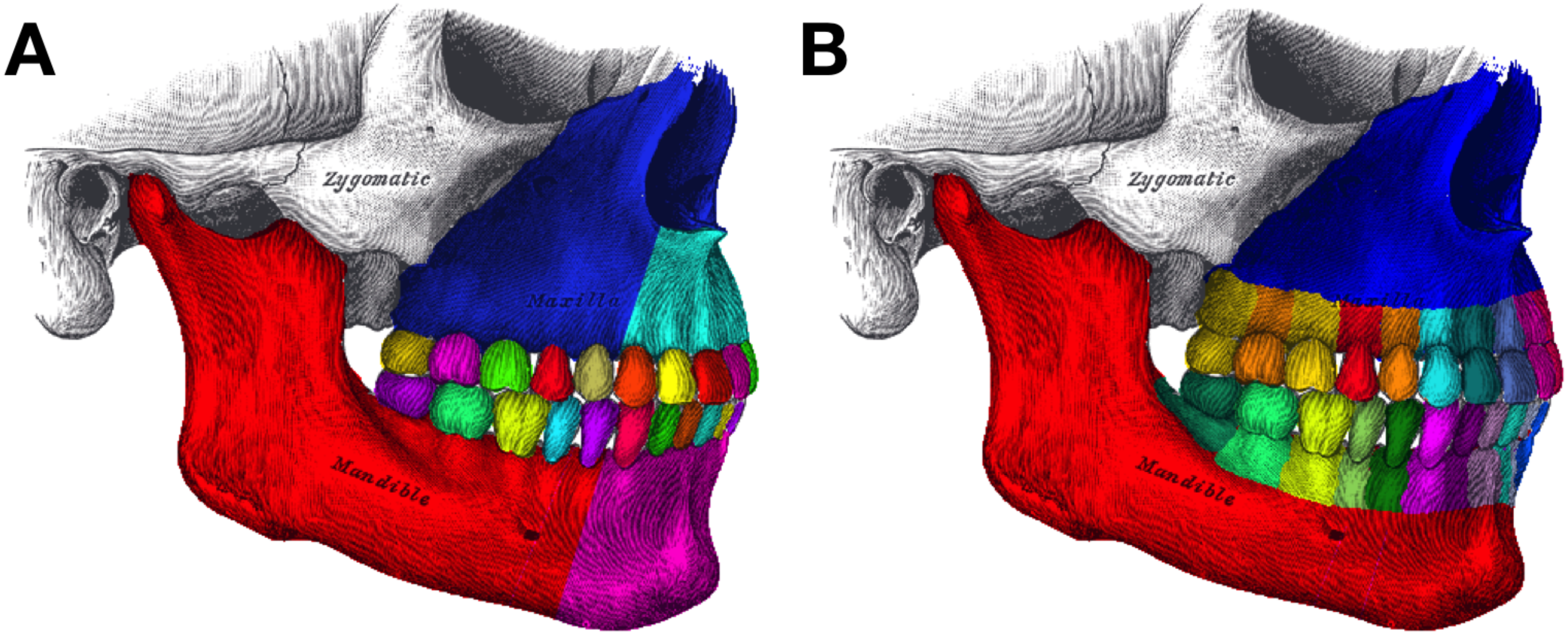

Figure 6.7: Cryptic polyclonal architecture underpins thecodonty. A: Under the traditional model of tooth and jaw development, the key distinctions are the distal (cyan or magenta) populations as distinct from the proximal populations (blue and red). Each tooth is autonomously defined (varied colours), while the alveolar bone is derived from the underlying jaw bone. **B:** Based on the model of migrational mixing and thecodont modularity, it would appear that the critical components of this architecture is quite different. Each tooth has a developmental relationship with its associated alveolar bones, which are distinct from the jaw bones. Each row of teeth of the same type derives from a common migratory population, resulting in similar but distinct lineage mixes (different shades of the same colour). While this is observed for molars, the assumption of a similar mechanism in incisors cannot be tested in mice.

velop on its own timescale without cross-talk between two parts of the same tissue. The likely independence of each also permits a role for alveolar bone as an active participant in tooth morphogenesis, as the casket could potentially have a role in confining and defining the growing tooth. As there appears to be a developmental link between the two structures, coordination is far more likely than if tooth and bone were entirely unrelated.

The key finding is that the tooth row is comprised of modular units comprising the tooth, periodontal ligament and alveolar bone, which are then ankylosed to the respective jaw, which is a fundamental departure from the idea of teeth growing out of the jaw with subsequent engulfment by projections of bone.

6.5 Conclusions

In this Part, evidence has been provided which entirely undermines the widely accepted morphogenetic field model. A model for tooth development has been developed based on observed migrations that removes all need for unsupported long-range signalling events. Instead, all key parts of tooth development can be explained through signalling of adjacent cell populations, cell origin identity and migration of cells.

As well as this, the nature of the tooth as a distinct developmental unit has been called into question. Based on the dynamics of growth, polyclonal architecture and proposed model of specification, it seems that the thecodont mammalian tooth is inextricably linked with the surrounding alveolar bone. This tooth-and-casket modularity is consistent both with developmental and evolutionary evidence.

The key novel observations proposed are as follows:

1. A distal to proximal migration of cells is present within both jaws, where previously stability of a morphogenetic map was presumed.
2. Each tooth, both incisors and molars, contain mixtures of distal and presumptively proximal cells, where previously incisors were believed to be entirely distal and molars entirely proximal.
3. There exists a moving front of cells that creates a time gradient of development along the distal to proximal axis, where previously it was presumed that all patterning occurs at once, and no mechanism for developmental delay in the most proximal teeth was demonstrated.
4. A lineage link exists between at least the distal contribution of molars, where previously it was assumed that each tooth was patterned from different regions of mesenchyme with no particular relationship.
5. A lineage link exists between tooth, periodontal ligament and alveolar bone, which are all more closely related to each other than any is to the dentary bone (maxilla or mandible). This demonstrates a developmental modularity arising from a common precursor population.
6. The lack of a lineage relationship between the mandible/maxilla and alveolar bone demonstrates that these two groups of bone are not from a common precursor, and are thus separable in both developmental and evolutionary

time.

7. Very few cells expanding greatly form the odontoblasts and mandible, rather a large group of cells being patterned towards these fates. Previously nothing was known about the size of the initiating population of any structure.
8. Heterodonty is a dynamic product of differing cellular mixtures arising from migrational events, where previously it existed as a readout of initial signalling pattern.
9. There is a medial to lateral axis of population in the molars, suggestive of a mechanism by which additional teeth may be generated.

On the basis of our findings now mutants will have to be reevaluated. Multi-coloured lineage labelling such as Confetti needs to be combined with conditional gene ablations to look at the changes in proximodistal migrations of odontogenic precursors that might cause new tooth phenotypes.

These observations are likely to be important for bioengineering of teeth: I have demonstrated not only the 'true' anatomy of the tooth by recognising its cryptic modularity with the alvolar bone, but also that their development is not a simple matter of a capable anlage receiving the correct signals, and rather a more complex program wherein at least two separate populations must be patterned and then mixed in the correct proportions.

Another important implication is that long range migration occurs, we cannot say *a priori* any longer where teeth come from, as there is no longer a direct link between dermal bone and odontogenesis. This means that existing competing models of tooth origins, such as the 'inside-out' model of Smith and Coates [2001] and the 'inside-and-out' model of Fraser et al. [2010], reviewed in Fraser and Meredith Smith [2011], will have to factor in at some point the migratory nature of the underlying odontogenic mesenchyme.

Part II

Global Clonal Architecture of the Mammalian Calvaria

Chapter 7

Introduction: A Novel invasive growth mode of dermal bones.

The skull is the oldest bone in the body, having evolved from the head cases of heterostracans [Donoghue and Sansom, 2002]. The upper surface, known as the calvaria, is comprised of intramembranously ossified dermal bone, which evolved prior to the occurrence of the endochondral ossification of most long bones and the viscerocranium [Francillon-Vieillot et al., 1990; Janvier, 1996; Matsuoka et al., 2005]. Despite its provenance and obvious relevance as the casing of arguably our most valuable organ, the nature of the dermal bones in the head is remarkably understudied. This thesis will examine for the first time the development of the skull as a dynamic system at single resolution by combining recombinase mediated (lineage specific) permanent colour marking with new tools of computational image analysis. This will enable me to investigate the composition of polyclones in 3 dimensions and their contribution towards dermal bone histogenesis.

One key gap in knowledge in the manner in which the skull grows in thickness. While some assumptions have been transferred from knowledge of endochondral bone development [Buckwalter et al., 1995; Ornitz and Marie, 2002; Lieberman and Friedlaender, 2005; Karsenty et al., 2009; Wuelling and Vortkamp, 2010], little work has been done to verify this for dermal bones [Abzhanov et al., 2007]. Other aspects of the bone, such as growth into sutures are apparently well characterised, but in attempting to investigate the dynamics of the skull evidence was produced that seriously called these long-held answers into question.

7.1 Anatomy of Calvarial Bone

This thesis focuses primarily on the frontal bone, and also on the nasal bones. These are dermal bones formed from loose condensations of Cranial Neural Crest Cells [Ornitz and Marie, 2002; Matsuoka et al., 2005; Wuelling and Vortkamp, 2010]. There is a strict three-layer structure to the frontal and nasal bones. There is an outer compacta layer, an inner spongy bone layer, and an inner (brain-adjacent) compacta layer. In this thesis these are referred to as Layers 1, 2 and 3 respectively. The ontogeny of this critical middle layer has not been investigated before, therefore critical aspects of how this layer can grow in thickness are unknown. It would not be unfair to say that the last major advances in knowledge regarding this structure were made by Hippocrates over 2000 years ago, whom first noted the presence and characteristics of this structure while dissecting a slave [Adams et al., 1849].

The genesis of this structure is still contentious. No attention has been paid to how cells behave within these layers, and how the layers interact. Evidently, the cells of Layer 2 must come from one of the outer layers, either by invasion or apposition. The latter is widely presumed due to apposition supposedly being the mechanism of osteogenesis in endochondral bone [Buckwalter et al., 1995; Lieberman and Friedlaender, 2005]. It is also entirely unknown whether there is a movement of cells between Layers 1 and 3. These assumptions are based upon a paucity of data, emphasising the importance of this thesis in exploring the Undiscovered Country of calvarial bone development.

This thesis attempts to tackle such questions. In Chapter 9 horizontal expansion within individual layers will be presented and examined. In Chapter 10 the vertical expansion of mixed polyclonal populations between different layers shall be mapped and explored. In Chapter 11 these two independently investigated processes of horizontal and vertical polyclonal expansion will be shown to spatially correspond in the structure of the bone. Chapter 12 explores the relationship of polyclonal expansion to other physical aspects of the bone, particularly biomineral growth. The subsequent two chapters present two vignettes around important structures within the calvaria: sutures and muscle attachment regions.

This thesis does not represent the first attempt to explore this undiscovered country with modern techniques, as it follows on from the very insightful work of Kate Jordan. As the key findings of this research remain unpublished, it is summarised in the next section.

7.2 Summary of the Work of Kate Jordan

This thesis follows on from the thesis of Jordan [2011]. In this she entirely disproved and replaced the model of dermal bone growth, spawning further projects to explore the impact of these findings. This was work sent to Nature as two articles, and the lab has now completed most of the revisions requested by the referees. My work contributes significant parts to these revisions. As it is unpublished still, I summarise it here.

The classical model of dermal bone growth is effectively transposed from observations of endochondral bone growth, wherein new bone forms around the outside of new [Buckwalter et al., 1995; Lieberman and Friedlaender, 2005]. In this model, the outer layers (1, 3, or both) must be depositing matrix to expand the Layer 2 by apposition. By examining deposition of matrix using fluorescent dyes that integrate into new matrix, it was shown by Kate Jordan that new matrix actually forms in the middle of Layer 2, necessitating an invasive process and bone remodelling.

Invasive growth would imply ‘vertical’ invasion of cells, *i.e.* the movement of cells in the direction perpendicular to the plane of the bone from one layer into another. Points of possible invasion were described, termed ’clasps’, where cells of Layer 1 and 3 were seen to be connected. Above these clasps small rings of cells were found, termed ’rosettes’ due to their similarity to a flower’s petals. These Layer 1 structures consist of a central cell that demonstrated nuclear Runx2, nuclear Hand2 and Osteopontin expression, surrounded by approximately 5 or 6 cells with cytoplasmic Runx2. Notch1 activation was also demonstrated within the Rosette, suggesting a stem cell niche activity similar to Calvi et al. [2003]. The role of these rosettes remains somewhat cryptic: molecular analysis would suggest that these may act as a stem cell niche, while the association with points of inter-layer communication suggest a role in modulating or organising vertical invasion.

A floxed Hand2 mouse line was used [Hendershot et al., 2008] that allowed for neural-crest specific deletion by Wnt1-Cre. This entirely removed the development of Layer 2, with cells accumulating within Layers 1 and 3 [Jordan et al., 2015]. While Hand2 in the nucleus down-regulates Runx2 activity [Funato et al., 2009], Jordan also demonstrated that Hand2 was necessary for nuclear import of Runx2, which drives invasion [Komori, 2002; Pratap et al., 2005]. This suggests that invasion of Layer 2 by the outside layers is critical for proper development, further attacking the argument that Layer 2 is merely secreted by Layer 1.

A molecularly distinct subset of Layer 1 was observed at muscle attachment regions. These cells express Periostin rather than Undulin which is found elsewhere in Layer 1. Jordan proposed that this came about via a partitioning within Layer 1, termed Layer 1-Attachment. This possibly distinct substructure is explored in Chapter 13.

It was shown that Layer 2 (the spongy middle layer) grows not by apposition but by an unusual inflationary process by which new matrix is deposited on the inside of older matrix. This fact necessitates an cellular invasive process and another student, Sophia Gibbs, has shown by labelling cells with fluorescent dyes that these invade into the growing Layer 2 from both the outer Layers 1 and 3 (hitherto unpublished).

7.2.1 Following the invasive processes of polyclonal spread with Confetti

While invasion has been observed by Jordan and Gibbs to be a key process in development of parts of the bone, it is not known where it might occur, whether the directionality of magnitude of invasion changes as the bone develops, nor and how it relates to the horizontal spreading of cells within the same layer.

Confetti labelling reveals lineage information, allowing for the surveying of both the vertical invasion between layers and the horizontal spreading of cells within the same layer. Using the same Wnt1-Confetti line described in the last Part to label all Cranial Neural Crest Matsuoka et al. [2005], the frontal and nasal bones can be entirely labelled and studied. The work documented in this Part will provide a global and quantitative perspective of this process: I shall demonstrate where these invasive events happen, which layers are in communication, present the non-random patterned nature of these invasions and explore whether there is any relationship between the directionality of cell invasion and the thickness growth of dermal bones. In doing so I hope to reveal how the frontal and nasal bones are shaped by these invasions, and present a model of bone development as a dynamic and active process rather than as the static sedimentary process it is currently thought to be.

As invasion is an entirely novel explanation for dermal bone development in the skull, nothing can be assumed about where it may happen, what form it might take and how it might relate to biomineral thickness growth. Thus whole bones must be considered, in three dimensions, and their characteristics and polyclonal architecture explored. Before polyclones might be identified, I had to develop a means of capturing single cells in a whole mouse calvarium and summarising this data in a manipulable fashion. This process is presented in the next Chapter.

While little is known about thickness growth, most assumptions about skull development centre on the sutures as the principal architects of bone development. This model of sutural growth, the problems and shortcomings of the model and potentially falsifiable means of assessing the model's validity are presented below.

7.3 The Traditional Model of Sutural Growth

It is a long held belief that the sutures are the principle sites of growth in the skull [Rice et al., 2000; Ornitz and Marie, 2002; Morriss-Kay and Wilkie, 2005]. Baer [1954] demonstrated through cessation of *in vivo* alazarin red staining that the periphery of the bone would be unstained, implying it had formed since withdrawal of the dye. The assumption implicit in this is that solid bone is not reforming, and that any region with no stain must be entirely novel. The traditional model has been expounded upon by numerous observers [Opperman, 2000]. Zhao et al. [2015] recently proposed that the suture is not only the site of growth, but the cells of the suture itself are stem cells that give rise to the bone, which is the strongest possible conclusion of the traditional model of sutural growth.

The sutural model of growth forms the basis of medical approaches to disorders of the suture. Craniosynostosis describes a condition wherein the suture closes prematurely, leading to distortion of the skull [Morriss-Kay and Wilkie, 2005]. It is assumed that this represents a loss of the site of sutural growth, with deformity caused by compensatory growth at adjacent sutures [Delashaw et al., 1989] though sutural compensatory growth has never been conclusively proved to occur at other sutures. The current treatment for this condition is surgical reestablishment of the sutures [McCarthy et al., 1995; Allareddy, 2014].

7.3.1 Problems with the Sutural Model of Dermal Bone Development

Despite widespread acceptance the sutural model of growth fails to address many aspects of bone development. Firstly it is limited, and does not truly address early bone development, as sutures only exist once nascent bones are already partially developed. This leads to the assumption that the osteogenic fronts form independently of sutures. Secondly, there is no true explanation of why sutures appear in the positions that they do, and how variant sutural patterns can arise, such as

Wormian bones and the developmental noise necessary to give rise to differences between species.

Wormian bones are small suture-defined ectopic bones that typically form along principal sutures. Their existence sits poorly with the traditional sutural model. Often Wormian bones have no real phenotypic effect beyond the additional sutures, which greatly calls into question the suture as the all-powerful definer of skull morphology. No clear solution to their aetiology has been found, with Berry and Berry [1967] and Finkel [1976] favouring genetic factors and Pucciarelli [1974]; O'Loughlin [2004] and others suggesting principally mechanical sources. Due to their sporadic nature, no true study on the formation dynamics of Wormian bones has been conducted.

While the sutures are held as the principal agents of skull growth, loss of sutures in craniosynostosis results in only a minor (10-20% loss of bone thickness growth) [Cohen, 2005; Cohen Jr, 2006]. This demonstrates that an unknown non-suture dependent mechanism is responsible for bone thickness growth. It was also noted in the past literature that areas of muscle attachment are characterised by ridges (called entheses). Somehow one would expect that some kind of modification of a basic dermal bone structure would have to account for these increases, irrespective of distance to suture.

With access to the polyclonal architecture of the bone, we can assess the sutural model. If the bone does indeed grow from the suture itself, then the polyclones within the suture should extend into the adjacent bone. If however the polyclonal architecture of the suture does not conform to this, then it cannot act as the principal architect of new bone, and a new role must be posited for its existence. This is explored in Chapter 14, where the PCA technique developed in the last Part reveals the suture as a recipient of the cells from adjacent bones, rather than as a donor of cells to to the bone. The dynamics underlying the peculiar structure of muscle attachment regions are explored in Chapter 13.

7.4 Summary

Currently it is believed that the frontal and nasal bones grow in thickness by apposition, with cells deposited into matrix as the bone grows from the inside out. The sutures are believed to be the principal generative regions, giving rise to the rest of the bone. Kate Jordan Jordan [2011]; Jordan et al. [2015] and Sophia Gibbs (unpublished) have demonstrated that this is false, and that the bone grows in an inflationary fashion, dependent on the invasion of cells from the outside Layers 1 and 3 and into the central spongy Layer 2. The key question to be addressed in this thesis is how this invasion proceeds in three dimensions to shape the bone.

In Chapter 8 I shall present a protocol and initial analysis pipeline for obtaining the full polyclonal architecture of a mammalian calvaria, through use of Wnt1-Confetti to label all Cranial Neural Crest cells and thus the frontal and nasal bones [Matsuoka et al., 2005].

In Chapter 9 I shall explore horizontal spreading of individual clones across single layers, which are expressed as roughly circular ‘patches’ of cells. These patches are observed to be roughly uniform in size across all three layers, but differ in arrangement across the three layers. In Chapter 10 I shall explore the other mode of elaboration and demonstrate that localised vertical invasion of mixed populations between layers exists in a distributed fashion across all parts of the bone, but with local organisation and patternation. This is accomplished by calculating the similarity or difference of polyclonal mixtures in the different layers of single column of bone, and repeating this process for every point across the entire sample.

In Chapter 11 I will demonstrate that vertical invasion is organised around the centres of the horizontally defined patches, and thus explore polyclonal relationships in three dimensions. This observation is used to propose that patch formation and the vertical communication of cells between patches of different layers is the principal generative process of bone development.

In Chapter 12 I will explore how these linked processes of horizontal spread and vertical invasion are organised around an axis of biomineral development, and demonstrate the changing dynamics of bone development as it matures. It is demonstrated that there is a time course of development, with Layer 3 initially acting as the principal donor of cells, and with Layer 1 taking over this generative role as the bone matures.

Chapters 13 and 14 focus on the polyclonal architecture of functionally distinct regions of the bone. In Chapter 13 the muscle attachment regions are examined, and polyclones found to integrate muscle and tendon into bone. In Chapter 14 the sutures shall be specifically assessed, and demonstrated to act as secondary buffers between bones, rather than generative regions.

Chapter 15 discusses the novel patch-based model of bone development with respect to clinical and evolutionary significance.

Chapter 8

Obtaining Single Cell Resolution in Whole Mammalian Calvaria

Jordan [2011] established that invasion, not apposition was the primary dynamic of calvarial growth. However this was an observation effectively on a cellular level, considering the dynamics of only a few cells in a section. It was not clear where in the bone this might occur, or when. Clasps could represent continuous breaches for cell invasion, or they could be transient structures arising from widespread invasion events. There was no clear organ-scale organisation of development arising from these critical observations.

Confetti labelling can provide context to the course of polyclonal expansions by denoting interlayer exchanges of cells, and charting the extent of population spreading across a layer of bone. Utilisation of the Wnt1-Confetti mice described in the previous part allows for labelling of the neural crest population, and thus the frontal and nasal bones. This is evidently a powerful tool, but as in Part I of this thesis, it is mostly employed on sections, which cannot explore organisation of a whole organ, or reliably explore dynamics both through the thickness of the bone and across the expanse of the bone at the same time.

Whole-mounts are necessary to address such questions. This technique involves preparation of large regions of tissue for *in situ* imaging, with minimal disruption to the structure. A ‘true’ whole-mount might contain the entire organism, but the preparation of large regions of tissue can also be considered a whole-mount. This large sample would have to be imaged in its entirety and segmented into layers *in silico*. Novel analysis techniques would be necessary to interpret the information of the hundreds of thousands of cells contained. The sample preparation, imaging and principal data sources are described here.

8.1 Methods

8.1.1 Choice of Clearing Method

Wnt1-Confetti mice Dissection of mice for calvarial whole-mounting is described in Appendix A.2. A key problem in microscopy with whole mounts is the attenuation of light by translucent tissue: light is reflected, absorbed or refracted by the tissue such that less reaches the subject and returns to the observer. This is negligible in a section, but the principle limiting factor in thicker samples. Some form of clearing was thus necessary to increase the translucency of the tissue, and allow access to deep bone. Several methods were attempted, and SeeDB [Ke et al., 2013] eventually used.

The depth to which microscopy can penetrate tissue is dependent on the opacity and light-scattering properties of the sample. Numerous methods have been developed to render tissue more translucent and accessible to microscopy. These are collectively known as ‘clearing’ as they render the tissue glassy and transparent. In most tissue the majority of light scattering occurs due to refraction at water-lipid interfaces within the sample, and it is this effect that is diminished in cleared sample, usually by the replacement of water with solutions that have a refractive index closer to that of the solid tissue, or by gentle removal of lipid bilayers. In bone, collagen and hydroxyapatite anisotropy create significant autoreflection and thus poor visibility through bony matrix. An ideal clearing protocol will render the sample completely transparent while preserving tissue structure, protein localisation, fluorescent protein activity and accomplish all this within an acceptable period of time.

‘Clearing’ has recently and incorrectly become recently synonymous with ‘CLARITY’, which has been proposed as an ideal solution for neuroscience experiments [Chung et al., 2013]. This method relies on electrophoresis to remove lipids from the sample, which is fixed in a hydrogel. This preserves fine cell morphology as well as protein fluorescence and antibody accessibility. The method however is complex and requires the construction of not only specialist equipment but also a number of hazardous reagents. While the challenges that CLARITY has been developed to address are pertinent to neuroscience, the preservation of long fine neuronal processes was not a concern in this study, and so more simple alternatives were explored.

BABB (Benzyl Alcohol/Benzyl Benzoate) treatment is a common method of performing clearing [Kay and Peng, 1992; Dent et al., 1989]. This procedure requires dehydration in ethanol, followed by incubation in hexane and finally in the BABB mixture. Hexane and BABB are hazardous. As the BABB mixture dissolves plastic, glassware must be used, and given that an inverted microscope was to be used, mounting in BABB presents a risk to the equipment. Furthermore, BABB treatment results in significant shrinkage and thus perturbation of the tissue [Ke et al., 2013]. While efficacious and reasonably expeditious, BABB clearing presents too many risks to operator, equipment and sample integrity and cannot be considered optimal. Chung et al. [2013] further criticise BABB and other similar clearing methods as promoting fluorophore quenching.

The Sca*l*e method uses various solutions containing urea, Triton X-100 and glycerol, which work to match the refractive index of tissue [Hama et al., 2011]. This is certainly a very simple and safe method, and good results are possible through incubation in one or two solutions of different components. However, Sca*l*e works very slowly. While clearing is ostensibly possible in a matter of days, samples may take months of incubation to achieve acceptable results. Furthermore, the samples are significantly expanded by the treatment, and protein is lost to a significant degree [Ke et al., 2013; Chung et al., 2013]. This method was trialled for this study, but no appreciable clearing was observed after two weeks: this may suggest that Sca*l*e is not appropriate for clearing of developing dermal bones.

The clearing method used in this study is termed 'SeeDB', which is an abbreviation of 'See Deep Brain' [Ke et al., 2013]. This relies upon incubation of the sample in progressively more concentrated solutions of fructose in distilled water, until equilibrium is reached with a maximally saturated solution which has a refractive index close to that of fixed tissue. A low concentration of thioglycerol is also added in order to prevent caramelisation by the Maillard Reaction. This method proved acceptably efficacious at clearing calvarial samples. The procedure requires less than a week, which corresponded well with our ability to image each sample. The components of the solution were simple and did not represent significant hazards. All of these factors made SeeDB the best available clearing method for this study. The fixation and clearing protocol is described in Appendix A.2.1.

8.1.2 Microscopy

Imaging of such large samples is possible on most automated microscopes through tiling, though inefficient. The software of the microscope used to capture these samples (Leica SP5) favours identically sized stacks in the same plane, forming a complete square grid, with no automatic coordinate generation beyond this limited facility. Therefore a work-around was developed that allowed for far more efficient imaging by exclusion of non-sample stacks, and by staggering of rows of stacks in the depth dimension, as described in Section A.6.1.

8.1.3 Initial Processing

The raw images produced contain discontinuities, noise and artefacts. These were ameliorated through the pre-processing pipeline detailed in Appendix A.6.3. The resulting images could then be stitched into complete sample-wide images, which required further work-arounds described in Appendix A.6.2.

Finally, software was developed that allowed for the manual segmentation of these cleaned and stitched samples into their constituent layers. This process is described in Appendix A.6.4. In brief, lines are manually drawn into cross-sections of sample, and sub-stacks generated containing only the parts of the sample which are sandwiched between two particular lines. The result is a set of stacks, each containing only one layer of the sample.

8.1.4 Generation of Maps from Stacks

Sample-wide stacks are large and unwieldy, each exceeding 30 Gigabytes. While the limitation will doubtlessly seem quaint within a short few years, a current high end lab desktop computer or laptop will barely be able to read half of this into memory before failing. This size is only multiplied by segregation of layers, as each layer occupies a separate stack of the same size as the original. However, this study focusses mostly on differences across layers, and differences between layers, rather than on dynamics of overlying cells within a single layer. As such, these stacks can be flattened to give ‘maps’: two-dimensional representations of the original three dimensional sample that rank on the order of Megabytes, dispense with unnecessary information and preserve the critical information of the original sample.

Two principle maps form the basis of the rest of the analysis of this Part. The technical detail of their generation is described in detail in Appendix A.7. The first required operation is to dispense with the Z-dimension of each layer, and dispense with differences in labelling. We are only interested in whether a voxel (a pixel in three dimensions) contains part of a cell or not, and we are only interested in where these voxels are across the plane of the skull. and not where they lie within the thickness of the layer. The same thresholding volume-based approach is used as in the PCA of Part I to remove labelling differences: a manual threshold is set to exclude non-labelled voxels and include all labelled voxels. A specialised form of Z-Projection is then performed, giving a map of the total voxels in a particular point of X and Y that are occupied by cells of each confetti colour. This outwardly resembles a simple Z-Projection with visible cells, and so is termed a 'Flattened Cell Map'. A by-product of this is a map of Layer Thickness, which will be presented and utilised in Chapter 12.

The second basic map is generated from a specialised blur of the Flattened Cell Map. While a human can perceive the density of cells within a certain area, our intuitive ability to do so hides complex subconscious abstraction. In order to allow the computer to perceive the density of labelling, the number of occupied voxels around a point must be convolved into that point: the literal description of a 'blur'. The 'Blur Map' convolves the population around a single point into a single value for each colour channel and point within the sample. This represents the mixture of colours around that point. A Gaussian kernel is used, with a $23\mu m$ radius. Given the size of cells within the calvaria, this means that each pixel of the blur map represents the colour mixture of dozens of cells. The key difference between this and a normal Gaussian blur is that the original volume of the layer is taken into account. The result is thus a measure of the degree of occupancy of the 3D space by labelled cellular material. .

These two maps form the root of all further analysis: the Flattened Cell Map contains all of the pertinent information about the shape, position and size of cells in each layer, but but discarding the vertical position of each voxel within that layer. This allows for further analysis where the actual original cells are required, such as estimation of cell number or visual observation of morphological differences. The blurred maps on the other hand go further into abstraction, creating a more machine-readable format of small regional colour information, from which the boundaries of groups of cells within the same layer can be detected, presented in 9, and mixtures of cells compared as in 10.

8.1.5 Estimation of Cell Number per Layer

The method for estimating the number of cells is described in Appendix A.8.1. In brief, estimates were made of the average volume of individual cells of each colour from measurement of 40 cells. The total number of occupied voxels in each layer was then divided by these conversion factors to give the estimate of the total number of labelled cells.

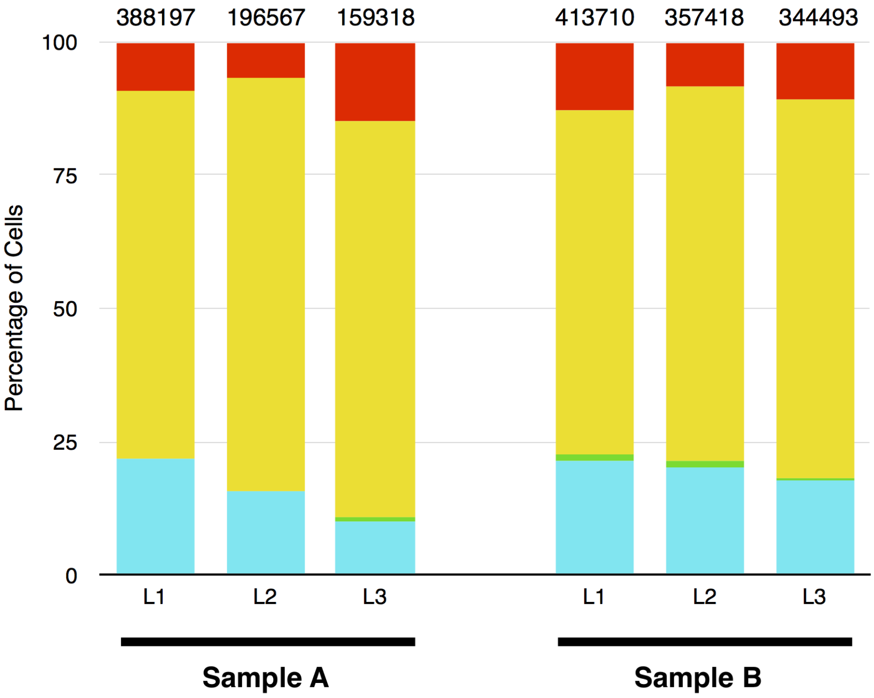

Figure 8.1: Estimated Proportions of Confetti Colours For the two samples, the estimated counts of confetti cells of each colour, in each layer. Numbers at the top of each bar represents the total number of cells within that layer.

8.2 Results

8.2.1 Anatomical Map and Landmarks

Figure 8.2 shows the anatomicals map of the samples used. Note that unusually, both samples possess an interfrontal bone, a deviation from the canonical pattern of bones in mice and mammals in general. This trait is common amongst the genetic background of Confetti Mice, C57BL [Johnson, 1976]. Its presence allows for examination of dynamics around a notionally ‘ectopic’ bone. If it has no apparent differences in its polyclonal architecture compared to other bones, then this will demonstrate evidence against the sutural model of growth, as a far more parsimonious explanation will be that sutures arise secondarily between any developing bones. This is explored in detail in Chapter 14.

8.2.2 The Four Confetti Colours are present in different proportions

The relative proportions of the four confetti colour markers across all layers and two samples was remarkably consistent (Figure 8.1). This is most likely explained by the mixing of the populations across the three layers. Were no mixing to occur, one might expect each layer to develop a relatively distinct colour profile as individual polyclones differentially expand. However, as this evidently does not lead to an appreciable difference in overall colour proportions, a method of communicating these regional changes across the three layers of the bone must be anticipated.

The absolute numbers of cells are stated for perspective only, as the two samples had different areas and thicknesses. The noticeably different trend across the two samples implies that there are differences that may arise from the biology of the sample, such as randomly incomplete labelling or a staggeringly large difference in cell number between two samples, but the differences more likely arise from differences in dissection, the method of cell count estimation, efficacy of sample clearing and reliability of imaging. This difference demonstrates the need for careful normalisation and interpretation of only relevant biological statements arising from the data.

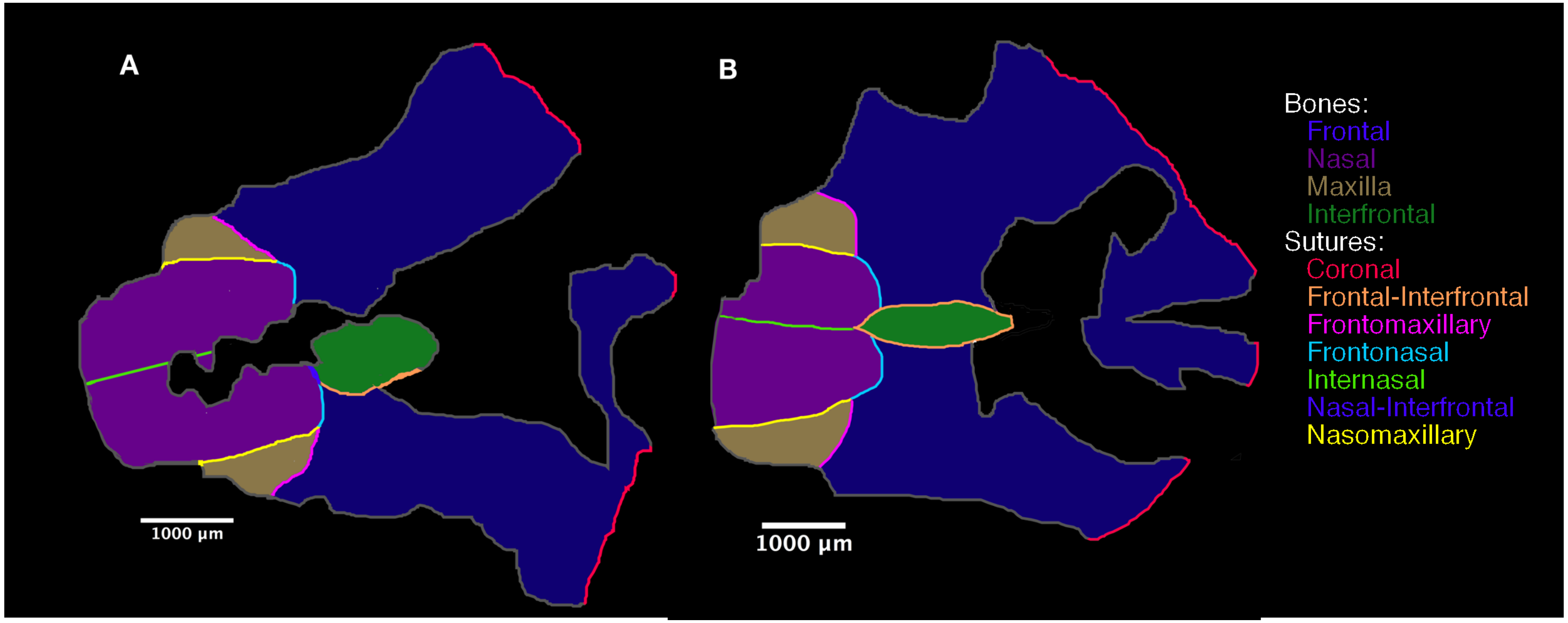

Figure 8.2: Bones within each sample The bones and suture of (**A**) Sample A and (**B**) Sample B.

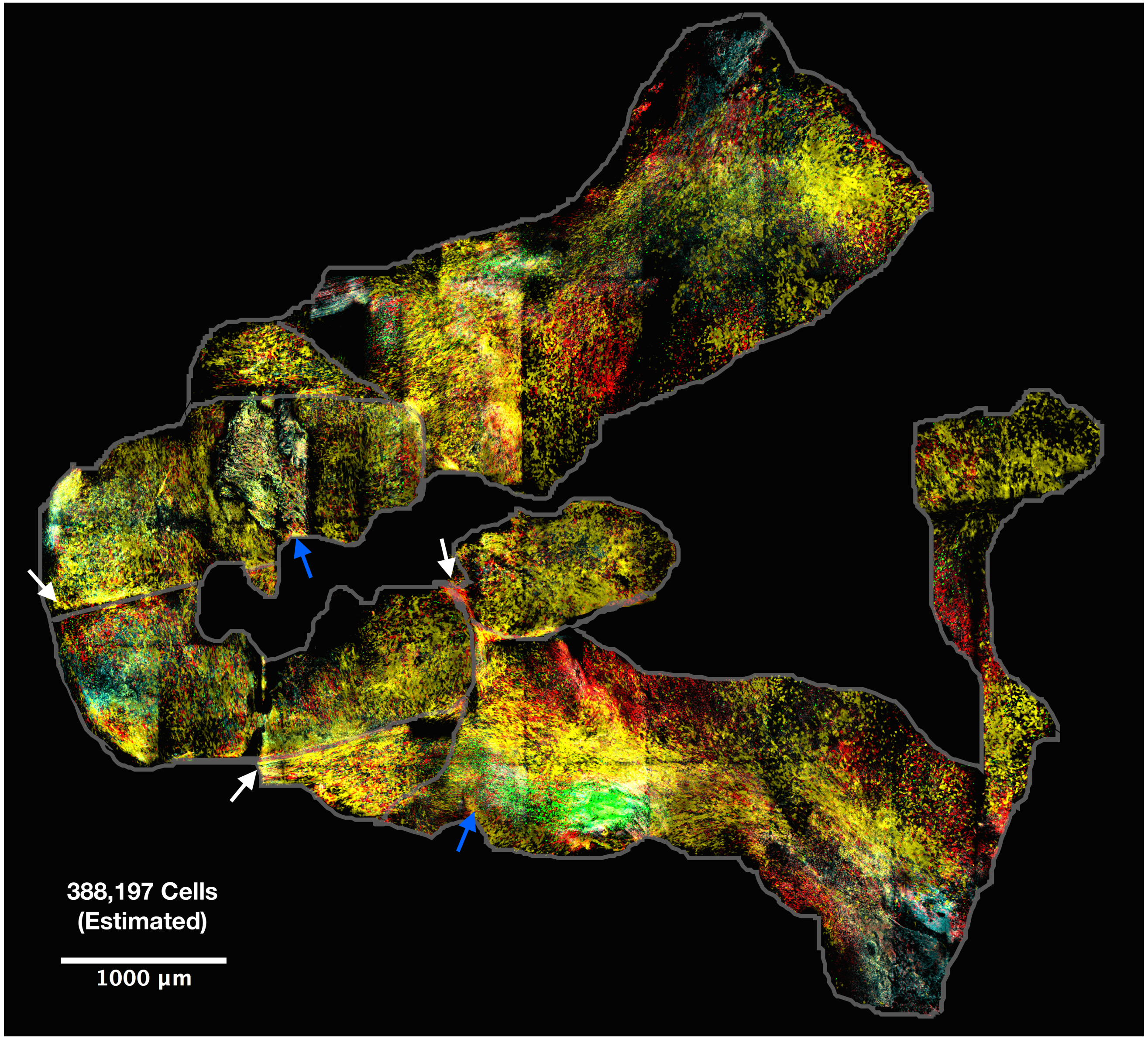

Figure 8.3: Flattened Cell Map Of Sample A, Layer 1. - *Caption on page 126*

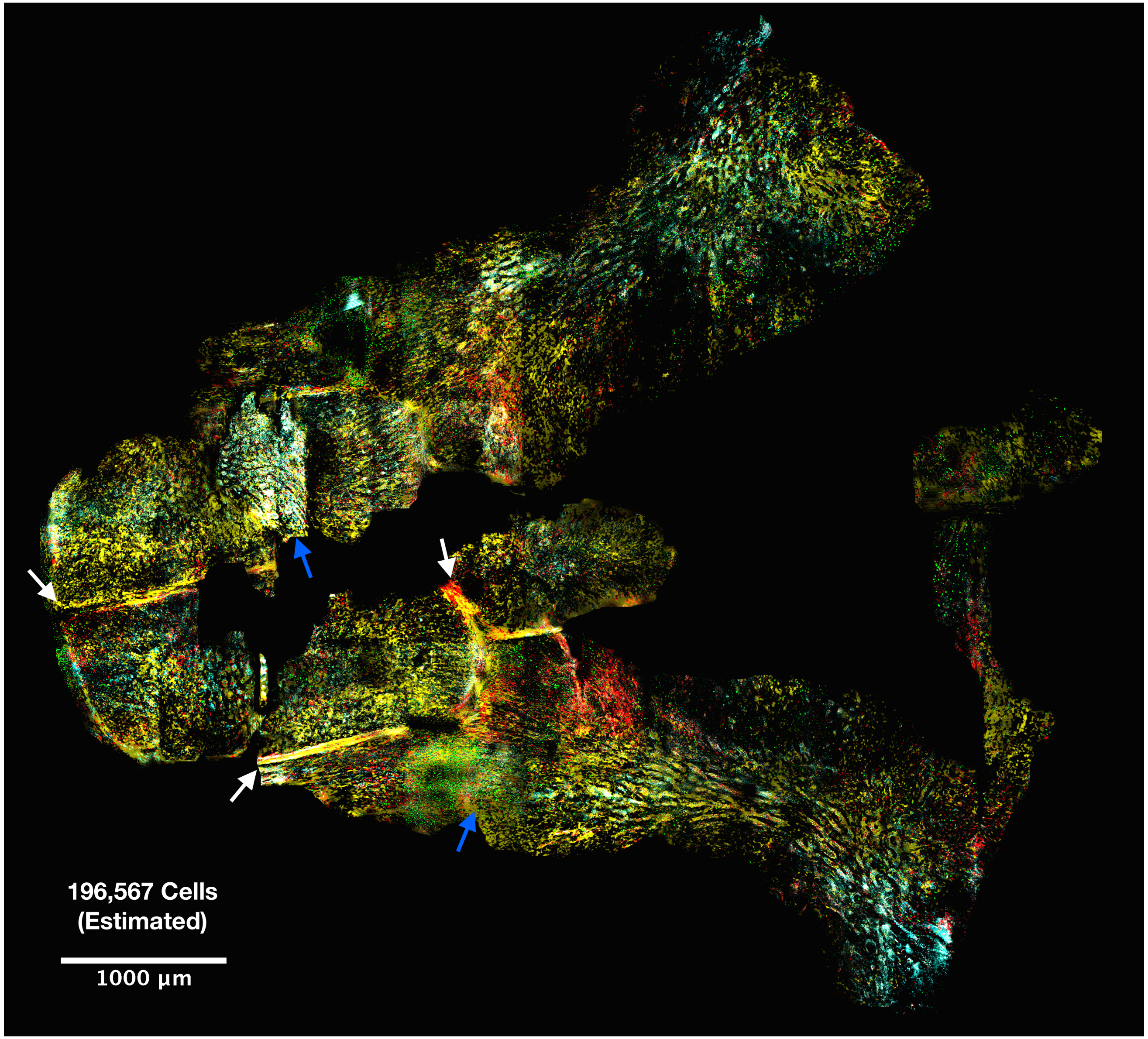

Figure 8.4: Flattened Cell Map Of Sample A, Layer 2. - *Caption on page 126*

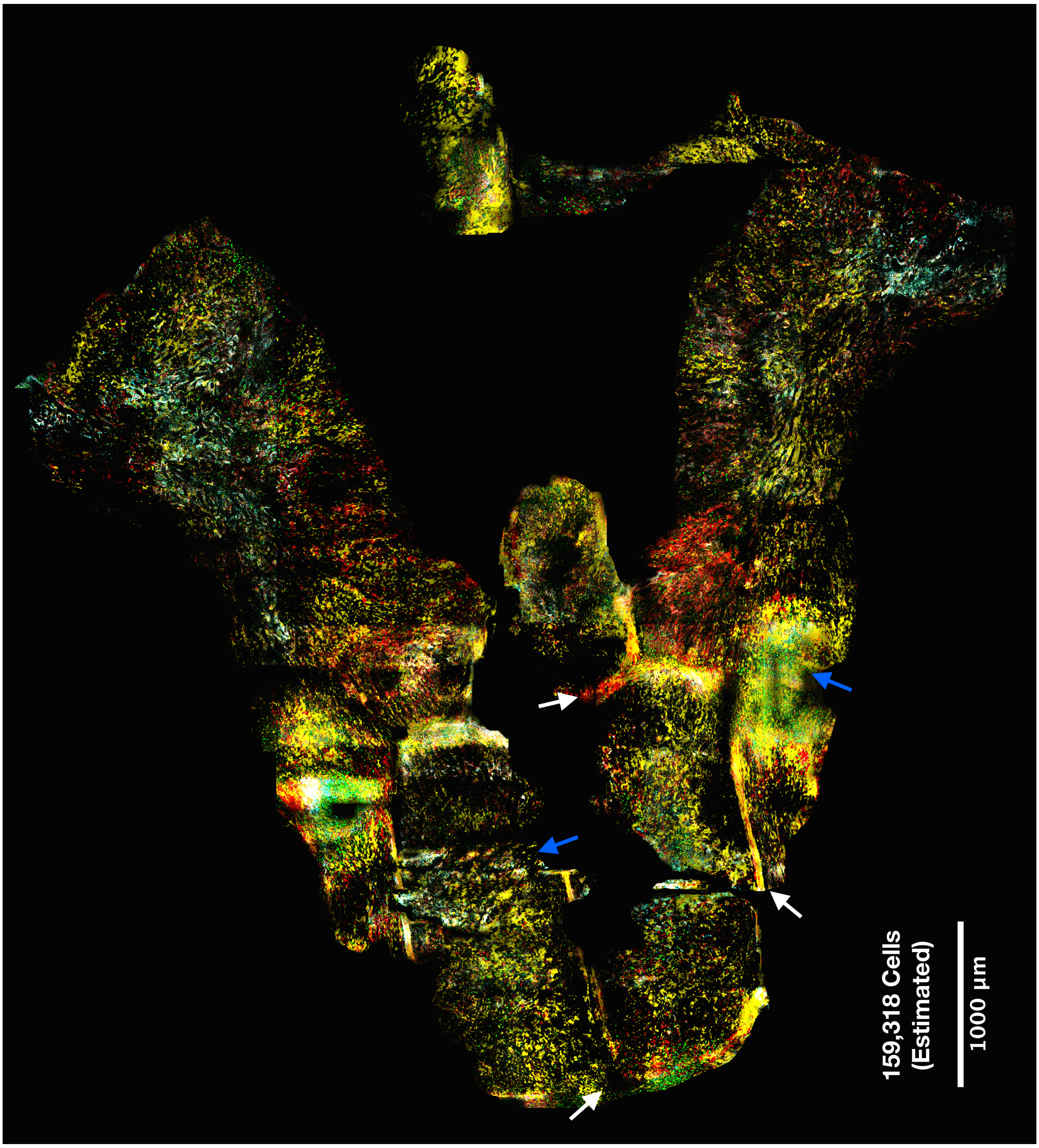

Figure 8.5: Flattened Cell Map Of Sample A, Layer 3. - *Caption on page 126*

Figure 8.3, 8.4 and 8.5: Flattened Cell Map Of Sample A, Layer 1, 2 and 3 respectively. Boundaries from 8.2 are displayed as lighter stripes in Figure 8.3. There is an apparent dense organisation of cells along sutures, with similar colours replicated along the extent of the suture (white arrows). Muscle attachment regions appear as islands of distinct colour, mostly defining Layers 1 and 2 (blue arrows). There are definite differences in the dominance of colours at different points of the bone, penetrating all layers but all parts are mixed, suggesting a means of vertical mixing as well as horizontal spreading of polyclones.

Figure 8.6, 8.7 and 8.8: Flattened Cell Map Of Sample B, Layer 1,2 and 3 respectively. Boundaries from 8.2 are displayed as lighter stripes in Figure 8.6. As in Sample A, sutures are cell dense in all layers (white arrows), and entheses appear as isolated islands of colour (blue arrows). There is a very distinct exclusion of the abundant cyan cells from sutures (red arrows), which suggests that these cells do not arise from the suture, in violation of the sutural model of dermal bone growth.

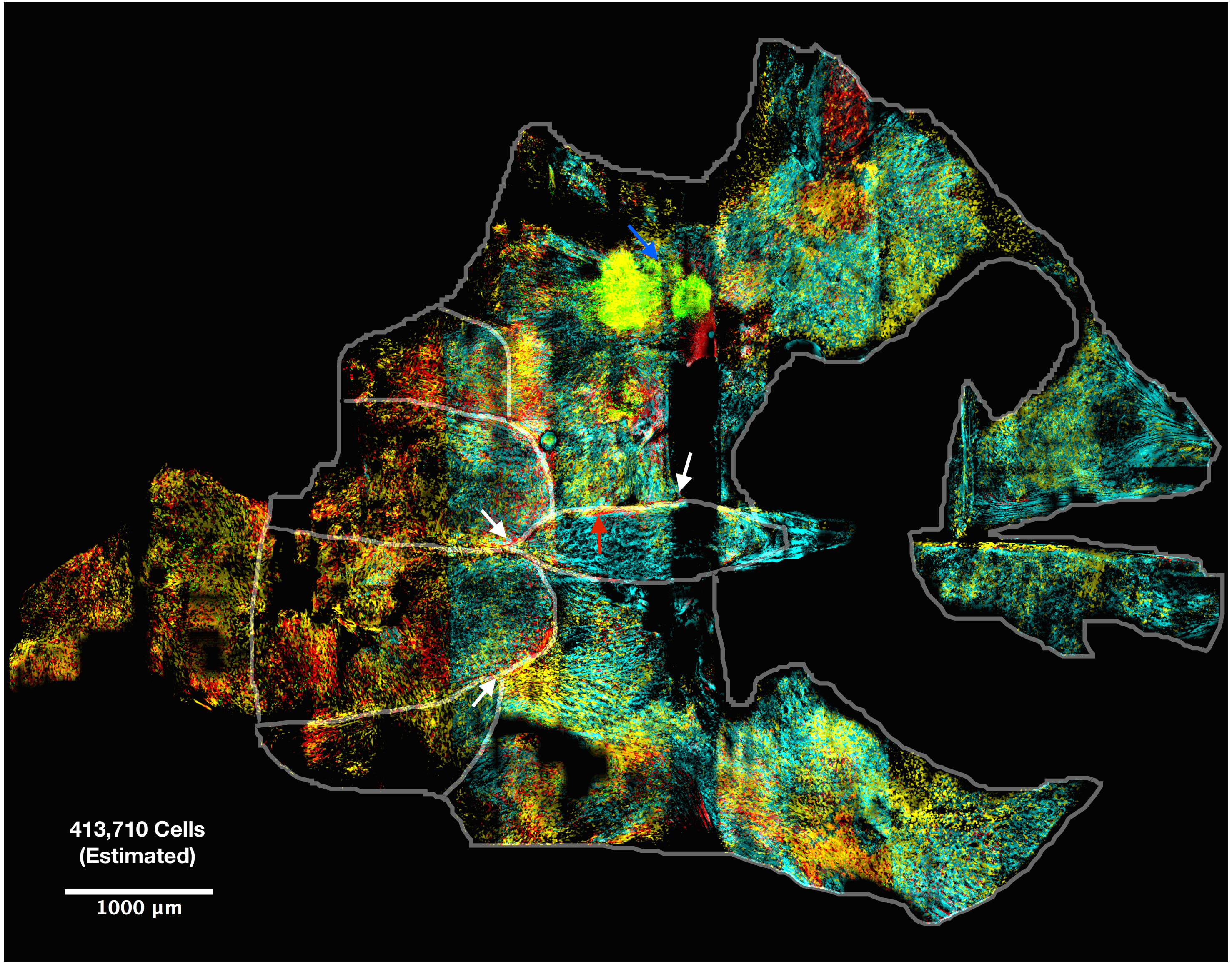

Figure 8.6: Flattened Cell Map Of Sample B, Layer 1. - *Caption on page 126*

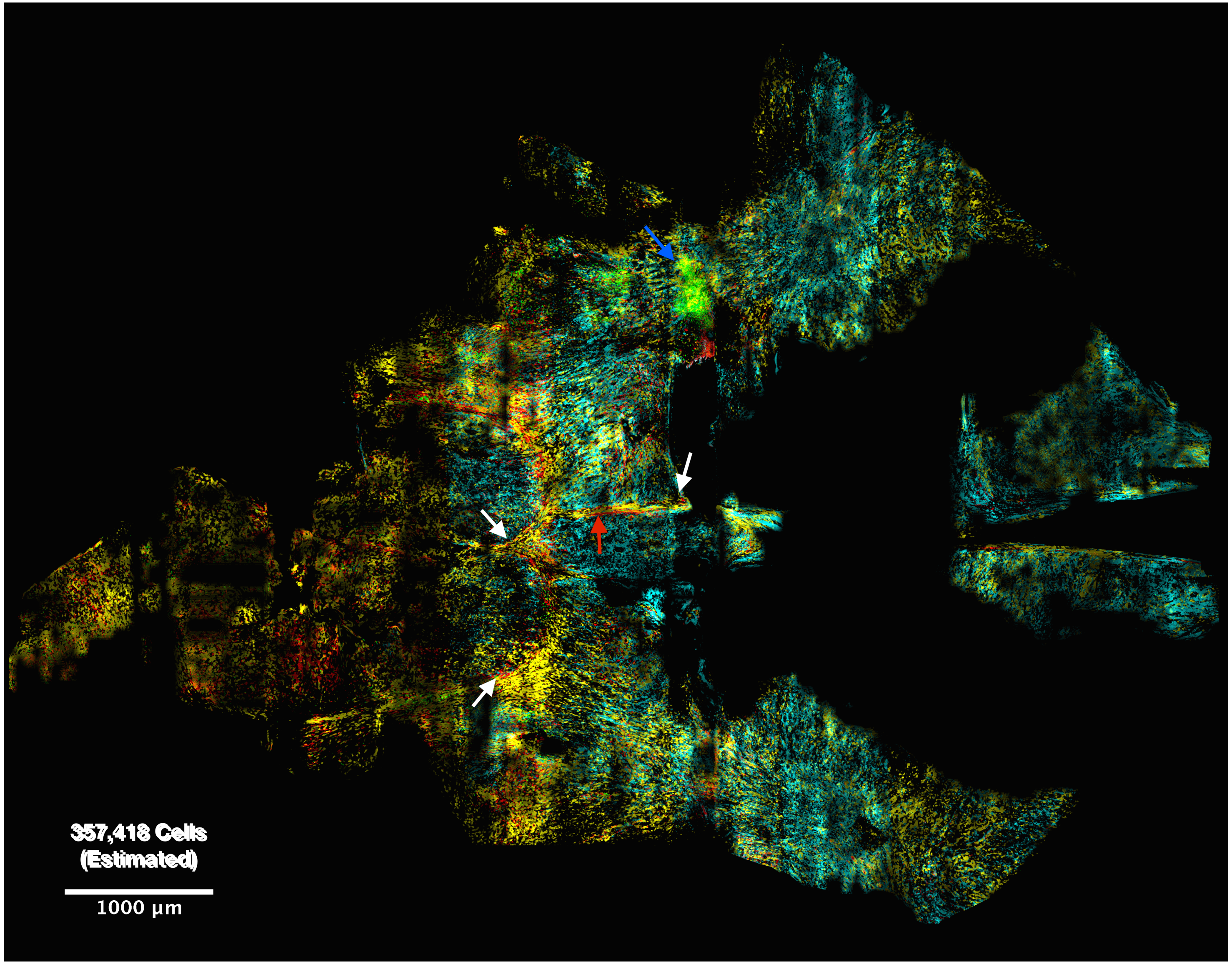

Figure 8.7: Flattened Cell Map Of Sample B, Layer 2. - *Caption on page 126*

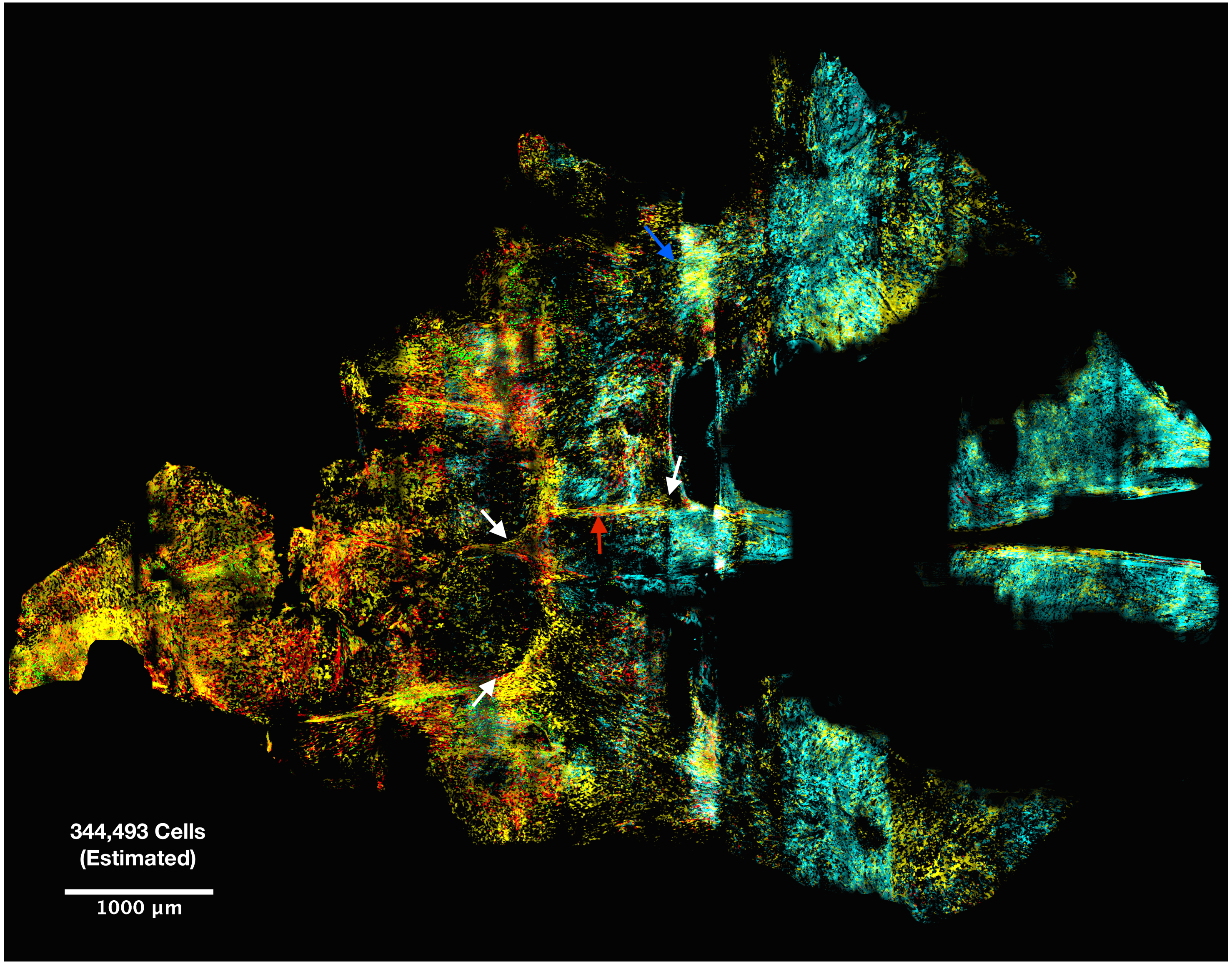

Figure 8.8: Flattened Cell Map Of Sample B, Layer 3. - *Caption on page 126*

8.2.3 Single Cell Maps of Whole Calvaria

Figures 8.3 to 8.8 show the flattened cell maps of each layer in both samples. There are several noteworthy oddities even from casual inspection of these deep data sources. Sutures appear to be cell dense, but also appear to exclude polyclones within the bones (Figures 8.6-8.8, blue arrows). This conflicts with the sutural model of dermal bone growth, which insists that these cyan cells must have originated within the suture. Instead, the sutures appear distinct from the bones. This is explored in detail in Chapter 14. Muscle attachment regions also appear quite distinct from surrounding bone, and are discussed in Chapter 13.

It is clear that there is similarity of colour between overlapping bone, and that single colours can extend out to dominate a region. This implies that cells can both spread across their own layer horizontal (discussed in Chapter 9) and move between layers (discussed in Chapter 10).

8.2.4 Maps of Cell Density in Whole Calvaria

Figures 8.9 to 8.14 represent the Blur Maps as described previously. While these are principally for the purpose of enabling computer analysis of polyclonal populations over an area, the human eye can still discern some useful information from them.

It is clearer from these maps than the previous that polyclones extend through the different layers of the bones. This implies vertical invasion between different layers. The true value of these maps is that information about the colours of many cells has been integrated into each pixel, allowing for comparison of cell mixtures in different Layers, and thus the invasive behaviour at each point. This is performed in Chapter 10.

The blur maps appear to contain many ‘blobs’ of different colours, implying grouping of cells. This represents the spreading of single colours over an area. These are explored in the next chapter.

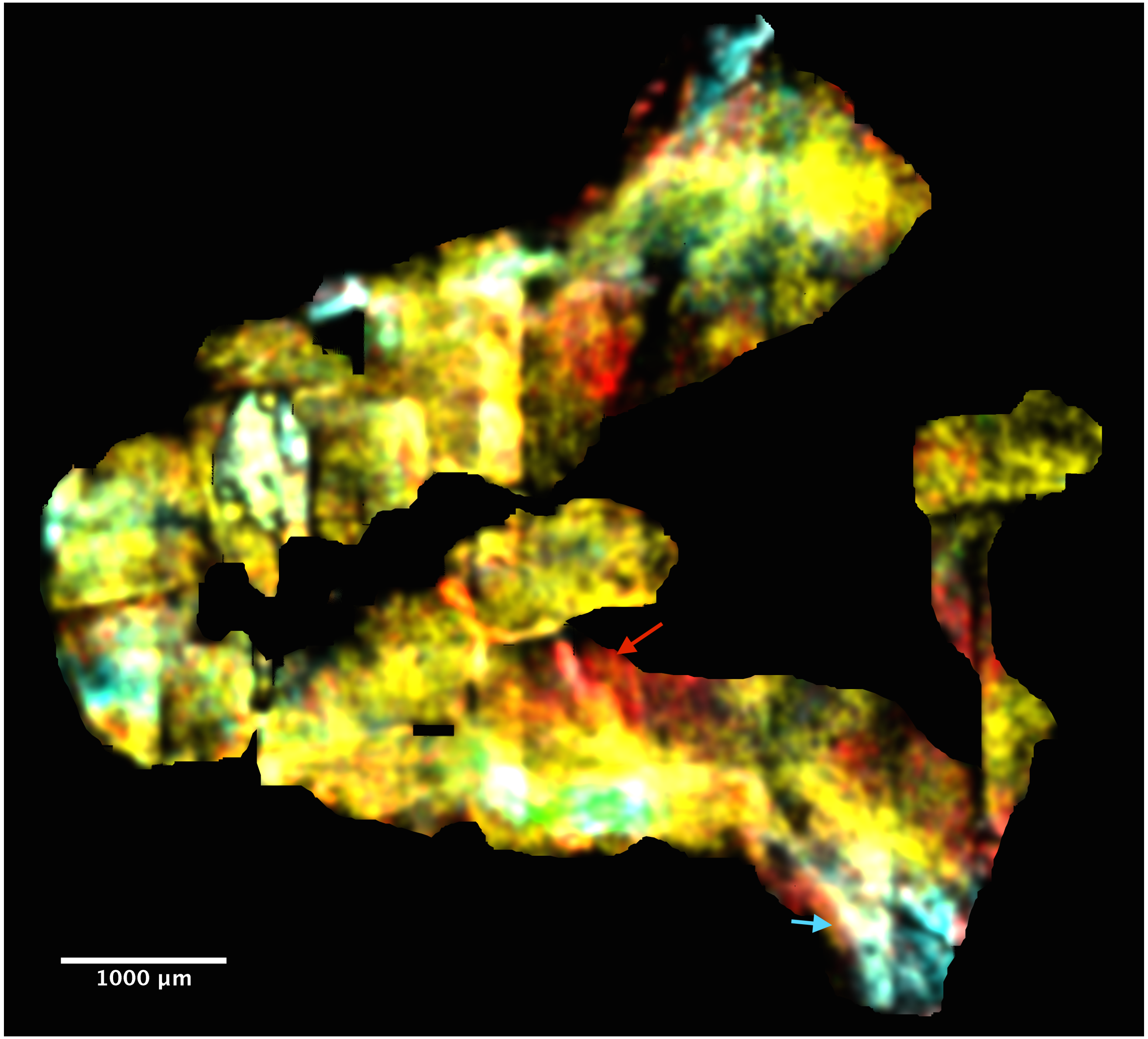

Figure 8.9: Blur Map Of Sample A, Layer 1. - *Caption on page 134*

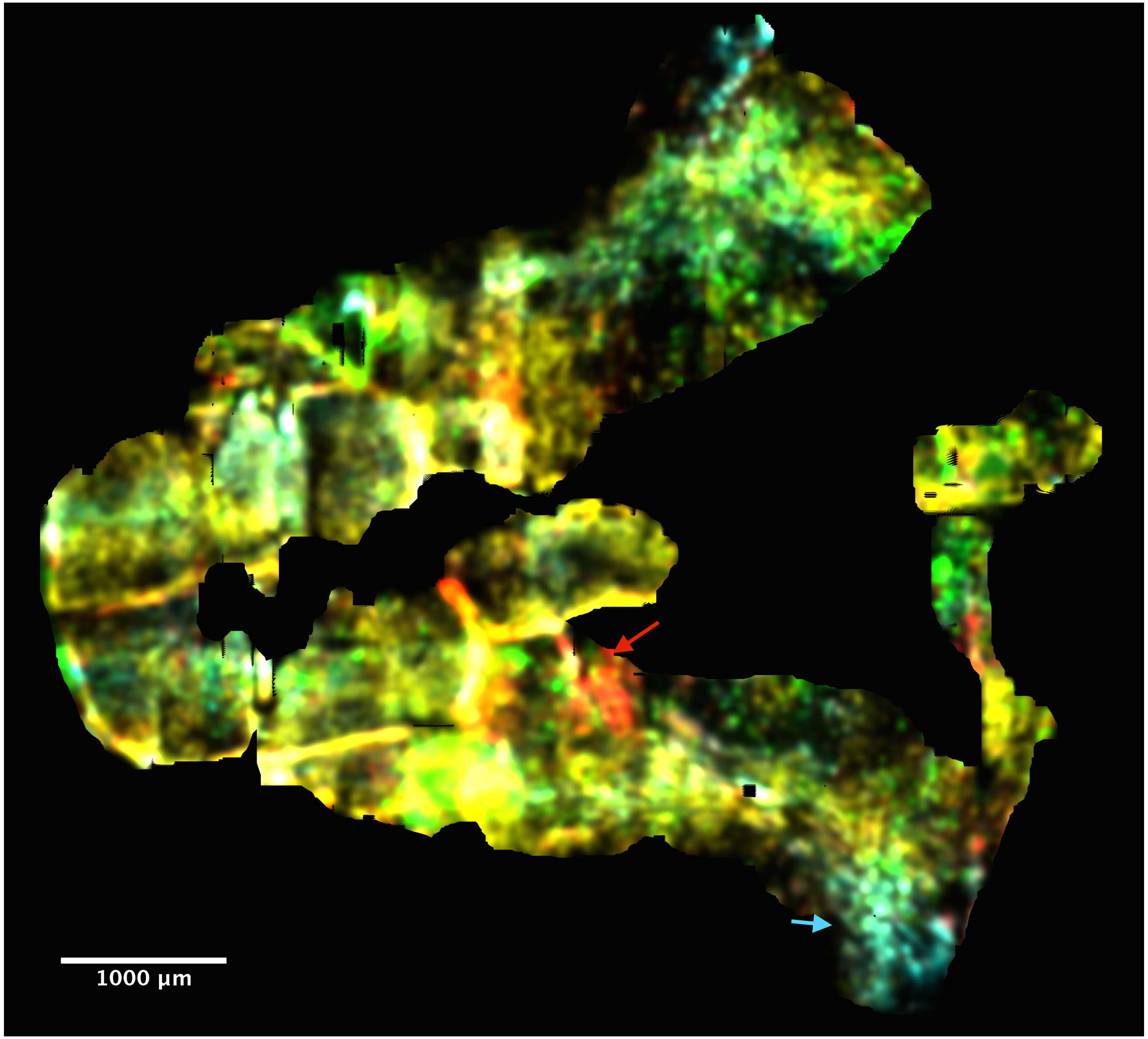

Figure 8.10: Blur Map Of Sample A, Layer 2. - *Caption on page 134*

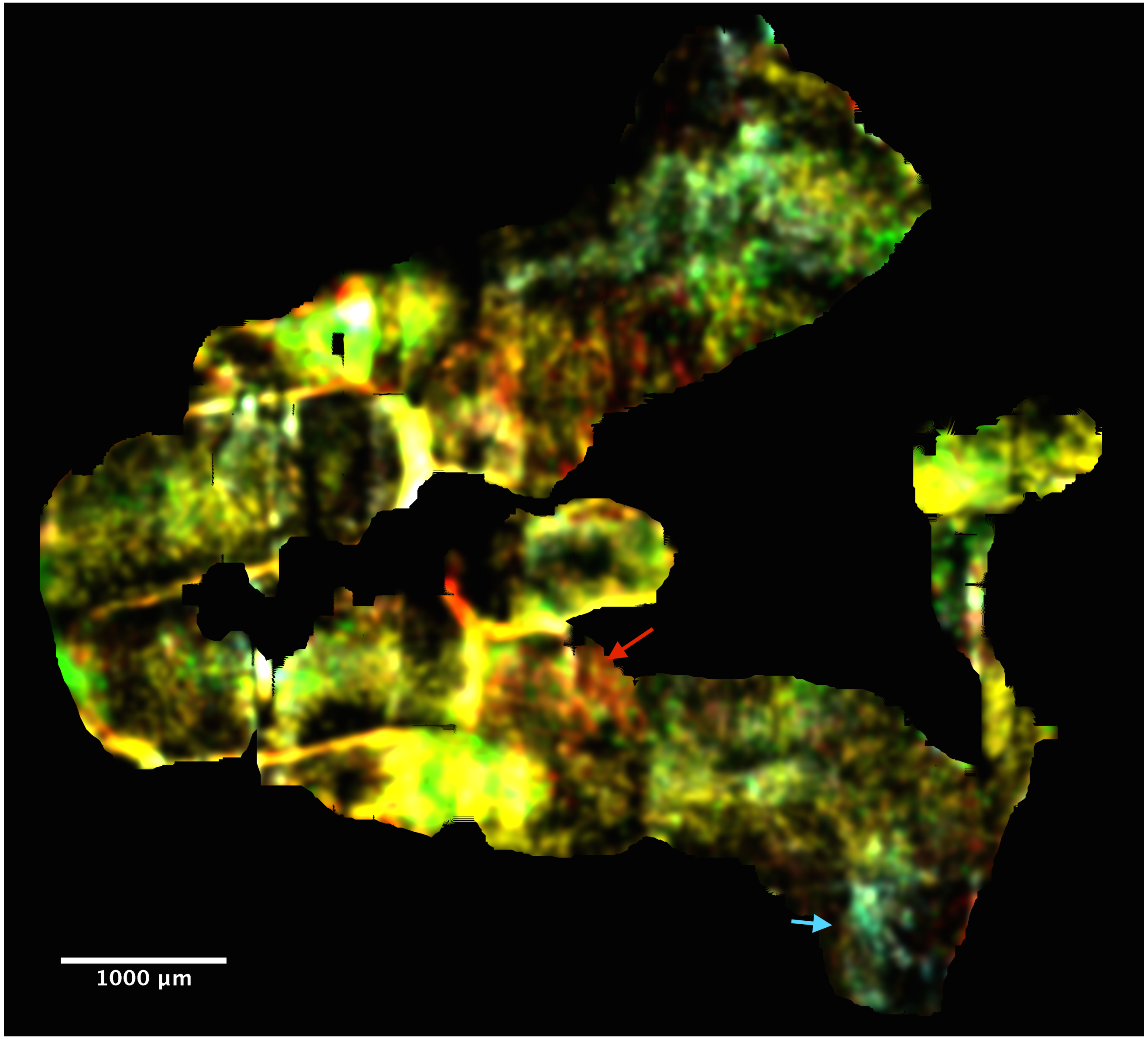

Figure 8.11: Blur Map Of Sample A, Layer 3. - *Caption on page 134*

Figures 8.9, 8.10 and 8.11: Blur Maps Of Sample A, Layer 1, 2 and 3 respectively. The cell landscape of the Flattened Cell Maps has been encoded as blurred maps of cellular density. This integrates the mixed polyclonal identity of the surrounding cells into each pixel. It is notable that the same labelling colours appear to penetrate all three layers, such as the red labelling at the red arrows, and the cyan labelling at the cyan arrows. This heavily implies invasion between layers.

Figures 8.12, 8.13 and 8.14: Blur Maps Of Sample B, Layer 1, 2 and 3 respectively. The cell landscape of the Flattened Cell Maps has been encoded as blurred maps of cellular density. This integrates the mixed polyclonal identity of the surrounding cells into each pixel. As in the Blur Maps of Sample A, there is penetration of labelling colours between Layers. Strikingly, cyan cells appear to be tightly excluded from the suture (red arrow in Fig. 8.12). Cell density is not even across layers: at the white arrows in each point to the same spot, yet where cells are dense in Layer 1, they are sparser in Layer 2 and almost absent in Layer 3.

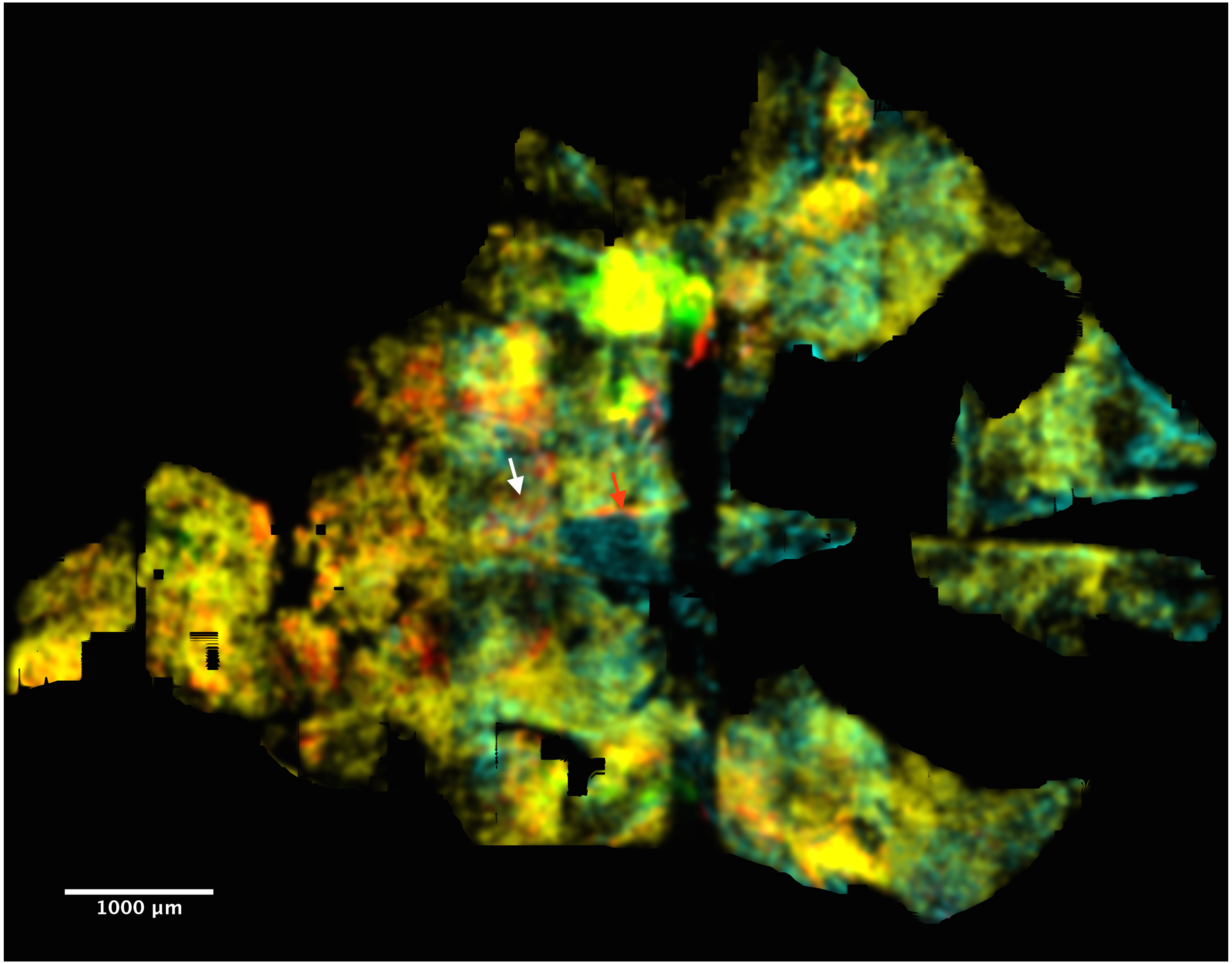

Figure 8.12: Blur Map Of Sample B, Layer 1. - *Caption on page 134*

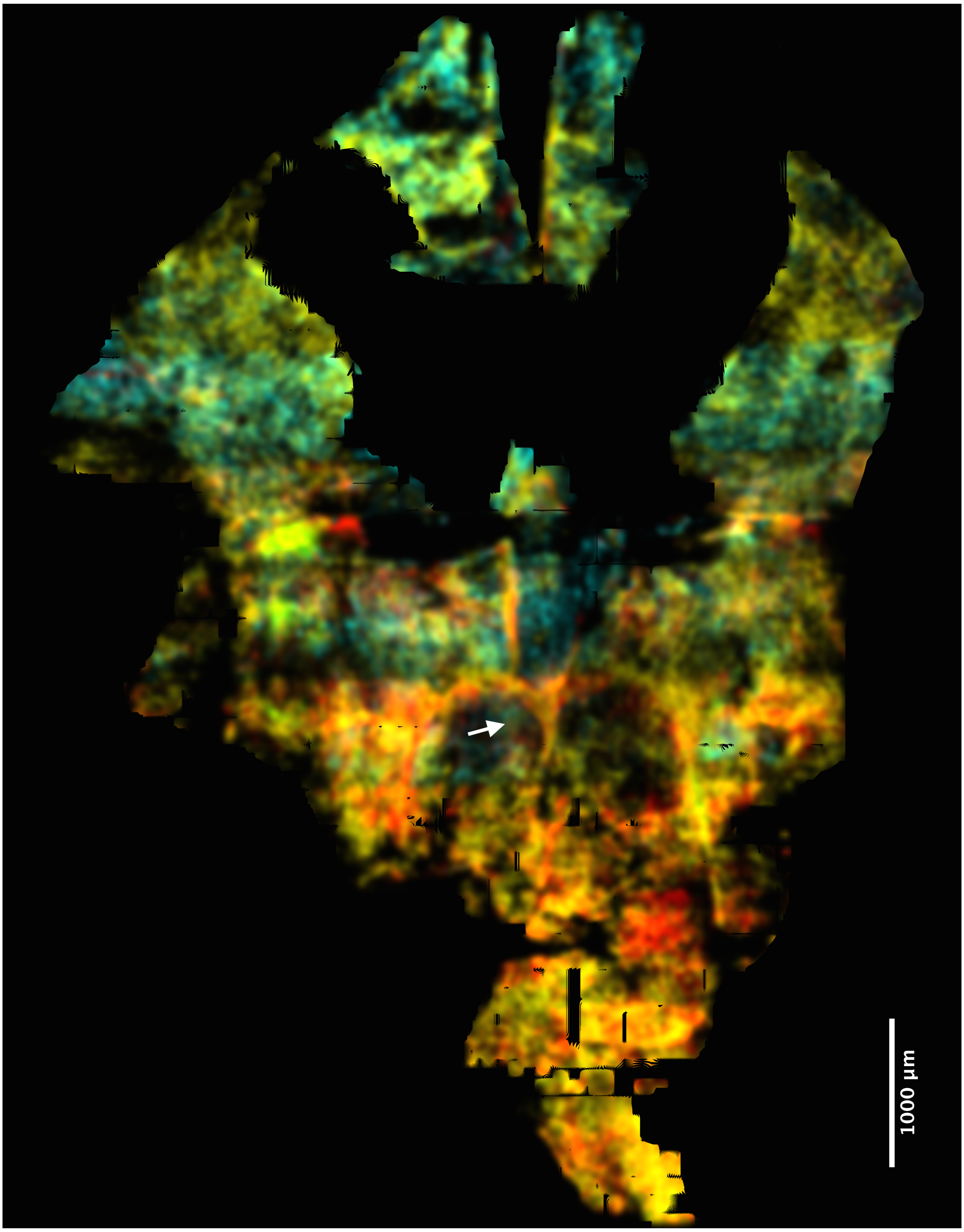

Figure 8.13: Blur Map Of Sample B, Layer 2. - *Caption on page 134*

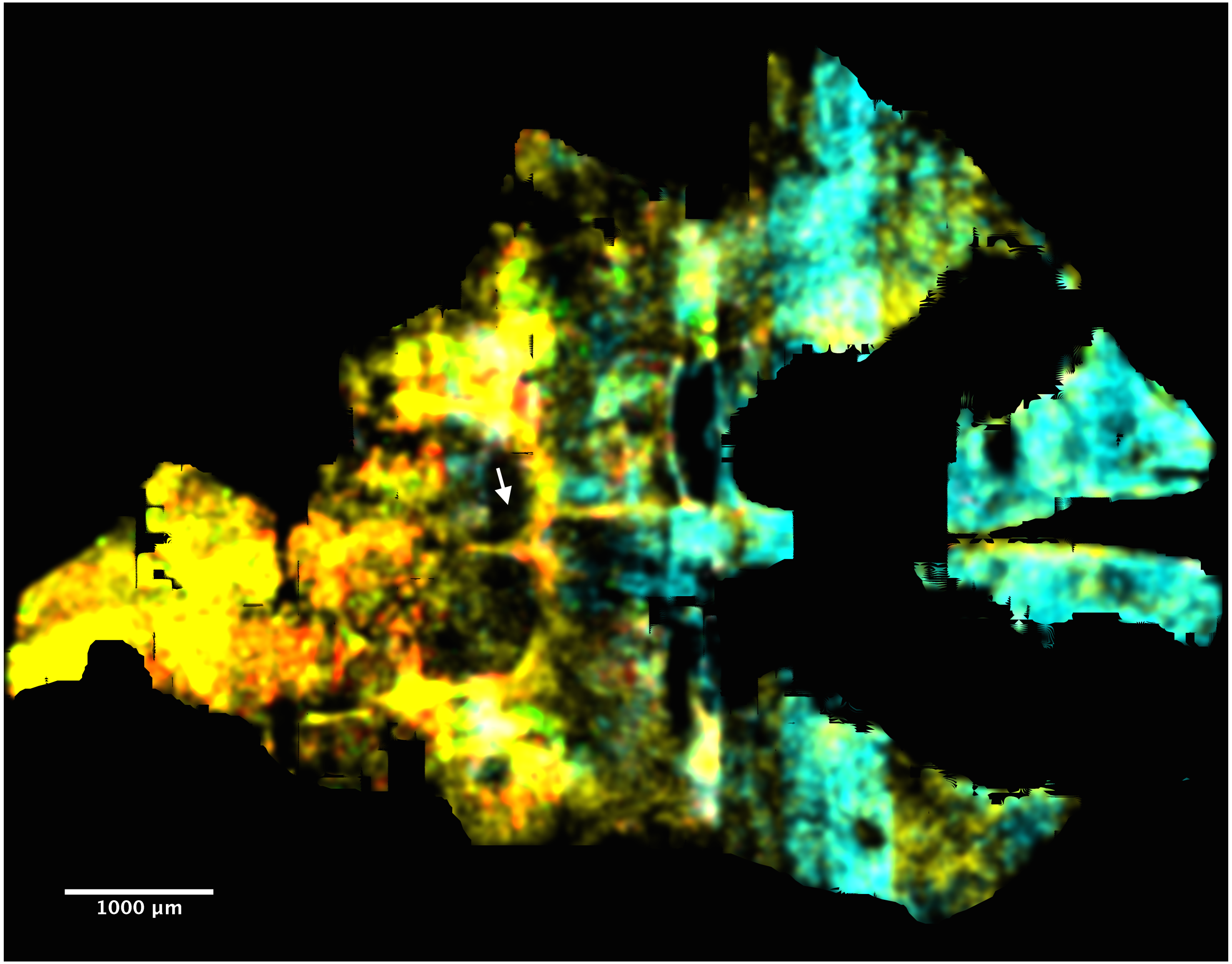

Figure 8.14: Blur Map Of Sample B, Layer 3. - *Caption on page 134*

8.3 Summary - Maps of Confetti labelled cells within Layers show no evidence of sutural growth

The maps of Figures 8.3 - 8.8 do not immediately suggest sutural growth: there is no apparent special organisation of cell colours emanating from sutures. These maps and the cell density Blur Maps in Figures 8.9 - reffig:B-L3-blur show that sutures are privileged regions with high density, distinct morphology and potential organisation, but this is not interpretable just on the basis of naive interpretation of maps. Strikingly, colours seem to be transmitted across layers, suggestive of an invasive mechanism,as predicted by Jordan [2011] and Jordan et al. [2015].

The key impression is one of complexity, requiring further analysis. This is an unprecedented approach to this question within mammals: without a whole-mount approach such as this, the apparent complexity of the global population would be entirely lost. The approach shall be to attempt to identify means by which cells can move around the sample, and then to explore whether these methods of movement are spatially linked into a three dimensional program of elaboration.

First, I shall analyse polyclonal groups of cells within the plane of each Layer, in the next Chapter. In Chapter 10 I will then look at how cell populations may move between layers. I will attempt to explore the relationship between these two processes in Chapter 11, and then compare this to biomineral thickness in Chapter 12. The apparent islands of muscle attachment regions will be addressed in Chapter 13, and the question of organisation around sutures will be addressed in Chapter 14.

Chapter 9

Mapping Horizontal Spreading of Single Presumptive Clones in the layers of Dermal Bone

9.1 Introduction

A cell that is sitting in a layer of the skull can move in two manners: either it can traverse the layer it is in horizontally, or it can move into another layer by vertical invasion. This chapter explores the dynamics of cells spreading across their existing layers.

The active growth of a developing organ requires cell division and movement to establish structures. In a planar structure such as a calvarial bone, the simplest way a group of cells can divide and spread out is radially, as this requires no additional directional impetus. This creates a characteristic pattern of cell density, as if cells are moving out from a central division point, then that point is likely to be the most dense as cells are expanding to cover an ever greater area (Figure 9.1). This motion need not be an active migration, as an apparent spreading of cells may arise as a function of cell division or invasion centred on a point.

By detecting and examining these patterns one can infer the degree of lateral spread of each group of cells, as well as consider other dynamics within each group. The area covered by a group demonstrates degree of lateral spread, thickness of Layer 2 demonstrates bone maturity, and changes in cell density demonstrate proliferation or invasion. These three factors can be compared to obtain an impression of how the skull develops.

The organisation and shape of these patterns gives valuable information about how the skull develops. Roughly circular patches would suggest that all points of the skull are undergoing cell division and spreading laterally in all directions, while stripes of contiguous colour would suggest a linear growth front. The latter would be consistent with the sutural model of growth, while the former would be antithetical to this model.

In order to map the extent of individual presumptive clones across each layer, the Blur Maps presented in the last Chapter were segmented by watershed analysis. This captures the shape of groups of cells based upon their local density. These patches can then be used as the basis for further analysis.

9.2 Methods

The methods for this Chapter are described in detail in Appendix A.8. In brief, the Blur Maps described in Chapter 8 are a representation of cell density encoded as image pixel intensity. These can be interpreted into regions of density by watershed segmentation, which groups all pixels into 'patches' around a local maxima of intensity. This was performed for each layer, channel and sample, to give a set of 'Patch Maps'. Each patch thus represents a group of cells of the same colour.

Software was developed to allow for data collection from patches. Patch area and Cell Density were tabulated for each patch. The method for estimation of cell density is described in Appendix A.8.1, and in brief relies upon using the average cell volume and tabulating the total number of occupied voxels within the patch. These values were then presented with R [R Core Team, 2013].

Furthermore, a means of visualising the density of patches themselves was developed, described in detail in Appendix A.8. This represents the number of patches within an area as a colour, allowing for the interpretation of how patches are organised in different layers.

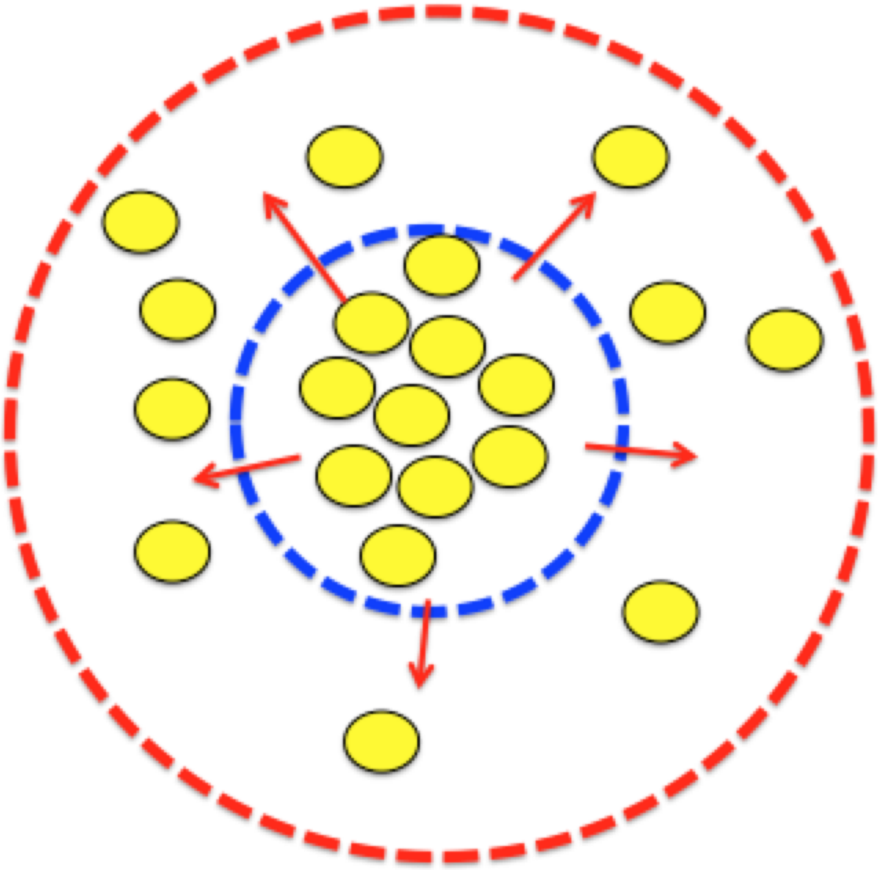

Figure 9.1: Conceptual basis of lateral spread leading to cell density loss The blue and red circles contain the same number of cells. Lateral spread is occurring from the centre of the blue circle (red arrows). The red circle has a far greater area, resulting in a far lower density.

9.3 Results

9.3.1 Early Confetti Labelling is Very Mixed

Figure 9.2 shows the nascent frontal bone at E14.5, before the development of a true layer 2. Layers 1 and 3 are present as sinuous flattened layers, with little colour consistency and no apparent communication of cells between the two layers. This demonstrates the starting condition for the development of patterns in the Confetti labelled calvaria. Organisation that evolves from this must be dependent on cell proliferation, invasion and migration.

9.3.2 Watershedding of blur maps reveals cryptic presumptively clonal patches

An example of a small region of patch watershed segmentation is shown in Figure 9.3. The green GFP-labelled cells of 9.3A can be blurred to give the blur map of 9.3B, which can be segmented by watershedding. The boundaries produced group the original cells into groups based on diminishing density towards their periphery. This demonstrates the general principle of the Patch Maps.

9.3.3 Example Patch Maps show organisation within the Bone, and a generally homogenous morphology

The full set of Yellow cell patch maps is displayed in Figures 9.4-9.9, which are broadly representative of the maps of all cell colours, though differences shall be discussed in later Chapters. Remarkably, there is very little visual difference between each layer, suggesting that vertical invasion perhaps synchronises growth across all three layers, which is explored in Chapter 10.

Most patches are roughly circular or rectangular. There is certainly no linear patterning of patches around sutures. This suggests that local spreading of cells in a non-directional fashion, as illustrated in 9.1 is the principal mode of cellular spread, and not linear growth from fronts.

Yellow patches do not appear to observe sutures. This topic is explored in detail in Chapter 14. There may be a degree of intermediate scale organisation, as many patches appear to align along cryptic boundaries that run for millimetres (Figures

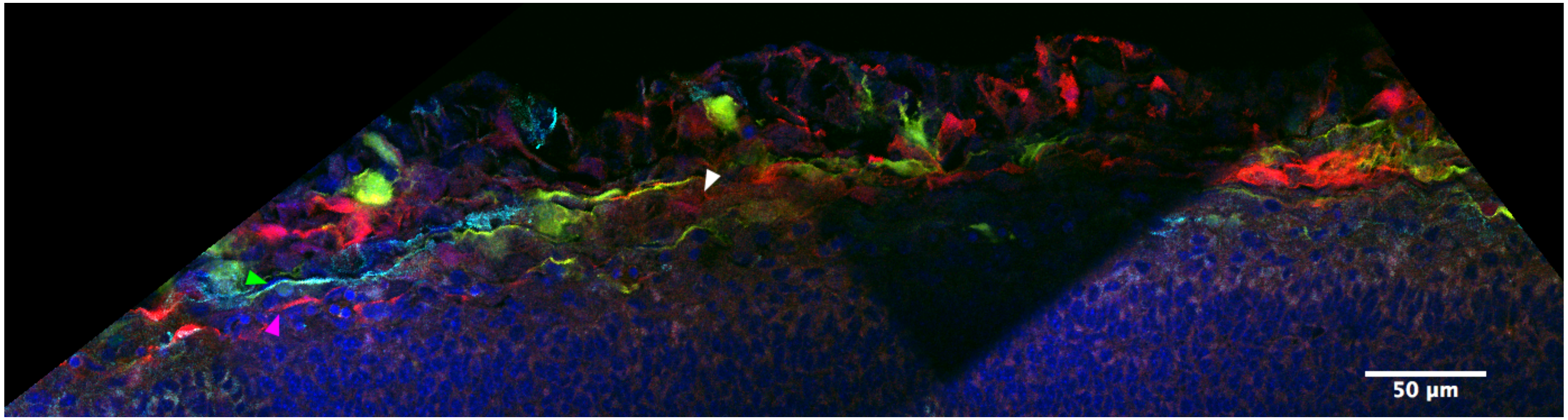

Figure 9.2: Wnt1 Confetti Labelling of the frontal bone at E14.5 At embryonic day 14.5 there is little apparent organisation of colour, with Layer 1 (green arrow) and Layer 2 (magenta arrow) having very few intervening labelled cells. The green and magenta arrows demonstrate a point where Layers 1 and 3 have entirely independent colours, while at places the two layers do match (white arrow). This indicates sporadic, random labelling with some contiguous expansion and little mixing.

9.4-9.9, between arrows of identical colour). This suggests a degree of developmental segregation above the level of individual patches, but below the level of the large bones. More importantly, there is no apparent gradient of patch size or orientation of patch shape towards or around patches. Therefore, there is no support for the suture model of growth in the patch map.

There is apparent long-range segregation of patches along cryptic lines, highlighted by arrows in the maps. Patches seem confined to certain regions with no apparent anatomical significance. This suggests an intermediate degree of cryptic modularity, between the level of the patches and the dermal bones themselves. This perhaps explains the appearance of the interfrontal bone in some animals and not others: it may only be present as a cryptic polyclonal boundary in some animals, and expressed as a genuine bone in others.

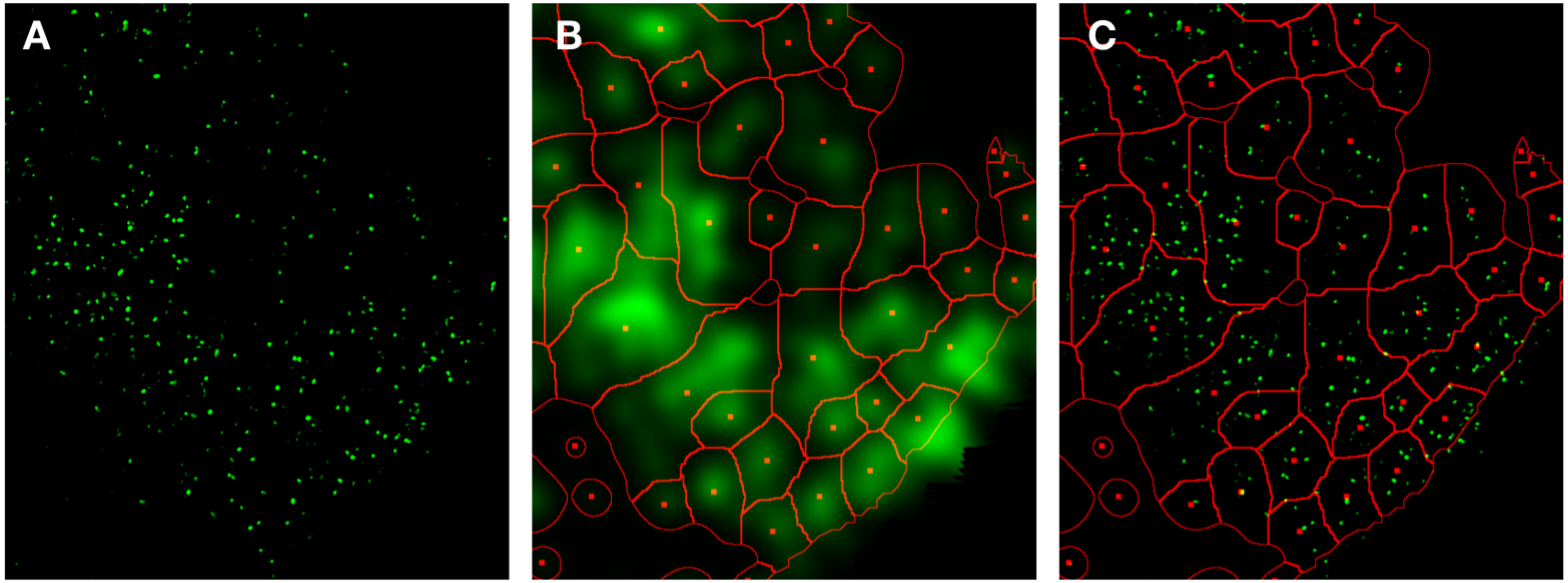

Figure 9.3: **Example of Patch Segmentation.** *Caption overleaf*

Figure 9.3: Example of Patch Segmentation. The green objects are GFP-labelled cells, while the patches that are identified within the population are shown in red. The lines represent the outer margins of each patch, and the red squares represent the geometric centroids. Outlined regions with no square are thus gaps between patches. **A:** A region of GFP labelled cells from the Frontal Bone of Sample A, Layer 1. This is a complex structure that is not easy for humans to interpret. **B:** The same region in the Colour Map reveals local maxima and minima of cell density, with clear demarkations that can be interpreted into patches. **C:** The patches overlaid with the cells gives context to what previously appeared to be a disorganised assortment.

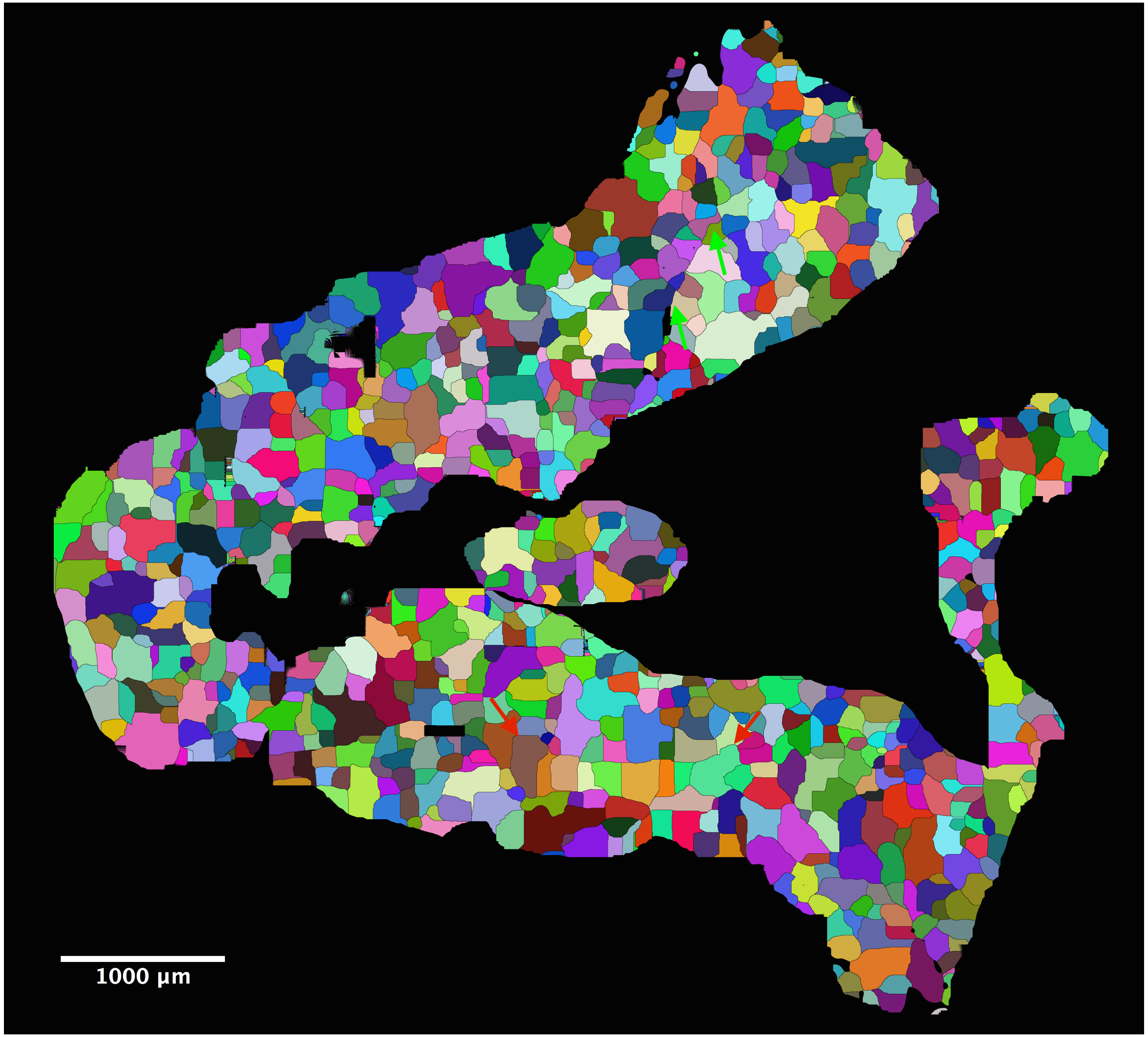

Figure 9.4: Yellow Patches In Layer 1 of Sample A *Caption on page 150*

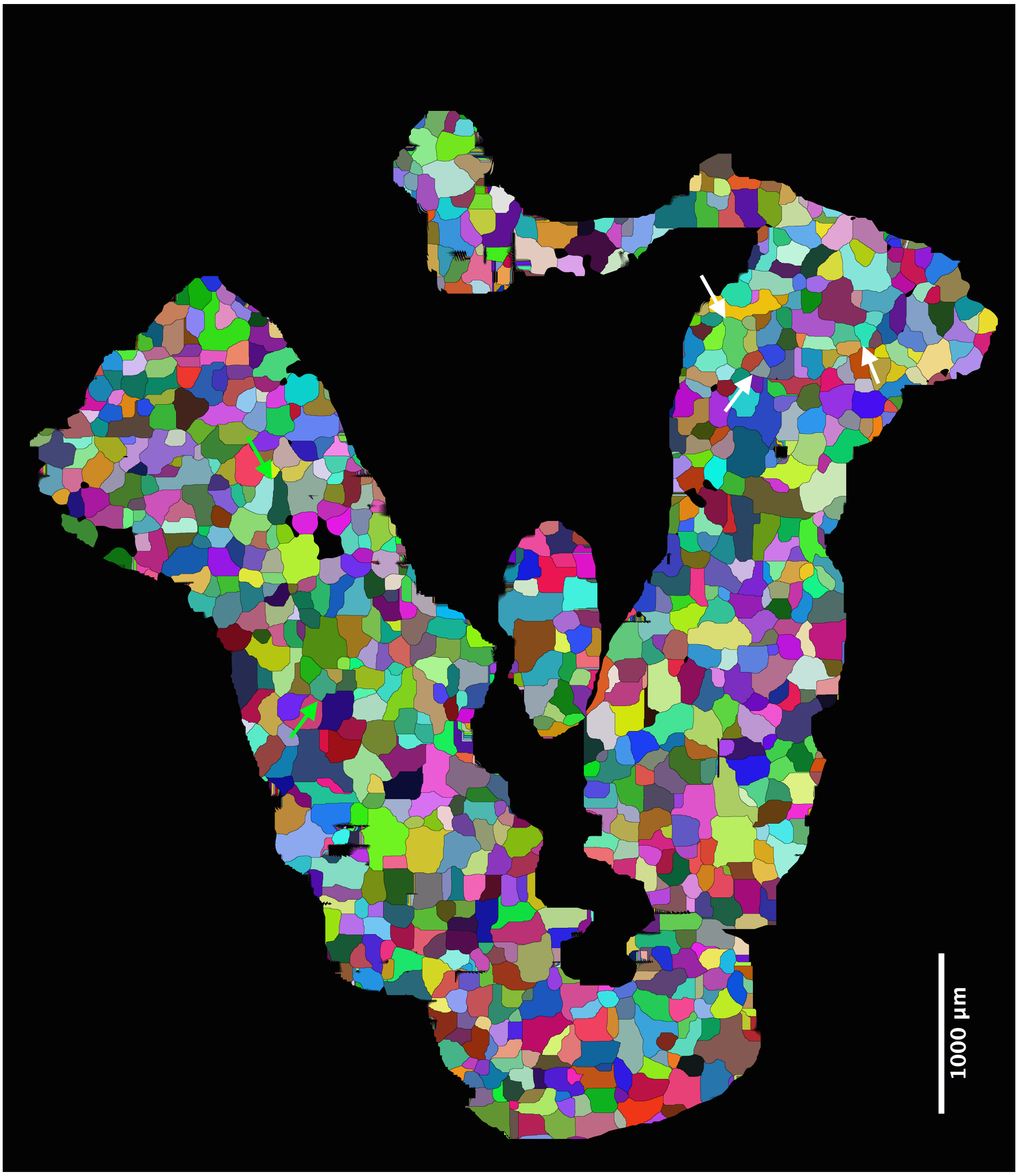

Figure 9.5: Yellow Patches In Layer 2 of Sample A *Caption on page 150*

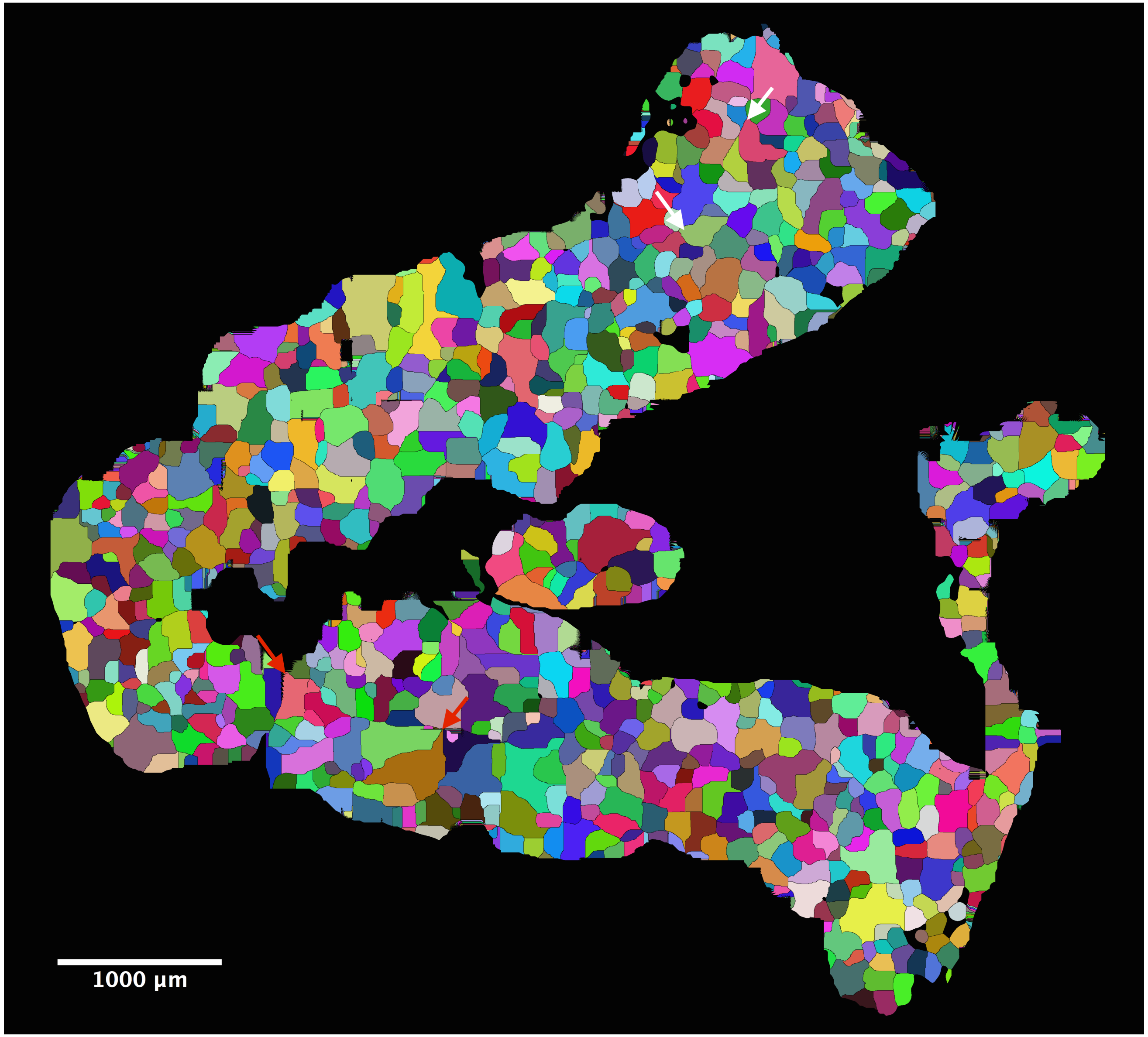

Figure 9.6: Yellow Patches In Layer 3 of Sample A *Caption on page 150*

Figures 9.4, 9.5 and 9.6: Yellow Patches of Sample A in Layers 1, 2 and 3 respectively. In each, the yellow cells appear to form roughly circular or rectangular patches. There is little apparent difference between each layer, suggesting a broadly homogenous distribution, though this is examined more quantitatively in Figures 9.10-9.12 and Figures 9.16-9.17. There is no apparent organisation around sutures, neither in the appearance of patches near where sutures are found, nor in terms of the general population's arrangement. There do appear to be long-range boundaries that are defined by aligned borders of patches over large distances, shown between arrow points of different colours, representing cooperative segregation of patches into different cryptic regions.

Figure 9.7, 9.8 and 9.9: Yellow Patchesof Sample B, in Layers 1, 2 and 3 respectively. As in Sample A, patches have a similar predominantly circular or square appearance. There is again no apparent gradient or organisation relative to sutures, which are effectively invisible (see Figure 8.2). There are however apparent long-range lines of patch segregation as in Sample A, again shown between two arrows of the same colour.

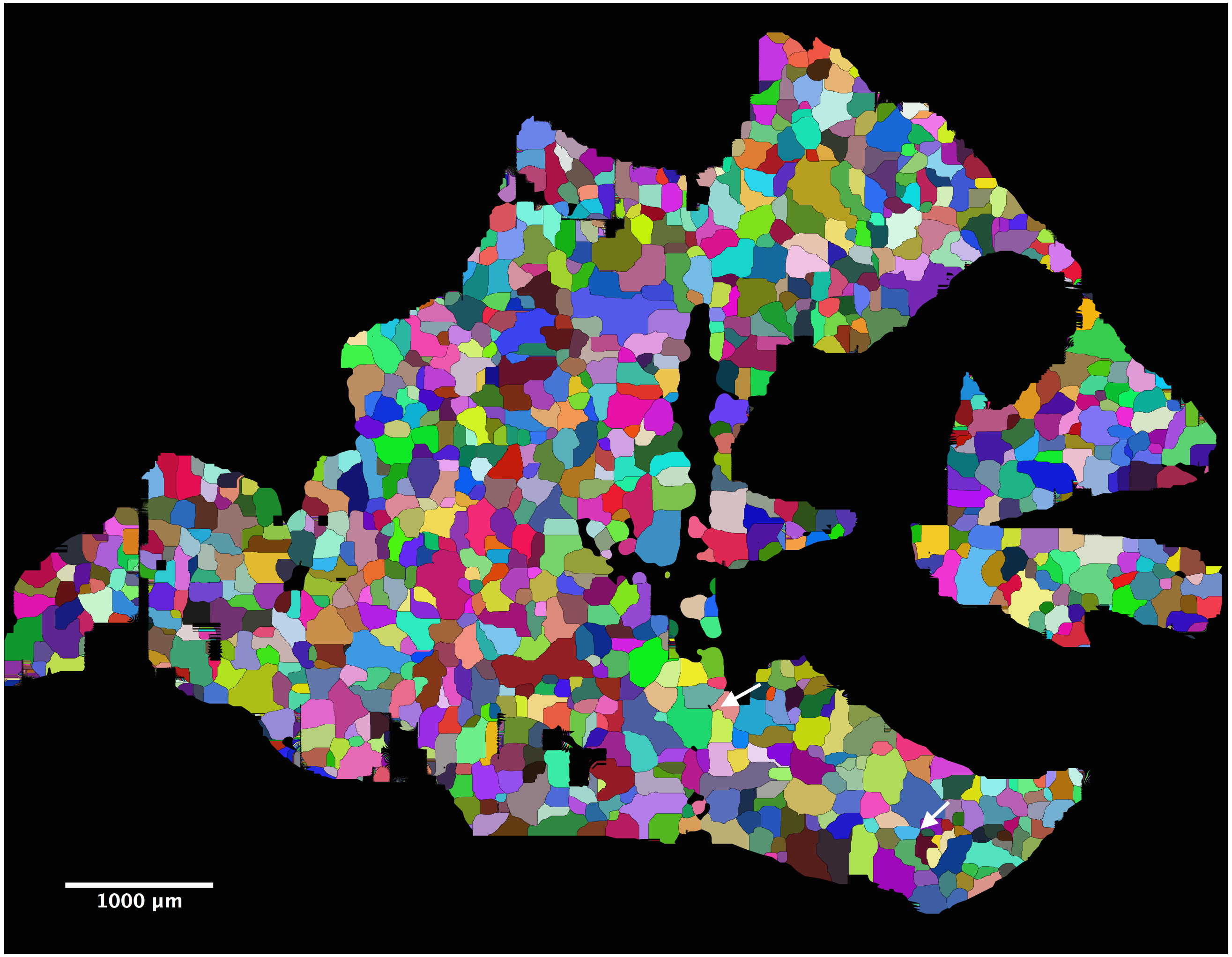

Figure 9.7: Yellow Patches In Layer 1 of Sample B *Caption on page 150*

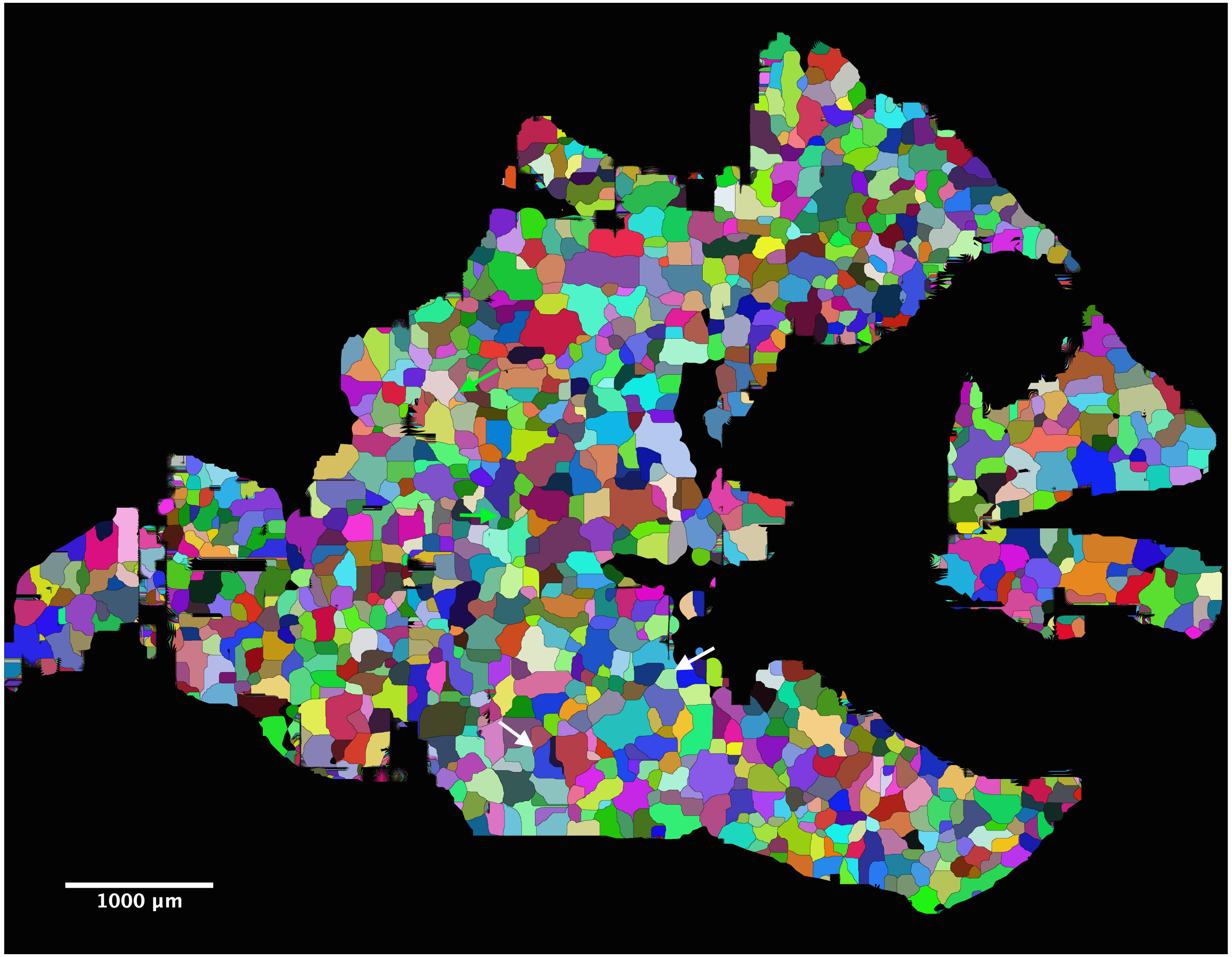

Figure 9.8: Yellow Patches In Layer 2 of Sample B *Caption on page 150*

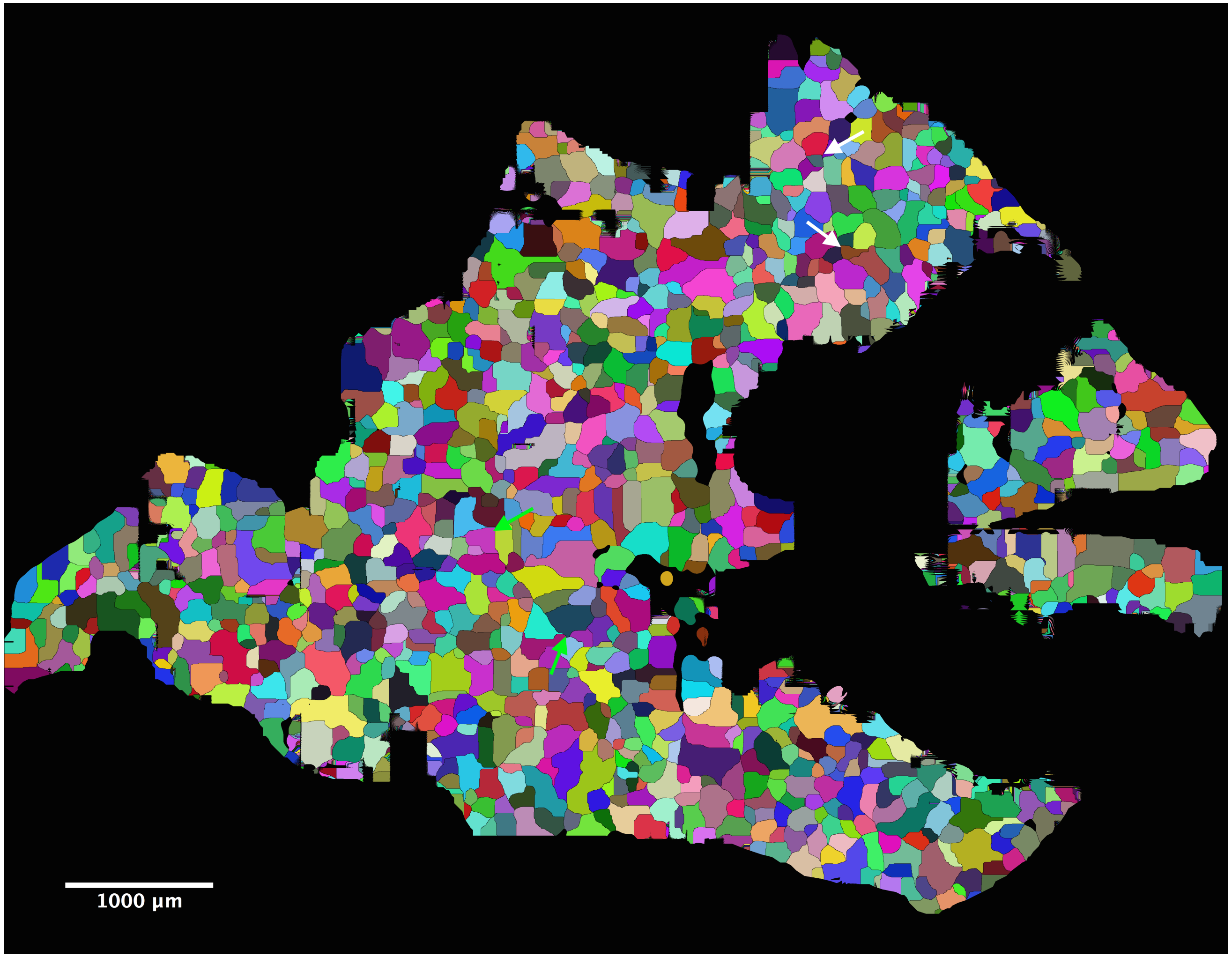

Figure 9.9: Yellow Patches In Layer 3 of Sample B *Caption on page 150*

9.3.4 Patch Density maps reveal differences between layers

Figures 9.10-9.15 show the geometric density of patches of any colour within a circle of area 1.79 mm^2. Layer 1 shows remarkable homogeneity, suggesting fairly uniform patch distribution regardless of position. It is notably the most dense layer within the interfrontal bone. Layer 2 has maxima close to sutures, and above the eye which is a muscle attachment region. Layer 3 has the most patches in the posterior frontal bone, where the bone is also the thinnest (Figs. 12.1 and 12.2). This suggests that each layer behaves slightly differently in different stages of bone development.

These observations contradict the initial assessment of homogeneity described above. This demonstrates the importance of approaching this data with novel quantitative tools, as this reveals aspects of development that are hard to perceive independently.

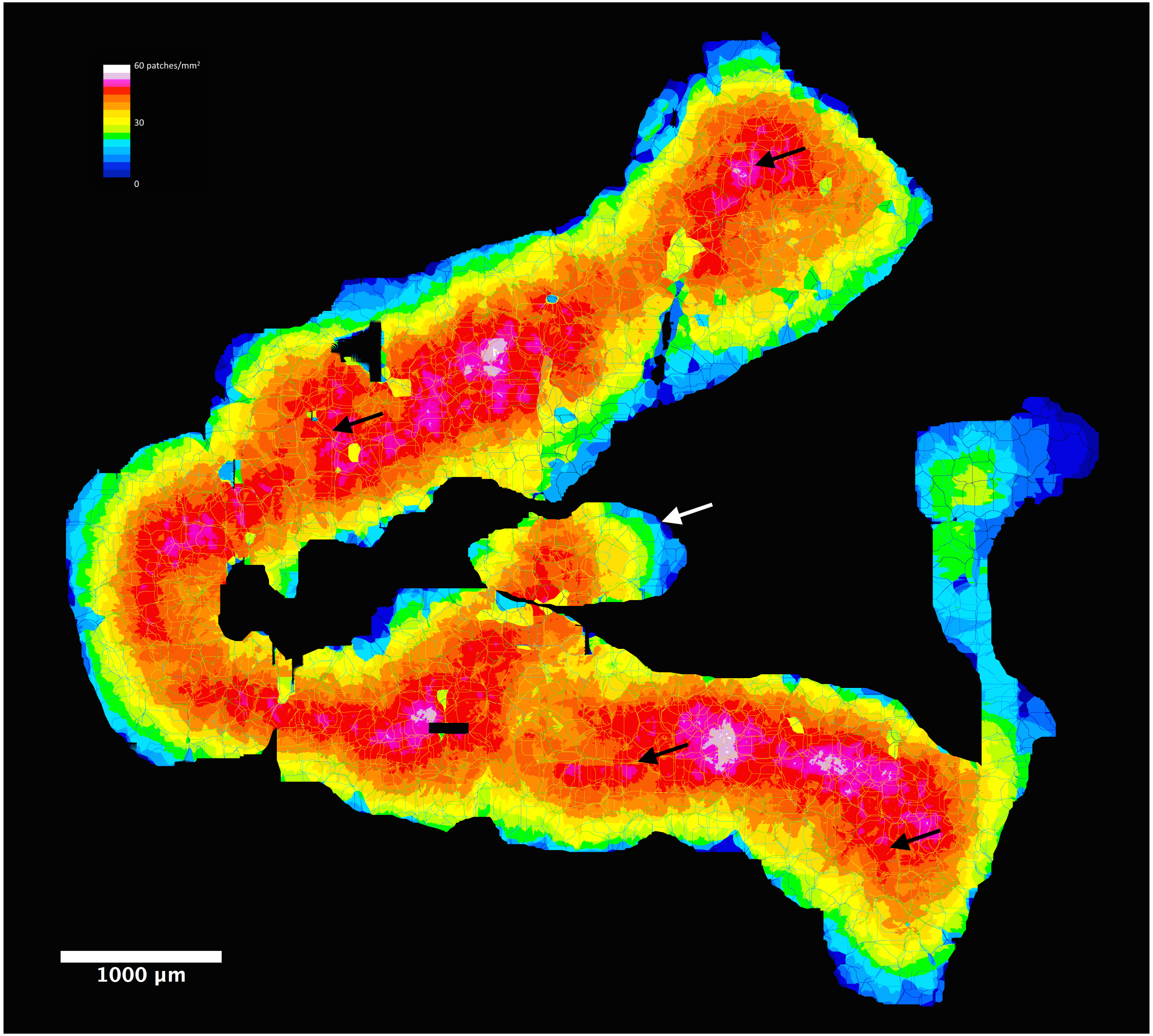

Figure 9.10: Density of Patches in Layer 1 of Sample A. *Caption on page 158*

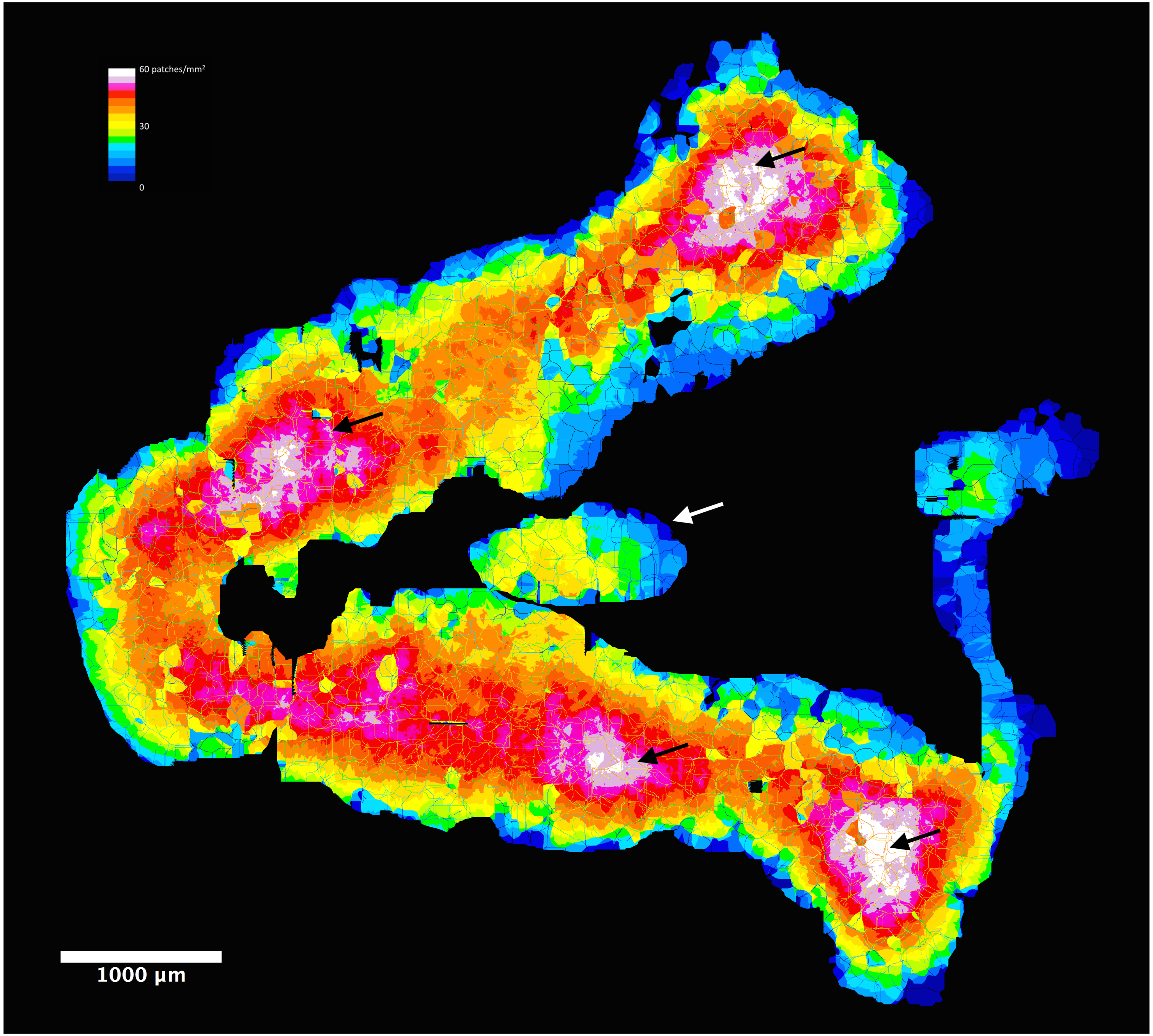

Figure 9.11: Density of Patches in Layer 2 of Sample A. *Caption on page 158*

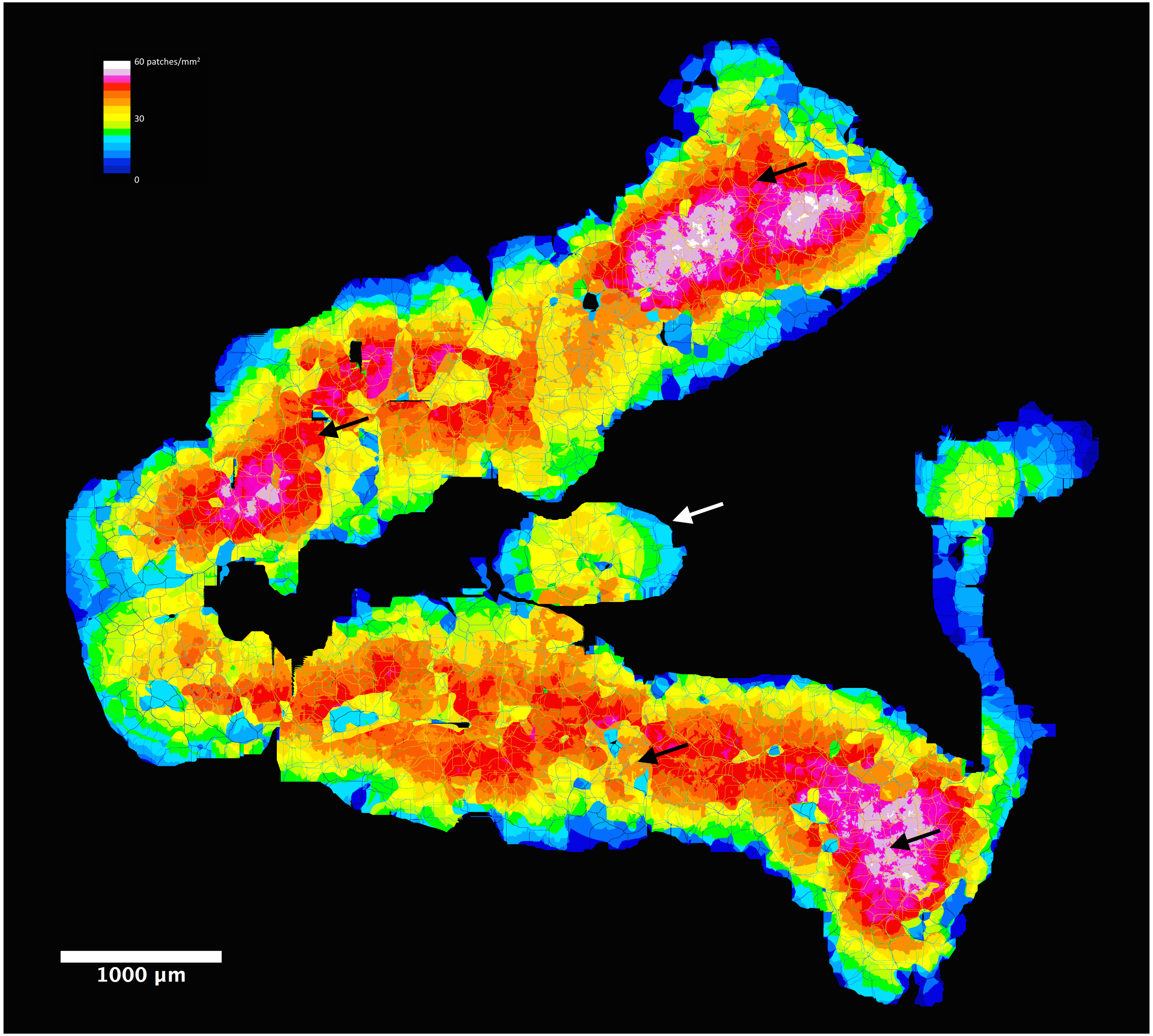

Figure 9.12: **Density of Patches in Layer 3 of Sample A.** *Caption on page 158*

Figure 9.10, 9.11 and 9.12: Yellow Patches of Sample A in Layers 1, 2 and 3 respectively. Density of all patches within of Sample A as evaluated by overlap with a circle of 1.79 mm^2. While Layers 2 and 3 have more patches concentrated in certain points (black arrows), Layer 1 is relatively homogenous, without such conspicuous condensations of density. It is notable that the interfrontal bone (white arrow) appears as a microcosm of pattern the larger bones, suggesting that it is enacting the same developmental program on a smaller scale.

Figure 9.13, 9.14 and 9.15: Yellow Patches of Sample B in Layers 1, 2 and 3 respectively. Density of all patches within of Sample B as evaluated by overlap with a circle of 1.79 mm^2. Layer 1 does have some greater foci of patch density in this Sample, though not as extensively as in Layer 2. Across both samples it is notable how there is actually a heterogeneity, though this does not appear to spatially conform to sutures. Again the interfrontal bone (black arrow) appears as a microcosm of the larger pattern, with increased patch density at the centre and diminished density at the edges, even where intersecting with other bones.

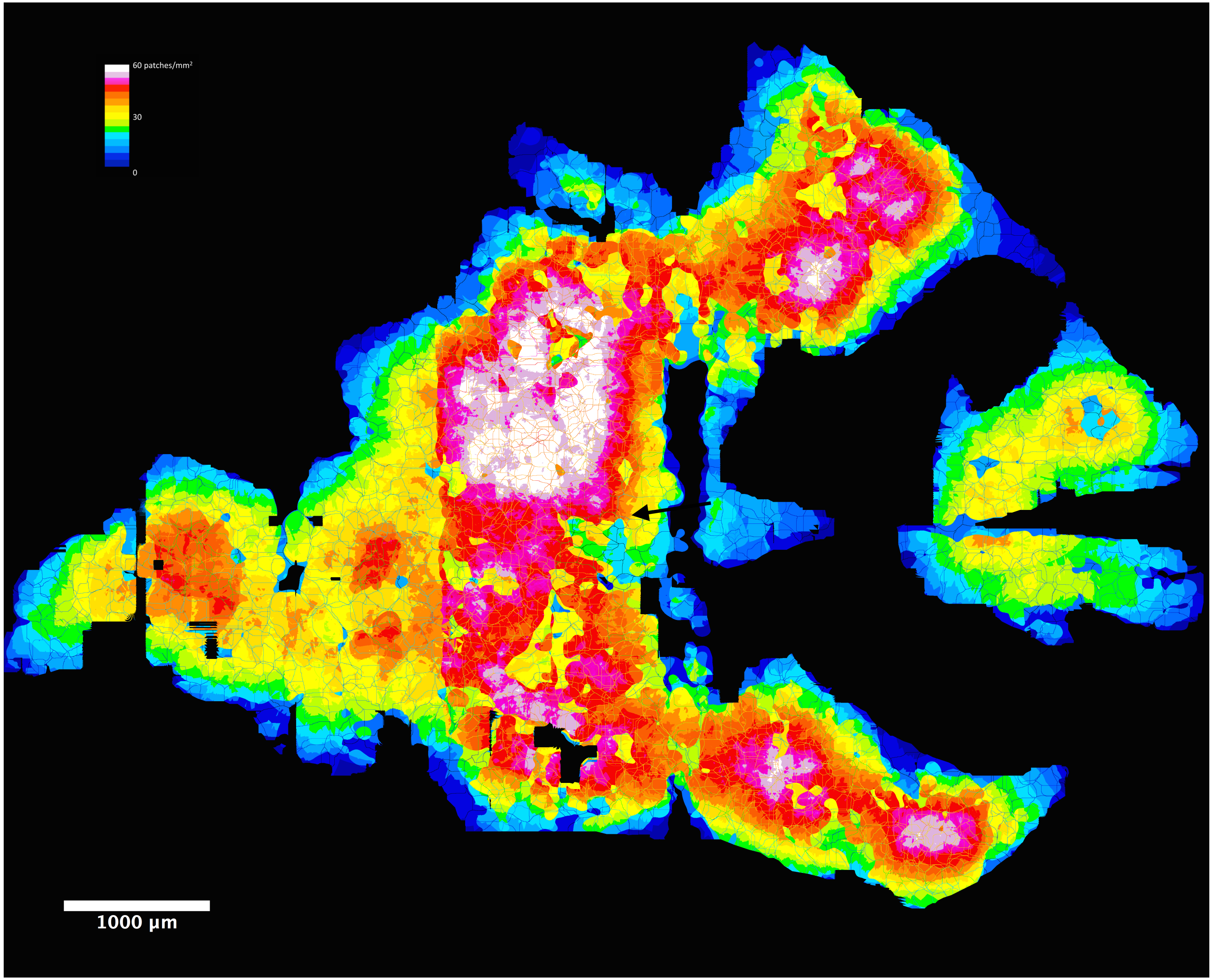

Figure 9.13: Density of Patches in Layer 1 of Sample B. *Caption on page 158*

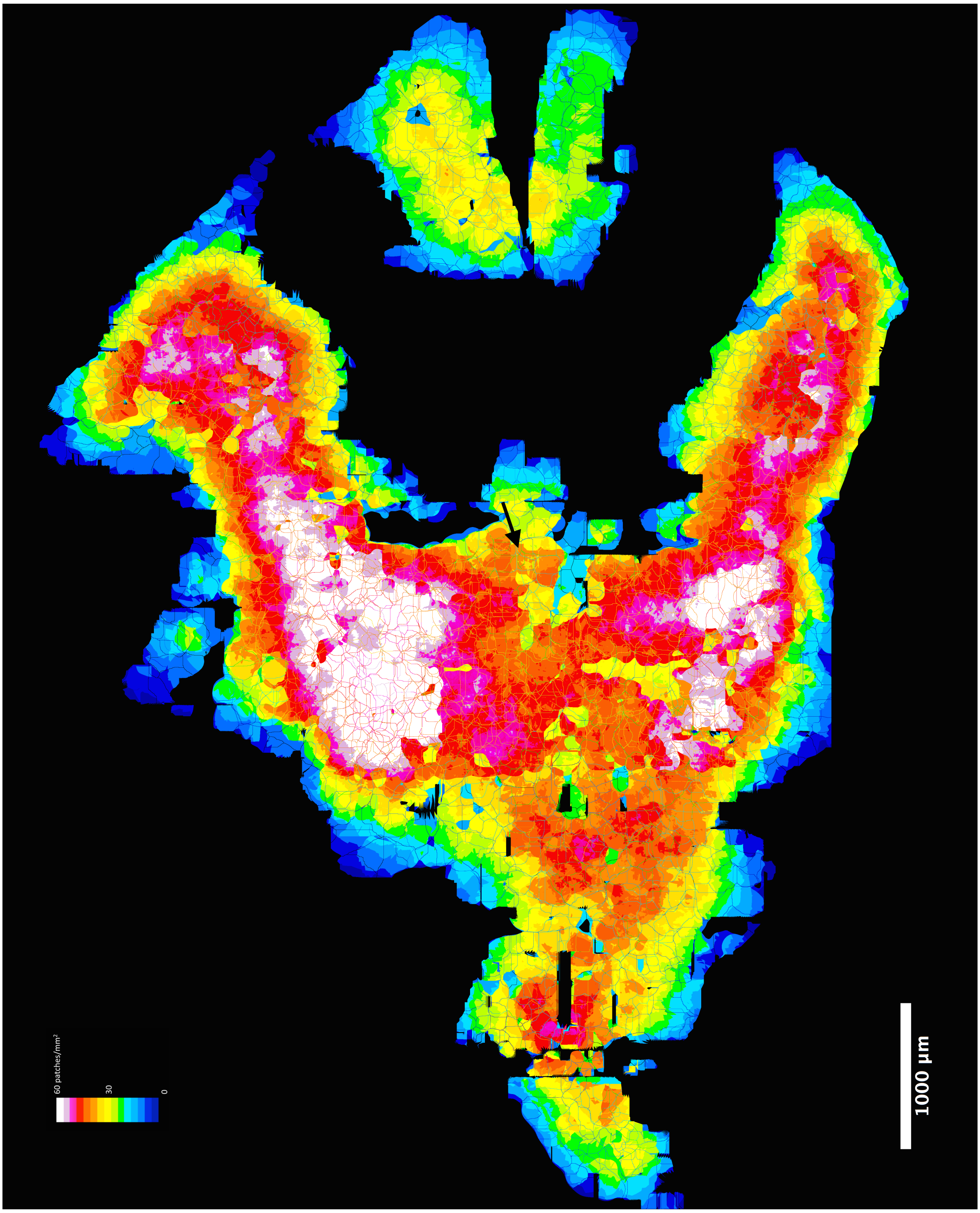

Figure 9.14: Density of Patches in Layer 2 of Sample B. *Caption on page 158*

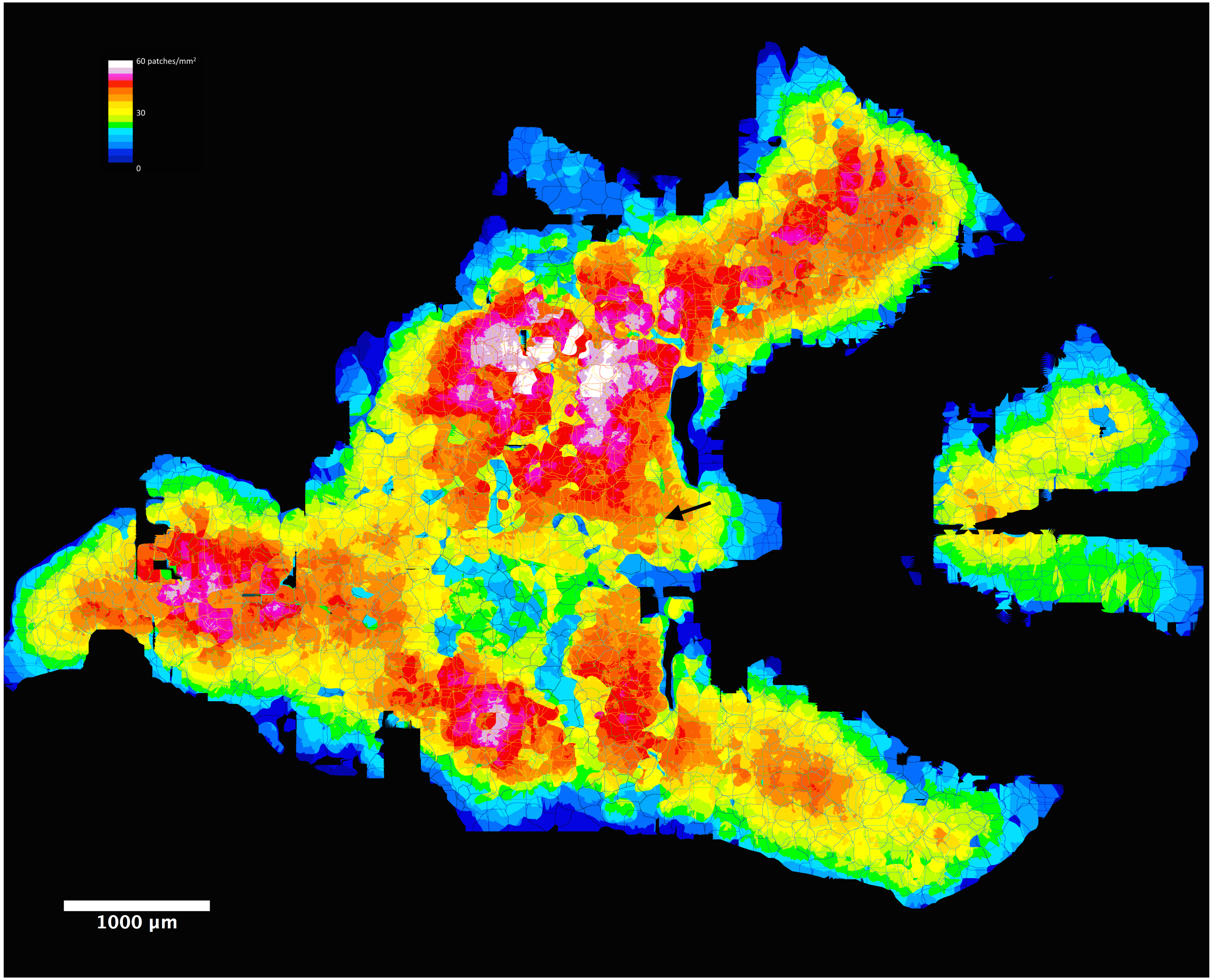

Figure 9.15: Density of Patches in Layer 3 of Sample B. *Caption on page 158*

9.3.5 Patch area is relatively constant between Layers and Samples, while Cell Density distribution varies across layers.

Area is broadly consistent between each Layer and sample, averaging just over 20,000μm ^{2} (Figure 9.16). Layer 1 Patches are indeed slightly larger in Sample B than all other sets, though this could be due to some erroneously large ‘false negatives’ where several patches are read as one. Regardless, the actual magnitude of this statistically detectable difference is small within the range of patch sizes. This implies that horizontal spread is largely equal across layers and patches, and furthermore suggests that some process integrates patches across layers, preserving their extents within a small range.

Conversely, there are strong differences between the layers and between the samples with respect to distribution of cell density (Figure 9.17). Note that this plot represents normalised density within each layer. This does not imply that Layer 1 is distinctly more dense than Layer 2, as such absolute comparisons can only be made within a single colour, which is analysed in greater depth in Chapter 12. What this does imply is that the majority of Layer 1 patches are closer to the peak density of Layer 1 than the other Layers, while Layer 3 is largely a lot more cell-diffuse and contains a small minority of very cell-dense patches. Layer 2 is intermediate between the two, which may imply that an early Layer 2 is quite homogenously cell dense like Layer 1, becoming progressively less cell dense as development of cell-sparse matrix progresses.

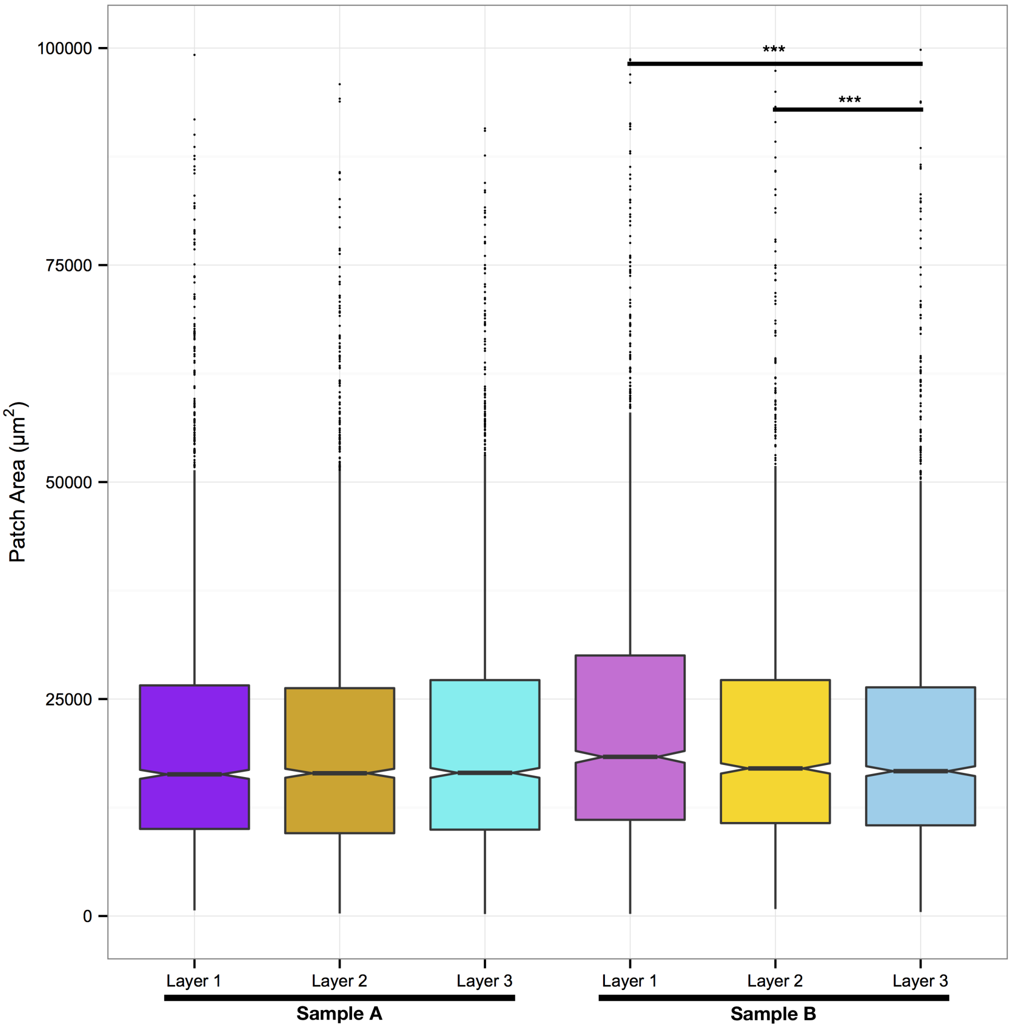

Figure 9.16: Patch Area is broadly consistent across all Layers and Samples. In each Layer and Sample, there is little difference in the distribution of Patch Areas. The only exception to this is that within Sample B Layer 1 Patches are slightly larger than the other layers, though this statistically significant differenceis not a large difference in magnitude. This demonstrates that Patch horizontal extent is organised across all three layers. $***p\leqslant0.001$, $**p\leqslant0.01$, $*p\leqslant0.05$, Student's T-Test.

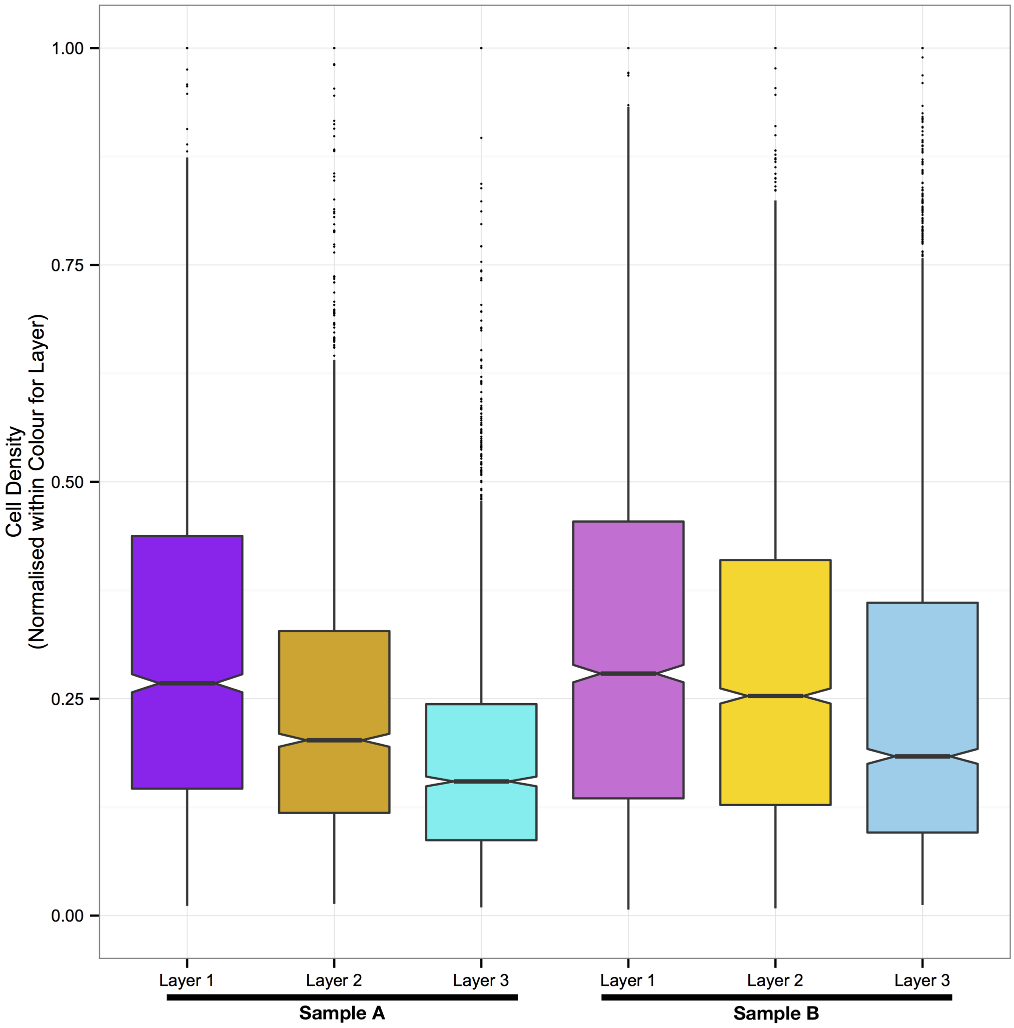

Figure 9.17: Layer 3 has very few dense patches, Layer 2 has more, and Layer 1 has the most Each boxplots represents the distribution of normalised cell density, and thus only differences of distribution within the layer. More patches in Layer 1 are closest to the most dense regions of Layer 1, while Layer 3 has a number of patches that are far more cell-dense than the generally more diffuse majority. Layer 2 represents an intermediate between the two in both samples. While not shown in the diagram due to clarity, all boxes are statistically significantly different from one another, $p \leqslant 0.05$, Student's T-Test.

9.4 Summary: Potential Cryptic Modules revealed by mapping Horizontal Presumptive Clonal Spread

In this chapter I set out to map the extent of single clones. The traditional sutural model would suggest that clones radiate out from sutures in some manner. Instead, I have demonstrated that presumptive clones adopt a patch-like arrangement, consistent with simple clonal expansion at all points of the bone. These expansions are further coordinated across all layers in a manner that is consistent between samples (Figure 9.16) while one measurable characteristic of the tissue, the cell density, varies based on layer in a predictable fashion 9.17.

The immediately striking feature of these patches is the degree to which they resemble both the tesserae of primitive heterostracan fish like Drepanaspis (Figure 9.18), and the condition of the skulls in those afflicted with osteogenesis imperfecta 9.19, wherein the skull is entirely comprised of small ectopic bones known as Wormian bones. Both of these observations have deep consequences for evolution and development, implying the persistence of tesserae as cryptic developmental modules within even large dermal bones, as well as suggesting an underlying mechanism of tesserae development as a consequence of laterally spreading polyclones. The degree to which these patches correspond with other aspects of bone development, such as thickness growth and cell invasion, will be explored in later Chapters to ascertain their role in bone development.

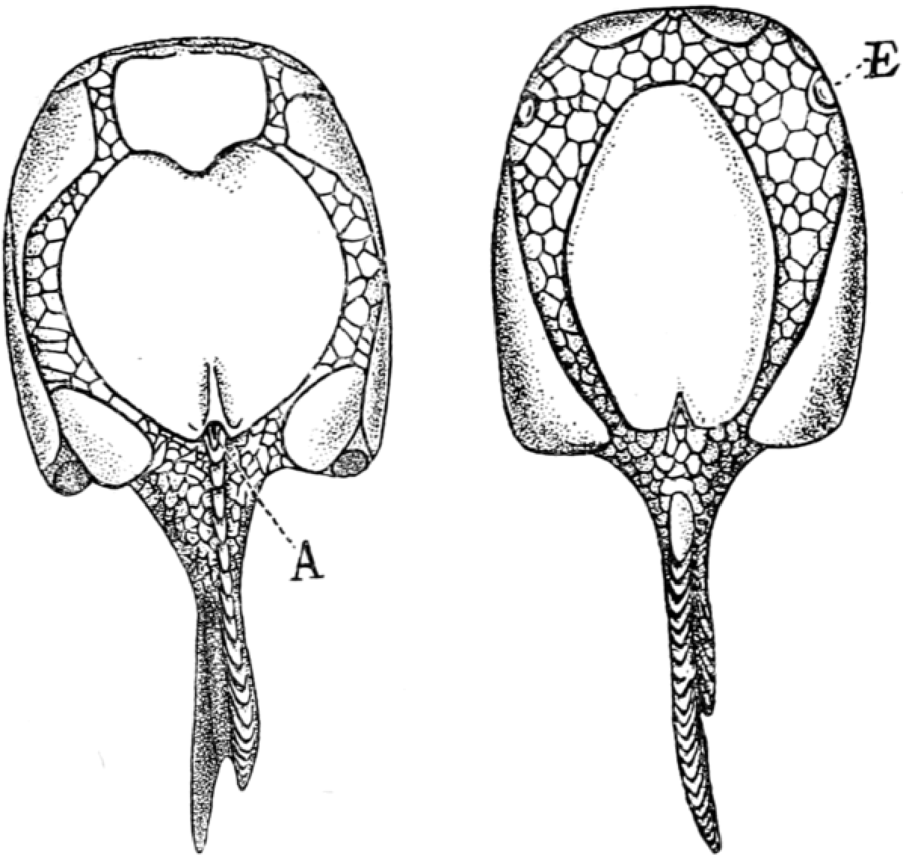

Figure 9.18: *Drepanaspis* **sp. have patch like bony tiles between large plates.** *Drepanaspis* represents a very early The presence of these small plates, known as tesserae in between large bones suggests that small bony tiles represent a primitive condition of dermal bone development. From Gaskell [1908], public domain. A - anus, E - eye.

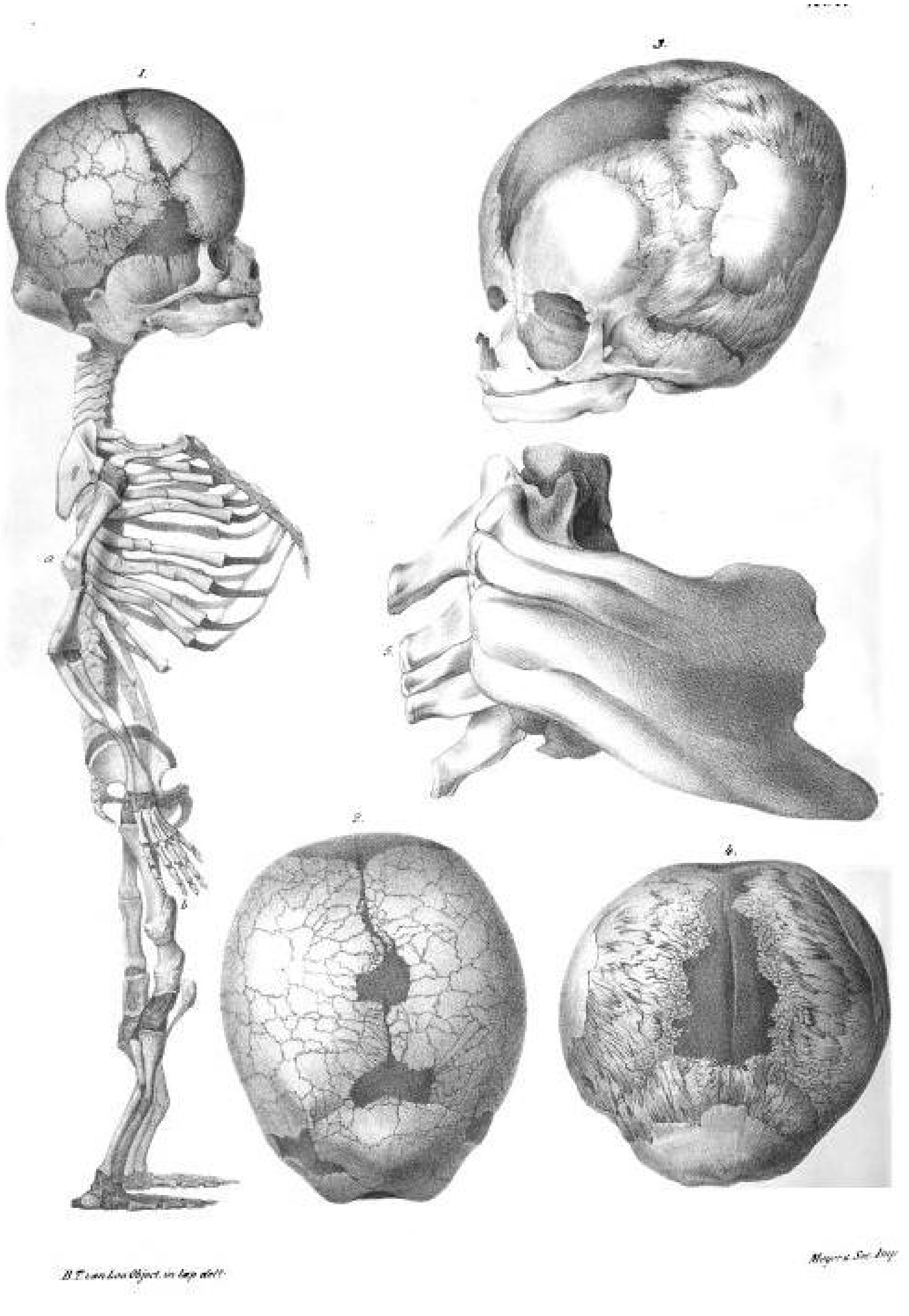

Figure 9.19: The extreme Wormian bone condition in Osteogenesis Imperfecta. Huge numbers of Wormian bones are visible in this individual, in a manner that is highly reminiscent of patches. In parts of the skull larger bones are visible, showing that this condition arises as a result of local dynamics and not as an unavoidable consequence of a global genetic mutation. From Vrolik [1849].

Chapter 10

Mapping Vertical Invasion between the Layers of the Calvaria

10.1 Introduction

The general approach to genetic lineage analysis in the past has been limited to either single cells [Livet et al., 2007] or to studies of groups of effectively static unmixed patches [Snippert et al., 2010; Rinkevich et al., 2011; Schepers et al., 2012]. Dynamic systems that undergo significant mixture and migration create problems for casual analysis and to date there are no tools to easily extricate information from these mixed lineages.

While the PCA based approach described in Chapter 5 is useful for small-scale observations, it is inappropriate on a large scale. PCA interprets variation, and thus assumes that important differences will occur along the same axes of variation. This is not the case in a random lineage labelling, and thus it can only be of use in classifying a few different mixtures of cells. However, the principle of mapping points into a new 'colour space' is valuable, and can form the basis of a new suite of analysis tools and approaches.

The method developed utilises a multi-dimensional distance approach to give a measure of how similar two populations are, which can then be considered relative to other populations. This was used to quantify the similarity of the three layers of bone across the span of the samples. The resulting maps have certain features that give insight to possibly important cross-layer structures and relationships. These can be tabulated against Layer 2 thickness to give insight to the developmental milestones outlined in summary of the previous chapter, and compared to other anatomical features as explored in later chapters. While this study examines only the four colours arising from the Confetti construct, the general approach is applicable to an arbitrary number of distinguishable reporters, and the software developed to enact these procedures can handle any number of markers.

10.2 Method

Invasion between layers communicates the mixture of cell colours between layers, as material of one polyclonal mixture is transferred vertically into a new layer. Therefore the mixture of cells in overlying points in different layers can be compared to estimate whether invasion may have taken place at this point. The technicalities of this method are presented in Appendix A.9, and discussed in broader terms here.

The aim of this approach is to generate a metric wherein a larger numerical result on an arbitrary scale denotes similarity of polyclonal mixture and a low numerical result denotes either dissimilarity of present cells, or absence of cells. Blur maps of each layer are compared, as each point of a Blur Map (described in Chapter 8) contains the density of each cell colour in the local area around that point, and thus also contains the polyclonal mixture identity of the surrounding population. Comparison of the same point in maps of pairs of different layers thus gives a relative value of 'colour similarity'. A cartoon of this process is shown in Figure 10.1.

The actual metric of comparison is based upon the same principles as PCA in the last Part, in that colour is used as four-dimensional space. However, to attempt to work out the greatest axis of variation as in PCA is useless in such a large sample, as so many different independent polyclonal mixtures exist that the global 'colour space' is saturated and uninterpretable. Rather, the relative euclidean distance between two points of the sample mapped into this colour space are used as a measure of their similarity.

The use of relative euclidean distance can be validated by stepwise approach to the four colours of Confetti. If one were to compare three sets of cells of different size but all of the same colour, one could say that the most similar two sets were those of nearest abundance: a simple numerical difference, or more pedantically a one-dimensional euclidian distance. If however two scales were present, and one were attempting to compare three sets of cells with different mixtures of two colours (say, red and green), then simple difference would not be possible. Rather, both scales could be considered: both the difference in the abundance of red cells and the

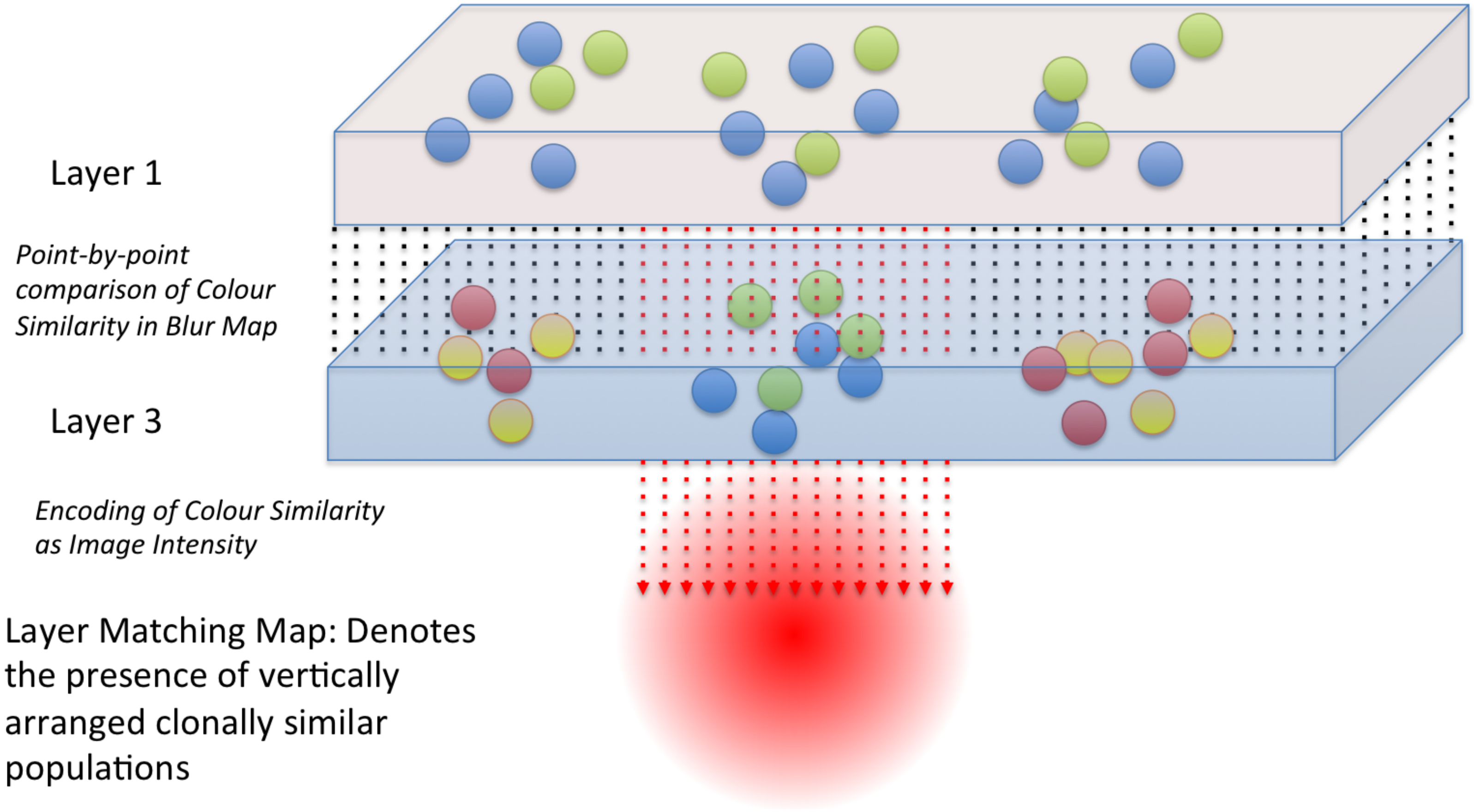

Figure 10.1: Similar polyclonal combinations can be encoded as an image intensity in a Layer Matching Map. In this example, the blue and green cells that make up Layer 1 have an obvious match to a small patch of blue and green cells of near-equal proportions in the underlying Layer 3, which are surrounded by non-similar red and yellow cells. By comparing the similarity of each point in either layer (using the Blur Map to convolve regional colour identity into single points) this matching can be observed, and translated into a spatial map of combinatorial colour similarity.

difference in the abundance of green cells. This defines a two-dimensional colour space, in which the relative distance between different sets can be compared, simply by using Pythagoras' theorem to calculate two-dimensional euclidian distance. As Pythagoras' theorem can be generalised to any number of dimensions [Yeng et al., 1990], this principle can be extended directly into the four dimensional colour space defined by Confetti.

It is self-evident a lesser difference in polyclonal colour combination would thus be encoded as a smaller difference. This is non-optimal, as it is similarity which should be highlighted and not dissimilarity. For this reason, the resulting value is inverted. This metric produces an impression of sharp, distinctive patterns when mapped out. This is termed the 'non-density encoded' metric. However it also gives high values for areas with few or no cells, as two points that share an absence of cells are indeed similar. For this reason, a further metric was developed that convolved the total cell density (*i.e.* image intensity across all four colour channels) to give the 'density encoded' metric. The patterns of the former metric are still present, though less distinct. For this reason the non-density metric is used to demonstrate patterns, while the density-encoded metric is used for more strict analytical purposes.

This process can be performed for every corresponding pixel in a pair of Blur maps and the values encoded as pixel intensity of 'Matching Map'. This process was performed for each pair of Layers in both samples. The different pairwise comparisons were encoded as different colours: red represents the similarity of Layers 1 and 3, Green the similarity of Layers 1 and 2 and Blue the similarity of Layers 2 and 3, as summarised in Figure 10.3. This colour code is used throughout this thesis.

This represents an entirely novel approach to the interpretation of mixed lineage samples. Through use of 'Layer Matching' and 'Colour Similarity' the likely sites of invasion can be revealed, and identified relative to other characteristics of the bone, such as distance from sutures and degree of bone development.

The more traditional sections of Wnt1-Confetti tissue shown in Figures 10.4 and 10.5 were sectioned and fixed, as described in Appendix A.2.

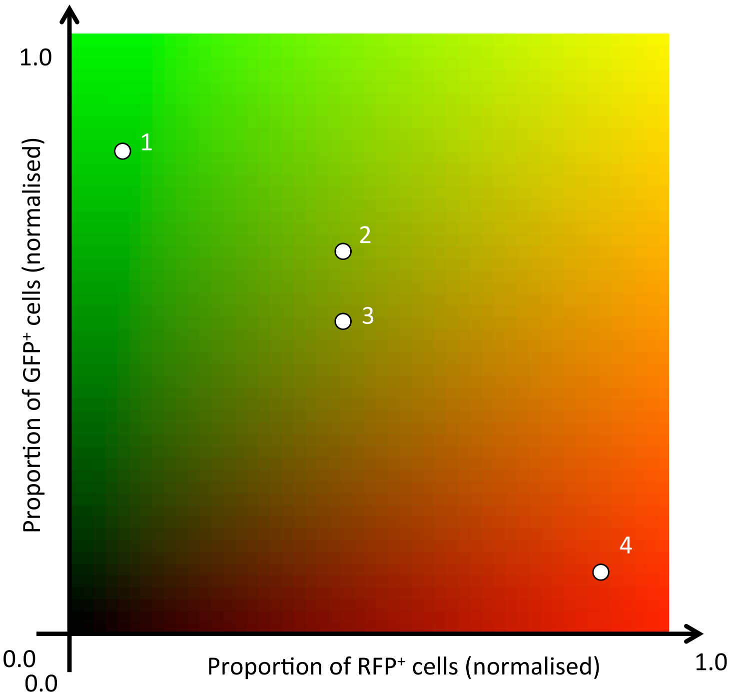

Figure 10.2: The Principle of 'Colour Distance'
A: Four different hypothetical populations of cells plotted relative to their proportions of GFP and RFP cells. Intuitively, populations 2 and 3 can be considered to be the most similar pair, as they are closest on the graph. Furthermore, 2 and 3 are both closer to 1 than to 4. These distances can be quantified with Pythagoras' Theorem. This principle holds true regardless of the number of colours (*i.e.* dimensions) used, with distance calculated by the n-dimensional generalisation of Pythagoras' Theorem.

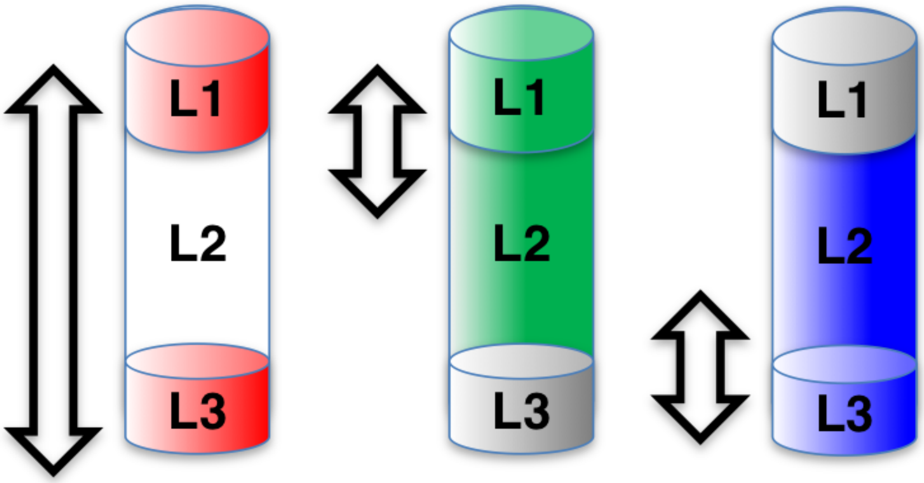

Figure 10.3: Colour Encoding of Layer Matching For the purposes of all upcoming applications, a unified colour scheme is used to denote Layer Matching between pairs of Layers. Red is used to denote the degree of colour matching between Layers 1 and 3, Green similarity between Layers 1 and 2 and Blue similarity between Layers 2 and 3.

10.3 Results

10.3.1 Invasion is polyclonal and can occur at specific points

Figures 10.4 and 10.5 show a sagittal section through an E18.5 Wnt1-Confetti frontal bone. There are numerous apparent points of invasion, which appear to spread polyclonal identity outwards. These are furthermore polyclonal, suggesting that one must consider the mixed population of Confetti labelled cells when interpreting invasion between layers.

10.3.2 Layer Matching Maps

The Layer matching maps for each sample are displayed in Figures 10.6 to 10.9. Immediately it is evident that layer matching is a hugely heterogenous characteristic across the bone, with organisation at the fine local level as well as the level of the bone. Repeated patterns of nested circles of matching and linear arrangements can be identified, which are discussed in the next subsections. These appear to

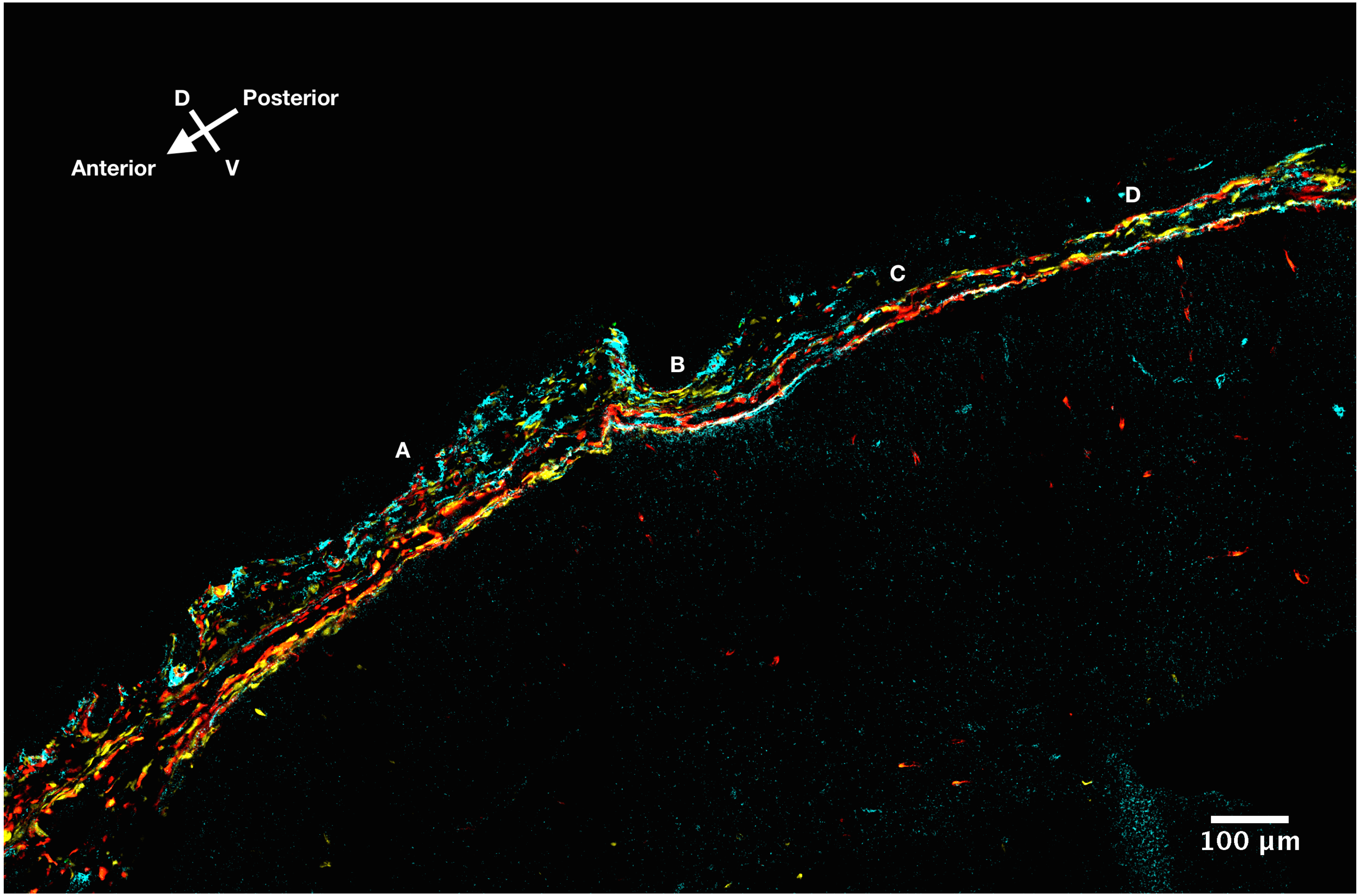

Figure 10.4: Sagittal section of an E18.5 Wnt1-Confetti frontal bone reveals vertically nested polyclonal invasions. Letters refer to the subfigures shown in Figure 10.5. The bone is clearly well mixed, but organised, with several points at which cells appear to bridge the two outer layers of the bone (letters). Imaging assisted by Dr. Chris Lagerholm, Wolfson Imaging Centre, Oxford.

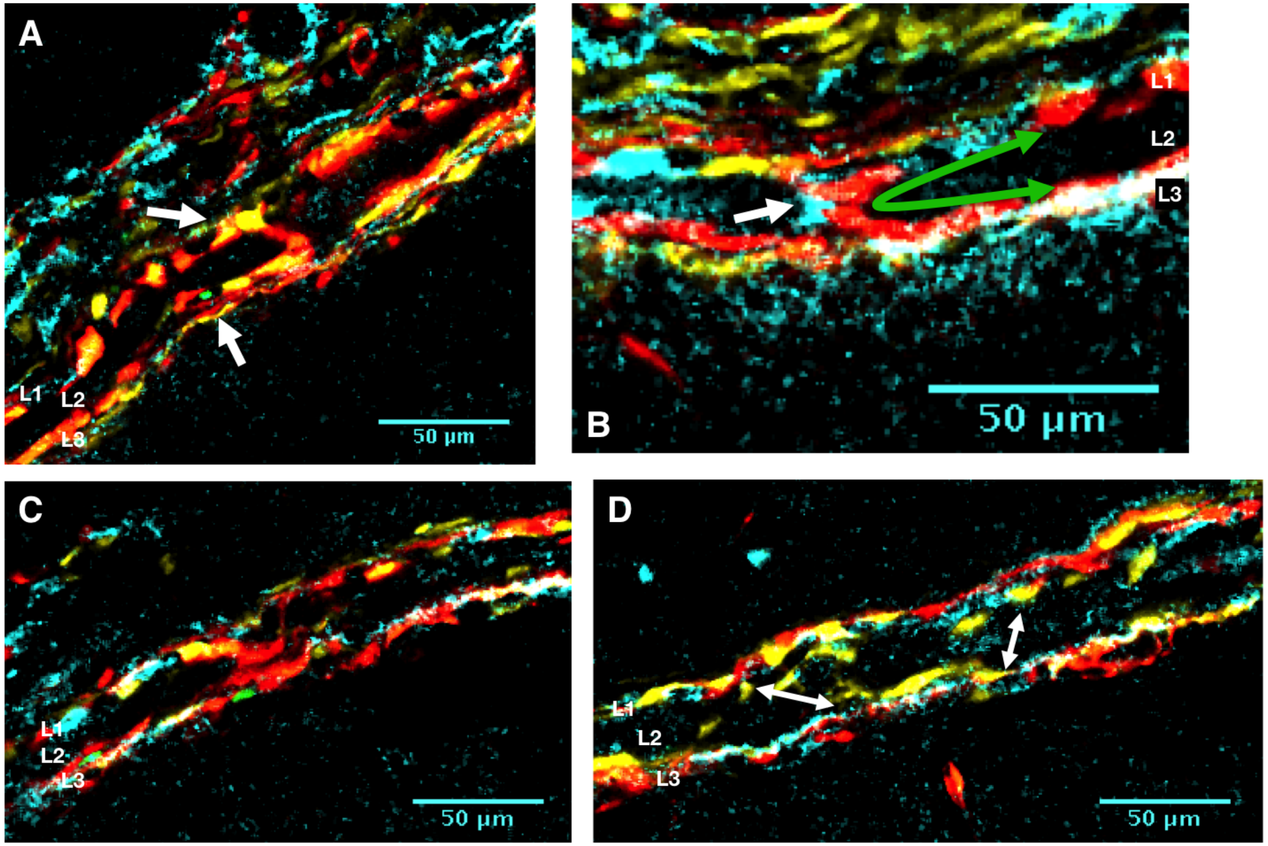

Figure 10.5: Individual nested polyclonal invasions in Wnt1-Confetti. Each subfigure is a region of 10.4. **A:** Successive invasions appear to be nested. At both white arrow tips a yellow cell encapsulates a red cell, while the red cells form a connection between the two layers of the bone. **B:** A column of red cells appears to be invading through the bone to coat the innermost surfaces of both outer layers (green arrow), though a cyan cell is also present (white arrow) demonstrating the polyclonality of invasions. **C:** another polyclonal invasion, this time red and yellow. **D:** The yellow cells which appear to be invading through Layer 2 at this point appear to spread in both horizontal directions (white arrows).

be somewhat dependent upon position in the skull. The relationship between this matching and a potential link to the thickness of the bone will be explored in Chapter 12.

As well as a general pattern of layer matching, there appear to be specialised regions. At least one muscle attachment region appears to disrupt the surrounding pattern of layer matching (Figures 10.6 and 10.7, yellow arrows), which will be explored in detail in Chapter 13. Sutures appear to have a mostly white labelling, denoting matching of all layers, though this will be explored further in Chapter 14 and the upcoming subsection 10.3.4.

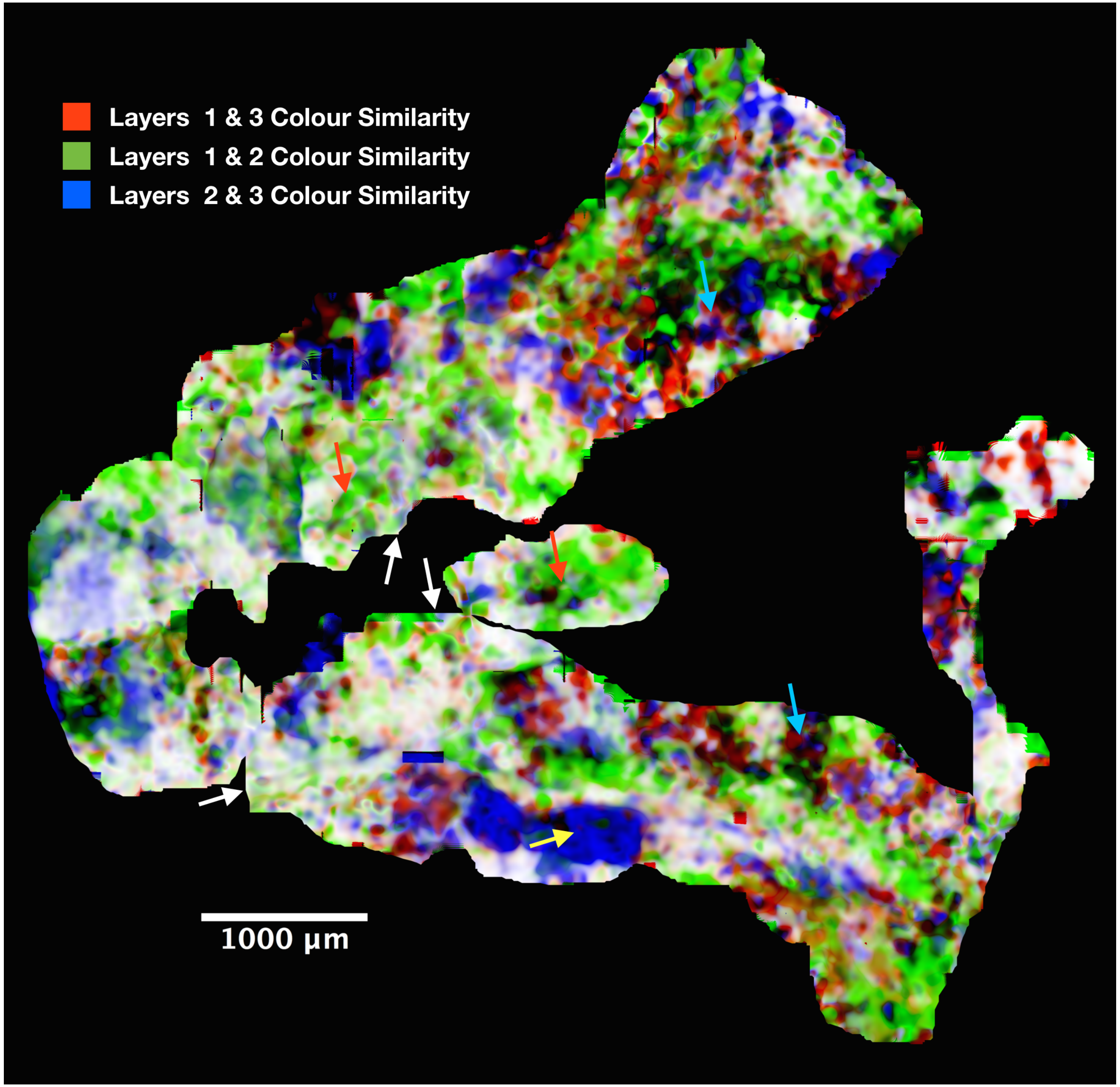

Figure 10.6: Non-Density Encoded Colour Matching of Sample A. *Caption on page 179.*

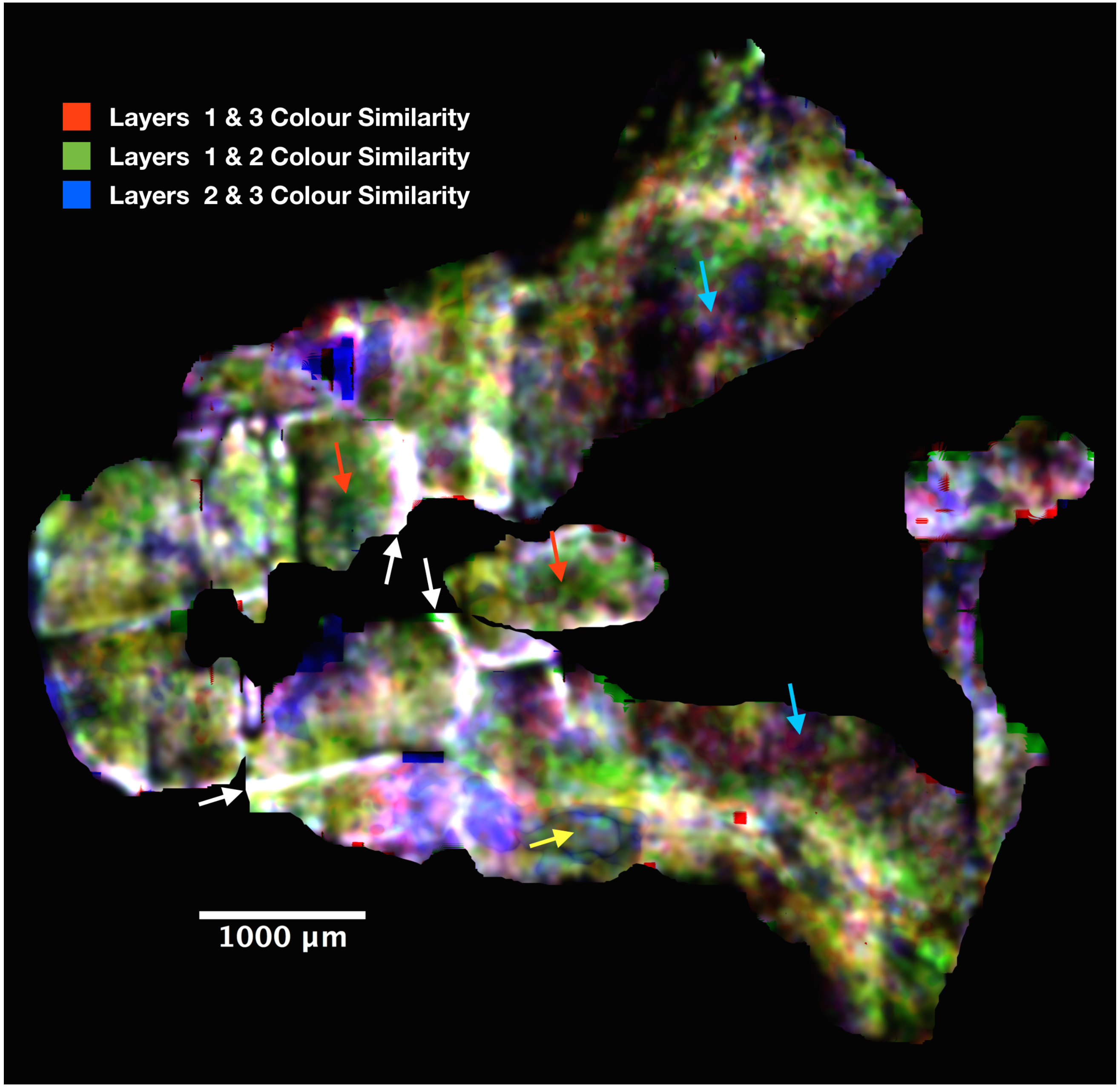

Figure 10.7: Density Encoded Colour Matching of Sample A. *Caption on page 179.*

Figure 10.6 and 10.7: Colour Matching of Sample A. $15\mu m$ map of colour matching of Sample A, generated using the non-density encoded and density encoded metrics respectively. Strikingly under both metrics, the sutures are labelled white, suggesting matching between all three layers (white arrows).This could support the idea that layers propagate from these points, but will have to be explored more closely in Chapter 14 and Section 10.3.4. Regions in the centre of bones appear mostly to contain matching between Layers 1 and 2 (green labelling, red arrows), though at the posterior of the frontal bone this is not the case, and instead a patchy red/blue labelling (matching to Layer 3) is present (cyan arrows). The interfrontal bone represents a microcosm of the larger bones, explored in detail in Figure 10.12. There is a large gap dominated by Layer 2 and 3 matching in (yellow arrow) which represents a Muscle Attachment region, explored in detail in Chapter 13. Layer matching can be observed to adopt small circular patterns and nested linear arrangements in both, but particularly in Figure 10.6.

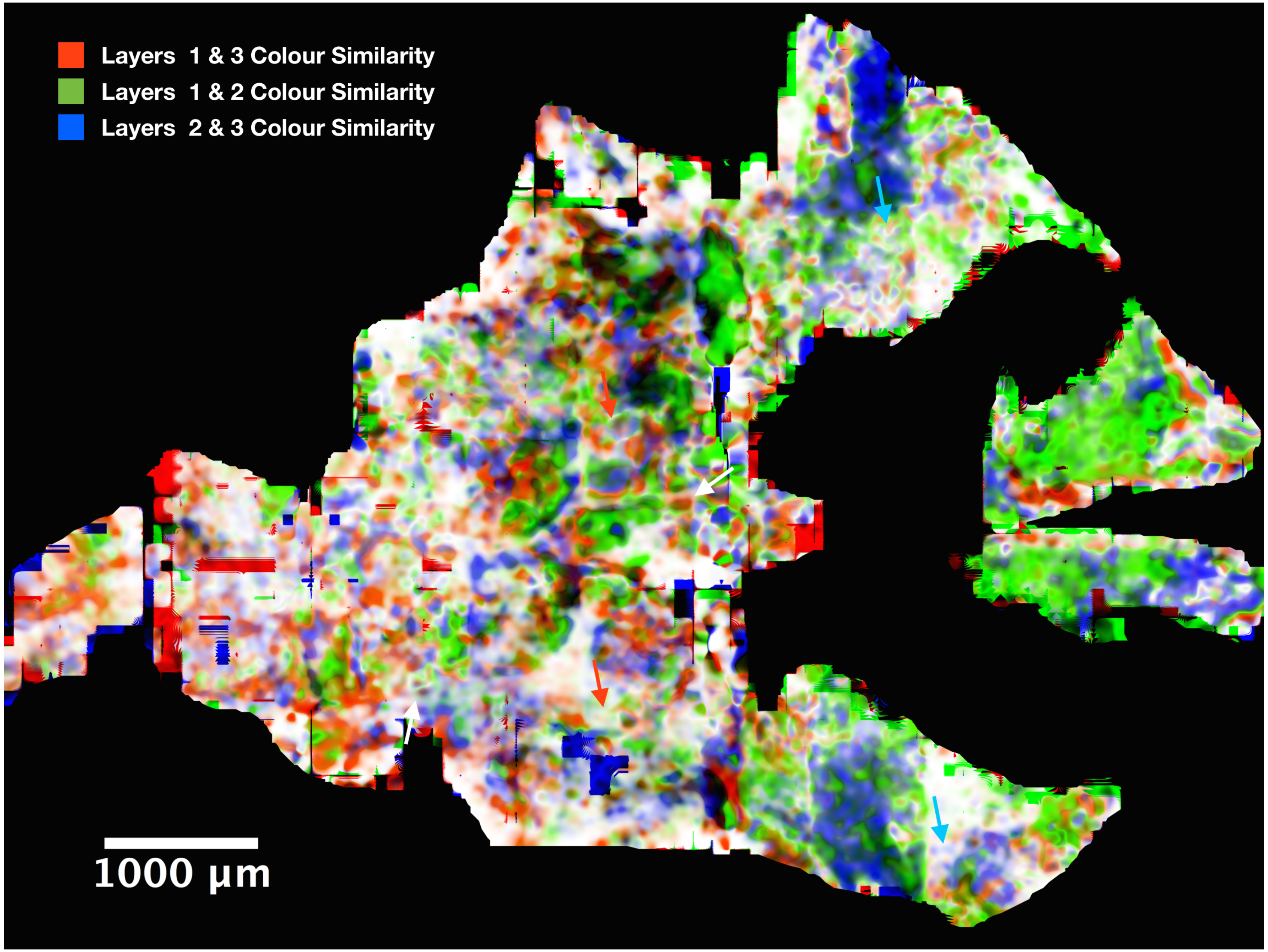

Figure 10.8: Non-Density Encoded Colour Matching of Sample B. *Caption on page 182.*

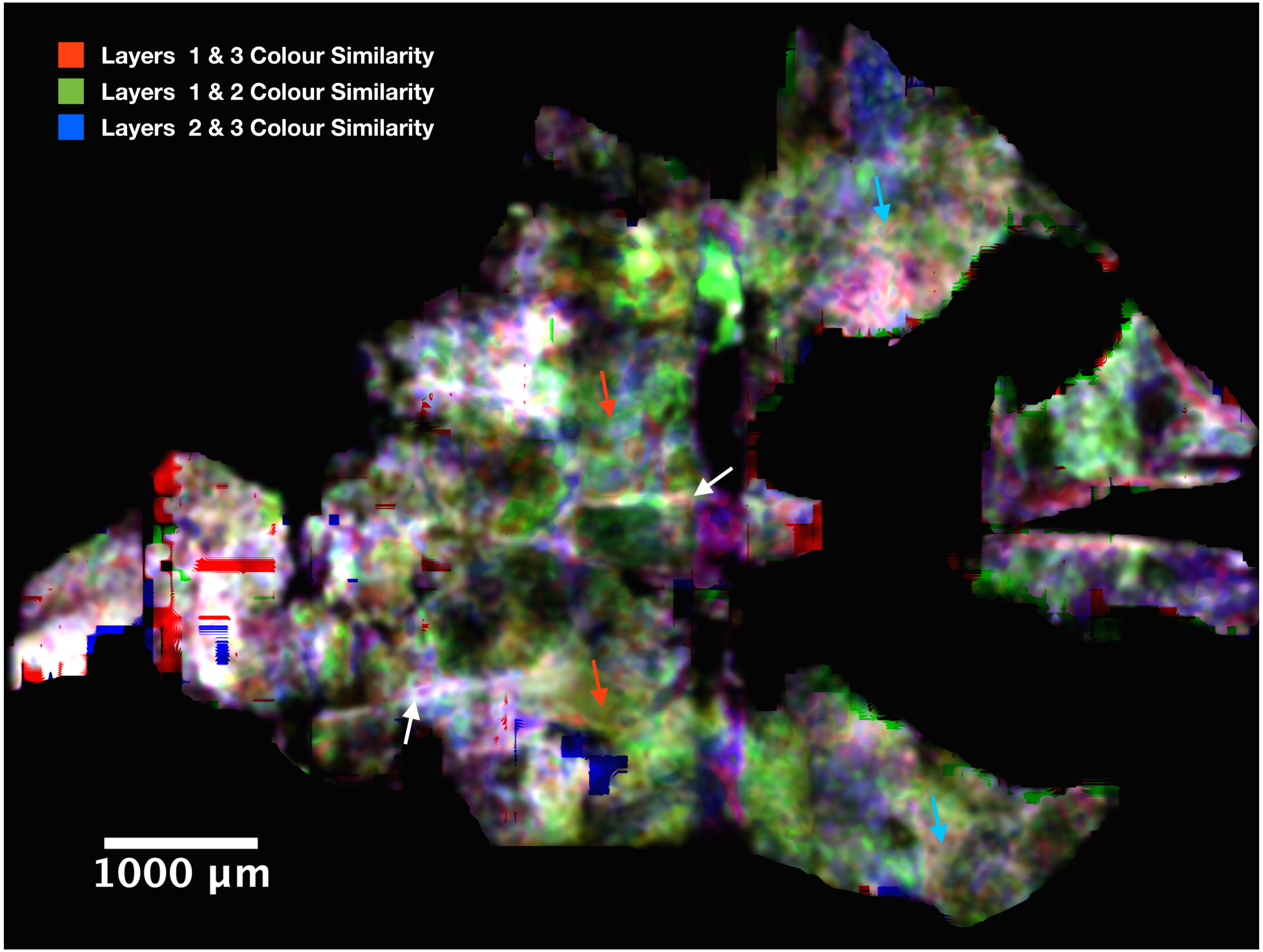

Figure 10.9: Density Encoded Colour Matching of Sample B. *Caption on page 182.*

Figure 10.8 and 10.9: Colour Matching of Sample B. 15μm map of colour matching of Sample B, generated using the non-density encoded and density encoded metrics respectively. As in Sample A, sutures are labelled white (white arrows) denoting matching across all layers at these points. Centres of bones are labelled green (red arrows), suggesting that matching of Layers 1 and 2 is more generally found in the centre of bone. Though again, towards the posterior of the bone (cyan arrows) there is more complex arrangement of layer matching, including points of all three colours and nesting of lines of colour, explored in Figures 10.10 and 10.11. The interfrontal bone repeats the same arrangement as the larger frontal bones.

10.3.3 Nested concentric points are visible across the samples

A common feature across these maps is a point of layer matching, surrounded by rings of matching of other layers. Some examples are presented in 10.10. These are be termed roundels, due to their concentric arrangement which is reminiscent of the Royal Air Force roundel. These most likely represent individual points of vertical invasion. These loci of invasion must be causing mixing across layers that preserves polyclonal identities. These patterns are highly indicative of convection patterns.

10.3.4 Colour Matching resolves into lines

Another feature that is present on a larger scale is the observation of lines of matching and non-matching. Some examples are presented in 10.11. Where large expanding fronts of cells meet, there could be induced invasion as a form of size restriction. Lines of non-matching could be due to interfaces of different patches, where the blur would span two different populations and obtain a mixed reading that would not match to related underlying patches. The latter possibility is evaluated later in Chapter 11.

Sutures appear to have a complex arrangement of lines. At the core of the suture this involves colour matching of all layers, suggesting a plane of cells of the same lineage crossing all layer boundaries. Parallel to these are further lines of matching, often between Layers 1 and 3, suggestive of the communication of cells between the outermost layers around the edge of the bone. The greater degree of three-layer matching within the sutures suggests that the non-layered mesenchyme within the suture freely mixes without containing cryptic layers.

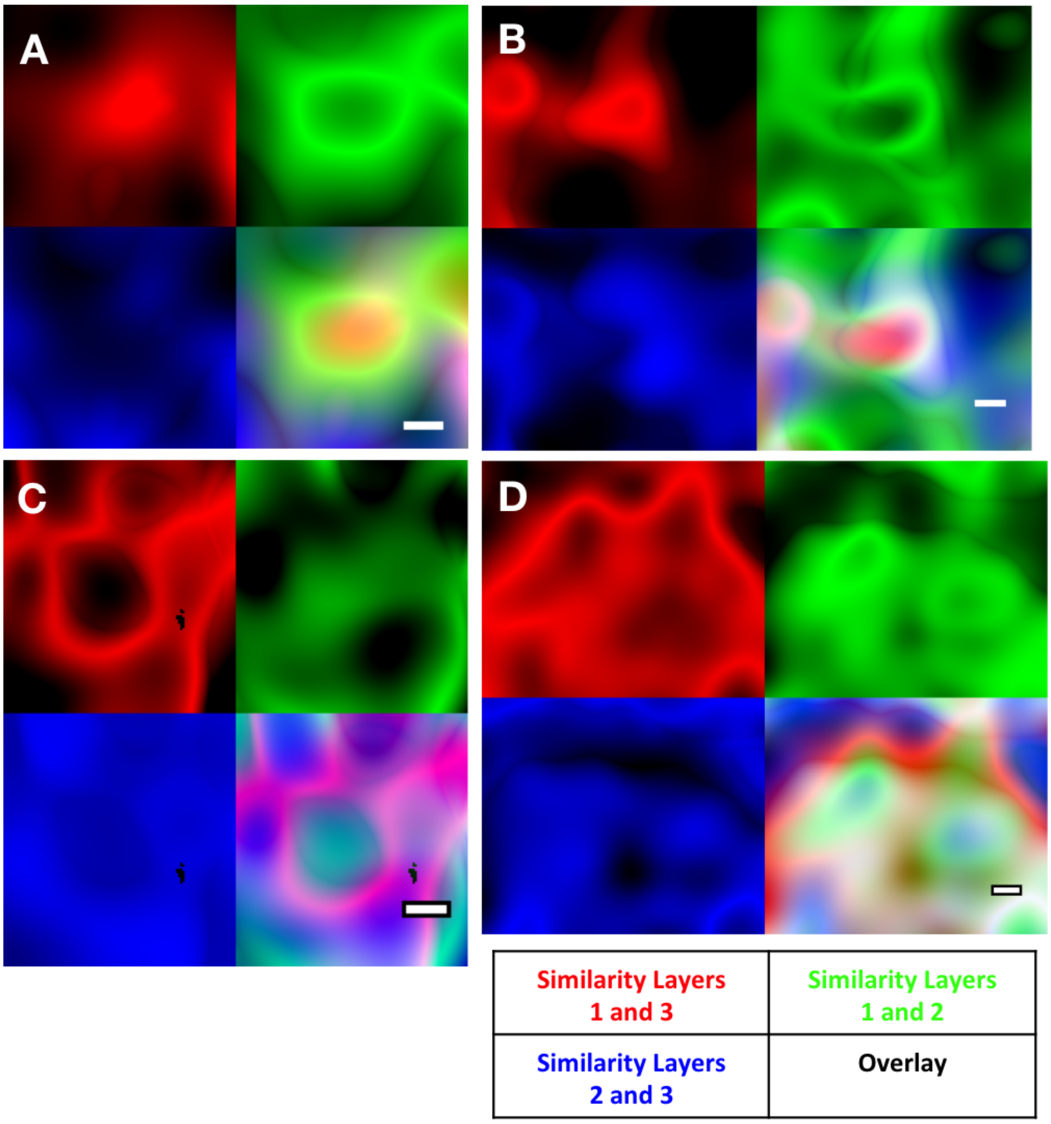

Figure 10.10: Examples of Roundel Patterning. Within Layer Matching Maps, concentrically nested patterns can be observed. Each represents a small region from Sample B with a 30μm scale bar. **A:** commonly a small point of Layer 1 and 2 matching is found surrounded by a tight ring of 1 and 2 matching.**B:** Some of these patterns show overlap, such as here where the right edge of the roundel's halo has colocalised three layer matching, displayed as white. **C:** The opposite pattern can be observed, with a point of Layer 1 and 2 matching surrounded by a ring of 1 and 3 matching. **D:** Complexes can be observed of several roundels. Here, two points of matching of Layers 2 and 3 (blue) are surrounded each by rings of 1 and 2 matching, with Layer 1 and 3 matching found in a tight ring around both.

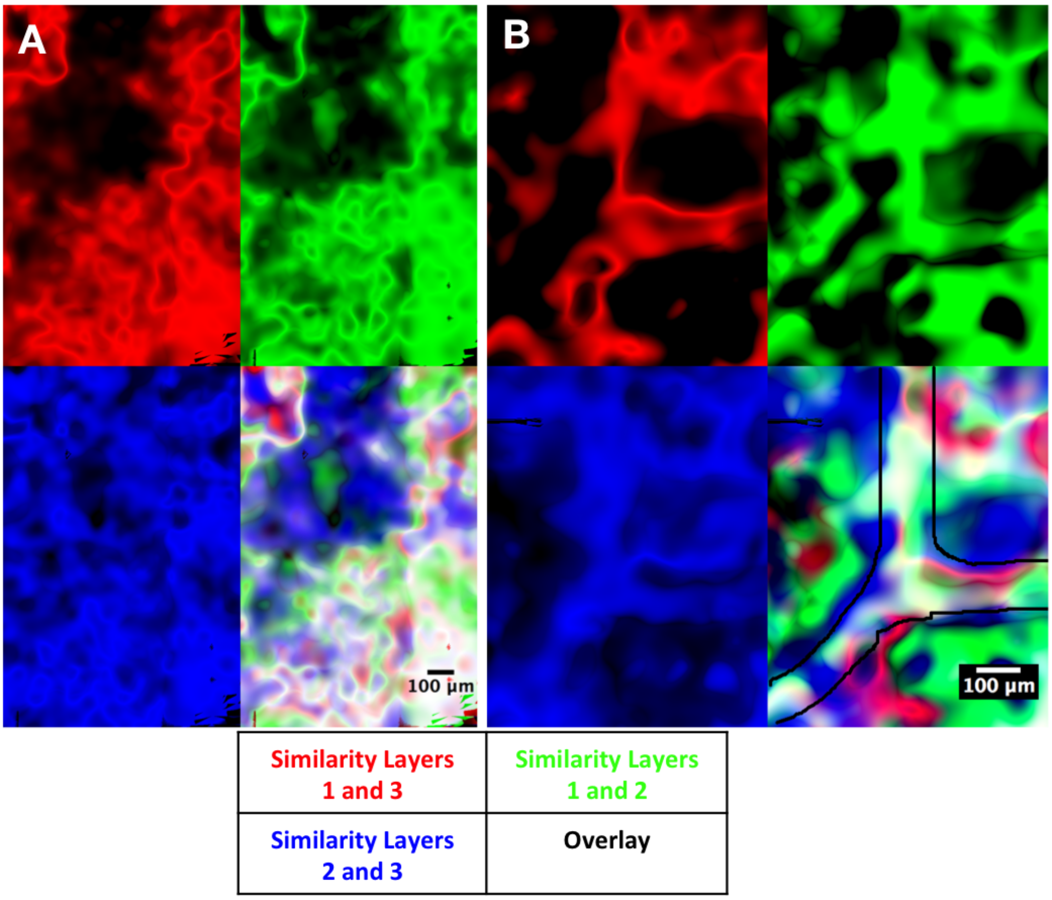

Figure 10.11: Examples of Linear Patterning. Within Layer Matching Maps, organised lines of common colour can be observed. Each represents a region from Sample B. **A:** Lines in the centre of the frontal bone. A complex and tortuous set of lines are visible across this region, often following the same routes, suggestive of coordinated invasion across all three layers. Roundels are also visible, which may simply represent microcosms of this linear organisation. Within these regions, layer matching can be fairly homogenous, such as the large blue region to the top left, indicative of Layer 2 and 3 matching. **B:** Intersection of the frontonasal sutures and interfrontal bone's sutures. The sutures (outlined in black) contain lines of different colours, as well as three-layer matching denoted by white regions. This is indicative of shared lineage around the perisutural envelope, and a loss of layer segregation within the suture.

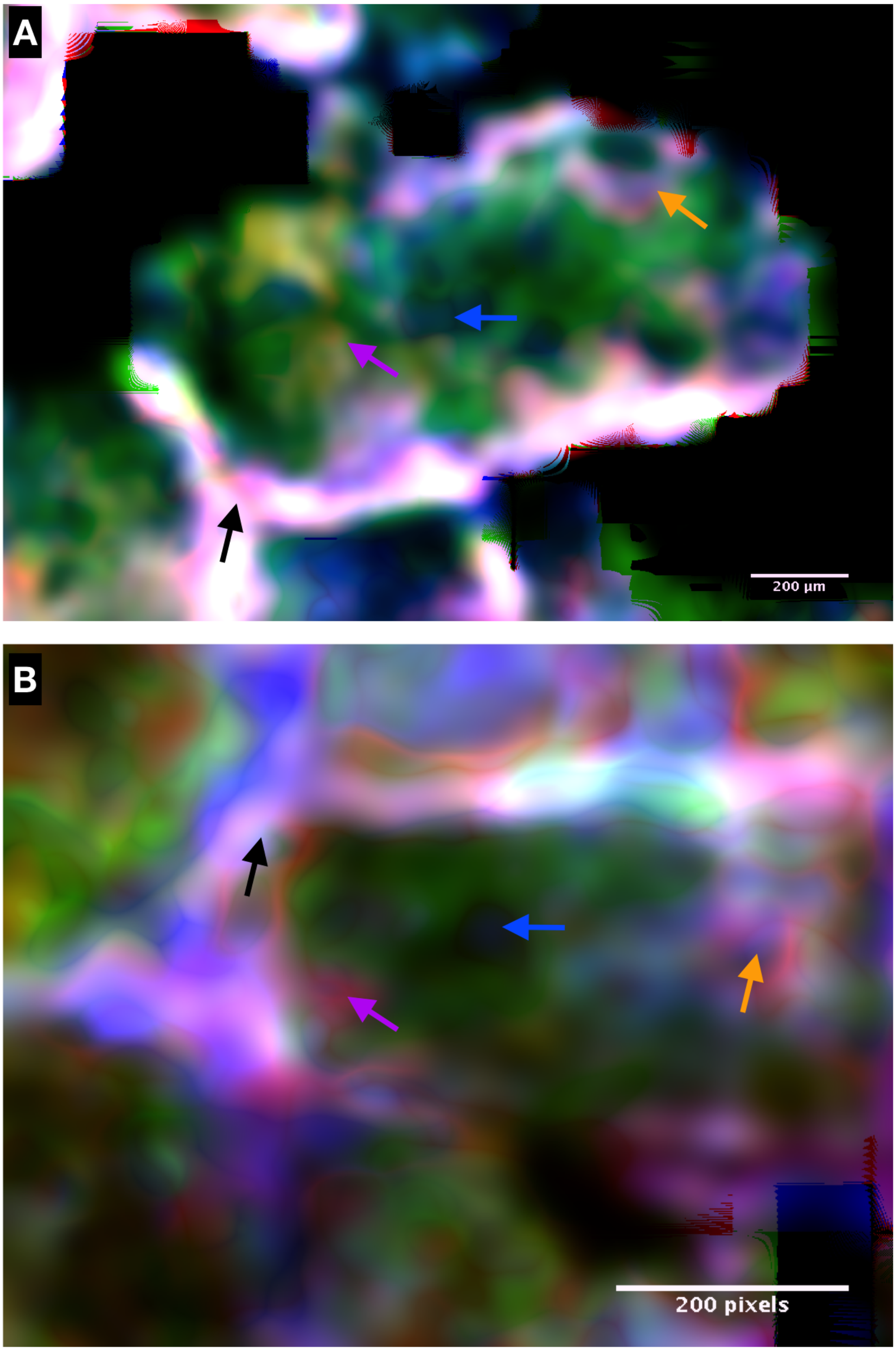

Figure 10.12: Organised Layer matching in the Interfrontal Bones. *Caption overleaf*

10.3.5 The interfrontal bone displays a pattern of nested development

The two ostensibly ectopic interfrontal bones display broadly similar patterns of organised colour matching and thus invasion, shown in Figure 10.12. The sutures display three layer matching and complex nested patterns, while the interior of the bone is largely dominated by colour matching between Layers 1 and 2. This is interspersed with points of Layer 2 and 3 matching, and nested roundels with Layer 1 and 3 matching on the exterior and 2 and 3 matching on the interior.

This broadly represents the main pattern of layer matching across both samples: a largely Layer 1/2 match interspersed with features of the other Layers. This may represent a preference between different invading streams at different stages of biomineral development. This possibility will be explored in Chapter 12.

Figure 10.12 Organised Layer matching in the Interfrontal Bones. A&B: The interfrontal bones of Samples A and B respectively, using the density-encoded metric. This figure uses the same red/green/blue colour key as the previous maps. Both samples display the same arrangement of layer matching. The bone is bordered by lines of three-layer matching with complex nesting patterns (black arrows). The interior is mostly defined by matching of Layers 1 and 2 (green). This is broken up by sharply defined points of Layer 2 and 3 matching (blue arrows) or roundels of Layer 1 and 3 matching (red) surrounding 2 and 3 matching (blue) at mostly posterior points (orange arrows). At points there is apparent three layer matching within the bone (purple arrows). Ultimately it is a landscape mostly of 1 and 2 matching with interspersed points of apparent invasion between other layers, consistent with Figure 10.4.

10.4 Summary - Invasion between layers appears organised

For the first time, we can map potential cell invasion in a whole organ consisting of hundreds of thousand of cells based on mixed population identity. I observe polyclonal invasion between layers (Figures 10.4 and 10.5) which can be mapped across entire square centimetres of bone (Figures 10.6 to 10.9) to reveal organisation, both around obvious structures such as sutures and the small interfrontal bone (Figure 10.12) but also on the fine scale (Figures10.10 and 10.11).

Exactly what these points of invasion are organised around is entirely unaddressed by the traditional sutural model: if the bones are defined by growth at the sutures, there should be no mixing between layers further from the suture, let alone organised nested invasions at points deep within the bone. Rather, the distributed nature of these points appears to be mostly consistent with the broadly distributed patches explored in the previous Chapter. The potential for correspondence between the two will be explored in the next Chapter. Layer matching at Sutures will be further discussed in Chapter 14.

This tool represents a powerful extension to the already significant advances detailed in the first Part of this thesis. I have developed a means for the relative comparison of polyclonal similarity in a manner that both produces striking visual representations of invasion, and provides a relative numerical measure which shall be used in later Chapters as a quantitate measure of invasion. This elevates the utility of clonal lineage labelling from one of subjective interpretation of simple presumptively clonal patterns to quantitative interpretation of complex structures based on a more reliable polyclonal mixture.

Chapter 11

Expansion and Integration of Polyclones in Three Dimensions

11.1 Introduction

In the previous two Chapters, I have presented maps of horizontal spreading generated by revealing patches of individual colours, and a map of vertical invasion produced by observing cell mixture ‘colour matching’ between overlying points of different layers. These two approaches are largely independent, as one relies on single colours and the other looks at multiple colours. However, what is not currently clear is whether horizontal spreading and vertical invasion are independent of one another, or are linked processes.

Vertical invasion may correspond with horizontal spreading, or it may be independent. This ‘correspondence’ may take many forms: vertical invasion could take place mostly in patch centres, suggesting that polyclonal expansion occurs in an integrated fashion across different layers. It may take place mostly at patch borders, suggesting that vertical invasion occurs where expanding fronts of cells meet, in the same manner as tectonic plate subduction. Both processes may occur, forming a simple convection pattern.

The correspondences between the patches of different layers and the map vertical invasion of different pairwise layers (*e.g.* Layer 1 and 3 Matching) can be assessed separately, and are likely to differ. For example, there is no reason why invasion between Layers 2 and 3 might affect Layer 1.

For this reason a metric was developed to allow for comparison of patch correspondence to layer matching. In brief this works by ascribing a value to the degree of

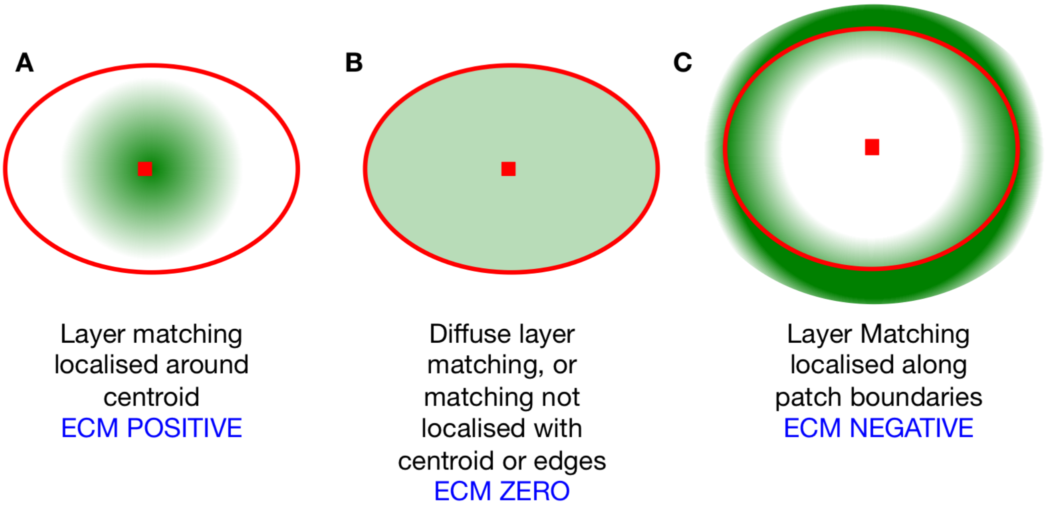

Figure 11.1: Diagram of Edge Centroid Metric Results. This demonstrates the relevance of certain values calculated by the Edge Centroid Metric. **A:** Where layer matching (green) is high at the patch centroid (red square) and low along patch edges (red line), the ECM will be positive. **B:** Where there is no particular relationship between the patch and the layer matching, ECM will be calculated as close to 0. While this diagram shows a general diffuse equivalency of layer matching across the patch, a similar value could be achieved by the presence of a pattern that does not align with the patch. **C:** Where layer matching (green) is organised along the patch boundary (red line) and absent in the patch centre (red square) ECM will be negative.

difference between layer matching at the centre and the edges, taking into account the more general local degree of matching. The software developed previously was extended to support this analysis.

11.2 Method

The ‘Edge Centroid Metric’ (ECM) was developed to assess the correspondence between Layer Matching and Patches. The purpose of this metric is to give an impression of how the edges of the patch compare to the centre of the patch with respect to intensities stored in the layer matching maps. A large positive value suggests greatest layer matching at patch centres, a large negative value suggests greatest layer matching at patch edges, and a value close to 0 suggests an absence of organisation between the patches and layer matching. This is summarised in Figure 11.1.

The value at the centre is easily gained by simply finding the patch centroid and logging the corresponding values of this point in the layer matching maps. The edges were evaluated by taking a concentric ring of pixels around the inside of the patch margins, and finding the average intensity of these pixels across the layer matching maps.

This absolute difference is inappropriate for large scale analysis, as it will report small differences between two large numbers as being equal to the same difference between small numbers, when the latter is proportionately a far greater gradient. Thus, values were weighted relative to the local degree of layer matching. This was accomplished by dividing the difference between the centroids and edges by the average intensity across the whole patch. This is described as the Edge-Centroid Metric, formally stated as:

$$Edge\ Centroid\ Metric = \frac{Centroid\ Intensity - \overline{Edge\ Intensity}}{\overline{Patch\ Intensity}}$$

The resulting values were tabulated in ImageJ/FIJI, and presented using graphical functions within R. Additional illustrations were facilitated through an extension to the plugin in ImageJ/FIJI, allowing the plotting of patch edges and centroids for the figures in this chapter. The values were calculated for each patch and each pairwise layer matching map, and an average taken for each layer.

11.3 Results

11.3.1 The Edge-Centroid Metric reveals correspondences between patches and layer matching, which are confirmed by observation

Figures 11.3 and 11.4 show the results of the Edge Centroid Metric analysis for both samples. The meaning of these charts is best discussed in tandem with examples, described in the following subsections. Trends can then be compared to the actual correspondence between patches and layer matching in a region of representative bone from Sample A, in order to verify the sample-wide findings. The region of bone used is detailed in Figure 11.2.

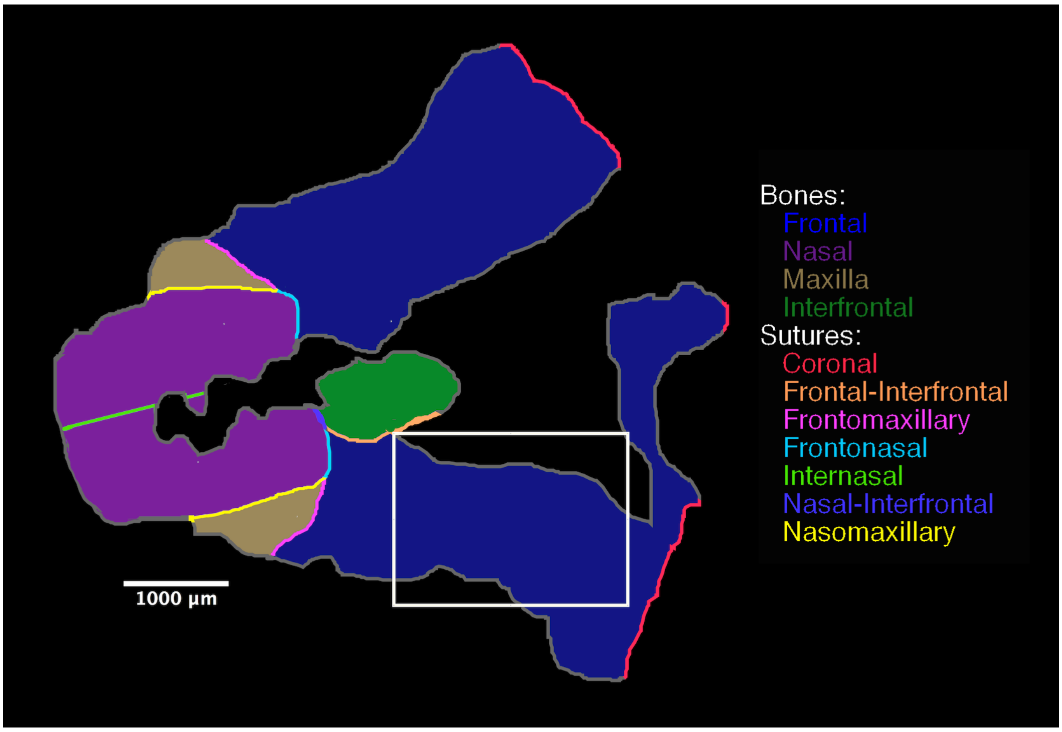

Figure 11.2: Region of Sample A for Edge-Centroid result verification. Region of Sample A for Edge-Centroid result verification.

The white box shows the region represented in the following figures. This area spans the frontal bone, and measures 2.2mm x 1.6 mm for a total area of 3.5mm^2. This region represents a good mixture of more developed bone towards the lateral and anterior ends, and less developed bone closer to the posterior and medial aspects.

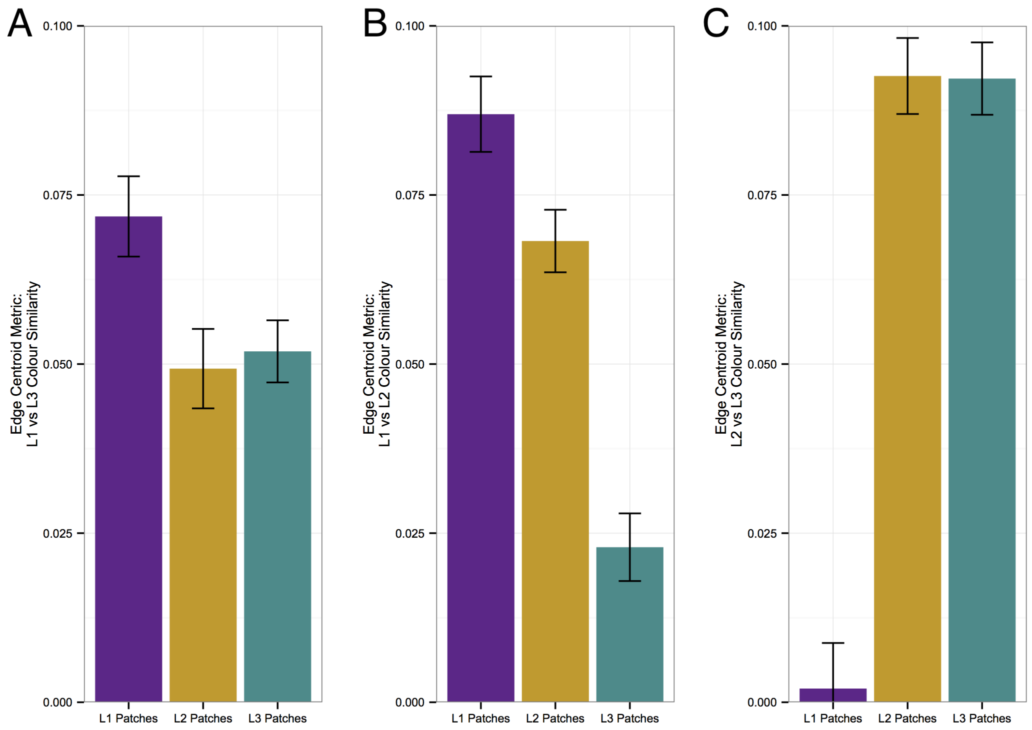

Figure 11.3: Edge Centroid Results for Sample A. A: Matching between Layers 1 and 3 has relatively strong localisation around Layer 1 patch centres and intermediate localisation around Layer 2 and 3 patch centres. **B:** Matching between Layers 1 and 2 is strongly associated with Layer 1 and 2 patch centres and appears to have only a very weak relationship with Layer 3 patch centres. **C:** Matching between Layers 2 and 3 is strongly localised to the centres of Layers 2 and 3, and has no relationship with Layer 1.

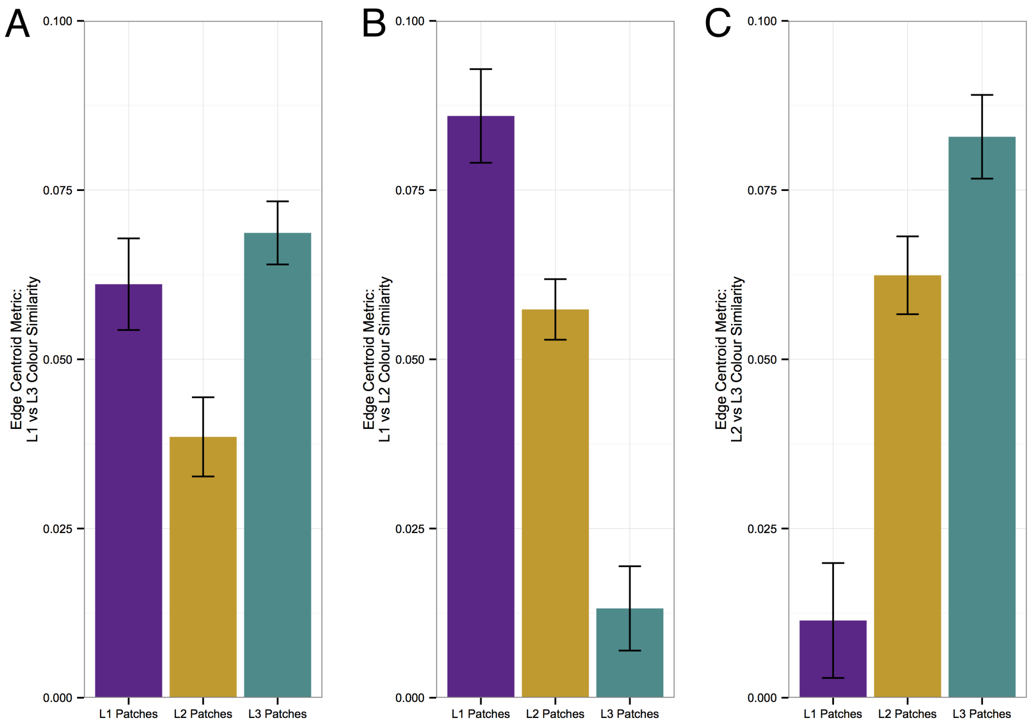

Figure 11.4: Edge Centroid Results for Sample B. A: Layer 1 and 3 colour matching is relatively strongly localised to the centres of Layer 1 and 3 patches, while Layer 2 patch centres have a weaker relationship with this invasion. **B:** Layer 1 and 2 colour matching is most strongly associated with Layer 1 patch centres, and has an intermediate relationship with Layer 2 patch centres. Layer 3 appears to not have a relationship with this invasion. **C:** Layer 2 and 3 colour matching is strongly localised to patch centres of Layers 2 and 3, and appears to have no relationship with Layer 1.

11.3.2 Invasion between Layers 2 and 3 occurs at the centres of patches in both of these layers

Figures 11.3C and 11.4C suggest that matching between Layers 2 and 3 occurs at the centres of patches in Layers 2 and 3. This is unambiguously supported by Figures 11.3C and 11.4C, which clearly demonstrate a strong tendency for the centroid to have stronger Layer 2 and 3 matching than the edges. Layer 1 clearly has no strong relationship with this invasion, as in both samples the average for this layer is close to zero. As Layer 3 precedes Layer 2 in development, this suggests that cells from Layer 3 migrate upwards mostly at patch centres, creating new patches in Layer 2 directly above themselves.

These sample-wide averages are verified by the region displayed in Figure 11.5, wherein patches in Layers 2 and 3 (B and C) have centroids overlapping regions of high intensity, and edges corresponding to regions of low intensity. Layer 1 patches on the other hand do not appear to follow the pattern of layer matching at all, demonstrating independence.

11.3.3 Invasion between Layers 1 and 2 occurs mostly at the centres of Layer 1 Patches, and not always at Layer 2 patch centres

In both Figures 11.3B and 11.4B the order of the layers' relationships to Layer 1 and 2 colour matching is preserved: Layer 1 has a very strong correlation, Layer 2 a strong but weaker correlation and Layer 3 the weakest correlation. This implies that invasion between Layers 1 and 2 occurs principally at Layer 1 patch centres, but not as strongly at Layer 2 patch centres. The weak or nearly absent association with Layer 3 suggests that this Layer does not define points of Layer 1 and 2 invasion, or that where there is an association it is secondary, due to close invasion through multiple layers.

Figure 11.6 demonstrates why Layer 1 appears to correspond best with respect to this form of layer matching. Where trabeculae are arranged into strips, small discontinuities of matching correspond to Layer 1 boundaries and not Layer 2 boundaries. This suggests that in this region invasion is principally from Layer 1 into 2, rather than 2 into 1, as these discontinuities respect Layer 1 patch boundaries only.

11.3.4 Invasion of cells between Layers 1 and 3 occurs mostly through the centres of patches across all three layers.

Figures 11.3A and 11.4A show the largest discrepancy between the two samples. In both, Layer 1 has a strong association with Layer 1 and 3 matching, suggesting that invasion between these layers regardless of direction is centred on Layer 1 patch centres. Layer 2 has the weakest, though this is still relatively strong, suggesting that invasion between the outermost layers does contribute to some but not all patches within Layer 2, or at least is inhibited where polyclones interface with their neighbours within Layer 2. The association with Layer 3 is quite remarkably different. In Sample B (Fig. 11.4A) the correlation to this match equals or exceeds the strong association of Layer 1, while in Sample A (Fig. 11.3A) it is approximately equal to the weaker association of Layer 2. This suggests that while Layer 1 patches are still centred around points of communication late in development, Layer 3 is not.

Further investigation at the level of individual patches shown in Figure 11.7 provides insight into this phenomenon. In Sample A, several localised maxima of layer matching exist within single Layer 1 patches, scatted around the centroid, while some patches show single central points of matching. Meanwhile many Layer 3 patches do seem to tightly define local maxima of matching, but other patches clearly have no relationship with any form of Layer 1 and 3 communication.

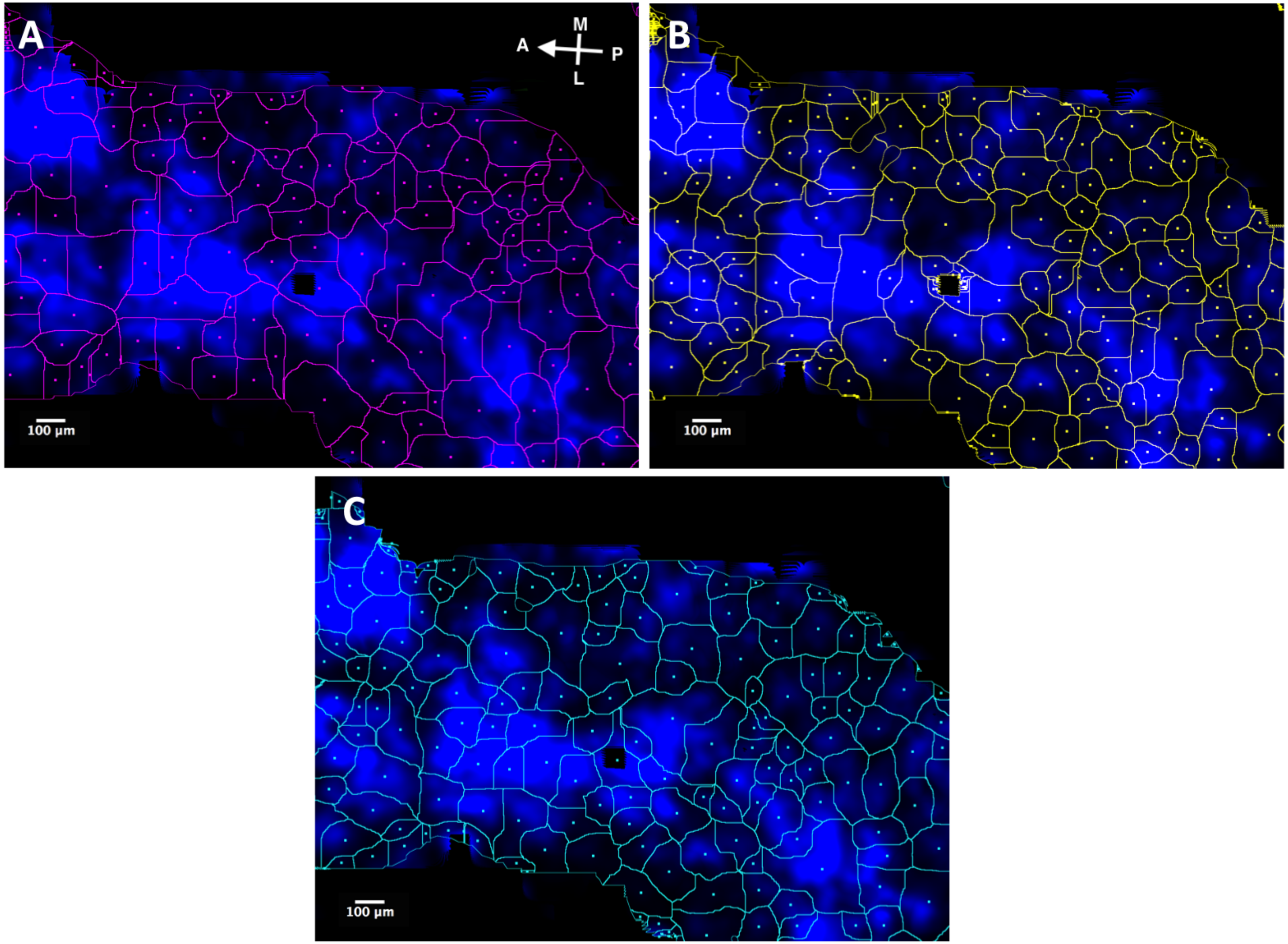

Figure 11.5: Correspondence of Patches to Colour Matching between Layers 2 and 3. - *Caption on 199*

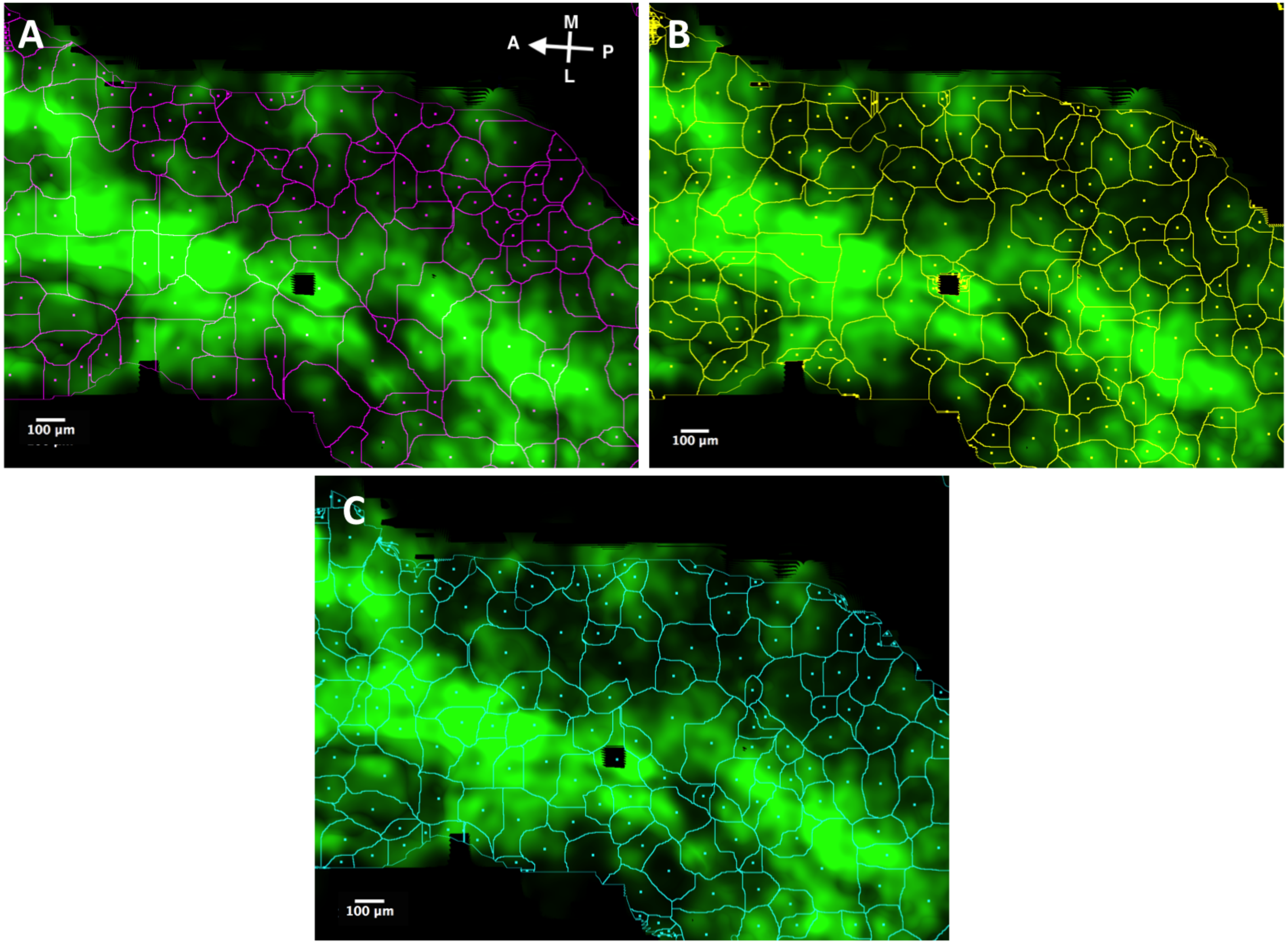

Figure 11.6: Correspondence of Patches to Colour Matching between Layers 1 and 2. - *Caption on page 199*

Figure 11.5: Correspondence of Patches to Colour Matching between Layers 2 and 3. A: Correspondence with Layer 1 patches. There does not appear to be any strong correlation, with maxima of matching found mostly within patches but off-centre, or along edges. **B:** Correspondence with Layer 2 patches. There is a strong correlation, with tight maxima of matching found at many patch centroids, and narrow trenches of low matching found along patch edges. **C:** Correspondence with Layer 3 patches. As with Layer 2 patches, there is a strong correspondence between Layer matching and patch structure. These three observations all correspond with the predictions of the sample-wide analysis.

Figure 11.6: Correspondence of Patches to Colour Matching between Layers 1 and 2. A: Correspondence with Layer 1 patches. While there is some correspondence with local maxima in the more medial, posterior portion of this region (top right), there is also very strong correlation between patch boundaries and minima in the more developed lateral region, suggesting that Layer 1 patch boundaries and invasion between Layers 1 and 2 affects architecture of trabeculation. **B:** Correspondence with Layer 2 patches. Many layer 2 patches sharply define local maxima at the centroid and minima at the edges, but in the more trabeculated region these boundaries cross perpendicular to the linear arrangement of cellularised regions. **C:** Correspondence with Layer 3 patches. Layer 3 patches do not appear to have any particular relationship with Layer 1 and 2 matching. These three observations all correspond with the predictions of the sample-wide analysis.

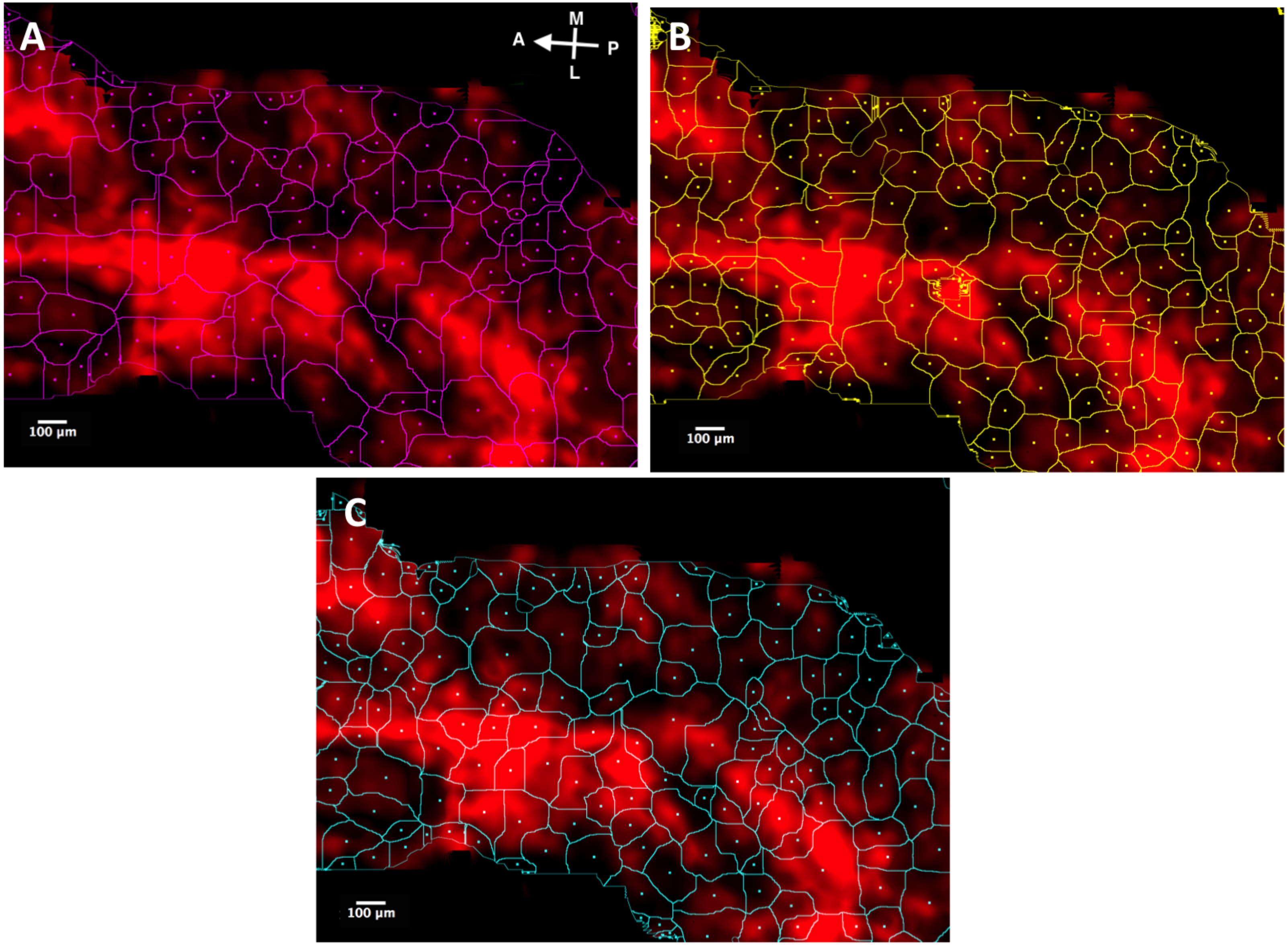

Figure 11.7: Correspondence of Patches to Colour Matching between Layers 1 and 3 - *Caption overleaf*

Figure 11.7: Correspondence of Patches to Colour Matching between Layers 1 and 3. A: Correspondence with Layer 1 patches. There is a reasonably good correspondence between patch arrangement and layer matching, though many maxima do not appear to be at patch centres. **B:** Correspondence with Layer 2 patches. There is good correspondence of patch borders to minima of layer matching, but local maxima appear off-centre relative to Layer 2 patches. **C:** Correspondence with Layer 3 patches. There are many patches that do correspond well with maxima and minima of layer matching, but also many maxima that do not fall at the centre of patches.

11.3.5 Correspondence of Patch Shapes in different Layers, and of different Reporter Colours

Each of these observations cannot stand entirely alone: the matching of patches in any given layer to both of the other layers strongly suggests a match between the two other layers. Overlaying the patches for one colour across all three layers shows the correspondence between patches in different layers, as shown in Figure 11.8. Correspondence between the layers is not ubiquitous, but can be very strong and exist cooperatively across several patches, particularly along patch edges. It would appear that both outer layers have some points of strong correspondence with Layer 2, but collectively they do not match well with one another (Fig. 11.8C). This suggests that while single routes of invasion are important for linking Layers 1 and 3, there is a more generalised diffusion of cells between adjacent layers, leading to better patch correspondence.

Similarly, given that growth is polyclonal and layer matching incorporates all four Confetti labels into one metric, it must be assumed that patches of different colours must correspond within the same layer. This is explored in Figure 11.9, where patches can be observed to overlap in many but not all areas. This shows that it is not only vertical invasion which is polyclonal, but also lateral spread, further suggesting a passive spread of groups of cells due to localised points of division or invasion, rather than a simple unmixed clonal 'jigsaw' pattern.

11.4 Summary - Invasion between layers is largely organised to patch centres, and part of a three dimensional polyclonal spread

Vertical invasion and horizontal spread clearly are integrated into a three dimensional pattern of polyclonal proliferation. The nature of these associations, when partnered with the observations about layer invasion in previous chapters, suggests an ontogeny wherein Layer 3 colonises Layer 2 independently of Layer 1, Layer 1 contributes to Layer 2 mostly independently of Layer 3 patches, and communication between the outer layers leads to colour integration across all three layers.

The localisation of layer matching to patch centroids strongly suggests an integration of vertical invasion and then horizontal spreading outwards from points of invasion. This horizontal spreading is polyclonal in nature as evidenced by Figure 11.9 and in

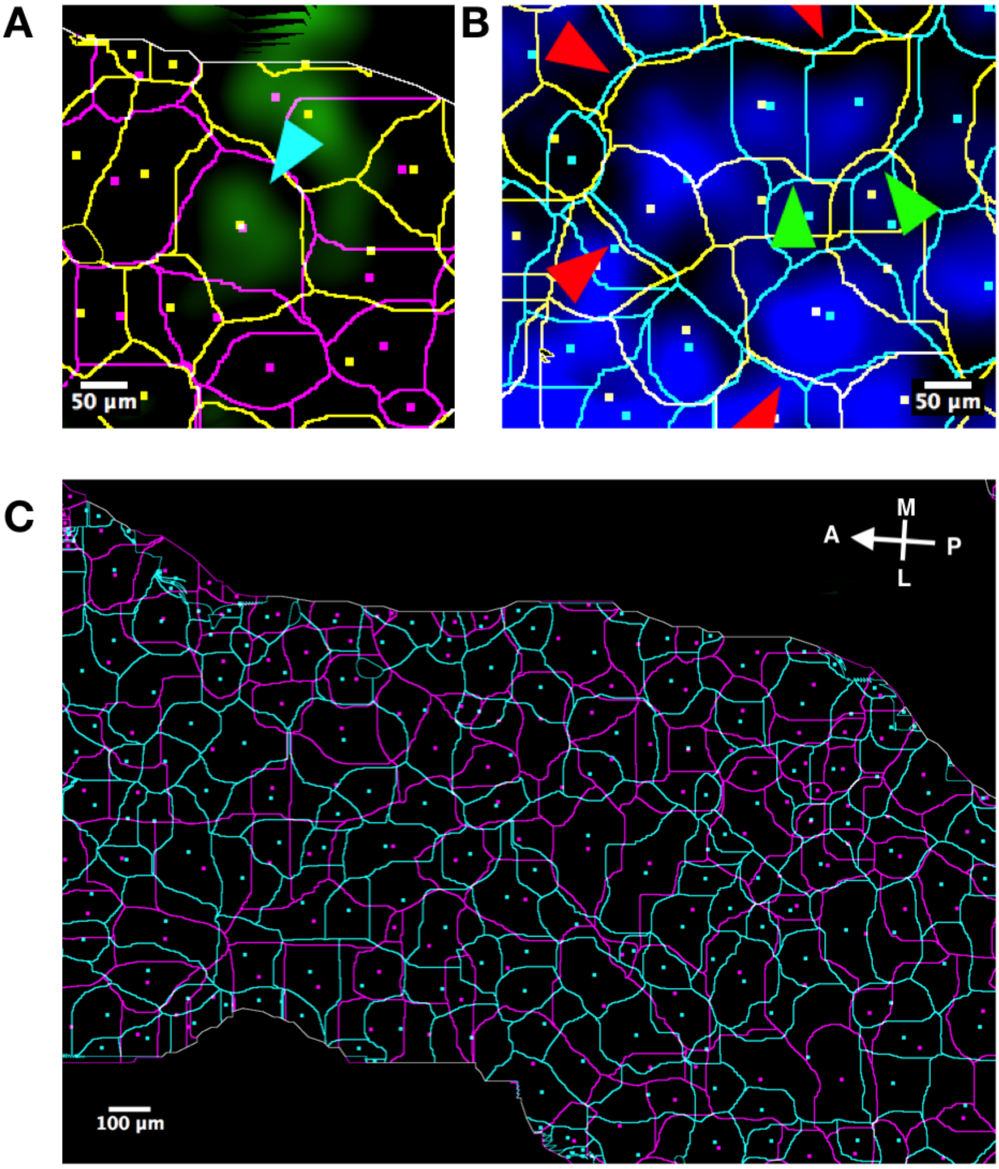

Figure 11.8: Patches of different layers share geometry when linked by vertical invasion. A: Layer 1 and 2 matching (green) at the centre of both Layer 1 (magenta) and Layer 2 (yellow) patches allows correspondence of patch shape across both layers (cyan arrow). **B:** Several patches can be linked by invasion into one overlying patch. Here several Layer 3 patches (cyan, green arrows) sit within the same Layer 2 patch (yellow). Very strong correspondence can be found between the borders of patches in different layers, suggesting a level of organisation across many patches (red arrows)**C:** Layer 1 (magenta) and Layer 3 (cyan) patches do not share strong relationships of geometry in the same manner that each does to Layer 2.

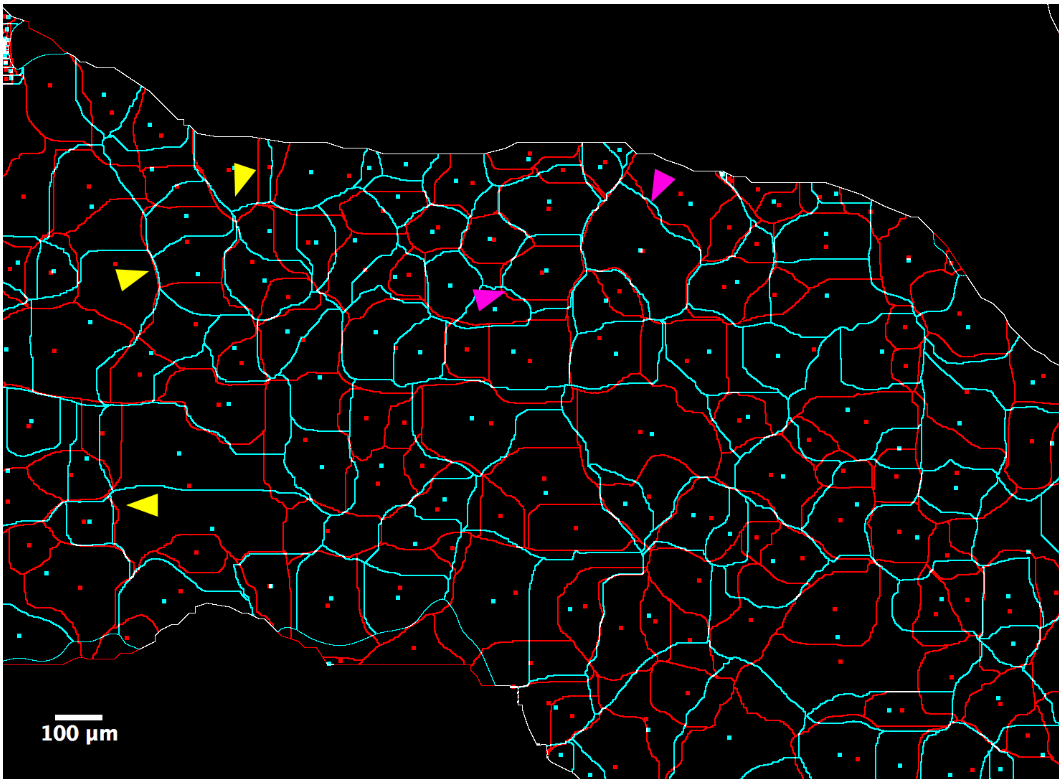

Figure 11.9: Patches of different label colours share geometry. Layer 1 cyan and red labelled patches are shown. Patch borders correspond very well along large distances (yellow arrows). Patches can also have remarkaby similar centroids and outlines (magenta arrows). This is not shown across all patches, suggesting that there are some regions where these two colours are co-migrating, and others where they are not.

certain points is coordinated to the extent that near identical patch geometry can be observed in different layers (Fig. 11.8).

The general inhibition of layer matching at patch boundaries suggests either that vertical migration is inhibited along these lines or that layer matching from shared origins is reduced at interfaces by differential mixing between patches in different layers. The latter is a more parsimonious explanation of this phenomenon, as it is reliant only upon two cell fronts migrating into one another which must happen as a consequence of growth, and does not require additional layers of regulation.

The presence of matching in some contexts and non-matching in other implies that the spatial relationships between the layers are shifting and plastic. From this we must conclude that while patches influence other layers where there is invasion, the shifting of the patch landscape does remove these links. This will only truly be elucidated by live imaging, however this is sufficient to conclude that the former interpretation of the bone as a static deposited structure must be rejected, and its true dynamic nature recognised.

Chapter 12

Integrated Three Dimensional Clonal Expansion Predicts Bone Biomineral Thickness Growth

12.1 Introduction

Thus far in this Part we have considered independent approaches to evaluating horizontal clonal spread and vertical invasion, and shown that these are spatially linked with one another. In this chapter, I shall explore to what degree these dynamics are related to the growth of bone thickness.

The biomineral of bone is deposited in Layer 2, and thus measurements of the thickness of this layer can be used as a proxy for the maturation of bone. Conventional wisdom would suggest that if bones are specified entirely by the sutures and by individual osteogenic centres, there would be some form of organisation around these structures. If this is not the case, then organisation of thickness growth around patches may present a better explanation.

Regardless of how thickness develops across the expanse of the skull, its progress is of central importance to the resulting skull. All species have thinner and thicker regions of the skull, facilitating mechanical plasticity in response to stresses of particular diets or restrictive environments, or to accommodate changes in the brain. The capacity to make fine-scale changes to thickness necessitates some form of modularity within the large dermal bones.

In this chapter I shall present maps of the thickness of Layer 2 biomineral and demonstrate that they do not support a sutural model of thickness growth organisation. I shall then present data showing how vertical invasion between layers is predictive of different ranges of biomineral thickness, and show the relationship of thickness to patch area and cellularity. This shall be used as the basis for a novel model of bone development based on patches.

12.2 Methods

The novel data of this chapter is the Thickness Map, though this is in fact a by-product of the maps generated in Chapter 8. This is simply a readout of the thickness of the layer, manually defined during the segmentation process for a grid of pixels and interpolated in between these points. Each pixel contains the number of voxels that were assigned to that layer, which can then be multiplied by the step taken between each Z-section while imaging to get a true thickness. While Thickness Maps can be generated for any Layer, only Layer 2 is presented here as this represents the key region for biomineral thickness growth.

A new metric arising from these maps is the Average L2 Patch Thickness. Each patch defines an area of the sample in reference to other layers: one can identify the area of Layer 2 that lies underneath a Layer 1 patch, or the area of Layer 2 that lies above a Layer 3 patch. The Average L2 Patch Thickness represents the average thickness of Layer 2 within the area defined by any patch.

This metric is defined for each patch and can be compared with the two metrics calculated for each patch within Chapter 8: the area of the patch, and the cell density of the patch. It should be noted that the cell density is defined only for the colour of cells that comprise that particular patch. Cell density can be normalised to correct for the differing proportions of Confetti recombinants: this is done for each colour, within each layer.

All plots and graphs are generated within R using Ggplot2 [R Core Team, 2013; Wickham, 2009].

12.3 Results

12.3.1 Layer 2 Thickness Maps do not support sutural definition of thickness growth

The Thickness Maps for Samples A and B are shown in Figures 12.1 and 12.2 respectively. Strikingly thickness is distributed unevenly. There is no gradient of thickness arising from the sutures, in contradiction of the sutural model of growth. Rather the distributed points of thickness are more consistent with patches locally specifying thickness growth independent from the sutures.

The figures of this chapter quantitatively compare these thickness maps to the patch maps and layer matching maps. However, we may also speculate based on a qualitative assessment. Comparing these maps to the layer matching maps in Figures 10.6-10.9 it seems that the thickest regions best conform with the areas of Layer 1 and 2 matching, with thinner regions bearing more Layer 1 and 3, and 2 and 3 matching.

Thick regions also appear to be relatively cell sparse in the Flattened Cell and Blur maps for each sample in Chapter 8. This might suggest that Layer 3 is sparser in thicker regions. The concurrent apparent loss of Layer 2 cell density in such regions is consistent with the thickness maps: as this layer grows in thickness, it also trabeculates, diluting cells with sparse matrix.

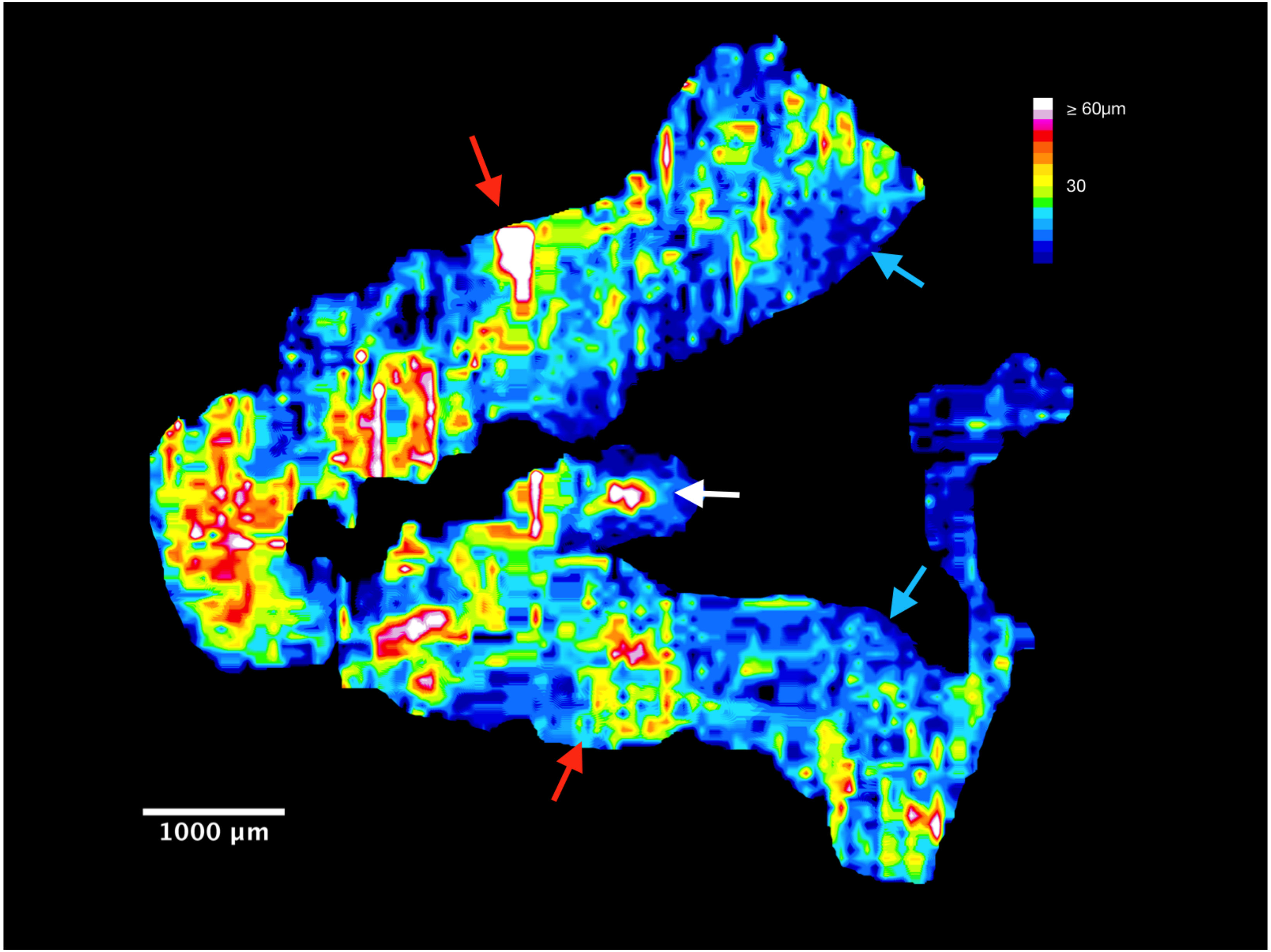

Figure 12.1: Thickness Map of Layer 2 in Sample A *Caption on page 211*

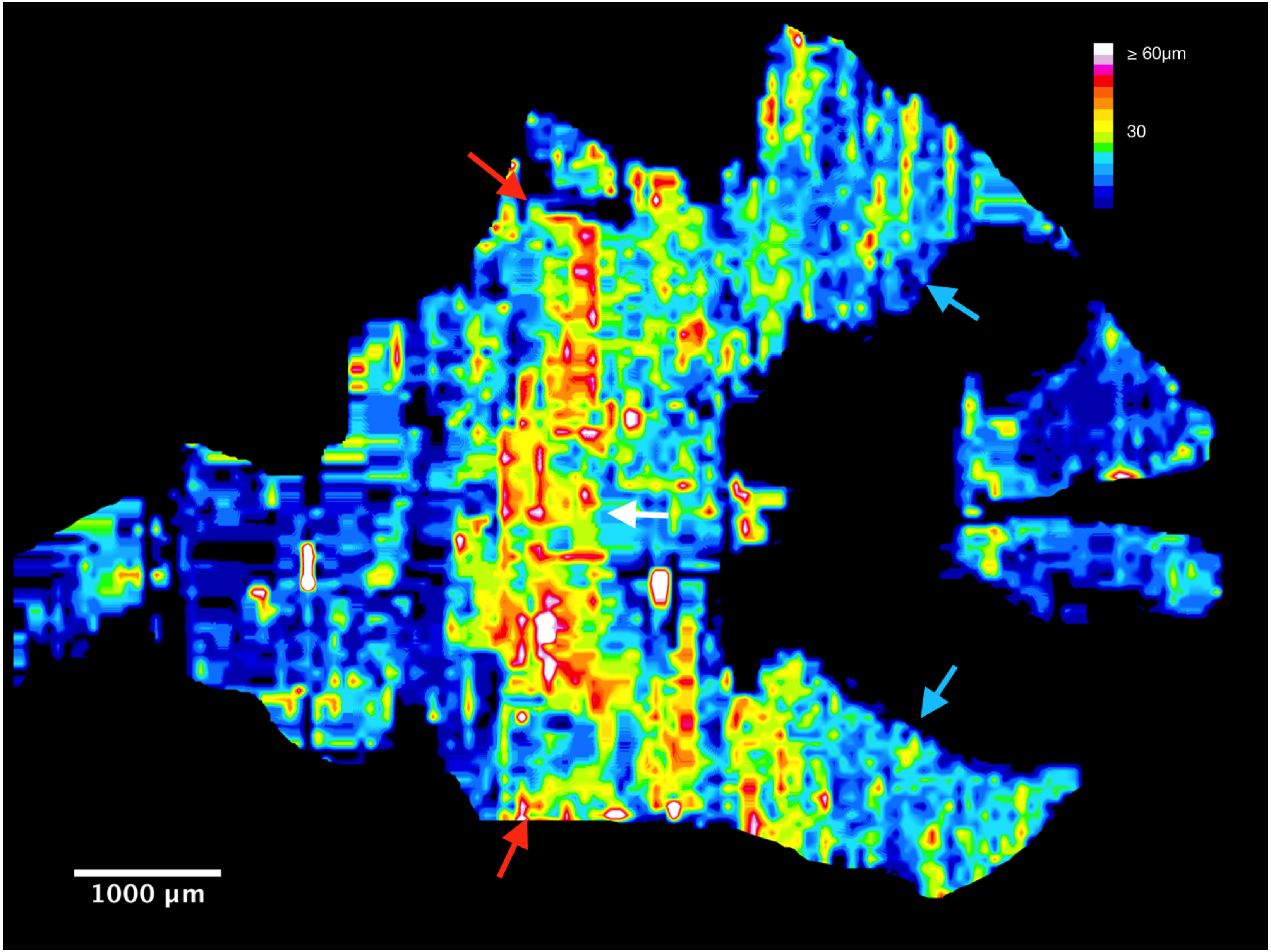

Figure 12.2: Thickness Map of Layer 2 in Sample B *Caption on page 211*

Figures 12.1 and 12.2: Thickness Map of Layer 2 in Samples A and B respectively. In both there anterior end of the frontal bone (red arrows) is thicker than the posterior end (blue arrows). The interfrontal bone also represents a local centre of thickness (white arrows). Thickness is notably not distributed in a smooth gradient, but develops in a more local fashion, consistent with independent growth of patches rather than growth organised from sutures.

12.3.2 More Layer 1 and 2 patches are found in Thicker Bone, compared to Layer 3

Figure 12.3 displays descriptive statistics of the Average L2 Patch Thickness for each Layer and sample. Interestingly, Layer 3 patches are on average 'less thick'. This is a somewhat difficult observation to comprehend, as the patches are indeed covering the same area of Layer 2. What this likely implies is that Layer 3 patches are less prevalent within thicker regions than they are in thinner regions, unlike patches of Layers 1 and 2 which appear to be more ubiquitous.

12.3.3 The relationship between area and thickness suggests synchronous and asynchronous phases of layer maturation

Small patches may be found at any point of the bone regardless of thickness, but the largest patches appear to be constrained to regions overlying intermediate Layer 2 thicknesses (Figures 12.4 and 12.5). Across all layers, there is a positive correlation between patch area and the maximum underlying thickness of Layer 2 up to approximately 10μm Layer 2 thickness, at which point each plateaus.

Above 15-17μm , the size of Layer 3 patches appears to decline relative to thickness, and the range of patch areas remains fairly constant in Layers 1 and 2. The two samples both display a decline in Layer 1 patch areas relative to Layer 2 thickness around 25μm , though this is a weak trend and does not correspond exactly. Both samples show a slight decline in Layer 2 area relative to Layer 2 thickness above 30μm of thickness, but this trend may be a result of the small number of patches with thickness above 35μm .

This trend suggests that up to 10μm patches are still spreading laterally to a great extent in each layer synchronously. A large patch area is potentially indicative of a single clone dividing and spreading across the bone, and the early trend towards this suggests a relationship between patch establishment of bone development. In intermediate bone (10-30μm) there is the broadest range of patch sizes, suggesting the most active phase of horizontal spread working in equilibrium with respect to Layers 1 and 2.

The decline in Layer 3 patch size may suggest a thinning out of Layer 3, and reduced cell division. This suggests that while horizontal spread approach equilibrium in Layers 1 and 2, emigration depletes Layer 3. In thick bones, the prevalence of large patches declines, suggesting that expanding single clone colour regions are no longer

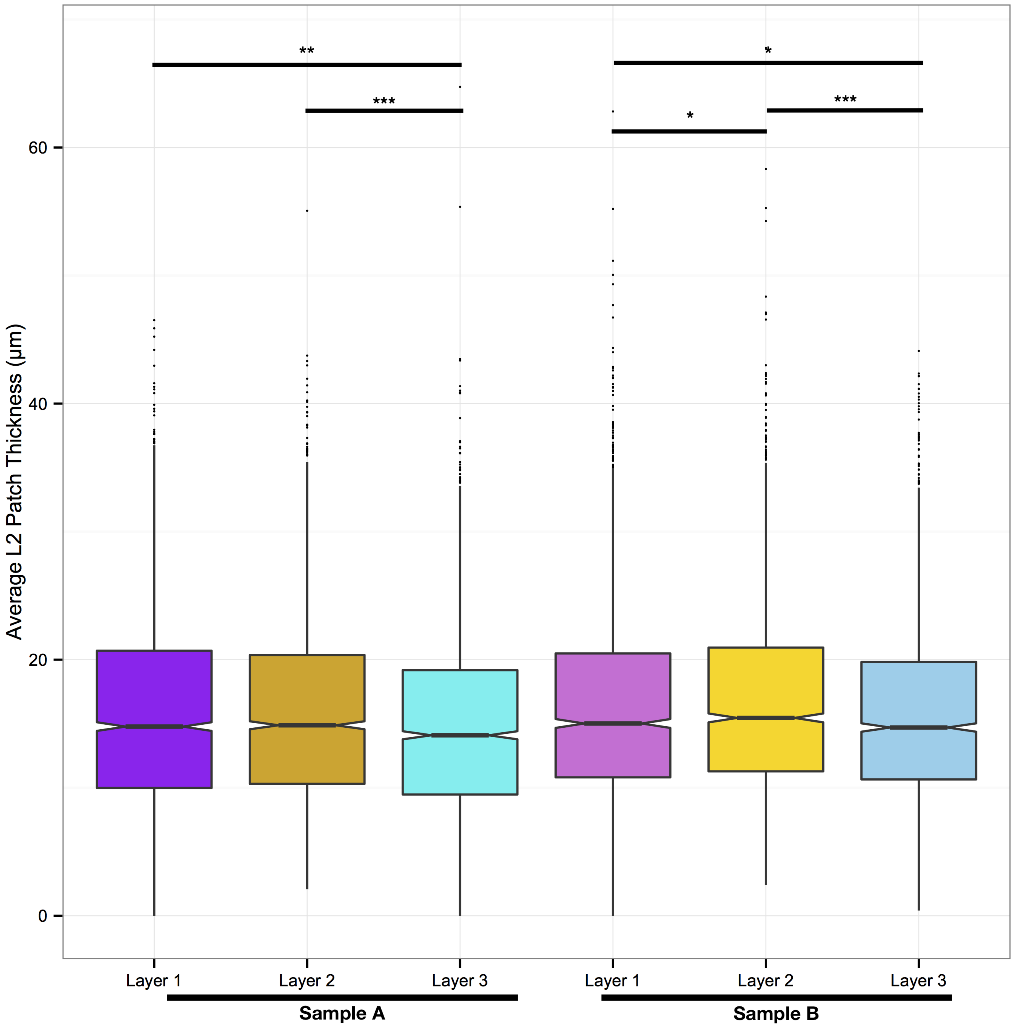

Figure 12.3: The Average L2 Patch Thickness of Layers 1 and 2 is greater than that of Layer 3. For both samples, the Layer 1 Average L2 Patch Thickness and the Layer 2 Average Patch Thickness are statistically significantly larger than the Layer 3 Average Layer 2 Patch Thicknesses. Patches of Layers 1 and 2 in Sample B are also different using the same metric, while Patches of Layers 1 and 2 in Sample A are not. While not annotated, Patches of one sample are also statistically significantly different to the corresponding Layer in the other sample. $***p\leqslant0.001$, $**p\leqslant0.01$, $*p\leqslant0.05$, Student's T-Test.

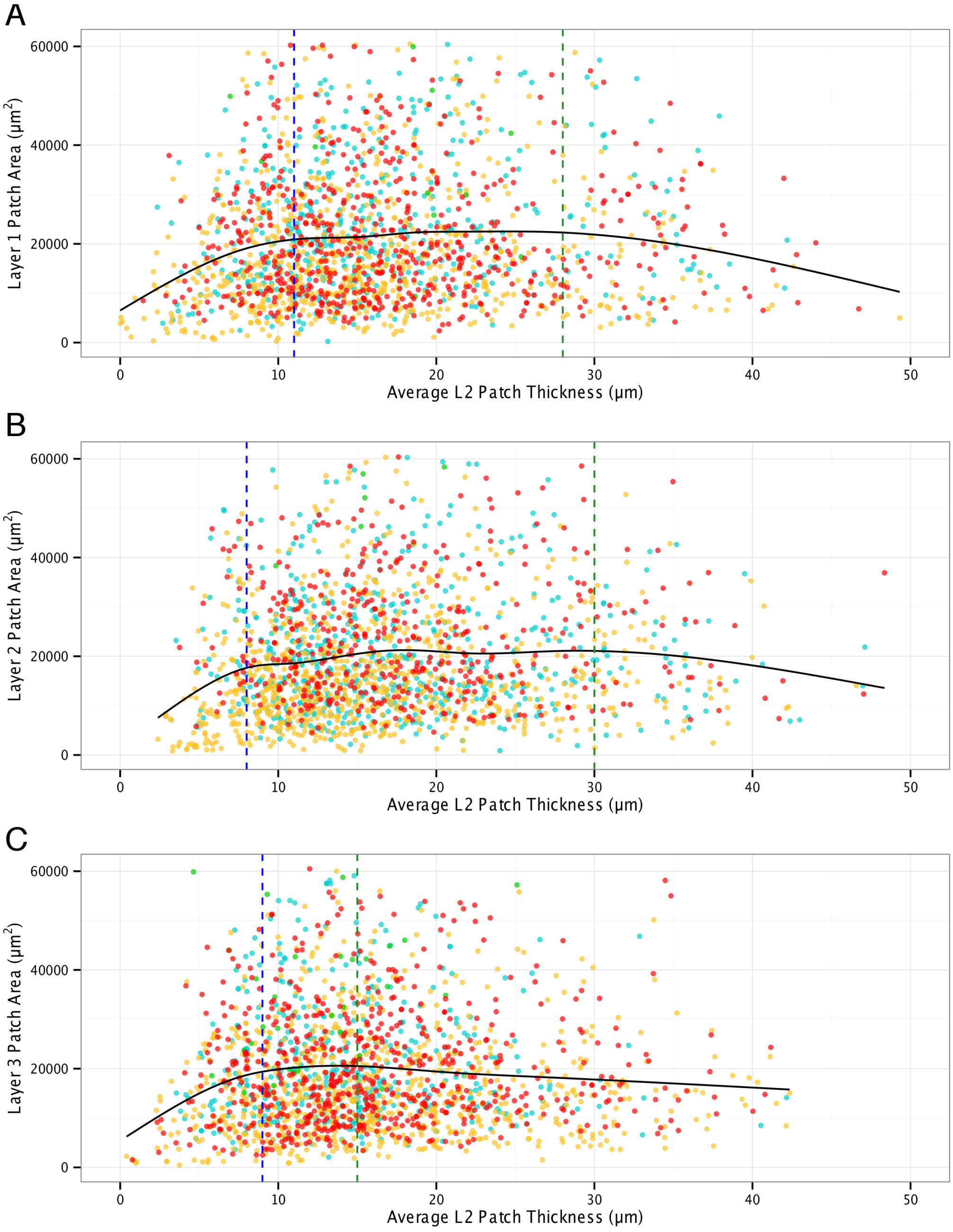

Figure 12.4: Sample A: Patch area shares a similar relationship with underlying Layer 2 thickness across all three layers. In Layer 1 (**A**), Layer 2 (**B**) and Layer 3 (**C**) there is a positive relationship between Patch Area and Layer 2 thickness up to point close to 10μm of Layer 2 thickness (blue dashed line within each). Past this point, each plateaued before declining at different thicknesses (green dashed lines). Layer 3 began to present smaller patches at the thinnest point of 15μm , with Layers 1 and 2 retaining a consistent average patch area until 27 and 30μm of Layer 2 thickness respectively.

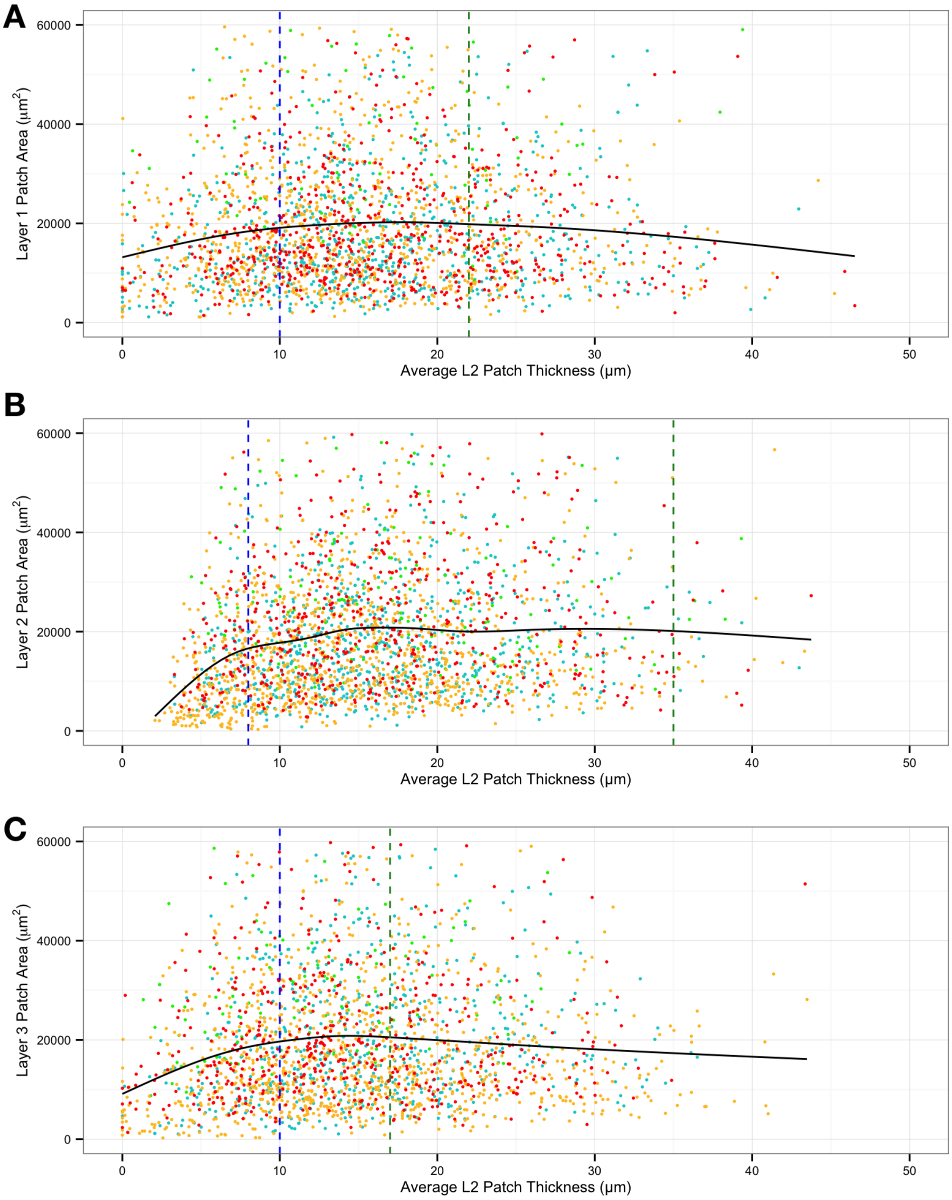

Figure 12.5: Sample B: Patch area shares a similar relationship with underlying Layer 2 thickness across all three layers. In Layer 1 (**A**), Layer 2 (**B**) and Layer 3 (**C**) there is a positive relationship between Patch Area and Layer 2 thickness up to point close to 10μm of Layer 2 thickness (blue dashed line within each). Past this point, each plateaued before declining at different thicknesses (green dashed lines). Layer 3 began to present smaller patches at the thinnest point of $17 \mu m$, with Layers 1 retaining a consistent average patch area until $22 \mu m$. Layer 2 only marginally declines after $35 \mu m$.

dominant, and may be disrupted by emigration, invasion, horizontal spread and Layer 2 trabeculation.

12.3.4 Cell Density changes suggest three phases of layer maturation, with synchronous and asynchronous components

Figures 12.6 and 12.7 contain the most revealing trends. In each except 12.7A & A', density has a sharp negative correlation with Layer 2 thickness up to around $10\mu m$, suggesting an synchronous initiation phase in which tight clusters of cells creates a small patch before spreading. The inconsistency of 12.7A & A' is due to a group of patches close to the origin of this graph, without which the profile of the points matches that of 12.6A & A'.

Above this point there is a general trend towards declining density relative to thickness. The rates at which this occurs are different, but in both samples there is a synchronised rate change: at $15\mu m$ of thickness in Sample A, and $20\mu m$ of thickness in Sample B. This suggests that a process linking the layers influences redistribution of cell density in bone of these thicknesses.

Figures 12.8and 12.8B show that cell density does not appear to change greatly with area, except in small patches where density is higher and decreases with size. This likely represent newly initiated regions where cells are only just beginning to divide, possibly having migrated from another layer. This would also suggest that new patches undergo an initial phase of cell division that creates a small patch of high density, followed by a phase of rapid lateral spread, reducing density, before further cell division reaches equilibrium with cell number changes.

The lack of a strong trend would suggest that cell density is somewhat homeostatic, with division and passive or active movements of cells balancing out in mature regions. What changes there are appear to be a result of the far stronger trends shown in Figures 12.4 - 12.7, with very small patches correlating with very thin bone, which also correlates strongly with high cellular density. The weak association between area and cell density is thus likely secondary, and cell density appears to be broadly homeostatic with respect to patch area,

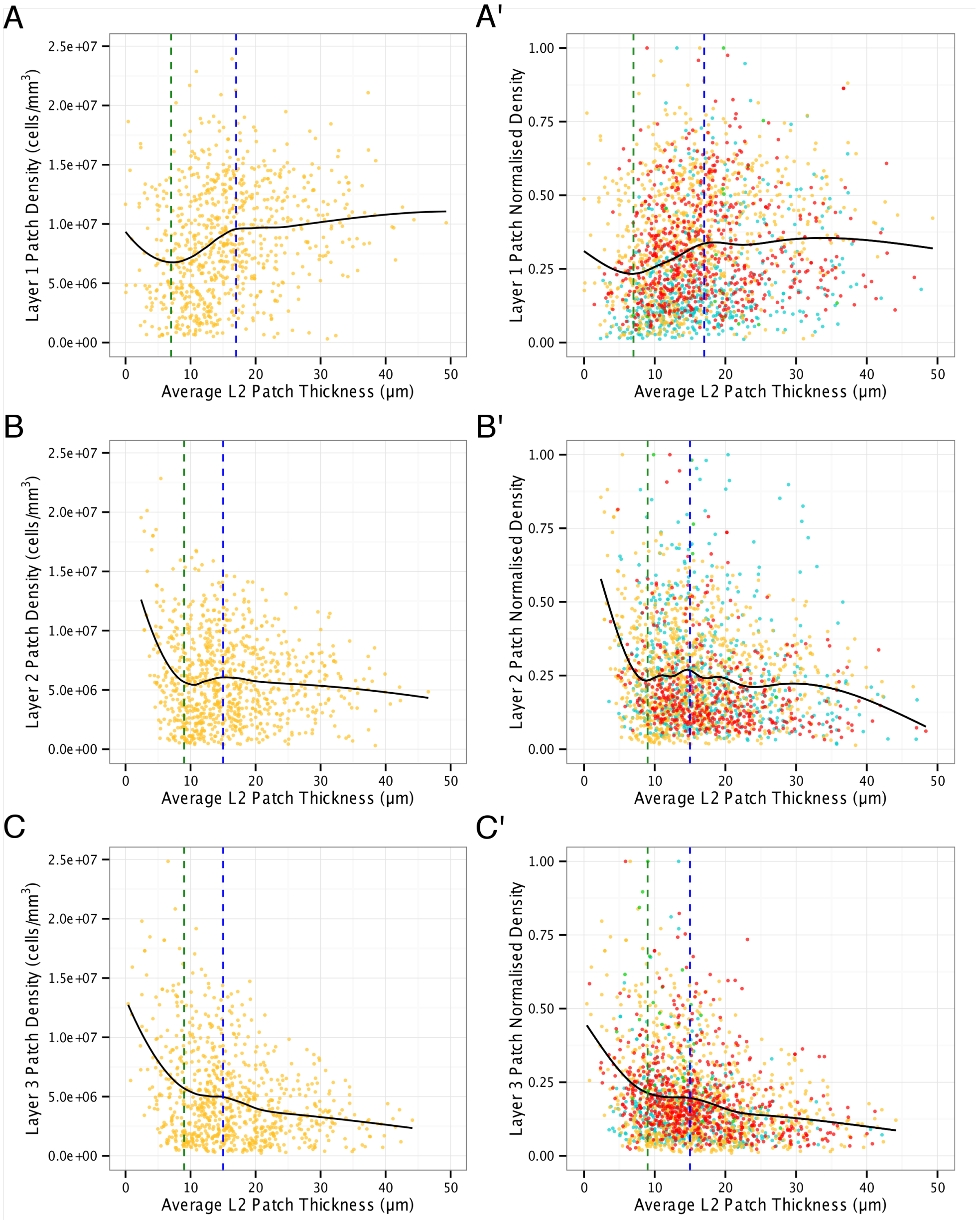

Figure 12.6: Sample A: Cell Density is related to Layer 2 thickness across Layers 2 and 3. Patches from Sample A, comparing Average Layer 2 thickness to cell density. Absolute densities for yellow patches (**A-C**) are provided for comparison to overall normalised densities (**A'-C'**). Across all three layers there is an initial negative correlation up to a thickness just below 10μm (green dashed line), with this effect most pronounced in layer 2. Past this point, in Layer 1 (**A** and **A'**) There is a subsequent positive relationship with thicker bone having denser patches up to 17μm (green dashed line), at which point average density plateaus. Within Layer 2 (**B** and **B'**) and Layer 3 (**C** and **C'**). There is a plateau of Density between 9 and 15μm of Layer 2 thickness, followed by a further negative correlation, with thicker bone having lower cell density.

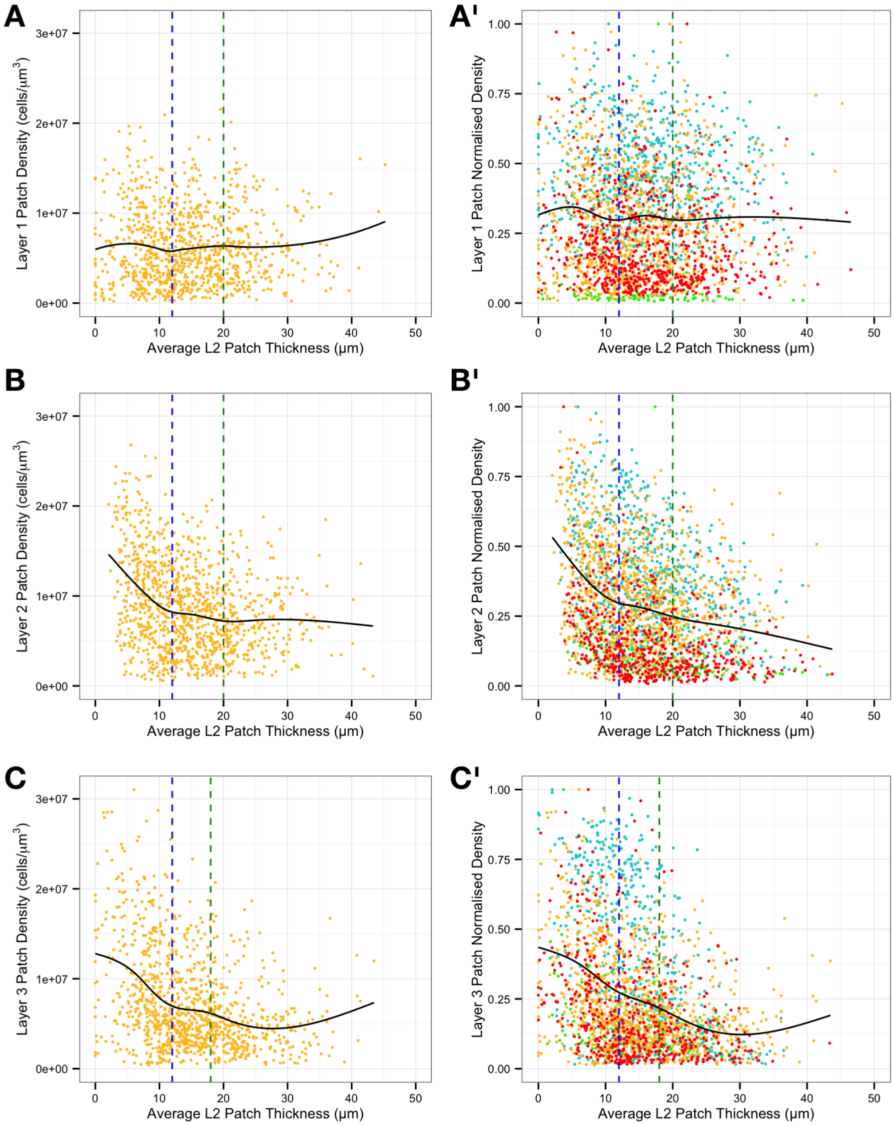

Figure 12.7: Sample B: Cell Density is related to Layer 2 thickness across Layers 2 and 3. Patches from Sample B, comparing Average Layer 2 thickness to cell density. Absolute densities for yellow patches (**A-C**) are provided for comparison to overall normalised densities (**A'-C'**). In Layer 1 (**A**) density is approximately even across all thicknesses, but does display fluctuations around the thicknesses that see inflections in other layer trends. In Layer 2 (**B**) and Layer 3 (**C**) there are precipitous declines in cell density relative to thickness up to $12\mu m$ of thickness, after which both decline at different rates. These rates change around $20\mu m$ of thickness, with Layer 2 declining more slowly and Layer 3 declining more rapidly.

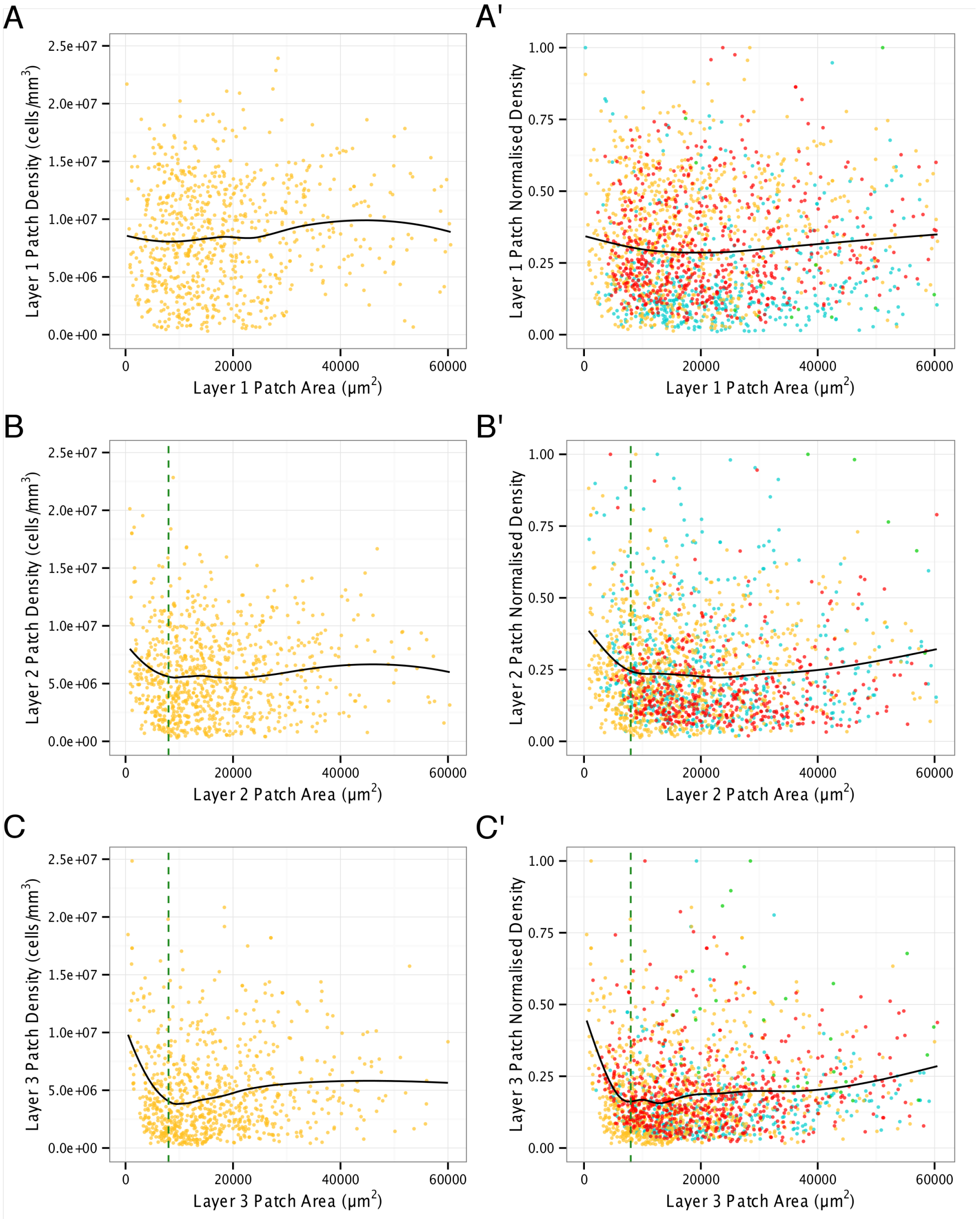

Figure 12.8: Sample A: Cell Density has no strong relationship with Patch Area across the three layers. Sample A patches, comparing area with cell density. Absolute densities for yellow patches (**A-C**) are provided for comparison to overall normalised densities (**A'-C'**). The smallest patches in Layer 2 (**B & B'**) and Layer 3 (**C & C'**) appear to have higher cell density, declining sharply before stabilising at $8000\mu m^{\ 2}$ (green dashed line). This feature is far less pronounced within Layer 1 (**A & A'**). Past this point each layer appears to have a weak positive correlation, with larger patches having higher cell densities, but this is a very slight relationship with a great range.

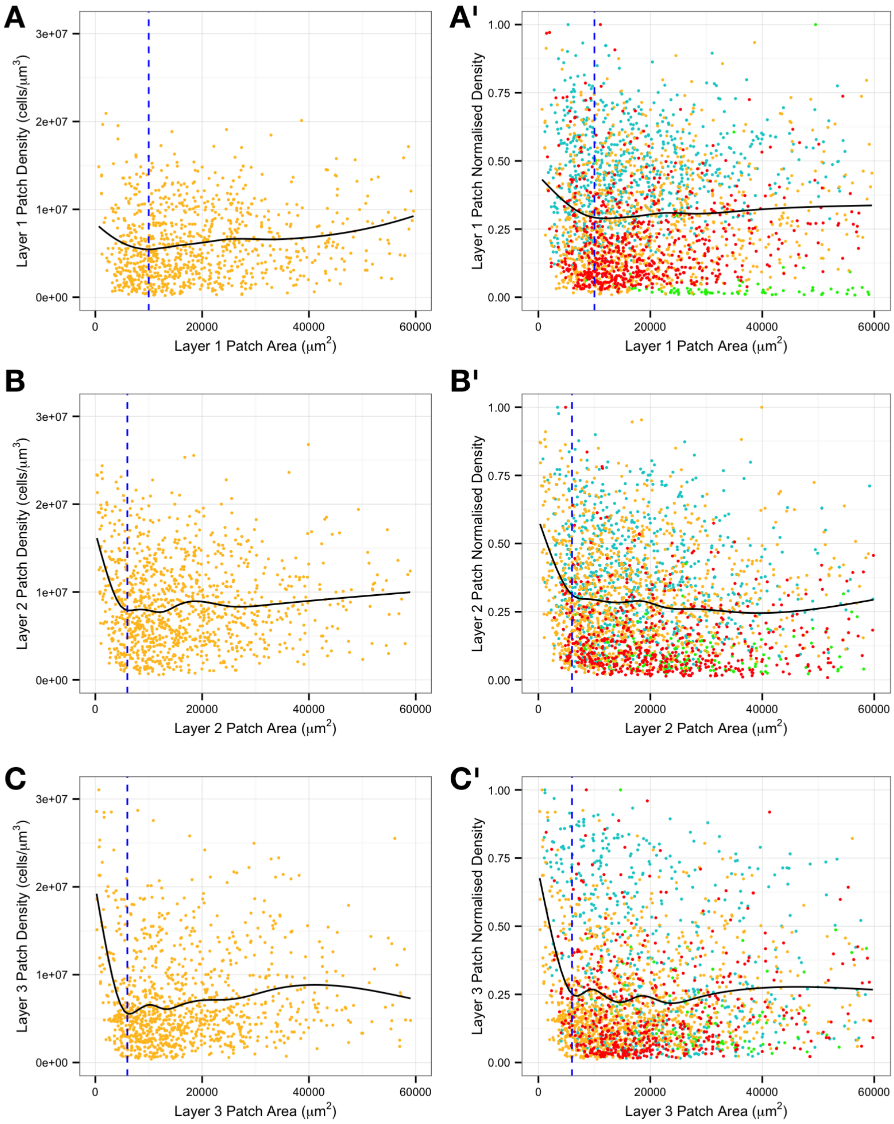

Figure 12.9: Sample B: Cell Density has no strong relationship with Patch Area across the three layers. Sample B patches, comparing area with cell density. Absolute densities for yellow patches (**A-C**) are provided for comparison to overall normalised densities (**A'-C'**). The smallest patches in Layer 1, (**A & A'**), Layer 2 (**B & B'**) and Layer 3 (**C & C'**) appear to have higher cell density, declining sharply before stabilising at $10000\mu m^{2}$ in Layer 1 and $6000\mu m^{2}$ in the other layers (blue dashed lines). Layer 1 has the weakest initial decline.

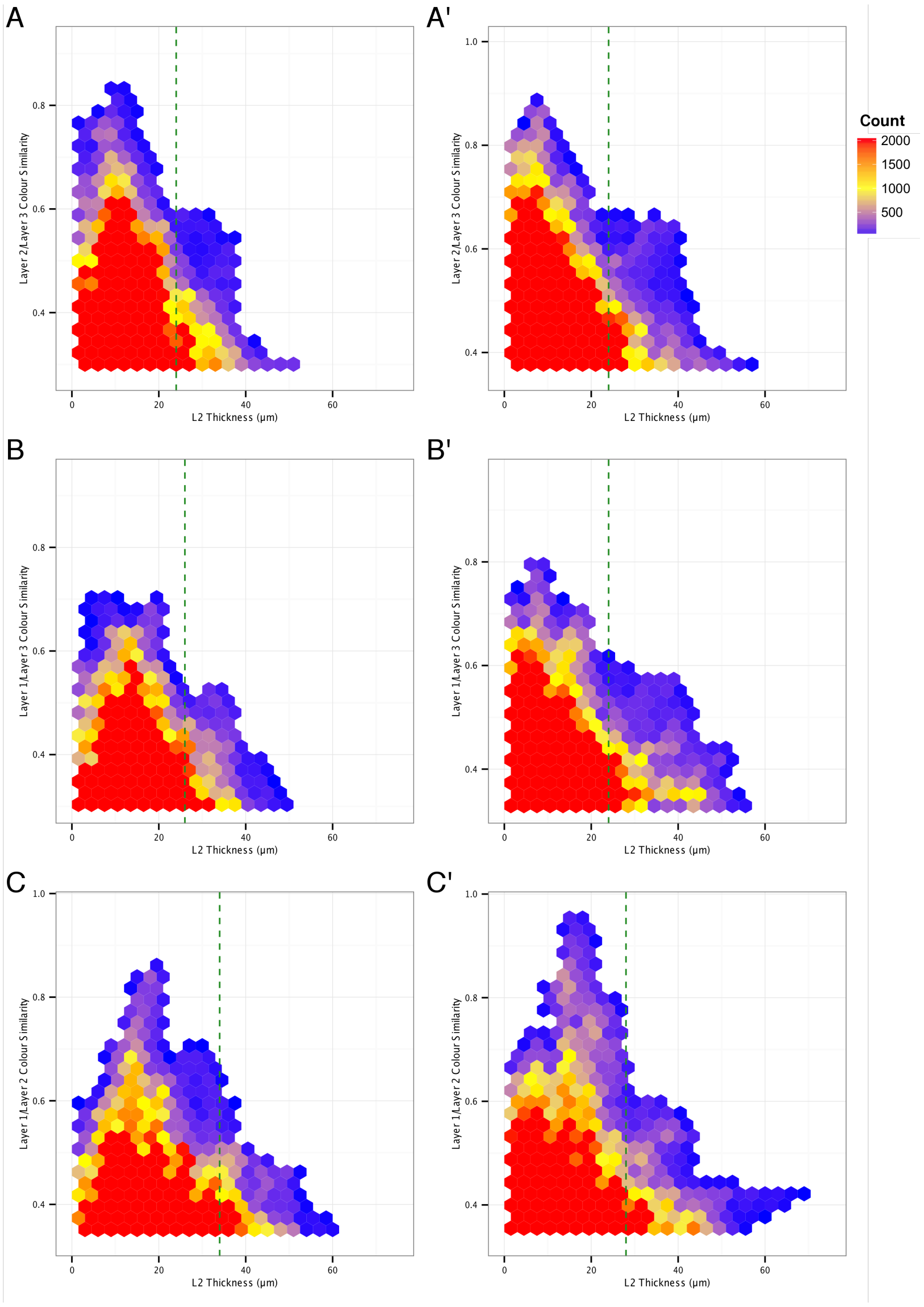

Figure 12.10: Colour Similarity Between Layers Plotted Against Layer 2 Thickness. Sample 1: A, B, C; Sample 2: A', B', C'. In each case, the strongest matching 10% of pixels are plotted. The same relative Y scale is used in each, though the origin changes. 95% of pixels lie to the left of the green dashed line in each plot. **A and A':** In both samples colour similarity between Layers 2 and 3 is found in regions with 10μm Layer 2 Thickness. **B and B':** In both samples strong colour similarity between Layers 1 and 2 is found at regions of 15-20μm Layer 2 thickness. **C and C':** L1 and L3 matching is more dispersed across a wide range of Layer 2 Thicknesses, though noticeably strongest in the range of 10-20μm.

12.3.5 Preferential layer communication is linked to the thickness of the deposited biomineral

The most parsimonious explanation for similar colour composition in two overlapping regions of bone is vertical invasion of cells between layers. As such, colour matching can be used as a proxy for vertical invasion, and this can be compared to other characteristics of the bone. Figure 12.10 explores the relationship between colour matching and thickness of Layer 2, and thus allows for exploration of which layers are communicating at different stages of bone development. Both samples show identical trends, which implies that any such observations are reliable.

Below 10μm Layer 2 thickness, bone can be considered very immature, with Layer 2 effectively represented as a thin border between Layers 1 and 3 with a small number of encroaching cells. At this stage, those cells in Layer 2 appear to best match Layer 3, implying that this is the generative layer for invasive clones. There also appears to be invasion between Layers 1 and 3, which may account for the matching between Layers 1 and 2, a possibility that will be explored through less abstract examples. At around 10-15μm of Layer 2 thickness, Layer 3 to 2 similarity is at its highest levels, implying that Layer 3 to 2 invasion is the most important process for population of Layer 2 up until a certain stage of local maturation.

At approximately 15-20μm Layer 2 thickness, Layer 1 and 2 matching appears to be the dominant characteristic. This may represent a shift in the characteristics of invasion such that Layer 1 takes over from Layer 3 as the main source of invading cells into Layer 2. As previously, Layer 1 and 3 matching remains relatively high, suggesting that communication is maintained between these layers.

Above 20μm thick Layer 2, colour matching tails off across all three layers. There is a notable population at approximately 35μm thickness where there is a significant degree of matching between Layers 1 and 2 (B and B') and Layers 1 and 3 (C and C'), though this is not substantially represented as a match between Layers 2 and 3 (A and A'). This suggests either that there is invasion from Layer 1 into both layers, but with the two invading populations being effectively isolated, or perhaps more likely that Layer 1 to 2 invasion entirely replaces Layer 3 to 2 invasion while cells from Layer 3 still travel to Layer 1 without contributing to the population of Layer 2.

12.4 Summary: Clonal Dynamics Change as the Bone Grows Thicker

From these plots a model of patch formation can be inferred for each layer. As Layer 2 thickness is a proxy for stage of bone development, changes in patch dynamics can be explored along this axis. In brief this points to three general phases for dermal bone growth: an initial invasion from Layer 3 into Layers 1 and 2, followed by a progressive movement towards Layer 1 supplying Layer 2 before each layer becomes largely independent above $30\mu m$ of growth. These three broad phases of invasion are depicted in Figure 12.11 and changes in patch dynamics of each layer discussed below.

12.4.1 A common synchronous phase of layer establishment

In all three layers the patches at the very thinnest areas of bone are very dense (Figure 12.6) and very small (Figure 12.4). This would be suggestive of a disorganised and random collection of cells dividing without spreading. As bone thickens, some patches expand laterally in proportion, though small patches are still present, which may represent either pre-existing patches that do not spread, or the appearance of novel patches as a result of invasion between layers.

The initial loss of density is least pronounced in Layer 1 (Fig 12.6), though there is not a commensurately lesser degree of lateral spread (Fig. 12.4), while Layers 2 and 3 show remarkably similar profiles, despite the fact that by definition Layer 2 is multiplying in volume as it thickens. Given equal cell division and no invasion, one would expect Layers 1 and 3 to show the same trends with Layer 2 losing cell density fastest. These results would suggest that Layer 3 is perhaps donating cells to other layers early on, which may be depressing the rate cell density loss in the other two layers. This process appears to dominate up to $10\mu m$ of Layer 2 thickness.

12.4.2 Layer 1 Patch Maturation

Following the common initiation phase, Layer 1 patches increase in cell density up to $17\mu m$ of Layer 2 thickness, at which point average cell density levels out. There is no commensurate change in patch area dynamics at this level of thickness, which suggests that a level of equilibrium density is reached, almost certainly facilitated by emigration of surplus cells into Layer 2, evidenced by their strong matching in

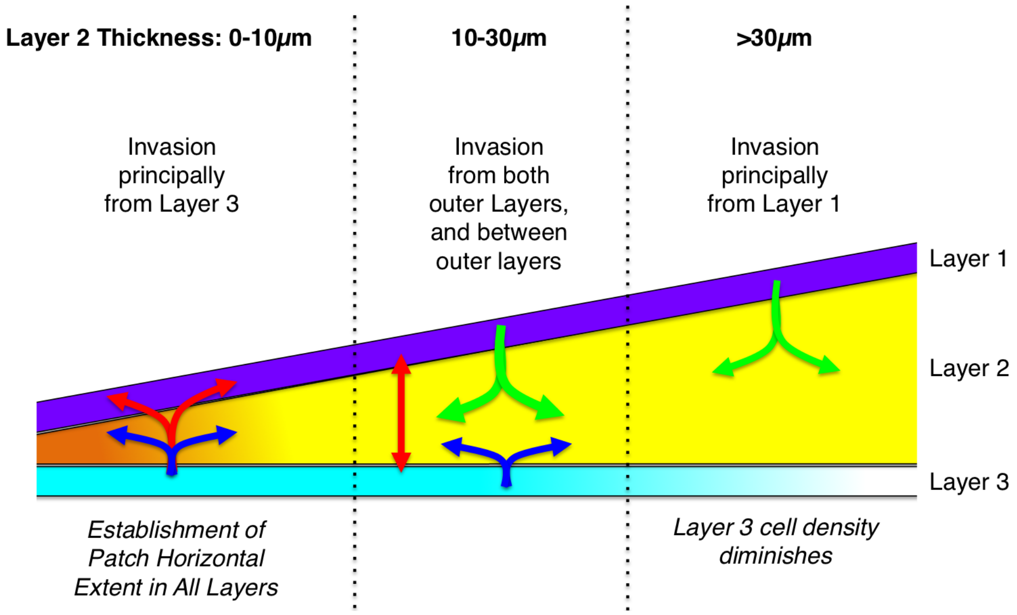

Figure 12.11: Three broad phases of invasion between layers. Below $10\mu m$ of L2 thickness, Layer 3 is dense with cells and has strong layer matching, and thus mostly likely populates the other layers. During this phase, horizontal spread defines the edges of patches across all three layers. Eventually Layer 1 contributes more to Layer 2 through invasion, supplanting the diminishing Layer 3 once the biomineral is at least $30\mu m$ in thickness.

intermediate bone. In very thick bone, the range of cell density reduces towards this average, which suggests that the mature L1 is more homogeneously dense than the other layers.

Patch area seemingly has little to no relationship with cell density or Layer 2 thickness, suggesting that lateral spread acts independently of these processes and maintains a similar range of density regardless of how developed the bone is. This homeostasis of density with respect to area suggests a relationship between lateral spread, cell division and vertical invasion that regulates cell density, though clearly there is still a broad range of density within Layer 1.

12.4.3 Layer 2 Patch Maturation

Above $10\mu m$ of thickness, Layer 2 is approximately stable following the initial decline (Fig. 12.6). As volume is increasing which would decrease cell density, this would suggest either invasion of cells into Layer 2 or rapid cell division. Cell density peaks again at $15\mu m$ of Layer 2 thickness before declining, which may represent the onset of trabeculation, which by establishing large cell free regions would by definition decrease cell density. This is synchronised with a decline in Layer 3 cell density (blue dashed lines in 12.6B' and C'). The decline in cell density relative to thickness is slow up to about $30\mu m$ of thickness when it becomes far more rapid.

After a brief initiation period it would appear that cell density of Layer 2 patches has only a weak positive correlation between cell density and patch area. The largest patches within Layer 2 are principally found within regions of intermediate thickness around $20\mu m$, which also correlates with relatively high cell density. Thus these intermediate regions where initiation has completed but trabeculation has not yet reduced cell densities likely account for the weak upward trend of Fig. 12.8.

12.4.4 Layer 3 Patch Maturation

Above $10\mu m$ of thickness, Layer 3 cell density briefly plateaus before continuing to decline above $15\mu m$ of Layer 2 thickness. This also corresponds with the point at which Layer 3 patch area begins to decline relative to thickness. This would suggest that above $15\mu m$ of Layer 2 thickness, Layer 3 is already relatively mature, and does not undergo any further drastic changes while slowly declining in cell density and degree of contiguous lateral spread.

12.4.5 Relationship between Layer matching and Thickness correlates with patch characteristics

The key regions identified within Figure 12.10 have remarkable correspondence with the landmark stages of development with respect to thickness outlined by the patches, in which the regions below $10\mu m$ of Layer 2 thickness were identified as undergoing an initiation phase. This appears to correspond with Layer 2 and 3 matching, and Layer 1 and 3 matching, suggesting emigration from Layer 3 into the other layers that would account for the precipitous drop in cell density of this layer observed in Figure 12.6, and the lesser drop of Layer 2 density in the same figure despite expanding volume.

The 15-$17\mu m$ thickness range marks a number of interesting features in the both independent approaches. In the patch-based approach this corresponds with the start of decline in Layer 3 patch areas, and changes in cell density dynamics across all layers and both samples. This range corresponds with a huge increase in Layer 1 and 2 matching, the apex of Layer 1 and 3 colour matching and the decline of a Layer 2 and 3 matching. This suggests that Layer 3 is undergoing further depopulation at the expense of patch cohesion, while Layer 1 becomes more important in feeding the expanding Layer 2 with new cells.

The final great trends within layer matching occur above $30\mu m$ of Layer 2 thickness, where in general there is a decline between all layers, with Layer 1 and 2 matching retaining the most influence in the thickest bone. This is in part likely due to later invasions representing infiltration of a far more populous and distinct population rather than replacement or initiation of a new colony from the same material. The persistence of communication between Layers 1 and 2 is reflected in a declining relationship between area and thickness in these layers in very thick bone, suggestive of invasions breaking up patches, though this is only a weak trend.

12.4.6 Conclusions

The data demonstrates that bone development is principally organised around, and thus predictive of, changes of Layer 2 biomineral thickness. Below $10\mu m$ all three layers undergo a synchronous period of establishment, with high density groups of cells spreading out and losing density rapidly. Above this point the three layers diverge in their characteristics. Layer 3 progressively loses density as it donates cells to other layers in younger bone and becomes more quiescent in more developed bone.

Layer 1 stabilises as a dense layer that is broadly homeostatic and homogenous. Layer 2 undergoes changes of density and degree of lateral spread that are linked to changes in the proportion of vertical invasion, which is initially from Layer 3 but progressively changes to come from Layer 1.

Excitingly, these findings also decouple the degree of horizontal spread from the degree of thickness growth, as this appears to be largely defined within the earliest stages of patch development. This suggests that new populations may be established, spread and contribute to lateral bone growth while generating local regulation of the developing bone thickness. A large patch with many cells may be held in a relatively immature state until the developmental program requires it to activate thickness growth. This plasticity lends further support to the concept of these clonal patches as developmental modules of the bone.

While the magnitude of horizontal spread of a patch and vertical invasion are not linked after the initiation phase, the previous Chapter demonstrated that patches within the different layers are spatially organised around points of invasion. This can be integrated with the findings of this chapter to give the model presented in Figure 12.12 This must furthermore represent a shifting and dynamic landscape, as there is certainly not a perfect correspondence between patch centres in all layers in all parts of the bone. Rather, the development of large dermal bones appears to consist of a communal output from the integration of many cryptic patch modules.

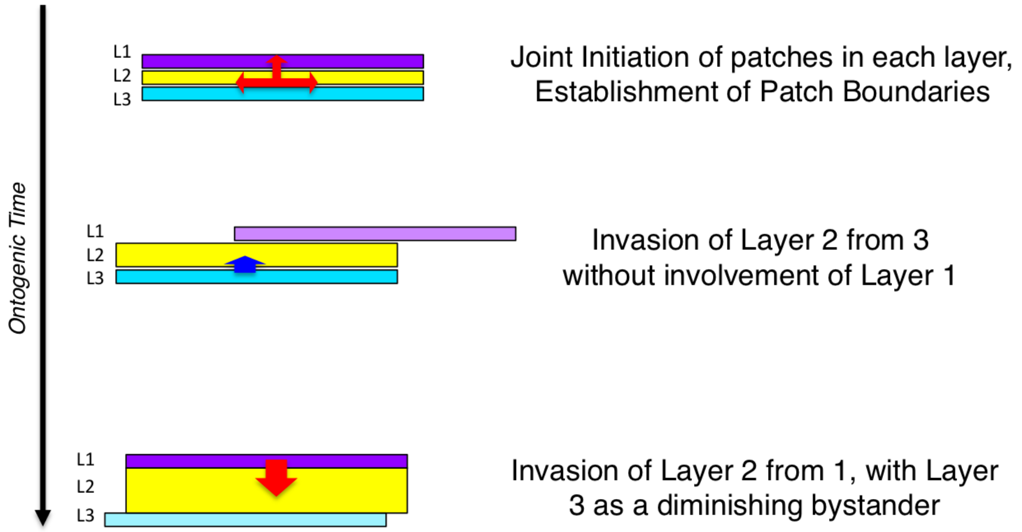

Figure 12.12: Layer invasion and patch dynamics are linked processes. Early patch development consists mostly of invasion from Layer 3 and horizontal spread in all layers to establish the patch. Layer 3 initially inflates Layer 2 by invasion, while Layer 1 develops independently of this. Later when the bone is thicker, Layer 1 becomes the principal donor of cells to Layer 2, as Layer 3 diminishes.

Chapter 13

Clonal Architecture of Muscle Attachment Regions

13.1 Introduction

Some of the most complex discussions in developmental biology centre around how different tissues come to be integrated in the mature organism. The coordination of entheses or muscle attachment regions is one such complex problem. With the exception of the tongue, every skeletal muscle in the body must attach to two bones in a specific position. These connections must be accurate and strong to ensure that appropriate force can be transduced through them.

Kontges and Lumsden [1996] showed that each muscle must attach to a region of the same rhombomeric origin: an 'organisation by origin'. It was later demonstrated that Cranial Neural Crest cells are not necessary for early craniofacial muscle development, but are required for proper muscle attachment [Rinon et al., 2007]. While Jordan [2011] demonstrated that muscle attachment sites have a structurally distinct Layer 1, termed Layer 1-Attachment it is still unknown how different cell populations interface at the enthesis. The existing model of muscle attachment is presented in Figure 13.1

The precise mechanism and role for neural crest cells in integrating muscle with bone in the head has not yet been described. While Layer 1 is clearly structurally different, it is not clear whether this is a simple adaptation of existing cells, or if the layer is replaced by a different population integrating into the bone. Confetti provides these answers. The classical understanding of the enthesis is that the tendon is a distinct structure from the bone, and attaches to it. If this is the case, then the bone, tendon and muscle will not be of the same colour. If they are, this implies that one population forms an effectively novel organ, integrating both into the bone and the muscle to establish a physical connection.

13.2 Methods

This section utilises the flattened cell maps and thickness maps described in Chapters 8 and 12 respectively, and density-corrected ratio mode invasion maps as described in Chapter 10. The regions represented are shown in Figure 13.3. The scale for Layer 2 thickness map colours is shown in Figure 13.2.

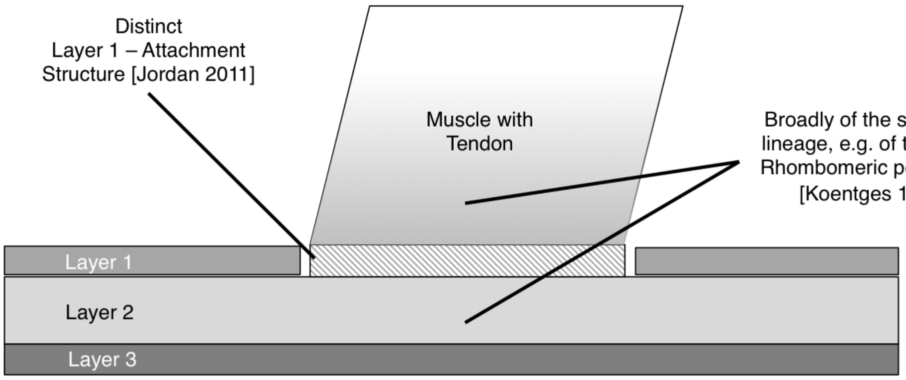

Figure 13.1: Current Model of Enthesis Structure. Kontges and Lumsden [1996] demonstrated that facial muscles only attach to bone of the same rhombomeric origin, and thus must have some organisation by origin. Jordan [2011] further demonstrated that there is a distinct structure termed Layer 1 - Attachment at the enthesis.

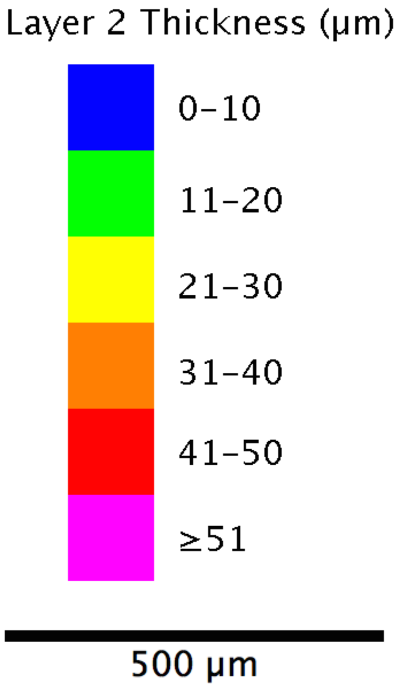

Figure 13.2: Colour Scale of Layer 2 Thickness. Used in subfigure D of the upcoming Figures 13.4-13.7.

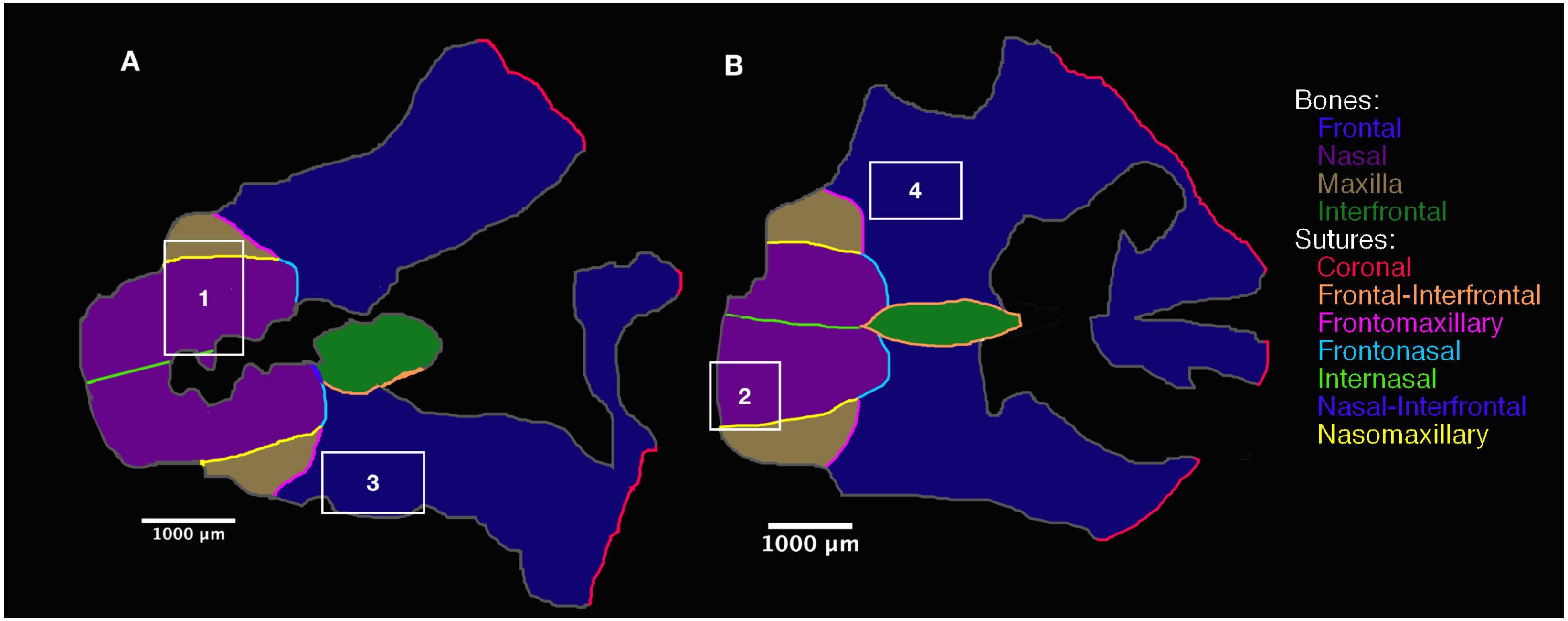

Figure 13.3: Muscle Attachment Regions investigated. 1 - Procerus and nasal bone, Sample A, analysed in Figure 13.4. 2 - Procerus and nasal bone, Sample B, analysed in Figure 13.5. 3 - Muscle medial to eye socket attaching to frontal bone, likely the orbis orbicularis, analysed in Figure 13.6.

13.3 Results

13.3.1 Muscles attaching to the nasal bone share a common lineage with an island of bone they attach to.

Figure 13.4 represents a muscle attachment region on the right nasal bone of Sample A, likely associated with the Procerus. Residual cyan-labelled muscle fibres are visible. Within the bone, there is clearly a cyan-dominated territory within a yellow and red region. There is a visible gap around this region, suggesting incomplete integration of the attachment bone and the nasal bone. Within Layer 2 (Fig. 13.4B) there is a distinct organisation into a cell-rich honeycomb, distinct from the surrounding bone. Cyan cells are starkly sparse in Layer 3 (Fig. 13.4)C, which has almost no distinction between the attachment site and the surrounding bone. There are clearly some knots of cells penetrating this deeply, but little invasion.

Colour Matching analysis further confirms these observations. The majority of the muscle attachment region displays matching of Layers 1 and 2, and suppression of 2 and 3 association. Only peripheral points have matching of all three layers, which correspond with dense knots of cells even in Layer 3. This suggests that there is a common cyan-dominated lineage that gives rise both to the attaching tendon and muscle, and to the Layer 1-Attachment Region. This furthermore penetrates deep into the bone, with a few anchoring points penetrating all the way to Layer 3.

Figure 13.5 represents a similar enthesis from the other sample, with a similar difference of lineage between attachment region and bone. Even in this instance, the distinct line around the region can be observed within Layer 1. The attachment region has a higher proportion of red cells than surrounding bone. Roundels of green within red are visible within this region. Only one centralised point of three-layer matching can be observed.

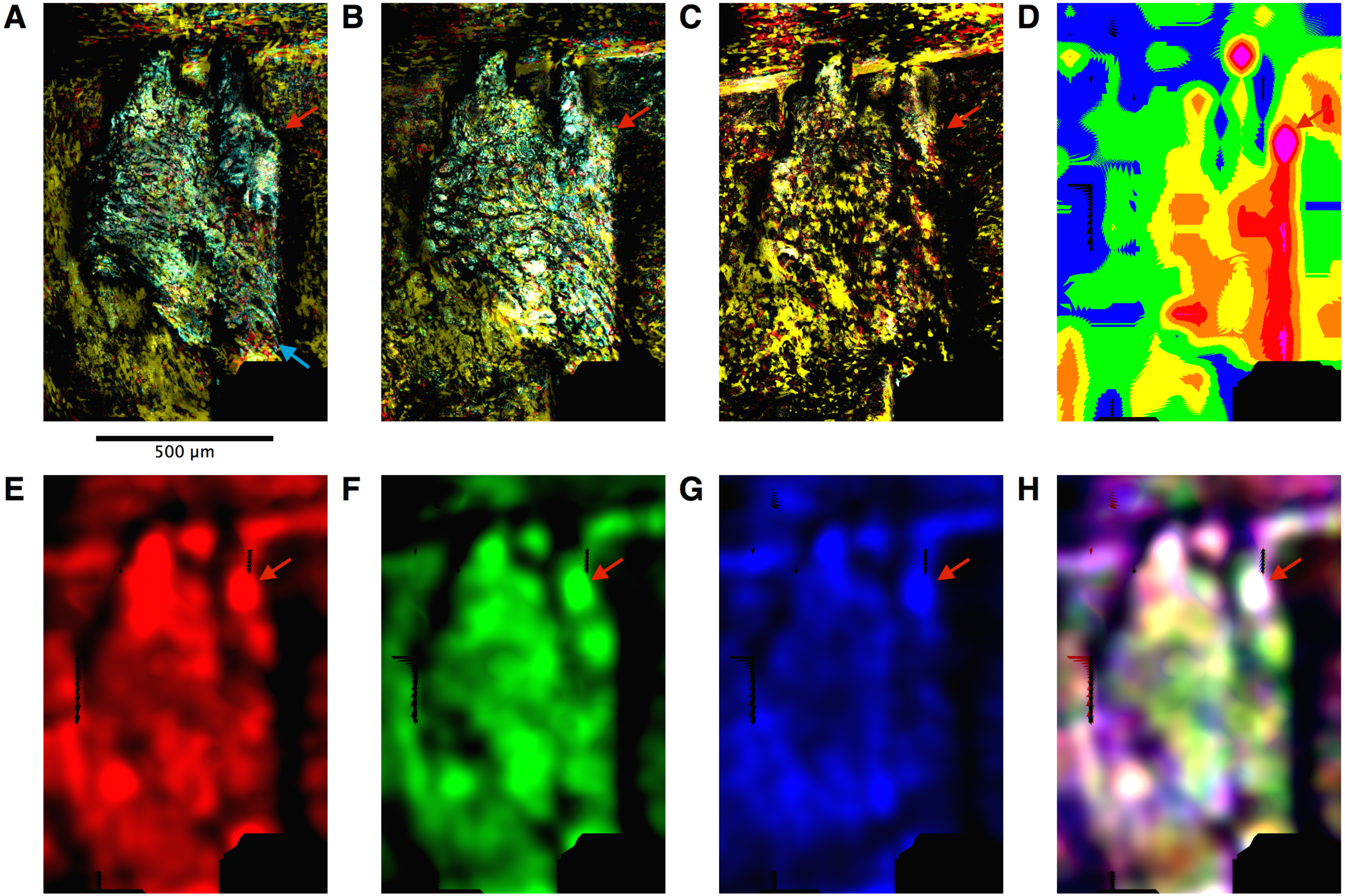

Figure 13.4: Sample A Muscle Attachment Region on Right Nasal Bone in Detail *Caption on page 236*

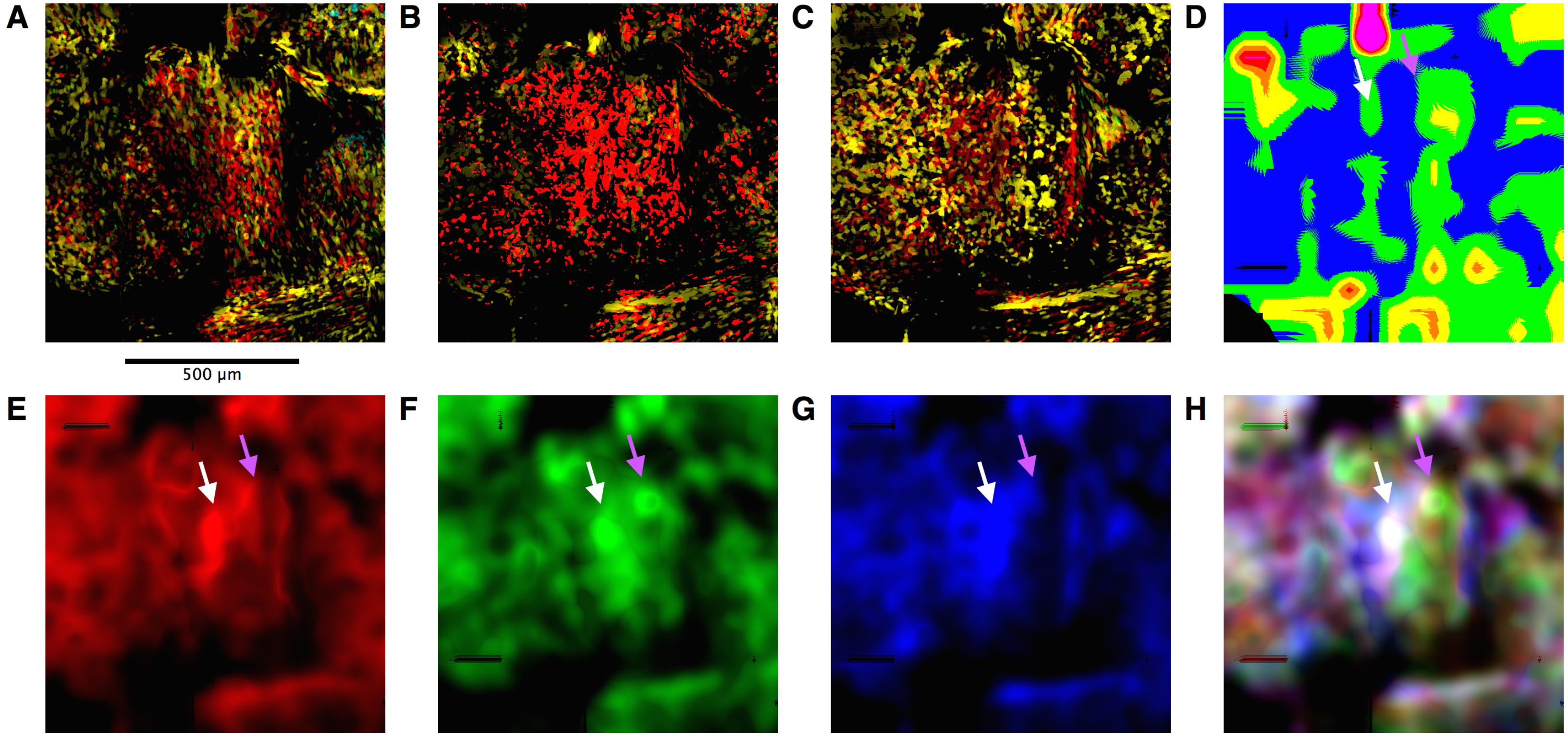

Figure 13.5: **Sample B Muscle Attachment Region on Left Nasal Bone in Detail** *Caption on page 236*

Figure 13.4: Sample A Muscle Attachment Region on Right Nasal Bone in Detail Scale bar is accurate for all images. **A:** Flattened representation of Layer 1. **B:** Flattened representation of Layer 2. **C:** Flattened representation of Layer 3. **D:** Heatmap of Layer 2 Thickness. **E:** Relative colour similarity between Layers 1 and 3. **F:** Relative colour similarity between Layers 1 and 2. **G:** Relative colour similarity between Layers 2 and 3. **H:** Overlay of subfigures E-H. The muscle attachment region in the centre of the image is markedly different to the surrounding bone. A Cyan and Green population dominates Layers 1 and 2, without penetrating into Layer 3 which is similar to the Yellow and Red dominated surrounding bone. The structure of Layer 2 is arranged into a honeycomb while the surrounding bone is more homogenous. The muscle attachment region is markedly thicker than the thin bone to the left (anterior) of the region. Within the colour matching comparisons, the nasal bone is very heterogenous, while the muscle attachment region is largely dominated by Layer 1 and 2 matching, with the other layers matching only where dense knots of cells run through all three layers (*e.g.* red arrow). Possible residual muscle fibres share the same colour as Layer 1 (blue arrow).

Figure 13.5: Sample B Muscle Attachment Region on Left Nasal Bone in Detail Scale bar is accurate for all images. Subfigure lettering same as above. This region represents a red-labelled muscle attaching to a red and yellow labelled bone. The density of red cells is noticeably greater in Layers 1 and 2 within the region of muscle attachment in the centre of the image when compared to the surrounding bone. There is no apparent correspondence between the thickness of Layer 2 and the point of muscle attachment, with the thickest regions running along the midline, at the top of the image. Within the muscle attachment region, the colour matching is organised such that strong Layer 1 and 2 matching is ensheathed by 1 and 3 matching, with 2 and 3 matching in the regions between these nested points. In the surrounding bone, colour matching is more heterogenous, with a three-layer matching creating a white line in the overlay that follows a suture running through the bottom of the image parallel to the anteroposterior axis. As above, there are points of three-layer matching (white and purple arrows) which are slightly thicker than surrounding bone, though this time apparently within the enthesis rather than at the periphery.

13.3.2 Muscles attaching to the frontal bone around the eye share a common lineage with an island of bone they attach to.

The same patterns are displayed within Figure 13.6 which shows a muscle attaching to the frontal bone above the eye socket. In this instance, a red and green attachment population is penetrating a yellow and red majority region, with green cells extending into the residual tendon. Red cells appear to define the outer sheath of the tendon, while green and cyan cells define the core, with this pattern transferring into the attachment bone. Penetration of attachment cells into Layer 2 is less than in the last example, but present. Spots of three layer matching appear to be more centrally organised, suggesting that this feature may vary between attachment regions depending on the role of the muscle.

There appears to be two quite different segments to this region, suggesting that this is perhaps two overlapping regions or perhaps more likely given the polyclonal patterns a region that has a strong deep anterior anchor (rightmost) and a more superficial attachment to the posterior (leftmost).While both regions have some penetration into Layer 2, Layer 3 underlying the anterior region is far more dense, and has the characteristic green cells of the attachment population.This is mirrored in layer matching: while both the posterior and anterior segments of this region have good Layer 1 and 2 matching, only the anterior portion has further integration of Layers 2 and 3 and strong foci of Layer 1 and 3 matching. The honeycomb pattern observed previously is not strongly shown here, and Layer 2 resembles more normal trabeculations, albeit with contributions of the attachment cells.

A similar pattern can be observed within Figure 13.7 which is from a similar periorbital muscle attachment region. A dense green and yellow attachment region connects into a red, yellow and cyan bone. Green cells penetrate into Layer 2, but are only in two spots within Layer 3, corresponding to points of strong three layer matching. The region overall is defined by Layer 1 and 2 matching.

Across all four examples bone appears to be relatively thin where three-layer anchor points are found, but can be thicker in other less dense parts of the attachment region.

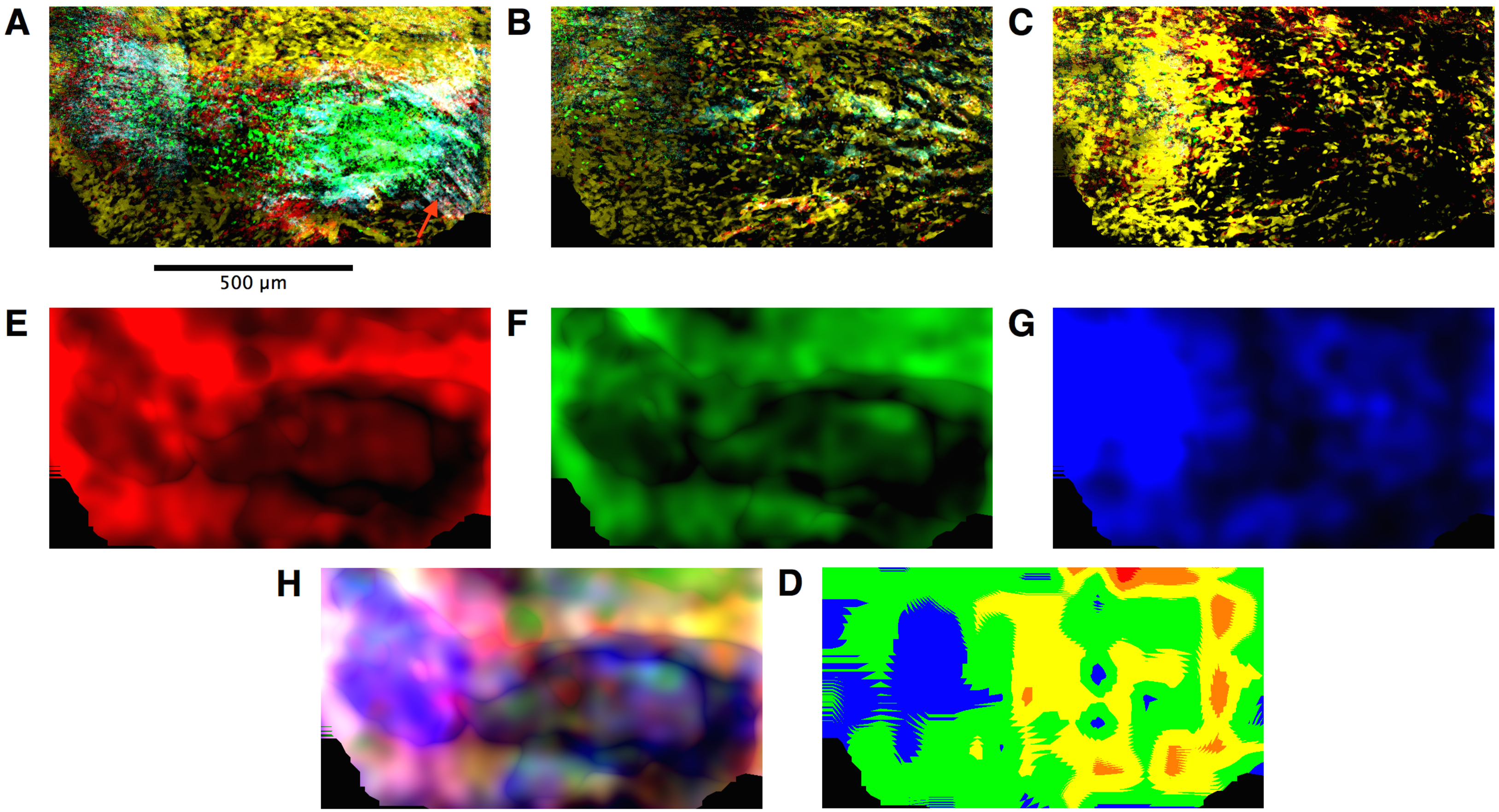

Figure 13.6: Sample A Muscle Attachment Region Close To Left Eye in Detail *Caption on page 240*

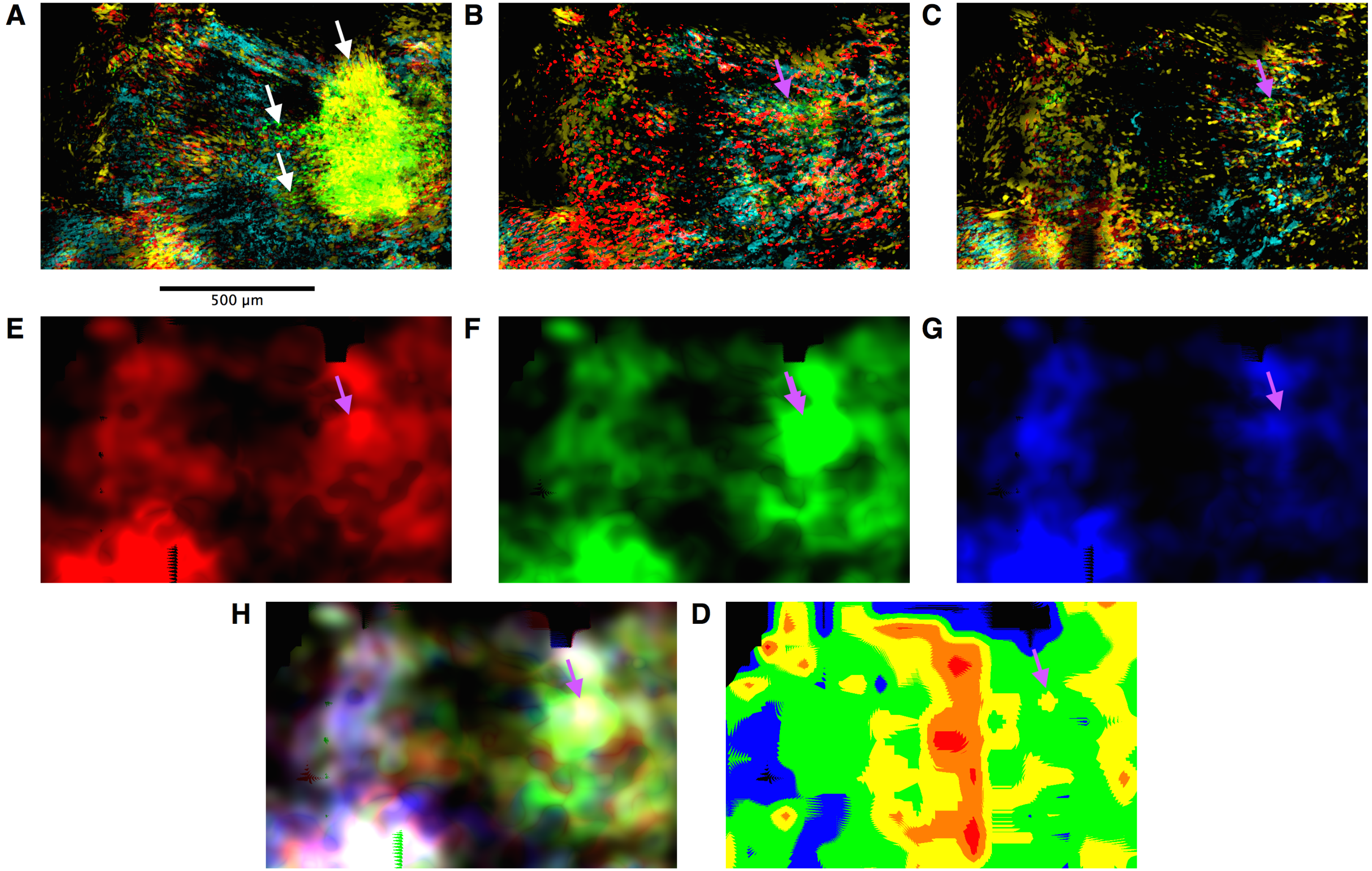

Figure 13.7: **Sample B Muscle Attachment Region Medial to Right Eye Socket in Detail** *Caption on page 240*

Figure 13.6: Sample A Muscle Attachment Region Close To Left Eye in Detail Scale bar is accurate for all images. **A:** Flattened representation of Layer 1. **B:** Flattened representation of Layer 2. **C:** Flattened representation of Layer 3. **D:** Heatmap of Layer 2 Thickness. **E:** Relative colour similarity between Layers 1 and 3. **F:** Relative colour similarity between Layers 1 and 2. **G:** Relative colour similarity between Layers 2 and 3. **H:** Overlay of subfigures E-H. The muscle attachment region at the most lateral part of this image is dominated by Green and Cyan cells ensheathed by red cells in Layers 1 and 2, which do not penetrate into Layer 3. The structure of Layer 2 is striated, with both the attachment region and the main frontal bone appearing striated diagonally towards the anterior midline. The attachment region is relatively thin compared to the more medial frontal bone, with a thicker line marking its posterior edge. It is surrounded by a a band of Layer 1 and 3, and 1 and 2 colour matching, while inside there is only small localised regions of strong colour matching. At the most medial and thick parts of the image, Layer 1 and 3 matching is reduced with 1 and 2 matching dominating and 2 and 3 matching being entirely absent. The cyan and green mixture that defines Layer 1 and 2 while being excluded from layer 3 extends into the residual attached muscles (red arrow).

Figure 13.7: Sample B Muscle Attachment Region Medial to Right Eye Socket in Detail Scale bar is accurate for all images. Subfigure lettering same as above. Green cells are present in the residual attached tendon and muscle (white arrows). These clearly dominate the enthesis in Layer 1. They also extent quite generally into Layer 2 (B, purple arrow) and in one point into Layer 3 (C, purple arrow). This point is slightly thicker than the surrounding bone (D). This also clearly translates into three-layer matching (E-H, arrow). This thicker point at which the muscle lineage penetrates deep into the bone is likely an anchor for the muscle, but would not be observable without lineage labelling.

13.4 Summary: A common progenitor population links bone and muscle

The four muscle attachment regions presented in Figures 13.4 - 13.7 all conform to a common pattern. Polyclonal populations intimately associated in the muscle also form the connective tissue, the Layer 1-Attachment and much of the underlying Layer 2. This leads to a polyclonal 'island' of muscle attachment bone in a territory of cells of different origins. Small anchoring populations further penetrate into Layer 3 in a few points. The nature of these regions is summarised in Figure 13.8.

Layer 1 seems to be entirely replaced by the muscle-associated population, while Layer 2 appears to integrate to some degree. Layer 3 underlying muscle attachment regions is naerly indistinguishable from surrounding bone, with some dense knots appearing to anchor the muscle to the full thickness of the bone. The lack of mixing into Layer 3 suggests that apparently normal cell invasion present elsewhere in the bone is suspended in these regions.

The extensive spread of few muscle-associated colours would suggest that there is a small progenitor population response for this integration: the proliferation of green cells within both 13.6 and 13.7 for example likely represents a proliferation from only a few 'Attachment Point Precursor Cells'. Each muscle attachment region appears to be defined by only two cell colours, which the Founder Effect model detailed in Chapter 3 would suggest that this Attachment Point Precursor Cell population derives from fewer than 20 cells.

These findings confirm those of Jordan [2011] and Kontges and Lumsden [1996]. Clearly there is close 'organisation by origin' - the bone and connective tissue are directly of the same close lineage. While the so-called Layer 1-Attachment is clearly distinct from surrounding Layer 1, it almost certainly comes from a different population rather than a specification within Layer 1, and is formed by invasion rather than differentiation. This technique also shows that Layer 2 is remarkably different within muscle attachment regions. Therefore it seems appropriate that Layer 1-Attachment be convolved with a new Layer 2-Attachment population in a fuller model of neural crest mediated muscle attachment. Indeed, this cryptic identity could justify the enthesis from merely a locational identity or substructure to that of a novel organ, a functional adapter bridging the gap between two very distinct anatomical structures.

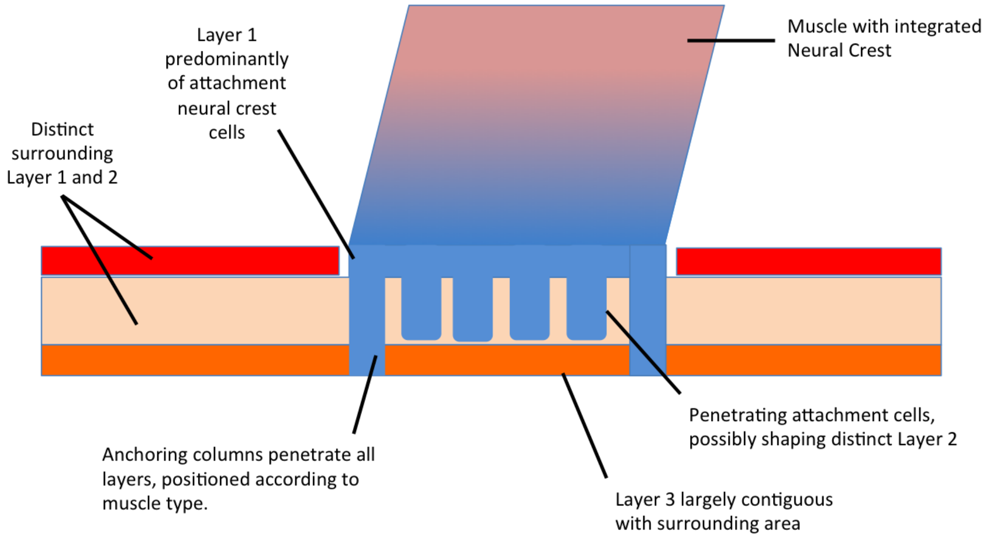

Figure 13.8: Schematic of Neural Crest Mediated Muscle Attachment Updated model from Figure 13.1. The attachment population (blue) integrates deeply into the bone population (red/orange) as well as the muscle (pink). A completely distinct Layer 1 is produced, while Layer 2 consists of a mixed population. The underlying Layer 3 is mostly unaffected, though does receive some deep penetrations running the full thickness of the bone.

Chapter 14

Polyclonal architecture of the sutures

14.1 Introduction

The sutures of the skull are of fundamental importance. Familiar even to casual observers, these sites are where bones meet. Several do not close until many years or decades after birth, despite the obvious structural weakness this represents. Though undermining the strength of the cranial vault, these sutures are clearly required, with defects at the suture such as premature fusion (craniosynostosis) leading to widespread malformations.

The general understanding of suture biology is that they represent the growth fronts of the cranial bones. Following the initial ossification stage, sutures appear to be maintained almost solely for this role. This is based upon the aforementioned bias to consider bone as an entirely solid and near immutable object, the growth malformations caused by premature fusion and a variety of biological evidence pointing to growth at the sutures [Baer, 1954; Opperman, 2000; Zhao et al., 2015].

A number of unresolved questions exist regarding the sutures, and particularly the relationship between the cells within the suture and the cells within the bones has not been conclusively explored. The bones may grow out of the sutural populations themselves, or the sutures may simply represent flexible 'buffers' between two expanding objects. This has fundamental implications for the aetiology of craniosynostosis: if the bones are dependent on sutural precursors, than it is likely that loss of maintenance in this population causes premature fusion. If the bones are merely separated by sutures that are polyclonally distinct, then another process must be acting.

If new bone is emanating from stem cell populations at the suture, then the colour mix of cells near the suture should match that of the suture. Furthermore unless the suture is polarised with respect to its growth or polyclonal arrangement, it would be expected that the bone either side of the suture would have the same polyclonal makeup. Arrangements of clonal populations arising from the suture are predicted in Figure 14.2. The clonal patterns are dependent on whether supposed sutural stem cells are long-lived or are themselves replaced. The key feature of the sutural model of growth is a symmetry about the suture or an apparent polarity within the suture, and a replication of the sutural clonal pattern across the bone. In the absence of this and with the body of evidence to suggest patch-based clonal expansions generate osteoblasts more widely, we must abandon the sutural model of dermal bone development and interpret the sutures as passive bystanders.

While some sutures are highly conserved, such as the frontonasal suture, others are heritable traits found in only a few individuals, such as those surrounding the interfrontal bone. Examining potential differences between these canonical and sporadic sutures may give insight into whether sutures shape the outside of bones, or if bones generate sutures wherever they meet.

14.2 Methods, Regions of Interest and Predictions

With the full suite of tools at our disposal we can examine the polyclonal architecture in and around the sutures, with reference to layer colour similarity, patches and polyclonal constituents explored by Principal Components Analysis (PCA).

Principal Components Analysis (PCA) allows for the comparison of polyclonal populations across the surface of the bone. Three regions were selected, representing three sutures: the frontonasal suture from Sample A and the internasal suture and a region spanning the interfrontal bone in Sample B. The exact locations of these regions are shown in Figure 14.1. For each, a $23 \mu m$ sigma was used, as described in Appendix A.5. Variances explained by each Principal Component in each analysis is presented in Figure 14.12.

PCA is a powerful tool for testing predictions in small regions of Confetti, as it can contextualise the distributed four-colour Confetti information in a far more easily interpretable fashion. However the caveats outlined previously must be taken into account. As before, the PCA overlay maps are illustrations to the true analysis present in the dot plots.

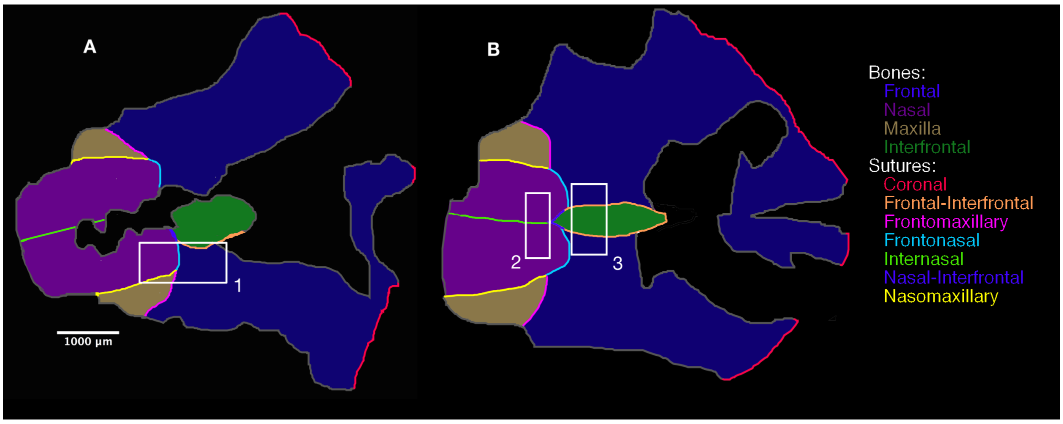

Figure 14.1: Regions selected for PCA Analysis 1 Region from Sample A **A** and two from Sample B **B** were analysed, shown as white boxes. Region 1 represents the left frontonasal suture of Sample A, and is explored in Figures 14.6 and 14.7. Region 2 spans the internasal suture of Sample B and is shown in Figures 14.8 and 14.9. Region 3 spans the interfrontal bone of Sample B and is explored in Figures 14.10 and 14.11

.

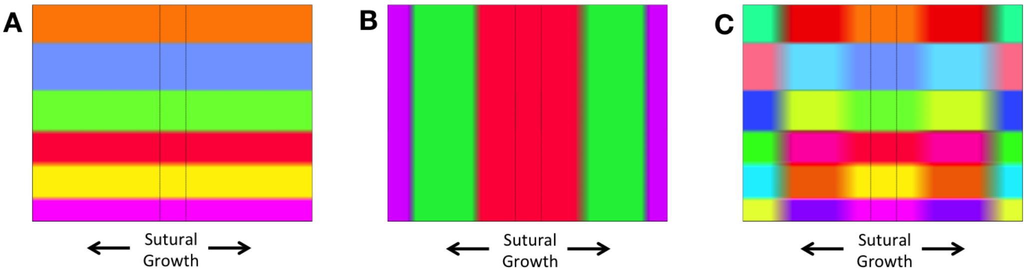

Figure 14.2: Predictions of sutural clonal architecture based on a traditional model of sutural growth. In each, colours represent different clonal populations, and the dotted region in the centre represents the suture. **A:** If the suture has stable heterogenous populations along its length then the resulting bones either side would be roughly striated with the clonal pattern of the suture. **B:** If progenitor cells in the suture are transient and periodically replaced then a symmetrical concentric pattern of growth would be observed in the adjacent bone. **C:** If the suture is both heterogenous and comprised of transient progenitors, the resulting bone would appear as a roughly symmetrical patchwork.

14.3 Results

14.3.1 Sutures exclude bone-resident polyclones, and appear to allow for spreading of polyclones along their extent

Figure 14.4 shows the nasion, where the sutures between the nasal bones, frontal bones and interfrontal bone converge.Contrary to the expectations raised by the traditional model of sutural growth, the sutures are quite distinct from the bones, which are relatively similar under casual observation. It would appear that there is mixture along the extent of the sutures, leading to apparent polyclonal similarity throughout this complex. The sutures are clearly acting as polyclonal boundaries, as cells appear to be both confined within the sutures and are confined from entering the sutures (Fig. 14.4 B and C respectively). The sutures of this region appear to contain yellow cells but exclude cyan cells. Yellow patches are thus recorded as spanning the sutures, while cyan patches terminate at sutures.

This suggests that the sutures are both capable of excluding cells, and allow for spreading of polyclones along their axis. The absence of cyan cells within the sutures begs the question of their origin, and suggests that not all of the cells within the bones came from the sutures.

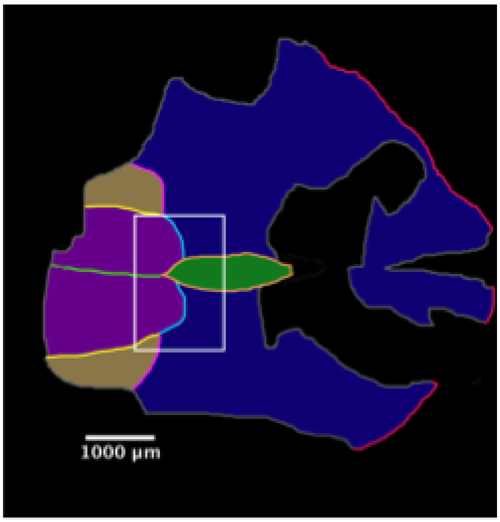

Figure 14.3: Anatomical location of Figure 14.4 within Sample B. Region shown is the junction between the right frontonasal suture and the interfrontal bone with associated sutures within Sample B, covering both the areas known as the nasion and glabella.

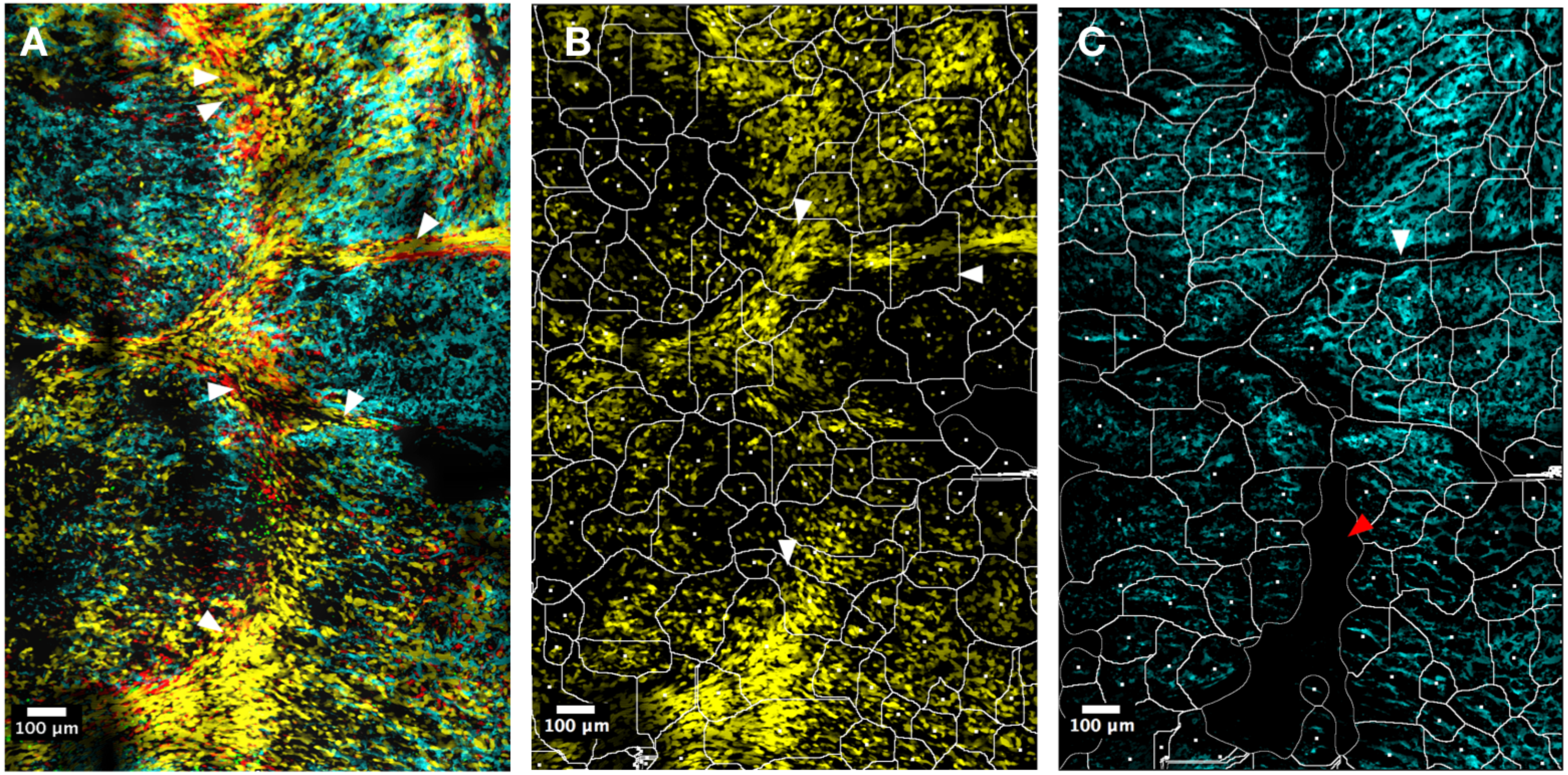

Figure 14.4: **Cellular and Patch characteristics of sutures.** *Caption overleaf*

Figure 14.4: Cellular and Patch characteristics of sutures. Figures show a region at the frontonasal suture of Sample B, within Layer 2. Detail given in Figure 14.3. **A:** Sutures appear to share colours along their length over large distances. Here the same red and yellow mixture defines large parts of several adjoining sutures (white arrows), at the exclusion of Cyan. **B:** In the patch map for Layer 2 Yellow cells, patches appear to bridge the suture (white arrows), likely due to the blur. Cells appear quite tightly defined to the suture. **C:** In the patch map for Layer 2 Cyan cells, patches show clean boundaries at the suture, either merging at its midpoint where narrow (white arrow) due to blurring, or registering as a void where the suture is wider (red arrow).

14.3.2 Vertical polyclonal cellular communication in and around sutures.

Sutures appear to have a relatively complicated architecture with respect to layer matching, as seen in 14.5. The bulk of the suture has three-layer matching, suggesting that the cells within do not observe the same layer restriction as the bone. There are also roundels present, suggesting active mixture. The perisutural regions appear to be strong in matching between Layers 1 and 2, as well as in places 1 and 3, suggesting either mixture or invasion of new cells into all three layers at these points. The apparent matching lines form parallel tramlines, suggesting that the polyclones within the outer layers of the suture effectively wrap back upon themselves at the periphery of the bone, rather than extending as a sheet into the suture itself.

14.3.3 Distinct polyclonal populations in the nasal and frontal bones are segregated by the polyclonal populations within the frontonasal suture

Figures 14.6A-C show a densely yellow nasal bone segregated from a red and yellow frontal bone by a yellow, red and cyan suture. In each of the PCA visualisations in 14.6A'-C' the frontal and nasal bones are clearly distinguished in both PC1 (red) and PC3 (blue). The suture is largely identifiable within PC2 (green). The perisutural region within the frontal bone also bears notable similarity to the nasal bone, though this region appears to be mostly defined by an abundance of only yellow cells, which may be spontaneous due to how common they are. Critically, there is no concentric pattern within the bones radiating from the suture, and the suture itself appears polyclonally distinct from the bones due to the abundance of cyan cells. This suggests that the suture is not the generative region for the cells populating the bones. There are however small groups of cells that match the sutural population in both, suggesting that they may have some specific role within the bone if they are not spontaneously similar.

The plots in 14.7 show a clear segregation of the constituent populations of the cells in the two bones, with the suture acting as the interface between the two. This suggests that the populations within the bones have different colour mixtures, and are likely of different polyclonal origins, while the suture may represent a mix of these two populations. If the suture is indeed a mixture of the two populations, then the small groups of suture-like mixtures within either bone (denoted by green patches in Figs. 14.6A'-C') might represent migrants through a somewhat porous

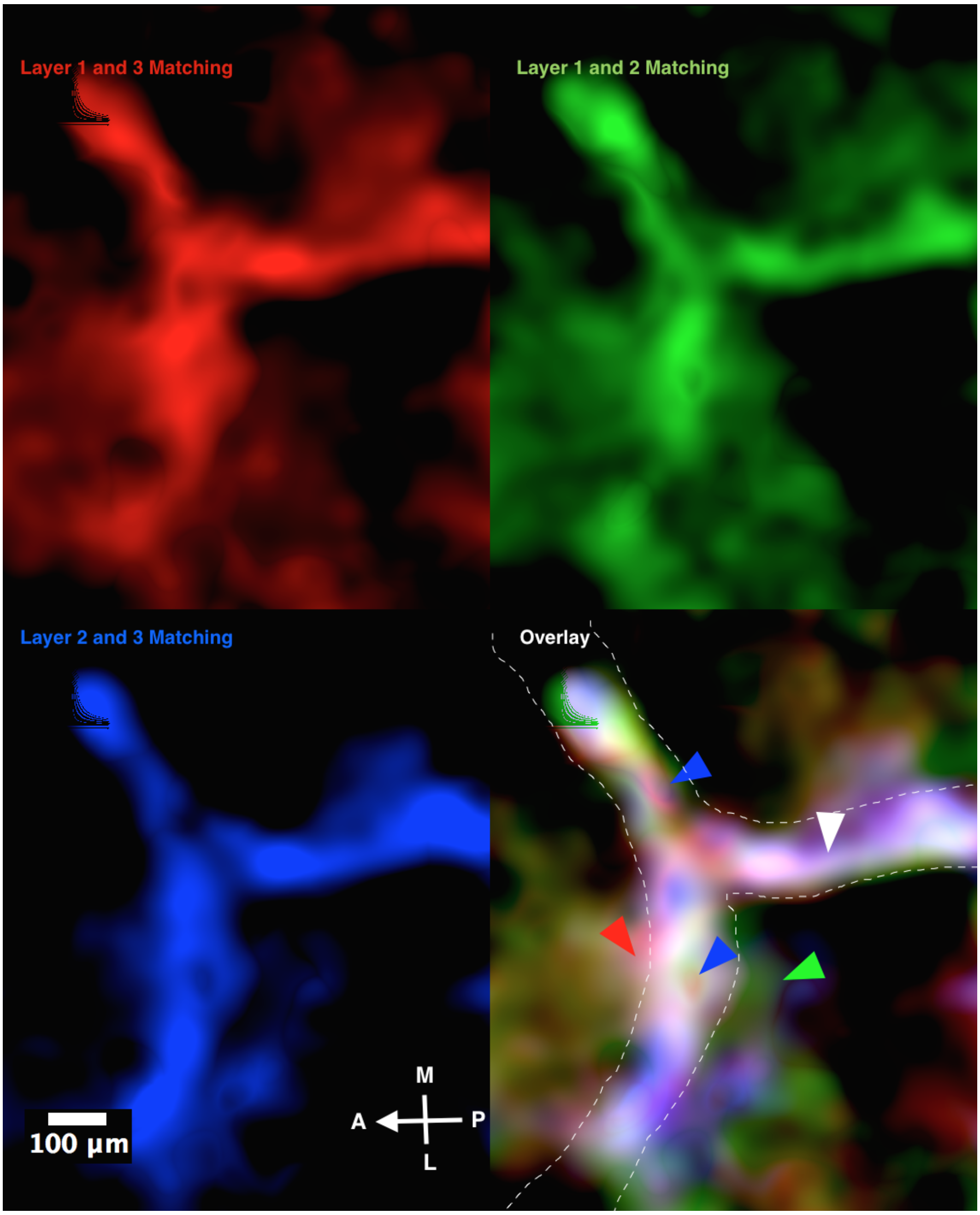

Figure 14.5: Layer colour similarity at sutures. Region shown is the junction between the left frontonasal suture and the interfrontal bone with associated sutures (top right). Approximate suture boundaries are shown as dashed white lines.The general appearance of the suture is that of three layer matching, shown in white (white arrow). In places roundels are visible within the suture (blue arrows). The perisutural region is high in Layer 1 and 2 matching (both green and red arrows) but also in places high in Layer 1 and 3 matching also (red arrow only). The matching of Layer 1 and 3 appears to surround that of Layers 1 and 2, with the suture on the inside.

sutural border. The largest suture-like region appears to map to a possible blood vessel in the frontal bone.

Overall there is no evidence to support the idea that this suture is the sole generative region for either of these bones: on the contrary, based on the mapping of the sutural region within Principal Component space, it would appear that the suture represents a mixture of the populations from the two bones.

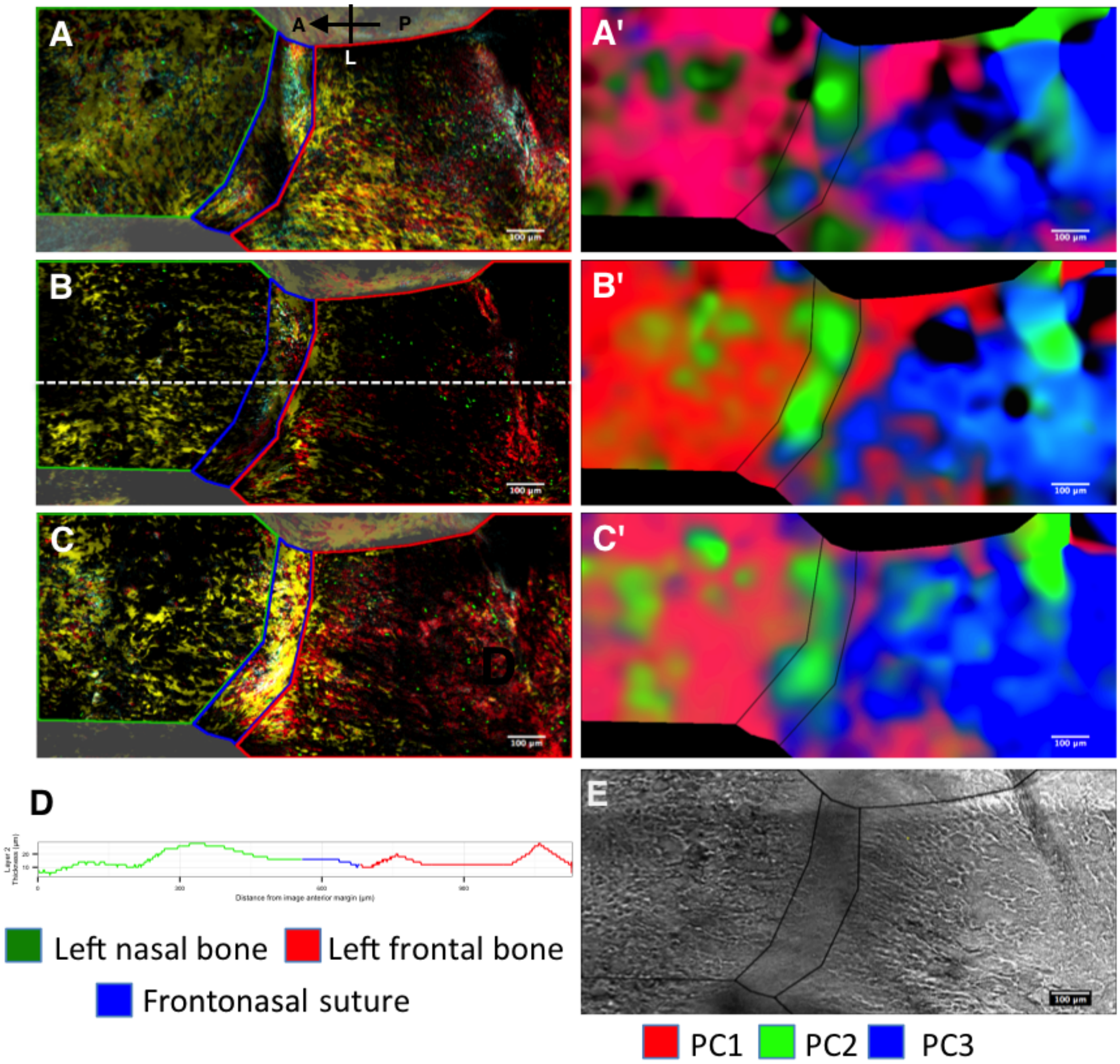

Figure 14.6: Visualisation of the PCA across the left frontonasal suture
Caption on Page 254

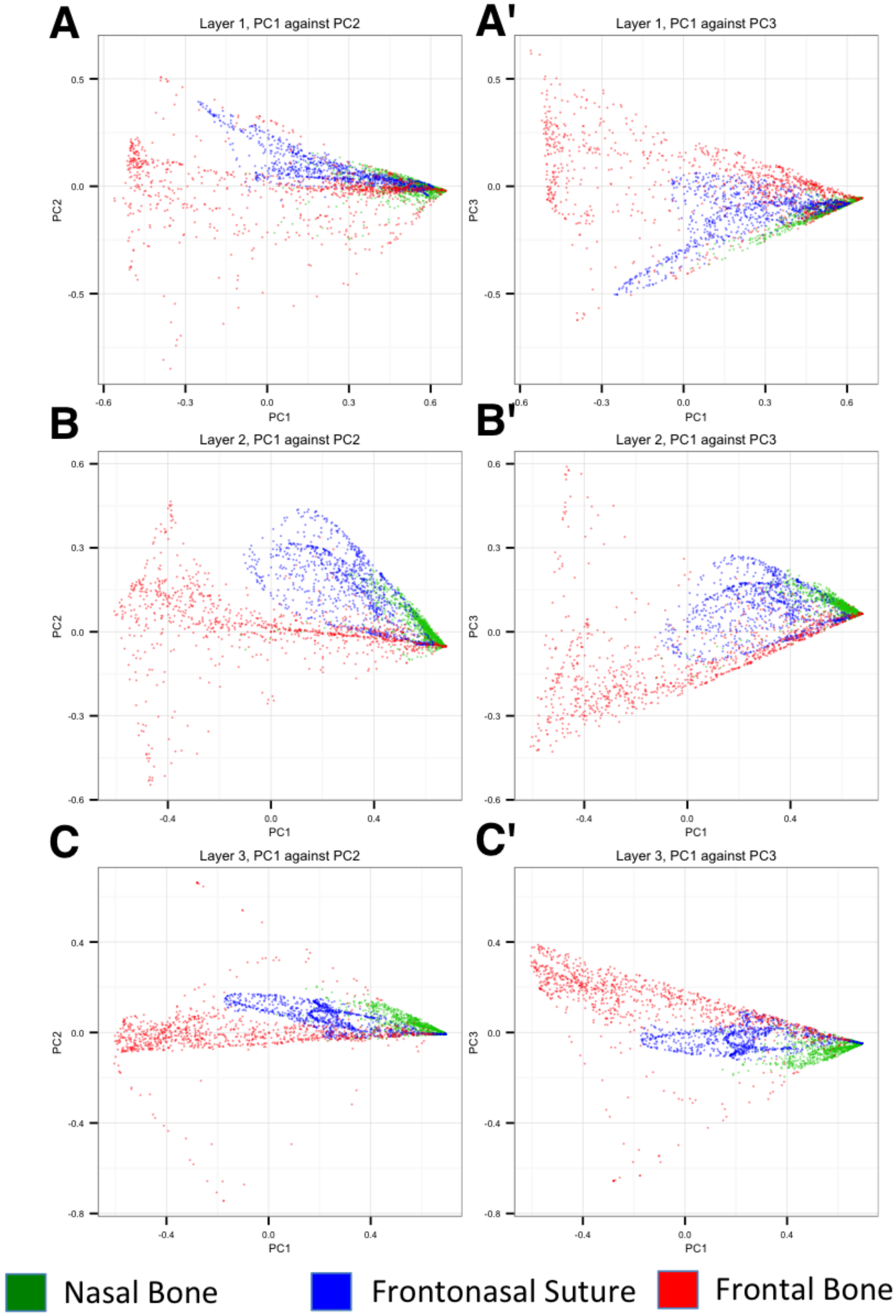

Figure 14.7: Plots of Principal Component Analysis across the frontonasal suture. *Caption on Page 254.*

Figure 14.6: Visualisation of the PCA across the left frontonasal suture. A, B & C: Flattened representations of Layers 1, 2 and 3 respectively, showing boundaries for the designations used in Figure 14.7. Legend refers to the compartments delimited by coloured borders on these figures. The greyed out region outside of these boundaries is not included in analysis. **A', B' & C':** Corresponding PCA visualisations of Layers 1, 2 and 3 respectively. In each of these PCA visualisations the frontal bone and nasal bone are clearly distinct. The suture is also clearly distinct from both, with islands of similarity in both bones. **D:** Layer 2 thickness plot along the dotted line in **B.** In both bones the perisutural region is defined by a thick ridge and a sharp decline into the suture. **E:** Layer 1 boundaries overlaid with bright field image. The suture can be seen as unornamented connective tissue between two regions of elaborated matrix.

Figure 14.7: Plots of Principal Component Analysis across the frontonasal suture. A, B & C: Plots of 1000 pixels from the compartments defined in Figure 14.6 across Layers 1, 2 and 3 respectively, showing values in PC1 against values in PC2. **A', B' & C':** As A, B & C, but showing PC1 against PC3. In each plot the frontal bone and the nasal bone are very clearly delimited, with the suture representing the interface between the two. This suggests that the two bones are polyclonally distinct, with the suture representing a mix of the two.

14.3.4 Distinct polyclonal populations in the two nasal bones are segregated by the nasal suture

The region displayed in Figure 14.8 shows two quite clearly distinct mixes of colours in the two nasal bones, with a more homogenous yellow-dominated mixture in the left nasal bone and a more heterogenous mixture in the right nasal bone. These are separated by a suture that is dominated by yellow and red cells. In the PCA visualisation, the two populations are clearly distinguished within Layers 1 and 2, with the suture acting as a demarkation line. Layer 3 is far less populated, and thus does not show such a clear delimitation of the constituent populations of the two bones, though the location of the suture still represents a demarkation line between two populations at points.

The suture is also distinctly highlighted, suggesting that it is a mixture that is distinct from either bone, rather than just a meeting of two populations. In both the cell images and the PCA visualisations, it is clear that the constituent populations of the bones are relatively homogenous both close to and far away from the suture, and extend right up to the suture. No concentric banded patterns are visible in the bones, and the suture is a distinct mixture from either bone.

The charts in Figure 14.9 give a more complicated impression than those of the previous region. Within Layer 1 it would appear that all three populations are relatively distinct. Within Layer 2, the former pattern returns with the suture representing the interface between the two populations of the bone. Within Layer 3, the impression of three distinct populations returns. Given this region's close proximity to the nasion and thus other sutures (Fig. 14.1) this be due to the spreading of cells along sutures as observed previously. Irrespective of this, there is no evidence to suggest that the majority of cells within the bones originated within the suture.

The suture appears remarkably thicker than the surrounding bone, which thins towards the suture (Fig. 14.9D). While the thinning of bone towards the suture is consistent with Region 1, the thickening is not.

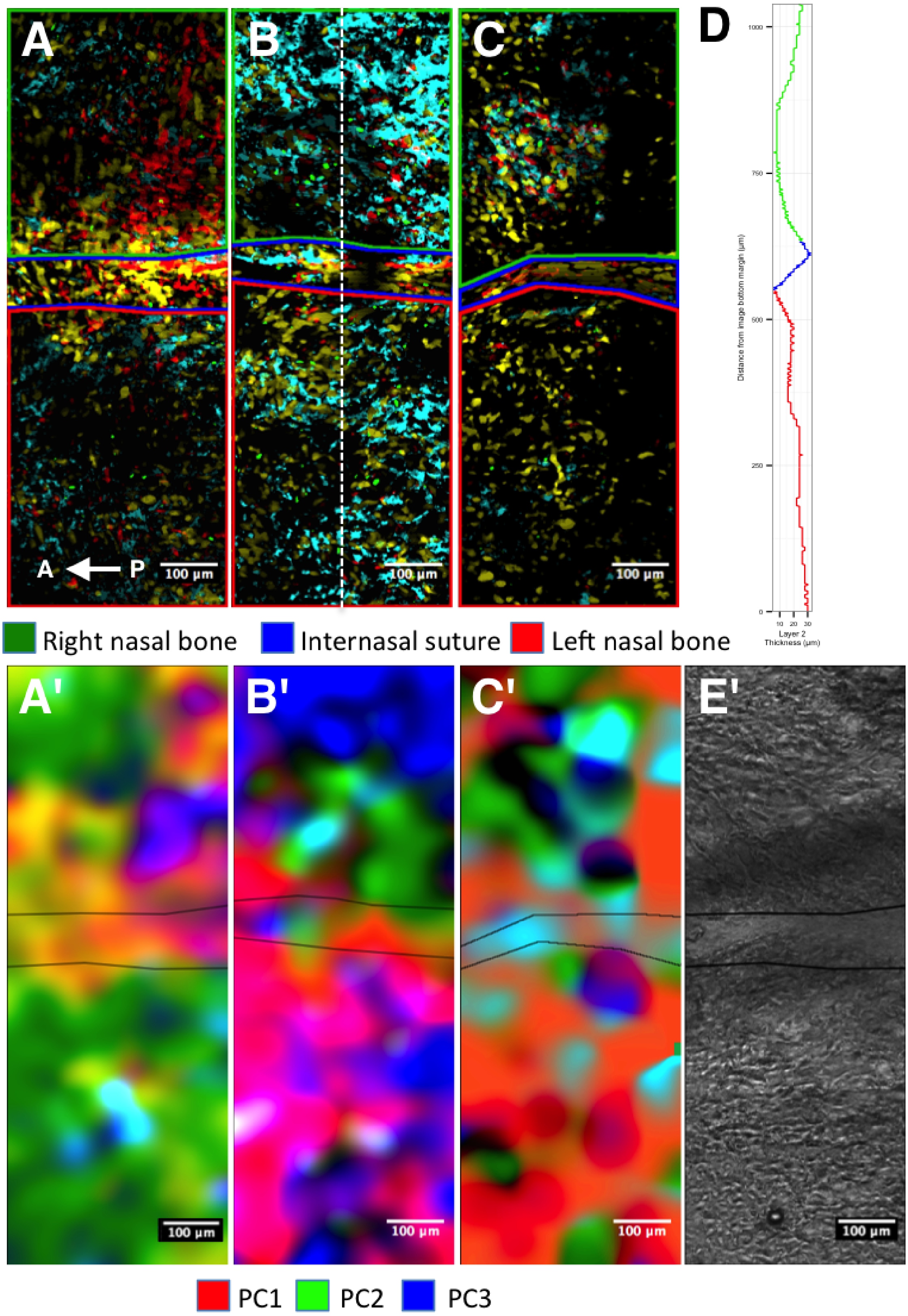

Figure 14.8: Visualisation of the PCA across the nasal suture. *Caption on Page 258*

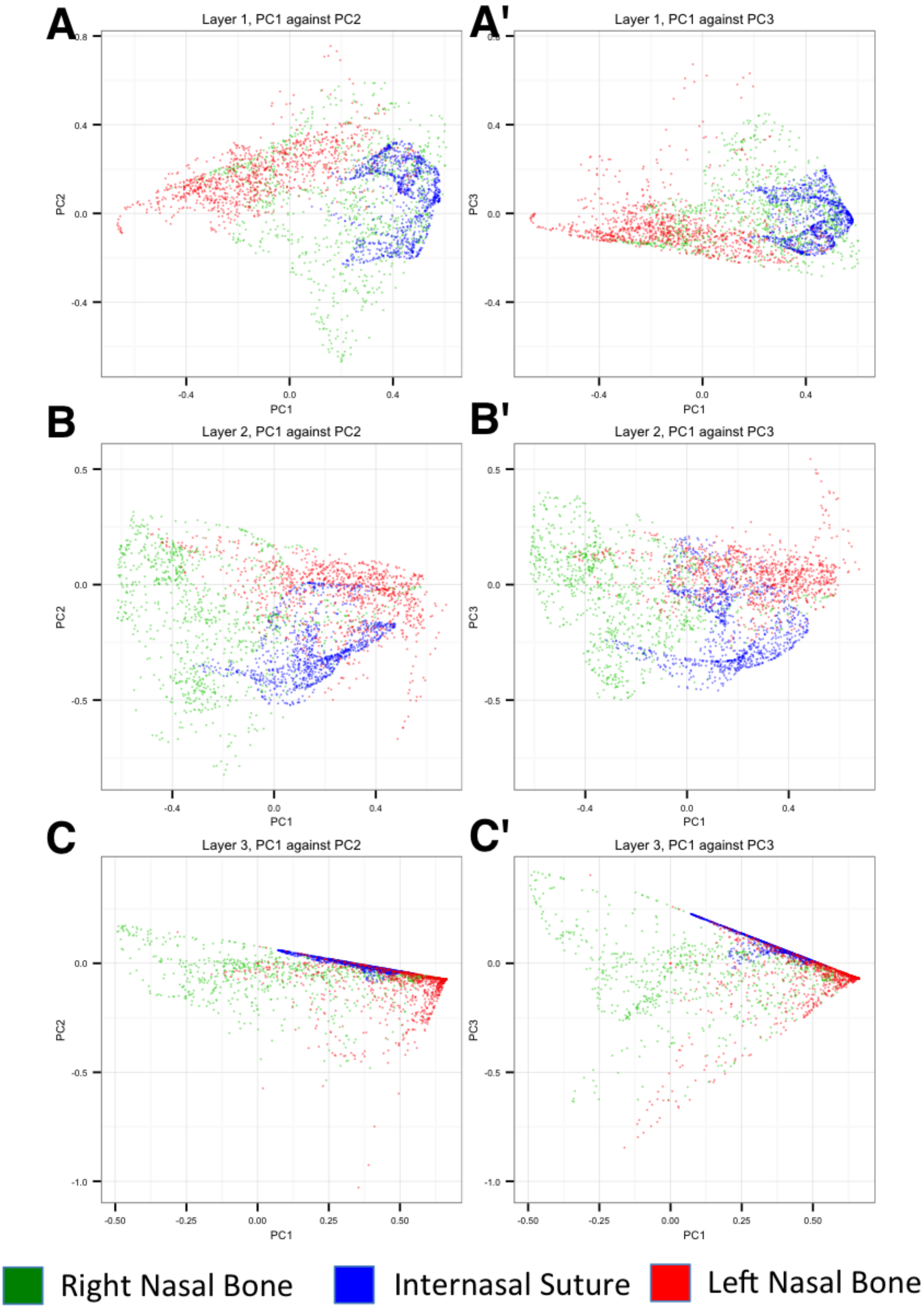

Figure 14.9: Plots of Principal Component Analysis across the nasal suture. *Caption on Page 258*

Figure 14.8: Visualisation of the PCA across the nasal suture. A, B & C: Flattened representations of Layers 1, 2 and 3 respectively, showing boundaries for the designations used in Figure 14.9. Legend refers to the compartments delimited by coloured borders on these figures. **A', B' & C':** Corresponding PCA visualisations of Layers 1, 2 and 3 respectively. In both Layers 1 and 2 (A' and B') there is a distinct difference between the left and right nasal bones, showing distinct polyclonal populations. The suture is a distinct population itself, and represents a relatively sharp boundary between the two bones. Within Layer 3 (C') the two populations are still relatively distinct, despite the relative paucity of cells.

Figure 14.9: Plots of Principal Component Analysis across the nasal suture. A, B & C: Plots of 1000 pixels from the compartments defined in Figure 14.8 across Layers 1, 2 and 3 respectively, showing values in PC1 against values in PC2. **A', B' & C':** As A, B & C, but showing PC1 against PC3. In each plot the two nasal bones (orange and pink) share some commonalities but are overall largely distributed across different regions of the PCA space, denoting their distinct polyclonal origins. The suture (green) appears to represent an interface between the two, suggesting perhaps that this constitutes a population that receives cells from both bones.

14.3.5 Distinct polyclonal populations are present in the interfrontal and the frontal bones, segregated by apparently normal sutures.

Figure 14.10, which spans the midline, shows a clearly distinct population devoid of yellow cells, flanked by two dense lines of cells that segregate this from yellow-populated frontal bones. Notably, the midline of the calvaria runs directly through the centre of this region. This is the relatively obscure interfrontal bone, discussed in depth in chapter 15.2. All three bones are relatively heterogenous with respect to the principal components, but do not appear to represent identical populations. The sutures themselves are quite clearly distinguishable in the PCA visualisations of Layers 1 and 2 when compared to the putative novel bone and the adjacent frontal bones, denoted by voids (values close to or below 0) in Layer 1 and either a void or a region high in PC2 (green) in Layer 2. Within Layer 3 these sutures are less distinct, but are still distinguishable, likely due to the relative paucity of cells in this layer.

Within the plots shown in Figure 14.11, the interfrontal bone appears to be well segregated from the frontal bones in at least one of the comparisons for Layers 1 and 2. This suggests that this region is a distinct polyclonal population. The sutures follow the trend of the previous two regions, in representing transitions between two bones, suggesting that they are mixtures of cells from either bone. In summation, the interfrontal bone and the sutures that surround it parallel to the midline follow the same trends as the previous well accepted sutures with respects to cellular appearance, profile of Layer 2 thickness, representation on PCA plots and appearance in bright field images. This means that the frontal-interfrontal sutures which are not present in all individuals display the same elaborate arrangement as the canonical nasal and frontonasal sutures.

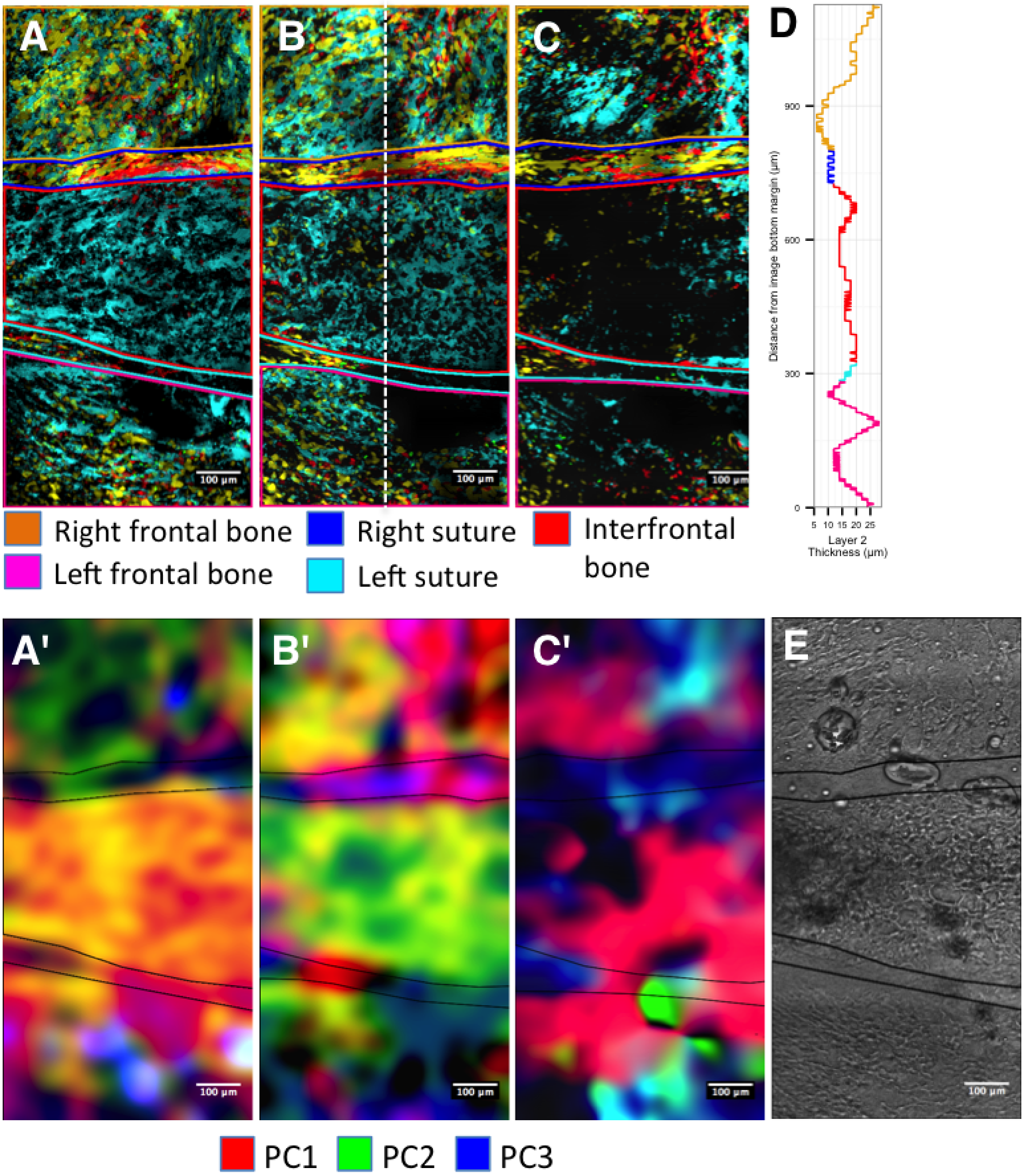

Figure 14.10: Visualisation of the PCA across the interfrontal bone. *Caption on Page 262*

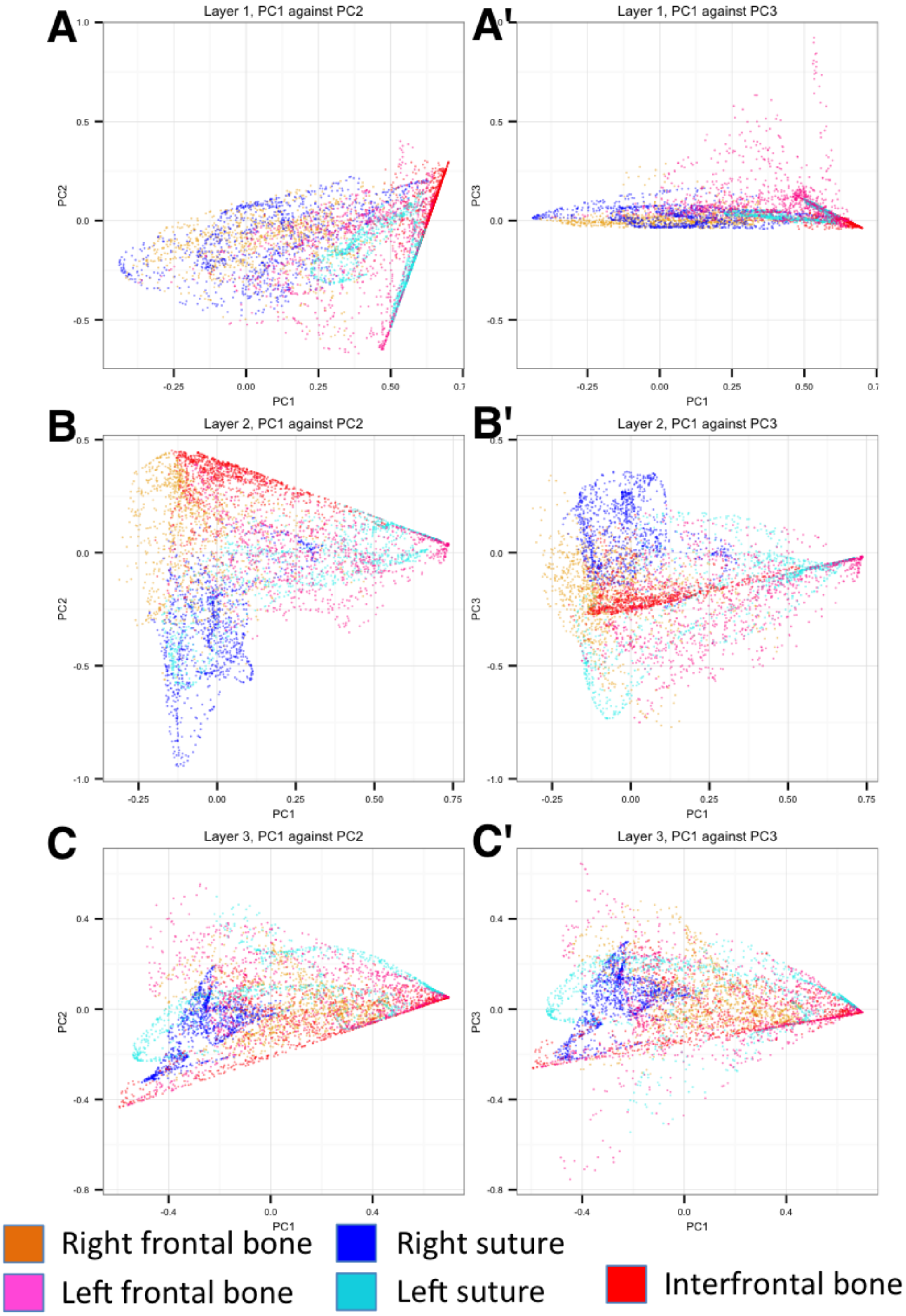

Figure 14.11: Plots of Principal Component Analysis across the interfrontal bone. *Caption on Page 262*

Figure 14.10: Visualisation of the PCA across the interfrontal bone.A, B & C: Flattened representations of Layers 1, 2 and 3 respectively, showing boundaries for the designations used in Figure 14.11. Legend refers to the compartments delimited by coloured borders on these figures. Sutures are typically cell dense, and do not appear to be of the same lineage as the adjacent tissue. **A', B' & C':** Corresponding PCA visualisations of Layers 1, 2 and 3 respectively, with boundaries as above. The sutures are very clearly distinct from the bones in Layers 1 and 2, and somewhat visible in Layer 3. **D:** Layer 2 thickness plot along the white dotted line from **B**. Both frontal bones have dips in thickness immediately adjacent to the suture, followed by thicker regions further from it. **E:** Bright field with Layer 1 boundaries drawn in. The boundaries define trenches of unelaborated mesenchyme between islands of complex matrix. consistent with a suture.

Figure 14.11: Plots of Principal Component Analysis across the interfrontal bone. A, B & C: Plots of 1000 pixels from the compartments defined in Figure 14.10 across Layers 1, 2 and 3 respectively, showing values in PC1 against values in PC2. **A', B' & C':** As A, B & C, but showing PC1 against PC3. In both Layers 1 and 2 (A and A', B and B'), the interfrontal bone is well segregated from the two frontal bones in at least one of the comparisons, demonstrating a distinct polyclonal origin. The left suture appears entwined with both the left frontal bone and the novel bone, while the right novel suture appears distinct from the novel bone and overlays only with the right frontal bone , suggesting that the sutures and these bones are derived from distinct polyclonal populations. In Layer 3 (C and C') each population overlaps, suggesting either that the lack of cells has reduced the discriminatory power of this type of analysis, or suggesting a shared polyclonal origin across Layer 3.

14.4 Summary - Sutural populations do not give rise to adjacent bones

In each and every suture examined in Figures 14.6 - 14.11, populations close to the suture and polyclonally distinct from the cells appeared to extend into the bone. There are no apparent concentric clonal relationships, no mirroring of clonal relationships across sutures and only sporadic matching of sutural populations to the bone. This leads to the strongly supported conclusion that the suture cannot give rise to the majority of cells in the bone.

The PCA dot plots show that the suture can fall intermediate between the two bones within principal component space. This would suggest that it contains a mix of cells from both bones. This represents a complete inversion of the model that sutures give rise to bones as well as going beyond the casting of sutures as passive buffers, to suggest that bones give rise to the populations within sutures. This contradicts the lineage analysis of Zhao et al. [2015], though they ignored some bone-resident stem cells, as well as perhaps misinterpreting some small re-invasion of the bones by sutural cells as being principal contributors to the bone. It should be noted that Figure 14.4 demonstrated that some polyclones are excluded from the suture, suggesting that there may be a polyclonal subpopulation that can enter the suture from the bone.

Interestingly the thickness landscape across each suture (Figures 14.6D, 14.8D and 14.10D) demonstrates a slight thickening near the suture. Were the suture the generative region and bone as static as that model implies, such a thicknening could not be expected. Rather, a modular patch model that allows for definition of local elaboration supports this thickening, as a response to the distinct environment of the suture.

By inverting the cellular dynamics of the suture, one must consider the developmental dynamics in a different light. It has classically been assumed that if the suture becomes quiescent, it will ossify and growth will cease. If the bones themselves are growing and contributing to a sutural buffer zone, then it would be more reasonable to think that cessation of growth would lead to breakdown of the suture and its eventual ossification. The absence of significant cellular contribution in perisutural bone removes the requirement for growth to be focussed around the sutures.

The sutures surrounding the interfrontal bone clearly have the same morphology as classically accepted sutures. This demonstrates that so-called ‘ectopic’ sutures are in fact as well organised as other sutures. The most parsimonious explanation for this is that sutures form wherever two bones developing bones meet, and are not independently specified.

In conclusion, the cellular architecture of the suture does not support the sutural model of growth, and rather places sutures as secondary bystander structures forming between the edges of bones that may be expanding far more broadly than simply at a narrow perisutural band.

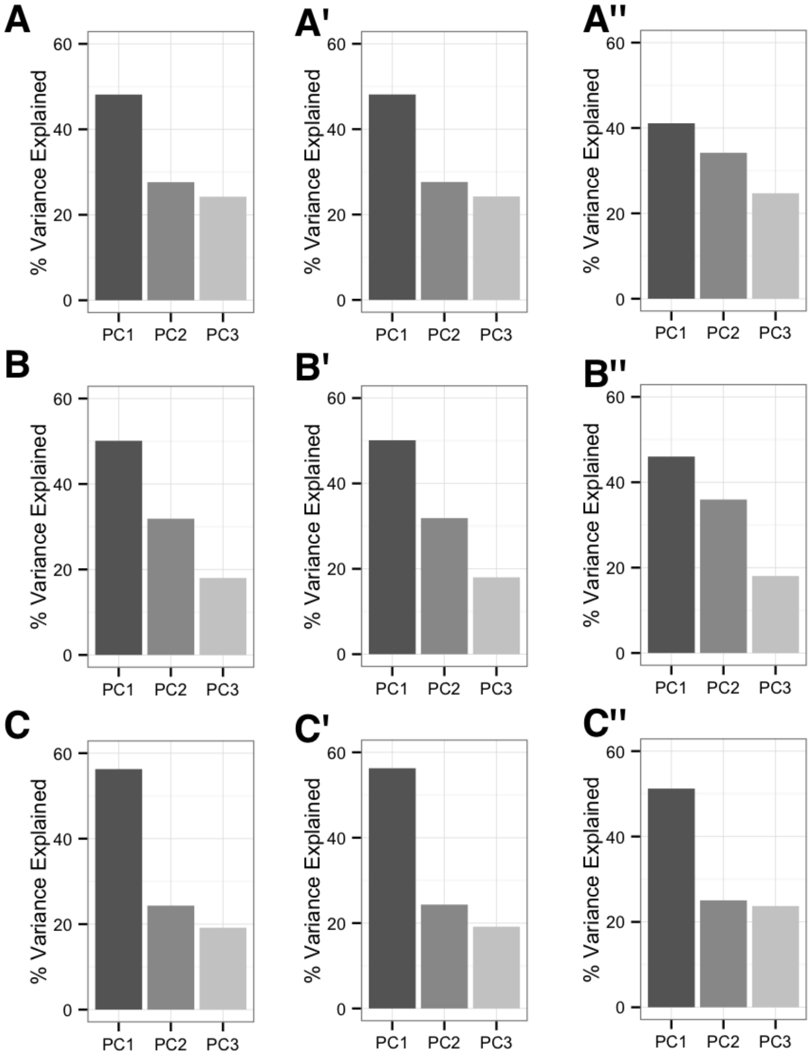

Figure 14.12: Barplots of variance explained by each principal component in each Figure of this Chapter Each bar represents the total variance within the image that is captured by the first three principal components. For each triad, A, B and C correspond to analyses for Layers 1, 2 and 3 respectively. **A, B & C:** Figures 14.6 & 14.7. **A', B' & C':** Figures 14.8 & 14.9. **A", B" & C":** Figures 14.10 & 14.11. In each instance, the first two principal components account for over 75% of total variance in the image, validating the analysis.

Chapter 15

Discussion: Cryptic Polyclonal Modularity Underpins Cranial Dermal Bone Development

In this Part we have explored the generative architecture of neural crest cells in whole-mount mouse dermal bones, particularly the frontal and nasal bones. This has revealed that polyclonal patches with a complex interlayer ontogeny represent a compelling explanation to several aspects of skull development. These are organised around points of vertical invasion of cells between layers, and can develop across layers while developing localised thickness growth, cooperatively creating the whole dermal bone. In this discussion we will further explore evidence for these structures as fundamental modules within dermal bone development.

15.1 Patch-like structures in human skulls

In Chapter 12 I presented a temporal sequence of vertical versus in-layer expansion that appears to underly dermal bone development, with polyclones cryptically fused except at privileged suture regions. If this is true, then there ought to be an evolutionary precursor to such a program, and there ought to be human pathologies which reflect disruptions to this process. In this section I present evidence of patch-like pathologies and discuss patch-like micromery in evolution.

15.1.1 Wormian bones as evidence for the patch-based model

Wormian bones are a common and often asymptomatic stochastic variation in mammalian skull development. They consist of supernumary bones, commonly located along the canonical sutures. Sites where three sutures between large bones join are particularly prone, such as the Asterion and Pterion [Charles and Parker, 1905]. Under traditional models of sutural development wormian bones are effectively unaddressed, in part because they are of little clinical significance to warrant producing a model, and they arise at random, frustrating attempts to properly chart their development.

The patch model provides a strong explanation for the occurrence of Wormian bones: if each patch is a quasi-independent unit awaiting organising signals then each Wormian bone may represent a single unit that either escaped repression, mistakenly underwent activation to generate thickness or otherwise failed to represent global patterning events. By extension this would imply that the sutures surrounding Wormian bones must arise secondarily from the presence of two structures that are independently attempting to grow as bones.

As shown in Chapters 8 and 14, the sutures surrounding the heritable interfrontal bone are indistinguishable from the universally conserved nasofrontal suture. This would imply that sutures form reactively to the presence of centres of ossification, and their positions are not independently specified. This corroborates the idea that sutures around Wormian bones are secondary consequences of escaped developmental suppression of patches.

Wormian bones may represent the strongest evidence for the relevance of patches in humans. Osteogenesis imperfecta is a set of syndromes caused largely by mutations in genes encoding a number of collagens [Byers et al., 1982]. In several subtypes, and particularly type III, a condition known as 'Significant Number of Wormian Bones' can arise, denoting greater than 10 Wormian bones. In very extreme cases, again most likely in type III cases, entire bones can be replaced by a mosaic of Wormian bones [Charles and Parker, 1905; Semler et al., 2010], demonstrated in even very early literature on the disease, as shown in Figure 15.1.

This would suggest that Wormian bones are merely patches that have attempted independent growth and formed a suture around themselves rather than integrating seamlessly with neighbours.

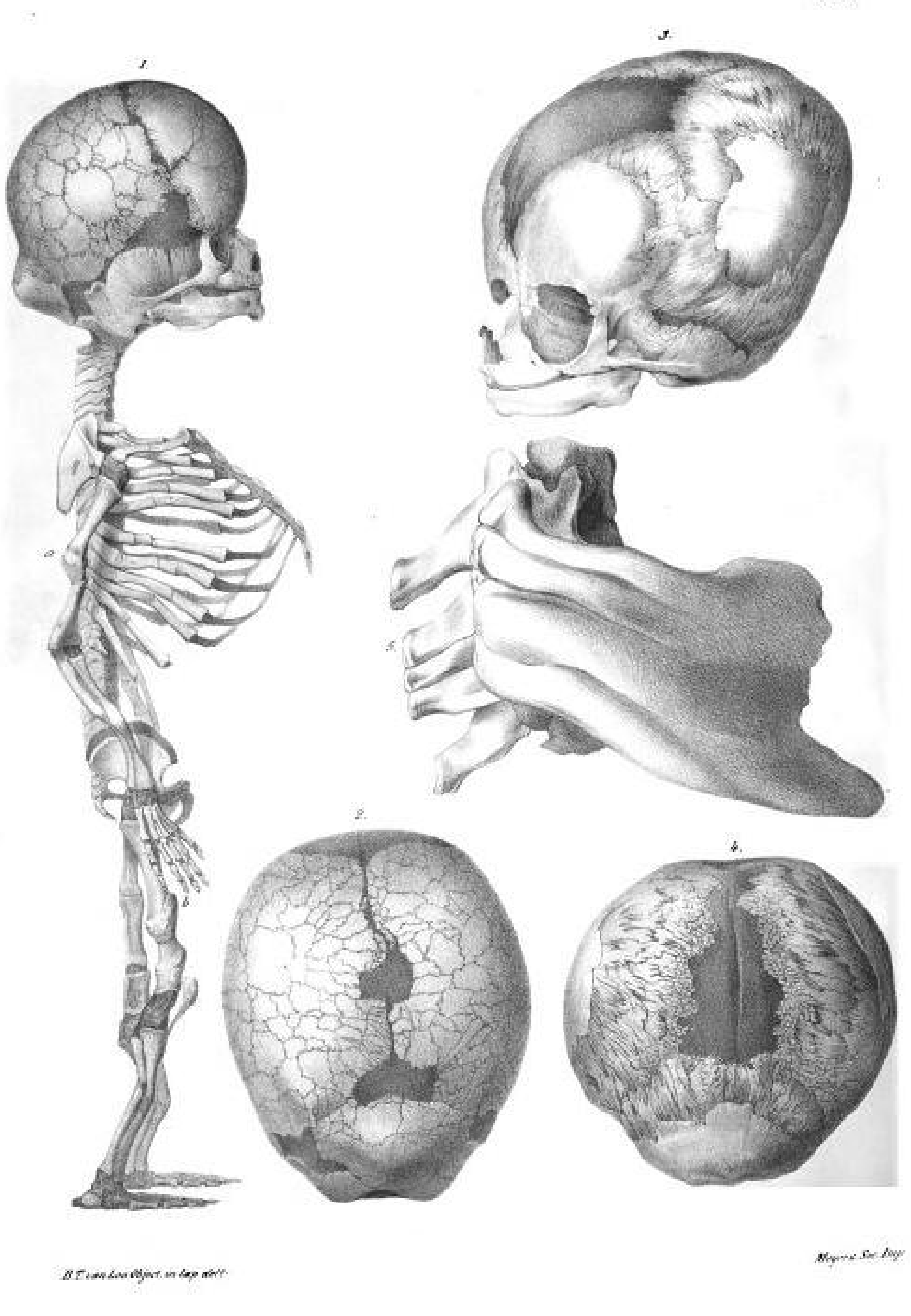

Figure 15.1: The extreme Wormian bone condition in Osteogenesis Imperfecta. Huge numbers of Wormian bones are visible in this individual, in a manner that is highly reminiscent of patches. In parts of the skull larger bones are visible, showing that this condition arises as a result of local dynamics and not as an unavoidable consequence of a global genetic mutation.

15.1.2 Craniolacunae explained in the patch model

Craniolacunae are focal thinnings of the dermal bone that can occur in parallel with numerous other conditions of skull development, such as Chiari, craniosynostosis and hydrocephalus but also can be observed without other abnormalities [Rio et al., 1981]. These form a very similar pattern the extreme Wormian condition of Osteogenesis Imperfecta, albeit in negative: only the edges of the bones remain while the centres are thinned or absent, as depicted in Figure 15.2.

As discussed earlier, it appears that the centre of patches represents the principal site of invasion, with horizontal expansion spreading out from these points defining the boundaries of the patch. In the absence of proliferation however, this would result in the depletion of the centres to the benefit of a buildup of cells at the interface between patches. This may explain the craniolacunia phenotype as a defect of proliferation within patches. If this interpretation is true, then this would imply that the horizontal spreading of cells is in fact an active process of cell migration across the plane of the skull, rather than a passive product of cells being 'pushed' by proliferation and migration at a point. An alternative explanation would be that patch biomineral growth is controlled separately at the centres of patches and at the edges. Regardless of the pathology, this phenomenon further testifies to the cryptic modularity of the large dermal bones.

15.1.3 The Patch model gives new insight into the evolution of micromery and macromery

The extant mammalian condition of large bones is described as macromeric, for they are as the etymology suggests, 'large parts'. However, the earliest known bones displayed a micromeric arrangement, wherein wide expanses of bone are built up from a mosaic of tesserae. The extreme condition can be observed in the Anaspid *Tolypelepis* - a skull vault comprised entirely of micromeric tesserae. A common question that arises is whether macromeric represent large derived individual micromeres, or alternatively if they are comprised of an aggregation of micromeres with cryptic boundaries.

Under the patch model the latter would clearly be the case: the persistence of micromere-like patterns that appear to integrate growth would strongly suggest that macromeric bones are composites of micromeres which persist as a developmental unit. The only change appears to be the method of integration between neighbours

- whether it is the formation of a suture, or mixing.

The appearance of micromeres and macromeres is inconsistent and widely spread throughout evolution and within individual animals. Zhu et al. [2013] argue that macromery evolved within the common ancestor of placoderms and was secondarily lost in the branch of gnathomes that gave rise to chondrichthyans and acanthodians. Furthermore they note that focal micromery can be observed alongside macromery even in sarcopterygians which ought to be highly derived. These structures can be observed in extant osteichthyes such as the garfish *Belone belone*, which has a micromeric condition at the opercular plate and posterior to the head (Figure 15.3).

A question raised by Zhu et al. [2013] is whether instances of focal micromery are significant when considering evolution. As it would appear that these structures are retained in a cryptic fashion, the answer to this question must be ‘no’. A simple developmental change appears sufficient to convert between macromeric and micromeric conditions, and so patterns of these two cannot be particularly reliable when considering taxonomy. More worryingly, there exists the possibility that sutures might be redrawn across this landscape of cryptic micromeres such that supposedly homologous bones in closely related animals might represent developmentally distinct tissue populations.

15.1.4 Summary

Patch-like structures can be observed in ancestral skulls and in parts of extant animals alongside large bones. Furthermore they can be identified within disease states of humans. This would suggest that patches are capable of creating the stand-alone supernumary bones known as Wormian bones, and that the large dermal bones present in skulls throughout evolution are in fact comprised of cryptic developmental modules.

A uniting observation in these examples is that these seem to operate on a scale slightly larger than patches. Wormian bones in particular can present in wide range of sizes [Charles and Parker, 1905]. In addition, the overlapping colours of Confetti reveals the presence of overlapping patches. This suggests that patches do act cooperatively over a small scale even in these more particulate examples. This furthermore proposes a simple means by which the extreme Wormian conditions can arise, or an animal might evolve from a micromeric to macromeric form: one need only to modify the range over which patches can coordinate themselves.

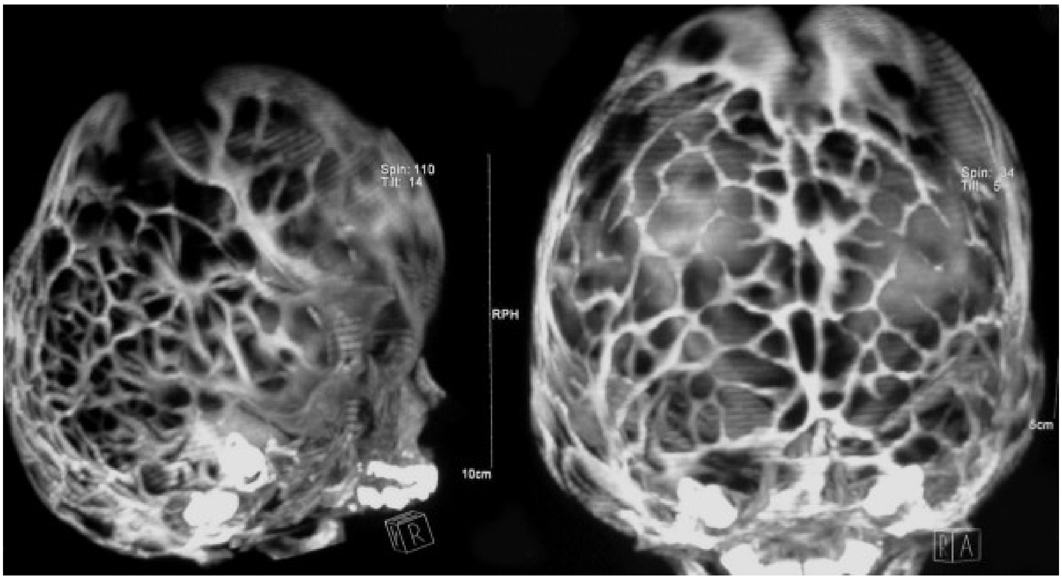

Figure 15.2: Filamentous remnants of bone in craniolacunia is reminiscent of patch boundaries. Under the patch model this can be explained by the persistence of horizontal spreading to patch boundaries in the absence of central proliferation. From El Khashab et al. [2010], reproduced under the Creative Commons licence.

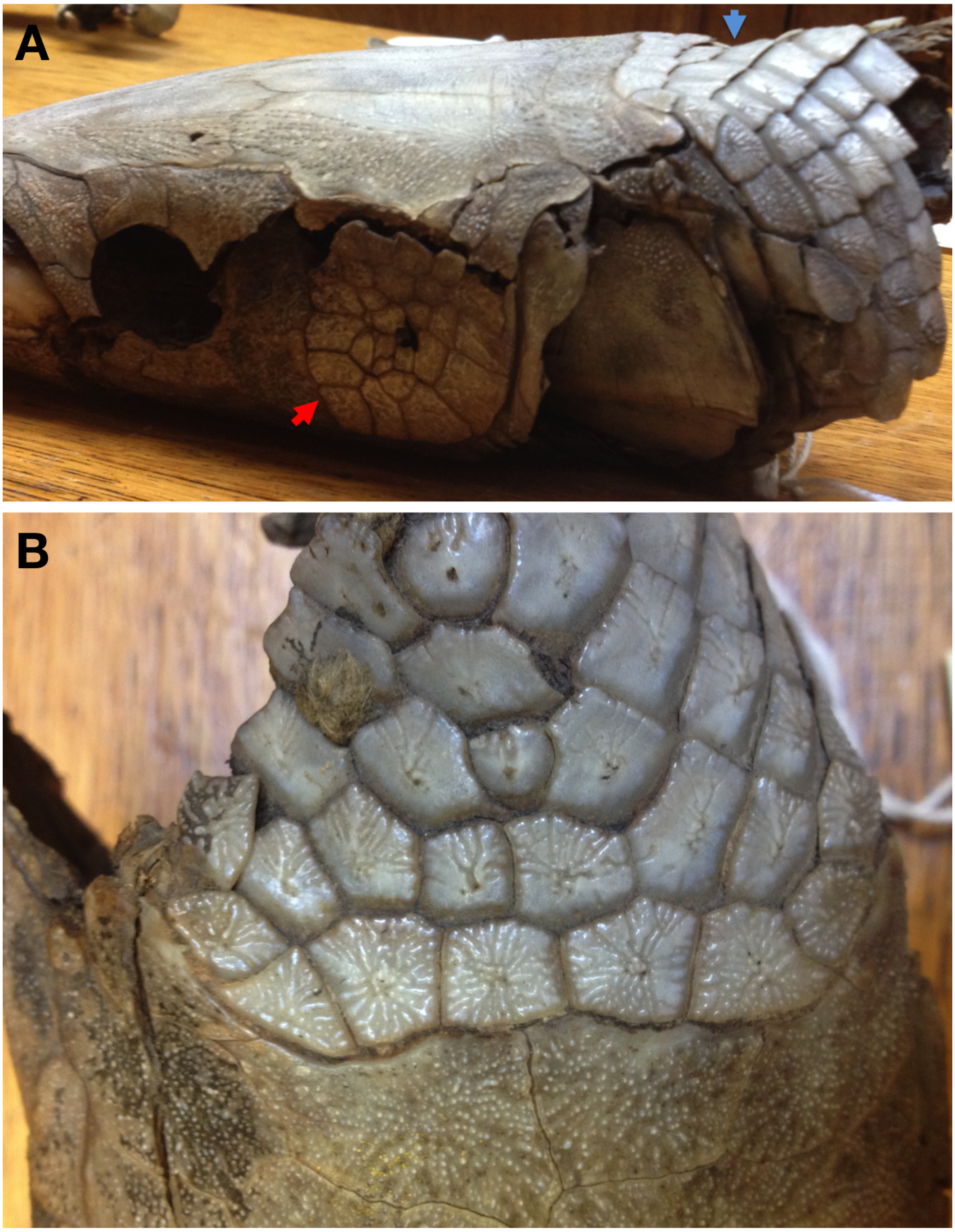

Figure 15.3: Patch-like architecture in the garfish ***Belone belone*****. A:** Oblique profile view. While the garfish has a largely macromeric skull, but the operculum (red arrow) has a micromeric structure. The neck region (blue arrow and **B**) shows a similar morphology where the scales meet the head, with a transition from macromeric bone, through apparently micromeric bones and into ganoid scales. This is a specimen of Guy's Hospital Natural History Museum, who I thank for its use

15.2 Comparative Anatomy of the Interfrontal Bone

In our samples were have observed the presence of an interfrontal bone, an unexpected feature when studying mammalian anatomy. This struture appears to have characteristics entirely similar to the surrounding 'canonical' dermal bones, including a layered structure, nested polyclones and identical suture morphology. As this appears to be such a well-developed structure, one must investigate whether it is conserved, or merely an aberrant occurrence.

If the interfrontal bone is indeed a genuine developmental unit of skull development, it would be expected to have been expressed as a visible characteristic somewhere within the diversity of life. In fact, this bone appears to be present in a very wide range of animals, suggesting that it is conserved in some fashion in all major vertebrate lineages. Broadly it is homologous to the dermally ossified dorsal surface of the so-called 'sphenethmoid' complex of many animals, which is principally comprised of endochondral bone. Calling this dermal bone sphenethmoid is certainly inappropriate as all ethmoid bones are endochondrally ossifying ones [Hanken, 1993]. In mammals, the ethmoid articulates with the proposed interfrontal bone via the perpendicular plate, which is clearly a separate structure. For this reason, it is inappropriate to refer to this as the sphenethmoid bone in mammals, and the proposed homology suggests that previously identified dorsal sphenethmoid surface ossifications should be re-evaluated as distinct interfrontal bones.

15.2.1 The interfrontal bone is a phenotypic trait in mice and rats

The interfrontal bone is a relatively well documented but obscure phenotypic trait in mice, first described by Keeler [1933] and most thoroughly explored by Truslove [1952]. This trait is particularly common in the background strain of Confetti Mice, C57BL [Johnson, 1976]. However these bones often appear far smaller than the observed sutural pattern within Confetti mice: while the cryptic sutures were observed join the respective midpoints of the nasal bones, this arrangement was described as a 'extremely large' interfrontal when observed in a Patch[1] heterozygote mutant [Grüneberg and Truslove, 1960]. The homozygote cross of this mutant produces a cleft face phenotype.

Independent ossifications at the glabella can be induced in rats through adminis-

---

[1] A wide deletion including Platelet Derived Growth Factor Receptor Alpha gene, not to be confused with Patched of the Hedgehog signalling pathway

tration of high doses of aspirin during pregnancy Mitala et al. [1984]. The resulting bones can either span the midline, or form a symmetrical butterfly-like pair. Some of the resulting bones exactly match the observed pattern of cryptic sutures observed in the mouse.

15.2.2 Homologues of the interfrontal bone within birds

Ratite birds such as the ostrich (*Struthio camelus*), emu (*Dromaius novaehollandiae*) and rhea (*Rhea americanus*) possess a clear suture-defined bone at the midline where the nasal and frontal bones meet (Figure 15.4A and B). This is identified as the a dorsal cover for the ethmoid. The fact that the dorsal surface is formed by dermal ossification while the bulk of the ethmoid is formed by endochondral ossification suggests that this is an association of at least two developmental units, as shown in Figure 15.5. Given the position and shape of this bone, it is likely homologous to the proposed interfrontal bone. Cassowaries (*Casuarius spp.* have large pneumatised casque bones that cover the dorsal surface of the head. The anterior portion of this appears to extend from the glabella, and likely represents the interfrontal bone of this ratite.

No example of such a clearly defined interfrontal bone has been identified in the Neoaves. The casques of the hornbills (Family Bucerotidae) likely represents an expanded interfrontal bone in the same manner as cassowaries (Figure 15.6). Even in species that do not have a suture-outlined interfrontal bone, within birds this region is often thinner than the surrounding frontal bone or depressed, suggesting that it is still present as an independently specified unit (Figure 15.4C).

15.2.3 The interfrontal bone in amphibians

While many anurans have predominantly cartilaginous skulls, hyperossified frogs such as *Triprion* and some *Gastrotheca* species also possess a bone that is apparently homologous to the interfrontal bone [Duellman and Trueb, 1986]. This bone is described variously as the rostral portion of the ethmoid, and usually described as the supraethmoid or more confusingly the mesethmoid, a term which is variously applied to this extremity of the ethmoid that sits on the midline and to elements at the centre of the ethmoid. This dermal bone characteristically develops during metamorphosis, and thus is only present in the adult [Smirnov, 1989]. *Bombina orientalis* also possesses this bone, but has a further set of supernumerary bones

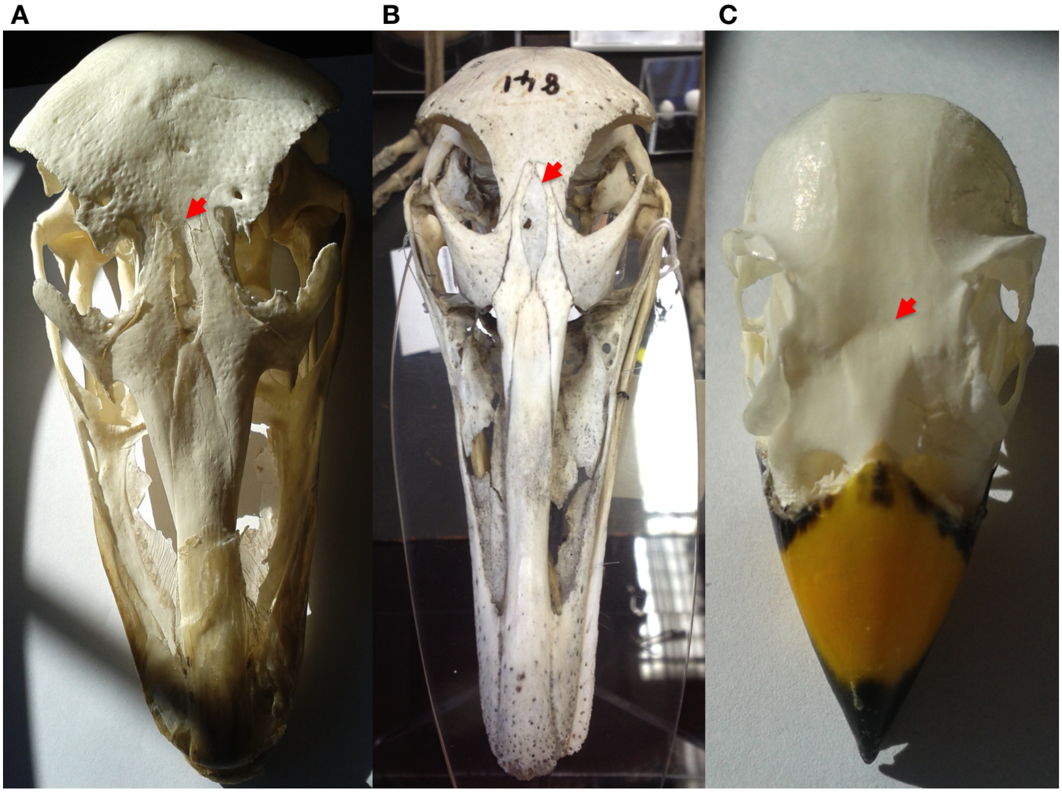

Figure 15.4: The interfrontal bone in ratite birds and neoaves. A: The Ostrich, *Struthio camelus*. An additional bone is observable, with sutures to the frontal bones and nasal bones (red arrow). The nasal bones surround this bone to a great degree, but the sutural pattern is preserved. This is described as the dermal covering of the ethmoid. **B:** This bone is also present in the closely related Rhea, *Rhea americanus* (red arrow). The frontal bones are only connected by a tenuous strand of bone, which demonstrates both the plasticity of bone morphology and the evolutionary pressure to maintain sutural patterns. This is a specimen of Guy's Hospital Natural History Museum, who I thank for its use. **C:** A finch of the Family Fringillidae, species unknown. There is no suture in the corresponding position of this Neoave (red arrow), but this point of the bone is depressed relative to its surroundings, suggesting that it still has distinct growth dynamics even in the absence of a visible suture. A&C photographed by Tobias Koentges, from the collection of Prof. Georgy Koentges.

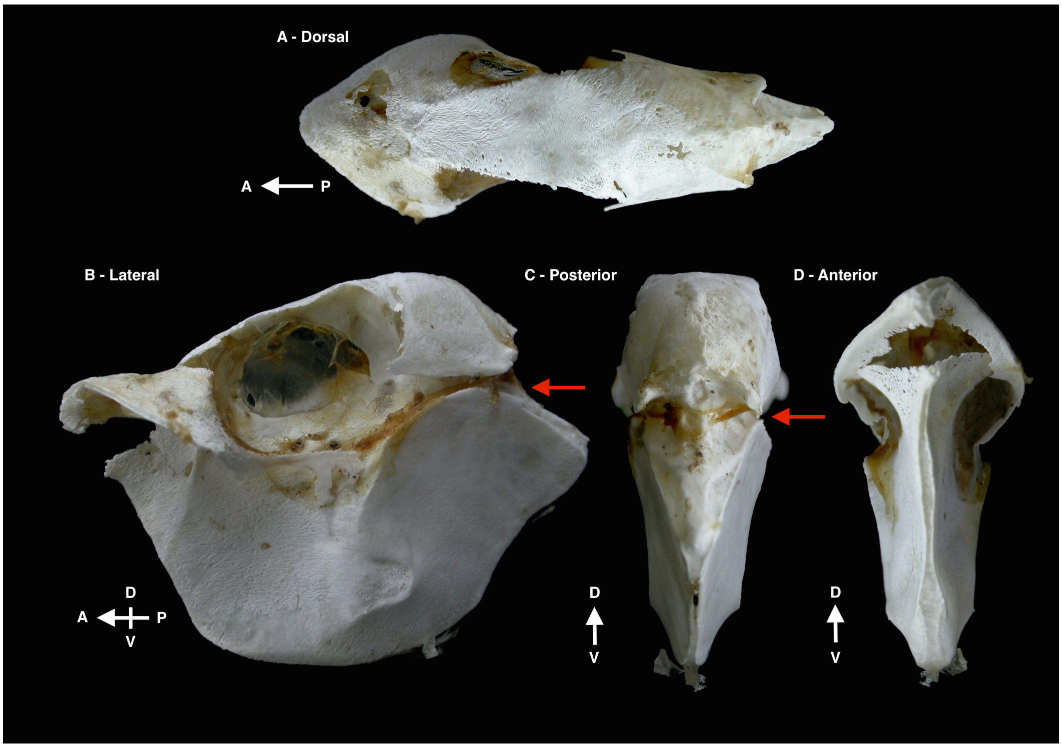

Figure 15.5: The composite ethmoid of the Ostrich, ***Struthio camelus*****.** The dermal upper surface of the ethmoid appears to be a pneumatised three-layer bone consistent with the rest of the skull. There is a discontinuity between this and the underlying endochondral bone (red arrows). This suggests that the dermal portion is independently specified and ankylosed to the ethmoid, rather than emerging from it, and furthermore is consistent with the notion that it is homologous to the interfrontal bone. Photo kindly contributed by Dr Mike Taylor, from his website 'Sauropod Vertebra Picture of the Week'.

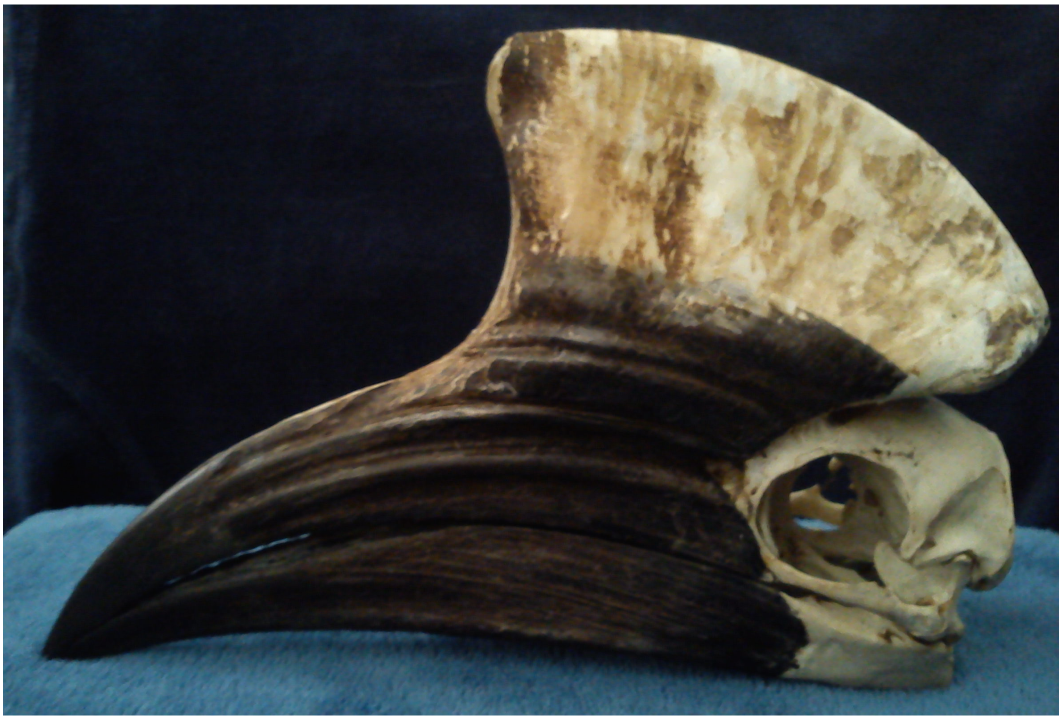

Figure 15.6: The tumescent casque of the hornbill *Ceratogymna elata* **is likely homologous to the interfrontal bone.** Many hornbill species have a large, pneumatised bony casque, the root of which conforms to the expected location of the interfrontal bone. Photographed by Tobias Koentges, from the collection of Prof. Georgy Koentges.

termed 'interfrontals' that form between the two frontoparietal bones during the final stages of maturation. This trait is not universally observed: some individuals compete skull formation by lateral ossification from the existing frontoparietals, while others form novel ectopic ossifications from cryptic centres within the mesenchyme [Smirnov, 1989]. These 'interfrontals' are in effect akin to wormian bones, representing secondary sites of ossification outside of the conserved pattern of specification.

The interfrontal bone is ostensibly absent in salamanders, but is present in some caecillian genera such as *Siphonops* [Kleinteich et al., 2008] and *Schistometopum* [Nussbaum and Pfrender, 1998], where it is referred to as the supraethmoid, dermethmoid, infrafrontal or mesethmoid depending on author [Duellman and Trueb, 1986].

15.2.4 The interfrontal bone in lungfish

Lungfish are basal Sarcopterygians that retain several Osteichthyan characteristics. Their skull vaults are more similar to the amphibians described above than mammals, possessing the same anteroposterior arrangement of frontoparietal bones. The Australian or Queensland Lungfish (*Neoceratodus forsteri*) is the most basal of the Dipnoi subclass, and this possesses a bone on the midline at the anterior edge of the frontal bone which is described either the dermal ethmoid, dermethmoid or EQ bone. This bone is also present in the more derived Lepidosirenidae. The interfrontal bone is likely at least part of this bone, though this could also be identified as including the nasal bones.

15.2.5 The interfrontal bone in humans

The glabella is the rarest site for supernumerary bone formation [Charles and Parker, 1905], though as Wormian bones are often asymptomatic and most deceased people are interred without a thorough description of their skulls being taken, this does not necessary imply a complete absence. The intrafrontal bone can be observed in some cases of the rare heritable condition acromelic frontonasal dysostosis. This disorder appears to be caused by mutation of the ZSWIM6 gene, and is characterised in part by a cleft-face phenotype, similar to the Patch phenotype described in mice by Grüneberg and Truslove [1960].

15.2.6 Summary of Comparative Anatomy

A dermal element, dorsal to the ethmoid, is a broadly and possibly universally conserved characteristic across the range of extant gnathostomes. Its representation is highly variable, ranging from apparent absence, presence in ornamentation, occasional phenotypical expression and up to ubiquitous appearance as a true bone. Its articulations and form is also variable, commonly forming a close association with the underlying ethmoid but appearing as part of the frontal bone in most aminotes. These characteristics would point to a conserved element, more conserved than even the frontal and parietal bones, that has been lost and regained many throughout evolution. Given that its independent presence or fusion with nearby elements has little effect on the overall fitness of the animal, there has been little selection pressure applied to conserve or delete it and it is thus unsurprising that it has not been fixed in the canonical register of cranial development. However its constant reoccurrence across and within species.

More importantly, in the context of this thesis, it may represent an intermediate module of bone development. In Chapter 9 it was observed that there is cryptic segregation of polyclones along apparently insignificant boundaries (Figures 9.4 - 9.9). It may be that the interfrontal bone exists as such an intermediate region of confined patches that is merely expressed as a true bone in some animals. This does present the rather worrying possibility that the presence or absence of certain sutures may not actually represent as reliable landmark for comparative anatomy as previously assumed.

15.3 Reflections upon methodology

The analytical approach presented allows for interpretation of mixed polyclonal colours. It was developed in response to the particular characteristics of Confetti: four labelling colours, targeted to different cellular compartments. While the approach used likely represents the best means of dealing with such samples, it is worth noting that more optimal solutions can be conceived of.

The principal problems with Confetti are that one cannot easily segregate individual cells *in silico*, requiring the volumetric approach used. If all of the reporter proteins were targeted to the nuclei, one could use existing automated cell counting software to obtain true counts of cells. The principle of using euclidean distances is easily compatible with discrete cell counts rather than the more nebulous ‘cell density’ I used. This would remove some of the ambiguity and assumptions that I inherently had to make in order to approach a global analysis.

More reporter colours would mean better lineage resolution. The only way to feasibly achieve this would be through use of multiple labelling cassettes in each cell, resulting in combinatorial colours. This however would absolutely require the targeting of all reporter genes to the same cellular compartment, as an additional analytical step would be required to encode overlapping colours as a distinct population. Regardless, the software developed for this thesis is largely compatible with an arbitrarily large number of different colour channels, and would be easily applied to such problems.

In summary, were I to attempt to re-start this project, I would attempt to use a labelling cassette that encodes only nuclear-targeted reporters, and use multiple copies of the reporter. However, no such reporter currently exists in a ubiquitously expressed locus, and so this would have to be generated. That is a worthy goal, as I have demonstrated both the relevance of interpreting mixed polyclonal populations and a novel means of doing so. It is my hope that others will be inspired to use this approach to investigate the polyclonal architecture of other organs.

15.4 Summary of Novel Findings

In this part I have tested the existing model of skull development and found it is not supported by the polyclonal architecture observed. In its place I propose the following novel observations.

1. Dermal bones are comprised of cryptic modular patches which can elaborate locally
2. Each patch is integrated in three dimensions through invasive points, usually linking patch centroids
3. Invasion between layers is predictive of the thickness of biomineral growth, and that there are at least three stages of patch development involving changes in invasion between layers
4. Patch development allows for local definition of thickness growth and cell density changes
5. There exists the possibility for intermediate organisation within bones, and

the cryptic persistence of ‘bones’ lost in evolution, such as the interfrontal bone, as a part of the developmental program

6. Sutures are not themselves generative regions of the bone, and lateral spreading of cells is possible in any part of the bone
7. Muscle attachment regions contain polyclonal attachment progenitor populations which elaborate from a small precursor population and integrate into both muscle and bone to establish an enthesis

These findings are likely to be of particular importance when considering craniosynostosis: if the sutures are relatively passive structures then they must be sustained by some signal that likely fails, leading to premature fusion. As we have identified the true dynamic modular units of dermal bone, these can be further investigated in order to identify potential mechanisms for suture preservation. This could potentially lead to a medical intervention for premature suture fusion rather than the surgical methods currently employed.

As in the previous part, cryptic modularity has been observed. The two parts shall be summed up in the next Chapter.

Chapter 16

Concluding Remarks: Common Themes in the Polyclonal Architecture of the Jaw, Teeth and Calvaria

In this thesis random lineage labelling, has been used to explore two distinct parts of the head: jaws and teeth, and the calvaria. In both, cryptic polyclonal compartmentation has been demonstrated. In the jaw, we observed that teeth and alveolar bones form cryptic modules distinct from the jaw. Within the calvarium cryptic polyclonal modules of large dermal bones were observed. A key difference is that the modularity of the jaw is apparently based upon long-range migration, while in the calvarium modularity arises from local polyclonal dynamics, with the only currently discernible active migratory process being invasion between layers.

As well as finding cryptic polyclonal divisions within anatomical structures, common lineages have been demonstrated across anatomical boundaries. The observation of small polyclonal groups in entheses giving rise to both bone-integrated anchors at one end and muscle-integrated tendons at the other not only solves an old developmental question, but greatly informs ongoing attempts to better integrate synthetic or prosthetic bone *in vivo*. This apparent presence of a distinct anatomical boundary within an apparent develpmental module is exactly mirrored in the modular tooth-and-casket modules observed in the jaw. Generally, one may start to doubt classical anatomical divisions, as the absence of a physical boundary does not seem to necessary imply the absence of a developmental division, and the presence of a clear anatomical boundary does not seem to necessary imply the meeting between two developmental modules.

The limitations of the approach used are that because I worked on fixed tissue, the techniques are still divorced from the temporal dimension. While migrations of cells may be the only parsimonious explanation for how putatively distal cells end up in a proximal territory, the nature of these movements cannot be surmised from static tissue. Ultimately, these observations provide a road map for future live cell imaging, which shall reveal the true nature of the development of these structures. This does not however undermine the value of the analyses developed in this thesis: as well as being transferable to lineage labelling experiments in other structures, the calvarium and jaw can be further investigated by using Confetti as an analytical background into which gene mutations can be bred. The tools used here are fundamental to our ability to assess complex polyclonal information, and greatly expand the potential applications for random lineage labelling

The unexpected identification of cryptic polyclonal modularity in both regions demonstrates that development works by dynamic elaboration, rather than simple implementation of an early defined program. It is a human trait to desire to reverse-engineer developmental programs from the perspective of a rational 'designer', which invariably leads to elegant and parsimonious models. However developmental programs are the product of a complex evolutionary history, and as biologists we must prepare ourselves to challenge other widely accepted tidy models when faced with the true complexity of life.

Appendix A

Technical Information, Methods and Materials

A.1 Animal Work

A.1.1 Husbandry

Animals were housed, reared and maintained by the BSU at the University of Warwick. All procedures were carried out in accordance with the Animals (Scientific Procedures) Act 1986 including the 2013 updated regulations. The reported days of embryonic development were calculated from timed matings.

A.1.2 Generation of Wnt1-Cre x Gt(ROSA)26Sor$^{tm1(CAG-Brainbow2.1)Cle}$/J Mice

Wnt1-Cre is a widely described marker for the dorsal neural tube, and thus the neural crest.
Gt(ROSA)26Sor$^{tm1(CAG-Brainbow2.1)Cle}$/J (Confetti) mice were obtained from Jackson Laboratory, where they are held as stock 013731. Wnt1 mice were crossed with Confetti mice and desired offspring identified by fluorescence within the skull.

A.1.3 Generation of Hand2-Cre x Gt(ROSA)26Sor$^{tm1(CAG-Brainbow2.1)Cle}$/J Mice

The Hand2-Cre line possesses a 7kb upstream promoter region [Ruest et al., 2003]. Mice were originally provided to the lab by David Clouthier. Hand2 mice were

Table A.1: Details of Mice Used

Cre Driver	Age	Sectioning Diagram	Figures
Hand2	E10.5	N/A	3.5 and 3.6
Hand2	E14.5	3.1	3.7 and 3.8
Hand2	E16.5	4.1 and 5.1	4.2, 4.4, 4.5, 4.6, 4.7, 4.8 and 5.11[a]
Hand2	E16.5	4.1 and 5.1	4.3 and 5.14[a]
Wnt1	E18.5	5.1	5.2[a] and 5.8[a]
Wnt1	E18.5	5.1	5.5[a]
Wnt1	E18.5	5.1	5.19[a]
Wnt1	P0	5.1	5.17 and 5.18
Wnt1	P0	N/A	Sample A in Part II
Wnt1	P0	N/A	Sample B in Part II

[a] PCA Figure. Also has associated PCA map and plots.

crossed with Confetti mice as described above, with desired offspring identified by fluorescent jaws.

A.2 Dissection

The mother was euthanised in accordance with all relevant regulations by cervical dislocation. Dissections were performed in PBS. Foetuses were removed and examined for the desired fluorescence. Desired tissues were removed and processed accordingly.

A.2.1 Processing of Whole Calvaria

The calvaria was liberated from the head by removal of the epidermis and circumferential dissection of the nascent bone. Incisions were made into the posterior of the calvaria in order to allow for easy flattening. Samples were fixed for 45 minutes in 4% PFA. The SeeDB protocol was carried out as described in Ke et al. [2013]. A series of sucrose (Sigma Aldritch, UK) solutions were prepared: 20%, 40%, 60%, 80% and 100% weight to volume, and a saturated solution, each with 0.5% thioglycerol (Sigma Aldritch, UK). Samples were incubated in the first three solutions for 4 hours each, followed by 12 hour incubations in the 80% and 100% solutions and 24 hours in the SeeDB saturated solutions.

Samples were mounted in the same SeeDB they had equilibrated with. Silicon grease was used to support a coverslip, which was gently pressed onto the sample in order to flatten it. Tape was used to maintain pressure on the sample, which was also sealed with nail varnish. Imaging was conducted immediately after mounting.

A.2.2 Processing Samples for Sectioning

Samples for sectioning were immersed in Optimal Cutting Temperature medium (TissueTek, VWR), rapidly frozen and stored at -80°C. Cryosectioning was performed on OTF 5000 Cryostat (Bright Instruments, UK) at a thickness of 15-20μm . Sections were fixed for one minute in 4% PFA. Samples were counterstained with 1:1000 DAPI (Invitrogen) for 5 minutes unless where otherwise noted. Mounting was done in Mowiol.

A.3 Simulating the founder effect in Confetti

Because Confetti colour labelling is inherited, the probable founder population size can be surmised from the variety of colours within a group of cells. Low variety (1 or 2 colours) implies a small founder population, as the probability of independently labelled cells randomly all adopting the same 1 or 2 colours is inversely proportional to the size of the population.

Calculating the actual probability of different Confetti outcomes in a group of independently labelled cells is only simple if all colours have equal likelihood. As this is not the case, deterministic calculation of the probability all possible outcomes became very complex and an unnecessary challenge. A simple Monte Carlo method was used, as the absolute accuracy of these calculations is not critical, and the 'law of large numbers' should provide reasonable accuracy. Populations of 'cells' were generated, represented by random numerical arrays. A scale was defined based on the probabilities of each Confetti colour as observed in Figure 8.1. These random arrays can then be translated into a result, and classified based on the number of different coloured 'cells' randomly generated.

This is performed iteratively, the resulting mixtures tabulated and an observed probability taken. Enough iterations will tend towards the true probability, and so 10^7 iterations were performed in each case. This was performed for arrays of increasing length (representative of different starting populations) to give the overall model. The output is the observed probability that a population of independently specified cells will contain cells of 1, 2, 3 or 4 different colours.

A.4 Extending Stitching within ImageJ/FIJI

Preibisch et al. [2009] describes the image stitching software that comes packaged within FIJI [Schindelin et al., 2012]. This valuable tool underpins many experiments which rely upon gaining large-scale high resolution images by taking many tiles and integrating them into one [Susaki et al., 2014; Ragan et al., 2012; Fietz et al., 2010]. This software relies upon making pairwise comparisons between stacks using the Fourier transform ($\Im$)-based phase correlation method described in Kuglin [1975]. From the pairwise overlaps an overall best-fit set of coordinates for each tile can be generated, and the images stitched together.

Broadly speaking, there were formerly three options of how to attempt this image assembly. If exact positions for each tile were stored appropriately in metadata, then these could be used (Stitching by 'File Defined Positions'). If images corresponded to known positions in a complete grid, then this could be used to match each tile to its neighbours (Stitching by grid). Finally, if exact positions were unknown and images did not correspond to a complete grid, the last option is to compare every tile to every other tile (Stitching by 'Unknown Positions'). This is obviously the least efficient method, taking the maximum amount of time - the triangular number of the count of tiles multiplied by the time for each pairwise comparison. Also it can lead to inappropriate stitching, wherein tiles from very different parts of the sample may erroneously have a better match than actually adjacent tiles, usually due to an exact correspondence of empty space.

Many of the images in Part I were taken on a Zeiss LSM 710 without motorised stage. While this is an excellent microscope, it was beneficial to add a novel option to the stitching software, allowing for concatenation of sequential images. While stage position is not saved, file structures preserve the order in which images are captured. If each tile is captured with a small overlap to the previous one, it is possible to resolve a complete stitched image by simply attempting to find correspondence between one image in a sequence and the next.

Due to the open source nature of FIJI, this was relatively easy to accomplish. The stitching plugin does literally assemble a list of comparisons it intends to make, and so the problem was elegantly solved by adding an additional list-forming algorithm to implement sequential stitching. This is implemented in such a way that comparisons could be made any number of tiles ahead in the sequence.

In practice this is unnecessary below perhaps 10 tiles, where stitching by Unknown Positions does not represent a large time burden. Some images used here are much larger, consisting of many tens of tiles. These were imaged in a serpentine fashion, manually scanning back and forth across the sample. Due to the pairwise comparison, errors accumulate between rows of tiles. Fortunately the stitching plugin creates coordinate text files which can then be used to attempt stitching by file defined positions described above. This two-stage stitching approach is still extremely fast compared to stitching from Unknown Positions in situations with large numbers of tiles.

This code was submitted to the original developer Stephen Preibisch and now forms part of the core FIJI distribution.

A.5 Principal Components Analysis as a means for interpreting Confetti data

Principal components analysis is a technique for condensing multi-dimensional information into a more easily interpreted two or three dimensions [Pearson, 1901; Hotelling, 1933; Jolliffe, 2002]. Data points that have information for n characteristics can be plotted in a new coordinate that best exhibits the discriminatory differences across the data. This is achieved by identifying the direction through the initial n-dimensional space in which the variance of the data is the largest, which is taken as the first principal component. The direction perpendicular to this with the largest variance is taken as the second principal component, and so on until n principal components are plotted. Plots can then be produced of each points position relative to the axes of the principal components. In practice, this reveals the most important differences between parts of the sample, and highlights the most different regions.

Given three regions of the same image with different heterogenous Confetti compositions, it is difficult for a human observe to intuit which two regions might be more similar to each other. PCA allows for the encoding of these four-dimensional colour components into their most discriminatory factors. Furthermore, the software developed for this purpose allows for the re-encoding of the principal component results as an image, giving an anatomical spatial context to the theoretical colour space explored.

A.5.1 Pre-analysis steps

The approach described below requires very little image pre-processing relative to methods described later in this thesis. However care must be taken to select an image that is appropriate for PCA analysis. There are two further steps that must be performed in order to allow for analysis: thresholding and masking.

Image selection

PCA is only appropriate for images where it can be reasonably assumed that there are indeed several polyclonal regions. PCA describes only relative differences, and without an ‘outgroup’ or comparison region, misleading results may be produced. The first principal component will always describe the most significant source of variation across the image, whether this represents differences between discrete polyclonal systems or variation within one region. Furthermore, if too many independent polyclonal populations are present then the PCA becomes less informative. Confetti creates a random labelling, and given enough pixel samples all physically possible points of the Principal Component space will be occupied, confounding attempts to meaningfully plot maximal variance. For this reason, all images analysed with this method consisted of a maximum of two adjacent teeth and the associated bone.

Binary definition of pixel identity

When considering cell identity, the intensity of labelling is irrelevant: a strongly fluorescent YFP+ cell is as informative as a dimly fluorescent YFP+ cell. This rule extends to pixels: a pixel either does contain part of a cell that is labelled or it does not, and so a binary definition of colour is required. A threshold can be set independently for each colour channel to segregate labelled cellular material from non-labelled background. This threshold was set manually by visual interpretation, though the software developed does not preclude use of a true binary image such as that provided by auto-thresholding plugins. This threshold is usually sufficient to remove any bleed-through fluorescence or other undesirable artefacts.

It would be possible to count actual numbers of cells rather than use a proxy, but the use of area to estimate cell density is preferable to cell counting methods in this instance. If one assumes roughly uniform cell size in a particular region of an image, then image coverage by cells is directly proportional to the number of cells. This coverage is also not localised to a particular pixel, which would be necessary if working from existing cell-marking tools. The 'location' of the cells would thus be determined by human subjectivity rather than a true representation of cellular material in the tissue. Cell counting is also prone to human error and far slower than thresholding.

Masking and channel preparation

Some care must be taken regarding the channels of the image. All channels that do not contain Confetti information must be removed prior to analysis, as the software is developed to treat all but the last channel as input information for the Principal Components Analysis. The final channel must contain a mask. This mask image consists of pixels with the value 0 for regions of the image that are to be ignored, and pixels with a value above 0 for regions that are to be analysed. These non-zero values further act as an index for later interpretation, and can also be used to define discrete regions of analysis, as described in the next section.

A.5.2 Regional quantification of colour proportions

In order to compare populations of cells areas of pixels must be encoded into a single value. This value represents the abundance of each colour within a region ('the evaluated area') around a single point in X and Y ('the evaluated point'). Therefore an approach was required that would evaluate areas within a certain distance from each pixel, and encode the colour proportions as a corresponding pixel in a new two dimensional image, termed a 'Colour Map'.

Obviously a metric that uses a roughly circular search area is the most appropriate, as this allows pixels to be evaluated evenly in all directions. A simple radius-based approach is however not sufficient: were all of the pixels within a simple radius to be evaluated equally, the net effect would simply be to reduce the resolution of the original image by propagating the information of each individual pixel over an area. It was deemed appropriate to include a bias that would give greater weight to pixels closer to the evaluated point than those further away. This allows the evaluated area that is nearest to the evaluated point to have the greatest influence on the value encoded: in effect a weighted average of the evaluated area. A Gaussian or

Normal distribution of weights was chosen for this purpose, due to its profile that gives greatest weight to values closest to the evaluated point, its general acceptance in the field of image processing and its ready availability in existing programming packages. Other distributions could conceivably be used to similar effect: a Lorenz or Cauchy distribution would give greater weight to the periphery of the evaluated area. This procedure is in effect a Gaussian Blur, but taking a binary map of images rather than a map of intensities as an input.

Implementation of the Gaussian Blur sampling filter

A Gaussian Blur is a kernel operation: an array is generated that describes the weights of each pixel surrounding (and including) the evaluated point. This 'kernel' is then overlaid onto each pixel and the new value calculated by multiplying the original image value by the corresponding kernel weight, and adding up the products. Kernels can have any number of dimensions. A multi-dimensional Gaussian blur is a separable filter, in that calculating a 2D kernel and applying it to every pixel in an image has the same effect as creating a 1D linear kernel, blurring in one direction (such as the X direction) and then subsequently blurring this image in the Y direction. The latter option is far more efficient: if we take the width of the kernel to be s then to use a 2D kernel requires s^2 calculations per pixel, whereas to use a 2-pass 1D Kernel requires only $2s$ calculations per pixel.

The kernels used in this study are generated by the existing ImageJ GaussianBlur package. The key variable in performing a Gaussian blur is the σ (sigma) value, the standard deviation of the distribution which in effect determines the size of the search area. Smaller values preserve finer details of the original data, and larger values are useful for sampling larger areas efficiently. As such, this variable is user-definable in the software developed for this study, and there is also a facility for performing multiple blurring operations on the same image varying the σ, bypassing the need for repeating the other upstream processing.

Two variables for Gaussian kernel generation that are hard-coded and not user-definable are the 'accuracy' value and the maximum width. The maximum width is how large the kernel can be permitted to grow: this is set to the largest dimension of the image, width or height. This is in effect no limit at all: pixels outside of the image would not be used in calculations anyway. The 'accuracy' value defines the minimum cutoff value for the kernel: in effect how 'thin' the tails of the distribution can get before the computer ceases to attempt to model them. Without this limit, the width of the kernel would effectively be defined by how accurately the computer can model a floating-point number, creating a distribution with long but mathematically inconsequential tails. This would decrease program performance without providing any benefits. To ensure accuracy, the floor of the Gaussian Distribution was set to 1×10^{-4}. These two settings ensure functionally ideal accuracy of the Gaussian blur operation and preserve program performance..

Edge Handling

Edge handling is an important concept in kernel operations. With no information beyond the edges of the image, it is impossible to perform a true gaussian blur and so some compromise must be made. This is of particular importance given that the tissue regions defined by masks may be irregularly shaped, and so out-of-bounds areas exist in many parts of the image. Common ways of approaching the problem are either to duplicate the value of the edge pixels, or to simply crop off all parts of the image for which the kernel cannot fully lie within the image boundaries.

The duplication method is inappropriate for a binary image, as in effect one would be defining the edge region's identity almost entirely from the edge pixels which may not be representative of the area that lies within the image. A sparse cellular population that lies exclusively on the boundary of a masked region would be artificially inflated by duplication of its presence into the masked region. The effect of duplication methods is to create a monotonous background near borders. The crop approach is likewise undesirable as it may be that very few areas of the image would actually be represented in the final output due to the presence of irregularly shaped out-of-bounds masked areas.

An alternative to these two methods was developed which estimated the true representation of the Gaussian distribution in terms of available pixels. As discussed above, a Gaussian Blur is in effect a weighted average, and there is an implicit division by 1 (the product of all weight values in the kernel) when calculating the final result for a pixel. An additional image channel was used to tabulate how much of the kernel lay within the analysis bounds, in effect the residual weight of the distribution. This value was then used to divide the weighted sum of pixel values to give a true result. This produces a Gaussian Blur where the edges do not appear to have any particular discrepancies at the periphery of masked regions, which implies this is a good approximation for calculating regional proportions of colours.

Use of the mask as a delimiter

An option within the software allows for the blur to be terminated at the boundaries of differently indexed mask regions. This is achieved by treating each masked region as an individual image, and then re-constructing a composite with each of the different blurred regions. The resulting colour map has sharp boundaries at the edge of each region. This feature is very useful when examining very thin masked regions, as it ensures that the different areas will not be blurred into one another. However, without this option enabled, sharp boundaries within the PCA can only arise from true biological interfaces of remarkably different populations. For that reason, this option was not used for any part of this thesis.

A.5.3 Normalisation

Following the blur-based sampling, normalisation must be performed. This can be very important within PCA, as without it whichever dimension has the greatest magnitude is likely to be detected as the source of most variation. However, deciding the approach to normalisation is non-trivial. The plugin developed allows for very flexible options, and the rationale behind the options used within this thesis is discussed here.

Normalisation within each pixel occurs first

Each pixel in the Colour Map represents a number of cells, convolved into a single identity. Local variation in cell density has a large impact on the sum of these numbers. For this reason, normalising the product of the four colours in each pixel should be conducted first in order to remove cell density bias. This is achieved by scaling each relative colour contribution in each pixel such that their product becomes 1.

Normalisation within each colour reveals the most discriminatory differences

Following the initial pixel normalisation, the resulting magnitude of an individual colour channel might be quite small. However a trebling of a very small and rare cell population, such as the green labelled cells of Confetti, is far more significant than a change of the same magnitude in a very dense cell population. Thus the values for each colour are normalised across every pixel within their respective channels.

A.5.4 Implementation of the PCA

PCA relies heavily on matrix mathematical operations, and as such mostly relies on the functions of JAMA, a numerical linear algebra package [Hicklin et al., 2012]. The first step of PCA is to compute a correlation or covariance matrix of each characteristic within the sample. These give non-identical results, though in practice the analysis highlighted the same characteristics within the sample. The correlation matrix was used for all PCA within this thesis. The eigendecomposition of this matrix is then computed, which represents the individual weighting that each Confetti colour channel has with respects to each principal component. By multiplying these weights by the respective proportions of each colour for a pixel in the sample, the position of that pixel within principal component space can be found and tabulated.

A.5.5 Generation of a PCA Map

The tabular data produced by the PCA plugin can easily be interpreted with use of R [R Core Team, 2013], using relatively simple dot plot and bar chart functions [Wickham, 2009]. The generation of a PCA map is also relatively trivial: the PCA results are translated from their native scale into an 8-bit scale and written into an image. The interpretation of this is however non-trivial. Within PCA, the difference between 0 and -1 is as important as that of between 0 and 1. The direction of this scale is entirely arbitrary. However, in the colour scale, only one end of each principle component scale can be faithfully reproduced. For this reason, a significant caveat should be noted: mutual absence of a colour within the resulting PCA maps does not necessarily imply similarity. As such, these illustrations should be used solely for context alongside the standard dot plots of PCA analysis.

A.6 Imaging, processing and segmentation of calvarial images

A.6.1 Automation of imaging

The microscope used for this study was a Leica SP5, which is operated by the Leica Application Suite Advanced Fluorescence (LAS AF) software, version 2.7.3.9723. The robotic stage on this instrument allows for automated scanning of many locations sequentially. The software has two modes of automation. A rectangular grid of stacks (termed ‘tiles’) can be generated quite easily: this requires setting a minimum of two points, after which a rectangular grid of tile coordinates will be generated that capture these points, and all intervening space. Alternatively the user may specify individual tiles of interest manually through the ‘Mark and Find’ interface.

Both of these options are insufficient to properly scan a large and complex sample. A grid may cover the sample, but unless the sample or are of interest is rectangular, large parts of the scanned image will be empty or redundant. Due to time constraints, this was not acceptable. Similarly, while the Mark and Find interface allows for the necessary degree of flexibility, the manual selection of more than 100 stacks necessary to cover a calvaria would take too long to be practicable. An alternative solution was necessary in order to permit the scanning of large samples such as those described in this study, specifically the ability to de-select parts of a grid prior to scanning.

Scanning of a partial grid in LAS AF

An exploitable feature of the Mark and Find interface is that the user-defined positions can be saved to disk and reloaded. The file is saved in a format called ‘.maf’ (mark and find), but are really simply XML (eXtendable Markup Language) text files. This is a format that is commonly used to save data in a format that is useful for programs, and it is commonly used for storage of the Objects of Object-Oriented languages. In brief, this file defines blocks of text that describe the user input, and all of the various settings necessary to instruct the scanning of a particular stack at a particular stage position. This format is partially obfuscated, but it was possible to create a program that could generate new ‘.maf’ instruction sets from relative image positions.

In order to do this, first a simple 2D image of the whole sample must be taken, which is easily accomplished by using the grid scanning feature of LAS AF with transmitted light (bright field) imaging. The built-in stitching features of LAS AF are sufficient to connect these images into a large overview of the sample. The coordinates of the points defining the outlines must be known, and saved within a ‘.maf’ file, which in practice means defining the points first within the grid scanning interface, and then immediately storing them in the Mark and Find interface without moving the stage. As the ‘.maf’-encoded settings of the extremities of the image are known, a new .maf-encoded coordinate can be calculated for any position in the image.

Software was developed that allowed ImageJ/FIJI to take the overview image, certain values from the corresponding '.maf', and the user-defined settings of grid overlap to generate a predicted virtual grid, which can be displayed on the image. This grid represents the same feature as the grid scan of LAS AF, with the added ability of allowing the user to click on any tile for which scanning is not required. As an added feature, the time required to scan a single stack can be used to estimate the total scanning time required for the currently selected tiles. This allows for the selection of an appropriate number of stacks to fill and not exceed the available time on the instrument. Once the user has selected the appropriate scanning area, a '.maf' can be generated and loaded within LAS AF. If operated correctly, the tiles defined within ImageJ correspond with the sample with sufficient precision to ensure scanning of the desired area of the sample. Each tile is automatically titled to reflect its position in the grid of images, for example the output image stack '(02,03)' would represent the tile in the third column, and fourth row.

Image stack settings in a large scan

It is possible to use the same stack definition for each tile. A stack is defined by a start and end position in Z, and the step taken between each slice, which defines the number of optical sections taken: conversely, the number of sections can be set, defining the step size. This is however less than optimal: it was found that one end of the sample was invariably at a different depth to another along the anterior-posterior axis of the sample. This could be due to a slight misalignment of the stage, or a product of mounting. If the same stack settings were to be used for each tile, then a very large stack would be required in order to capture the whole sample, creating a cost of time and increasing photobleaching (Figure A.1A. In order to circumvent this, a feature was added to the software described above which allows the user to define different start and end positions for the extremities in the X dimension, which was deliberately and invariably aligned with the anterior-posterior axis of the sample.

The number of sections and the step size are required to be invariant: stacks of equal size are taken at different depths along the anterior-posterior axis. Given the depth of this standard stack at the most anterior part of the image, and the depth at the most posterior part of the image, the depth was interpolated across the the grid (Figure A.1B). This optimised the size of the stack and thus the number of stacks that could be captured in a single imaging session.

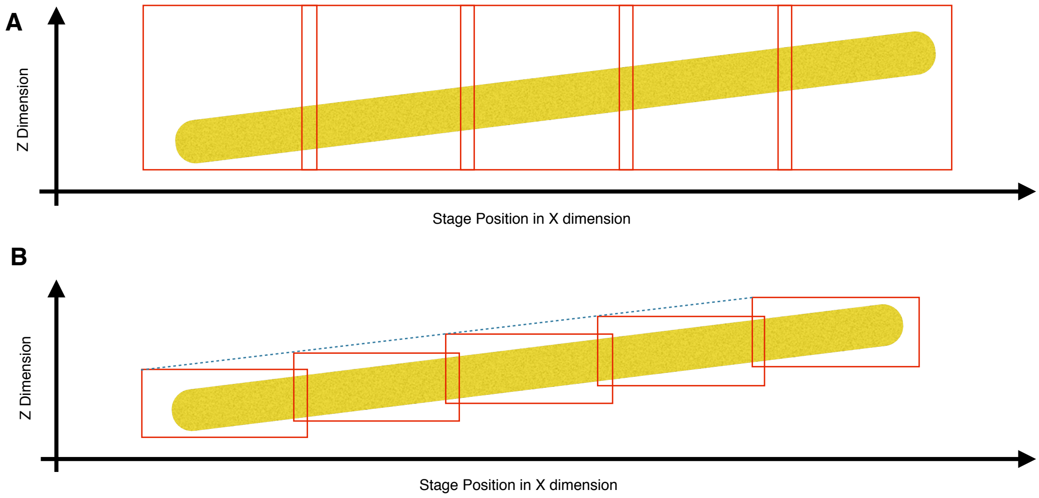

Figure A.1: Optimisation of scanning depth. A sample (yellow) which is not parallel to the axis of stage movement can still be covered in the Z (depth) dimension by overlapping scanning fields (red boxes). **A:** If the same stack settings are used for all points of a grid, the start and end in the Z dimension must be widely spaced. This increases scanning time and photobleaching. **B:** By stacks at both extremities of the axis, the start and end of the stack can be interpolated for each point along the axis, represented by the blue dashed line. This allows for a narrow stack, quicker scanning and less photobleaching.

A.6.2 Stitching of stacks

The output from the imaging regime described above is a collection of stacks that represent known positions in a partial grid, defined by their titles. The Grid/Collection Stitching suite as described in [Preibisch et al., 2009] and discussed in Appendix A.4 was used to recompile these into a single stack. As before, there is no immediate built-in tool for performing the necessary operation demanded by our experiment. However, the positiosn of the tiles in the grid are known even though the whole grid is not represented. Thus the best solution for stitching tiles from a partial grid is to define their approximate positions in a software-interpretable 'TileConfig' file, and to use 'Positions from File' mode within the software.

A 'TileConfig' file is a plain-text list of image files and their X,Y and Z coordinates in the final stitched image. These files are created as a secondary output of any stitching operation. When used as an input, images which are known to overlap due to their relative positions and sizes can be compared. A rough 'TileConfig' can be easily generated by taking the titles of the images, and multiplying their coordinates by the size of the image tiles in pixels, subtracting the overlap. This is sufficient to identify for the stitching software which tiles should theoretically overlap, and thus require comparison. No Z coordinate is given: this is calculated later.

While the Grid/Collection Stitching package can use virtual images to enable examination of very large datasets with limited computer memory, this was still insufficient to allow for the stitching of entire stacks at once. Individual channels had to be separated. Two channels could be stitched at once. In order to create an accurate 'TileConfig', with calculated Z coordinates, the Red and Green channels were used for image registration. This created a full and accurate 'TileConfig' that was then used to stitch all other channels, simply by applying the coordinates in transformations without calculation.

On occasion it was necessary to manually edit these configuration to remove tiles that were obviously mislocated: usually this was due to an empty or out-of-focus stack failing to find any similarity to its neighbours and thus defaulting to the origin location of the image. This is accomplished simply by removing that tile from the 'TileConfig' file.

A.6.3 Pre-Analysis processing

Raw images are insufficient for analytical purposes: they contain noise, bleed-through, background and reliable discontinuities that create visible defects in stitched images. A pipeline of pre-analysis processing was devised to create reliable 'cleaned' images for analysis.

Lateral Correction of discontinuities in Field Illumination.

When large stacks of low magnification are taken with a confocal microscope and then stitched together, the boundaries of the original tile are still visible. This is a reliable and predictable discrepancy: the same regions of the image are attenuated to the same degree in each tile, across each colour. This phenomenon is described in Zucker and Price [2001] as a discrepancy in Field Illumination.

To correct this, for each sample every slice in every tile in the dataset was summed together into one 2D picture and blurred with a large sigma (40 pixel) Gaussian blur to give four summed images: one for each colour channel. Each pixel in these images was then used to divide the average intensity of the summed and blurred to give four new images which mapped the degree by which each pixel deviated from the average. Every tile in the dataset was then multiplied by this map to give corrected images which when stitched together did have far better continuity along patch borders.

The use of an image that has been summed across all tiles rather than a reference slide means that we are addressing the actual dataset rather than a proxy. Each dataset consists of a minimum of 19000 z-sections. By making the assumption that no region of the individual image tiles has any particular bias for intensity, we can generate a true map of Field Illumination discontinuity.

Removal of noise, background and bleed-through

Raw images still contain significant background. This was removed by the Rolling Ball background subtraction method in FIJI. This plugin relies on an approach described in Sternberg [1983]. A 50 pixel radius was sufficient to remove background. Further background removal and bleed-through between channels was corrected using the Spectral Unmixing plugin by Joachim Walter. An unmixing matrix was generated by establishing cutoff values in each image channel for the four fluorophores and the background fluorescence. The plugin was modified to facilitate batch processing of our datasets. The resulting images contained significant pixellated noise. This was removed with the 'Despeckle' filter. Following these procedures, the images were stitched as described previously.

Focussing of Bright Field

The brightfield channel of each tile was of little use due to the highly contoured surface of the bone. This meant that for each slice only part of the image would be in focus. Fortunately, software exists to extract only focused parts of each slice and combine them into one focused image. The Stack Focuser ImageJ plugin by Umorin [2006] was used to accomplish this. Each tile was subjected to stack focusing prior to stitching from the same coordinates used for the colour channels. The resulting images are sufficient to show elaboration differences across the samples.

A.6.4 Delamination segmentation

The three layers of bone are central to this study, but are difficult to access for analytical purposes. There is currently no reliable and easy way to automatically determine where one layer ends and another begins, so manual segmentation of the images was necessary. To accomplish this, I created a segmentation tool for FIJI called Delaminator which allows the user to add modifiable non-destructive linear grid overlays to successive cross-sections of stacks, which can then be interpolated to extricate image stacks which contain only one layer of bone. These can then be analysed and compared. The operation and implementation of this tool are discussed in this section.

Delaminator initiation

Upon launching the plugin, the user must navigate a simple setup interface, shown in Figure A.2A. When starting a new Delamination procedure, the first step is to decide upon three key variables: the number of lines, the spacing of the grid in pixels and the degree of Z-scaling to apply for the interface. Lines describe the boundaries between layers. Our approach used six lines, thus segmenting our image into seven compartments:

- Empty image above the sample

- Tissue above Layer 1
- Layer 1
- Layer 2
- Layer 3
- Tissue below Layer 3
- Empty image below the sample

While deciding the number of lines is a facile task, choosing the grid size is not. A larger grid size will be less accurate and unable to properly follow the contours of the tissue, but a small grid size can make segmentation unfeasibly time-consuming owing to the number of points which must be manually placed. For the calvaria in this study, a grid size of 40 pixels was deemed a sufficient compromise between these two considerations.

The degree of Z-Scaling is a purely cosmetic interface feature. During Delamination the user must inspect YZ projected cross sections of stacks. By default, one optical section will be represented by one row of pixels in this projection. This scaling feature allows for multiple rows to be used for a single optical section, stretching the image in the Z-dimension. This can be beneficial if the XY scale of the image is far greater than the Z scale, and allows the user to correct what would otherwise be a very flattened image. This feature is entirely superficial and the program still saves the Z-coordinates of each dropped point as true locations, removing the scaling factor.

Loading and saving Delamination data

Naturally there are facilities for loading and saving the points and overlays created in Delamination. The *.delam* files created by the Delamination interface described below can be loaded by the setup interface. These files consist quite simply of comma-separated-values that describe each line as well as some metadata to allow for reloading of settings.

Working directly on a very large file such as our approach requires is not recommended: this will require a large amount of RAM or tolerance of the slow loading times inherent in using Virtual Images. Furthermore, the process becomes more vulnerable to crashes if one forgets to save, and to approach an entire stack as one monolithic task is psychologically daunting. For this reason, macros were created that split the main stack into several thin strips, representing 5 cross-sections. To allow for continuation onto the next strip where the last left off, there is a 'Load Last Only' feature within the setup interface that will retrieve the final cross-section overlay from a loaded file. Complementary tools to allow for concatenation of Delamination files were also created.

A.6.4.1 The Delamination interface

Once a Delamination file is initiated or loaded, the main interface will be displayed. This consists of two parts: a Delamination Window (Figure A.2B) and a control panel (Figure A.2C). One line (implemented as a Polyline ROI) can be selected in the control panel, at which point the regularly spaced vertices that describe it will be displayed along the line in the window. Clicking at any point in the image will move the nearest vertex to the cursor, and this vertex will then instaneously snap to a position described by three restrictions. First, the coordinate of the vertex along the X-axis of the Delamination window will be reset to its original point as defined by the grid. Then its Y-coordinate in the Delamination window (the Z-axis of the dataset) will be evaluated against the corresponding vertices in the adjacent lines, and moved to ensure that the lines never cross. If the new vertex is above the line above it in the window then it will snap to that higher line, and vice-versa for lines below. This process allows for rapid creation of line shapes from single clicks. It is also possible to transpose the entire line instantaneously by clicking and dragging, though this is often undesirable.

The control panel is largely self-descriptive. The 'Next' and 'Previous' buttons control which cross-sections are to be examined. 'Save' creates a new *.delam* file. 'Process' initialises the segmentation procedure described in the next subsection. 'Change Colour' allows the display colour of a Delamination line to be edited. 'Undo' will revert the last modified line back to its state prior to the last modification: this feature only works for one modification. The check box 'Delaminate to Disk' controls whether the output from 'Process' will be displayed within the program or saved slice-by-slice to the hard drive, which is necessary for larger images.

Upon progressing to the 'Next' cross-section, the overlay lines from the previous cross-section will remain. These act as a starting-point for the next overlay, so that only minor modifications will be necessary. This behaviour only applies if the cross-section in question has not been annotated previously: moving to a cross-section that has already been visited will load the previous lines.

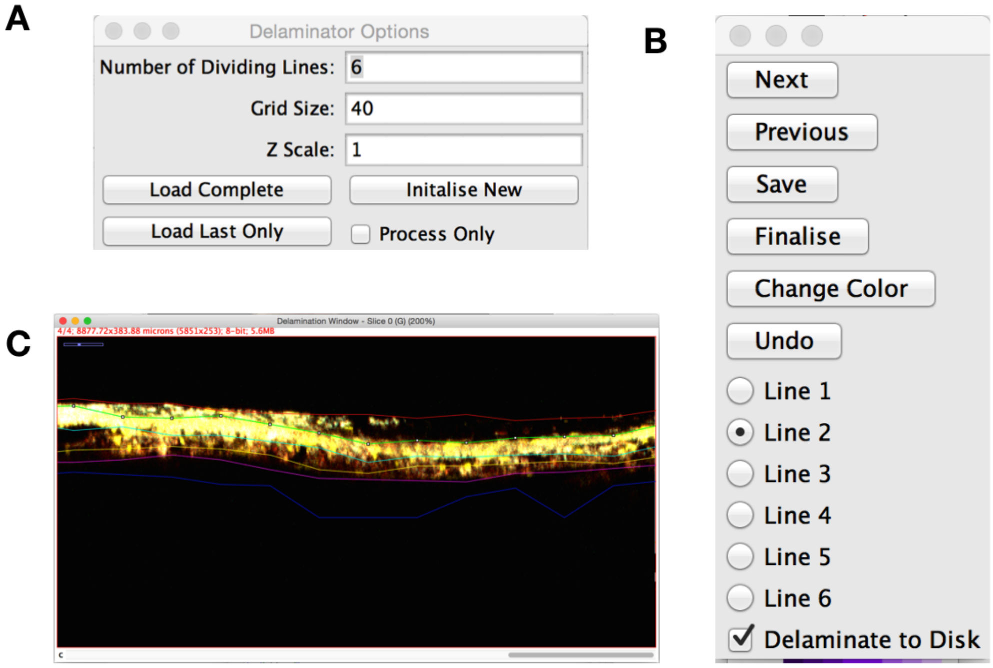

Number of Dividing Lines: 6
Grid Size: 40
Z Scale: 1
☐ Process Only

○ Line 1
● Line 2
○ Line 3
○ Line 4
○ Line 5
○ Line 6
☑ Delaminate to Disk

4/4; 8877.72x383.88 microns (5851x253); 8-bit; 5.6MB

Figure A.2: Delamination plugin interface. A: The initiator interface. **B:** The Delaminator Control panel which controls the Delaminator Window. **C:** The Delaminator Window, showing six editable lines forming an overlay on a cross-section of an image stack.

Once the user has defined the layer locations for each cross-section of the image, a final *.delam* file can be created which in effect describes a set of image-wide two dimensional segmentation boundaries described by their vertices in Z. This allows for the segmentation of the original stack into its constituent layers.

Delamination output

In order to segment the original stack, the vertices described in the final image-wide *.delam* file must be interpolated to work out the precise points of segmentation for each layer at each point in X and Y. The interpolation used is a bilinear interpolation of the thickness of each layer, thus achieving the same result as a trilinear interpolation. First, the thickness of each layer is quantified at each point in the segmented grid - as the order of the layers is invariant then this unambiguously describes the information that the user has provided. A 'Segmentation Map' is created into which the layer designations of each voxel can be written. This stack is filled in a stepwise fashion, through evaluation of four neighbouring points at a time which shall be referred to as 'tiles'. Each tile is interpolated first in the X direction, defining the upper and lower boundaries. Then these tiles are interpolated across the Y dimension to fill in the area. This is done for each layer to create a map of the layer thicknesses across the tile area. As the order of the layers is invariant, these can be then written into the segmentation map.

Once this process is completed for all tiles, the original image stack can be easily segmented. Each image in the stack (defining a single channel at a single point in the Z dimension) is segmented into the appropriate number of recipient images pixel-by-pixel through reading the corresponding layer index value in the segmentation map. If 'Delaminate to Disk' is selected then these slices will be saved to the hard drive with a nomenclature appropriate for subsequent reconstitution. If not, then these slices are added to a stack within the program.

An additional mask channel is added to each segmented image that denotes the volume within the layer, so that non-labelled tissue within the layer can be distinguished from areas of the stack that are not included in the layer. The choice to segment these to separate stacks rather than simply add an annotation to one stack was based on a desire to leverage existing features of ImageJ/FIJI such as Z Projection and 3D Projection without requiring further scripting or processing. The trade-off is that the output stacks occupy a lot of hard disk space - the original stack size, plus an additional channel, multiplied by the number of layers created.

A limitation of this procedure is that the segmentation map is not a Virtual Image, and thus cannot exceed the available RAM without creating instability or slowdown. The size of this stack is minimal, as it is a single channel 8-bit image. The output represents a bottleneck for inferior computers: with stacks of the size used here, at least 8GB of RAM should be made available to ImageJ/FIJI.

A.7 Flattening and Blurring

The stacks produced by delamination represent a expansion of data, rather than a refinement. Each layer has a stack of the same size as the original data, plus a mask channel. The task remains of summarising this data into easily analysed forms. Our characteristics of interest within our sample are found across the surface of each layer and between each layer, rather than within the depth of an individual layer. This means that flattening each stack into a single plane spanning the anteroposterior and mediolateral axes of the skull would give us all the necessary information. However, as the thickness of each layer varies from point to point, simple projections are not appropriate. More specialised tools that take into account the variability of the sample are required.

As well as dispensing with the Z dimension, the intensity of fluorescence is likewise unnecessary. The high density of cells and the use of membrane-bound fluorescent proteins within the Confetti construct made segmentation of individual cells impossible, requiring a volumetric approach to labelling. The key information contained within it is the position and size of cells: a voxel either contains part of a cell of a certain colour or it does not. A binary identity is sufficient to categorise this. Finally, while the positions of individual cells is valuable, the identity of the wider population and polyclonal mixtures is also informative. Therefore a means of measuring across several cells are necessary, and were developed for this purpose.

A.7.1 Colour encoding procedure

Both individual cell maps, termed ‘Flattened Cell Maps’ and maps of population identity, termed ‘Blur Maps’ are produced by the same process: indeed the Flattened Cell Map is necessary for producing the blurred Colour Map.

A worked example of the colour encoding process is shown in Figures A.3 and A.4.The principle of colour encoding in three dimensions is identical to that described for two dimensions in section A.5, only with an initial step of 'flattening' the third dimension. The first step of encoding is to count for each Z-column of voxels in the X and Y dimension the number of voxels that are occupied by each colour, and the number of voxels that are covered by the 'mask' channel which defines the portion of the 3D Image Stack that was considered to be within the layer under evaluation.

The mask channel in this 'flattened' image has a secondary use as a 2D map of the thickness of the layer, and it is reintroduced later on in this role. The flattened image itself is saved, as it is a good representation of the fine cell architecture of the bone, and can be used in the same manner as a Z-projection for examining the characteristics of individual cells. It is more appropriate for this task than a simple Z-projection of the delaminated stacks, as it contains no information that has not been entered into the Blur Maps, and because cell volumes can be easily derived from it.

A blur operation is required to convert the Flattened Cell Map into a map of population identities. Blur operations take weighted averages of all values around a central point, thus sampling several cells. The profile of the blur kernel defines the weight given to close and distant cells. A Gaussian blur was chosen for this purpose, as it has the greatest acceptance within the field of image analysis, was easily implemented through existing features within ImageJ, and fulfilled the role of giving reasonable population identities that assumed a stronger association between close cells than distant ones.

A Gaussian Blur is performed on each channel of the 'flattened' image, including the mask: a new 'image' is created (but not displayed) where each pixel is the sum of the adjacent pixels, multiplied by their corresponding value within the kernel. This is in effect a weighted average, similar to the method used in A.5. The limits of the mask channel is not respected in this first step: values are calculated for pixels outside of the masked 'within layer' area in order for the blur to handle concave objects appropriately. In the second pass, values are only calculated for pixels that lie within the original masked area, as those outside of these areas are not within the sample. The final value for each pixel in each of the colour channels is in fact the Gaussian Blur result for each channel, divided by the Gaussian Blur result for the mask channel. This weights the average of the Gaussian Blur to respect the volumetric contributions of each original pixel. The original summed mask channel replaces the blurred mask channel in the final Colour Map, as it is a true map of layer thickness.

The resulting Colour Map appears similar to a blurred Z-Projection of the original image. In fact, to get the same result through existing ImageJ/FIJI operations, one would take a Sum Z projection, a 2D Gaussian Blur, divide each channel by the mask channel, re-apply the original mask and delete any pixel that lies outside of the mask. Furthermore, a ‘hard’ thresholding process would be required first: a new image calculated where each voxel either 0 or 1 (or more commonly 255, the maximum 8-bit value) based on the threshold. The process developed here is more efficient than performing the operation as a macro and user-friendly in that thresholding is performed entirely through the ‘Brightness and Contrast’ control panel, without requiring the creation of any new input images.

A.7.2 Normalisation of Blur Maps

It is necessary and appropriate to normalise these Blur Maps: the maximum intensity value of each channel is found, and all values within that channel divided by this maximum such that the map exists on an intensity scale from 0.0 to 1.0. The justification for this is in part described in the next section, which describes how the populations represented by each pixel in a Colour Map are compared, but there is also an independent and general justification for this process. Specific channels such as the GFP channel have far lower densities than others such as the YFP in most images. This is due to the asymmetric probabilities of specific recombinations in the Confetti locus, as described in section 1.3. Normalisation amplifies the signal of less populated channels relative to more populated channels. This is a valuable correction: the presence of a rare population is far more discriminatory than the presence of a common one. Normalisation enables the pixel comparison procedure described in the next section.

A.7.3 Trimming of Samples

The resulting samples had a significant proportion of useless or uninterpretable tissue around their peripheries, due to the difficulty of correctly identifying within-sample tissue during delamination. A mask was created and used to trim each sample down to represent only the bones of interest.

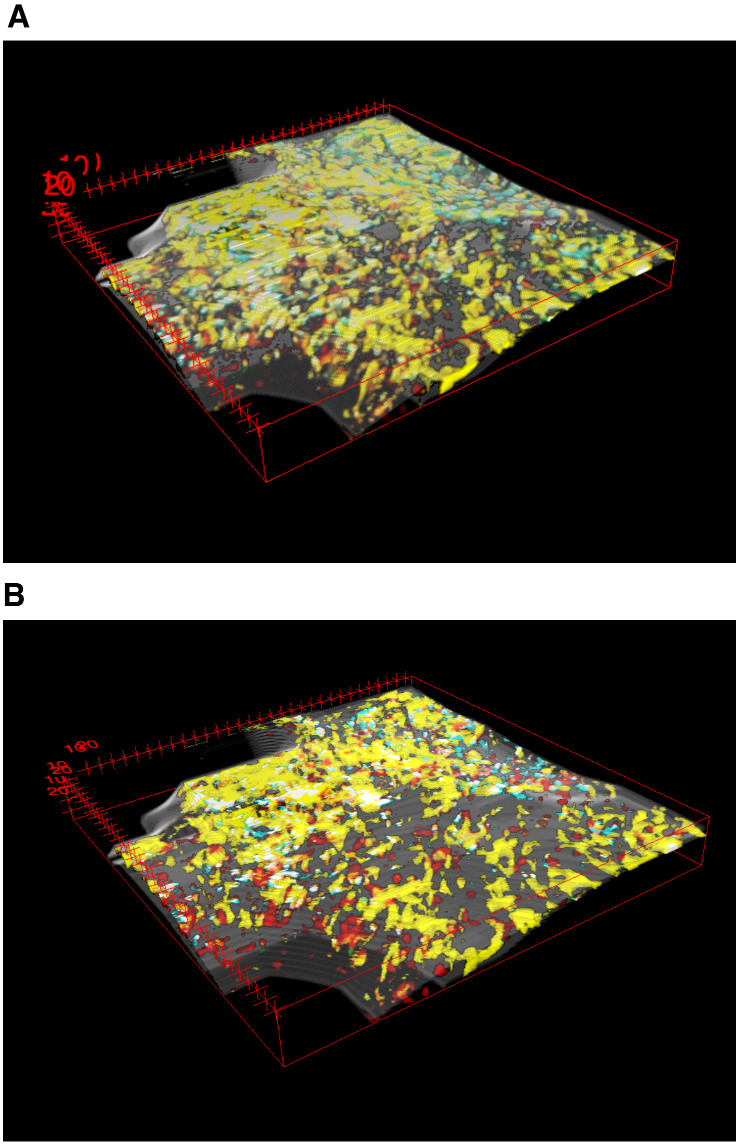

Figure A.3: Encoding of a 2D Colour Map
A: A 3D Volume projection of a small region of Confetti-labelled cells. The layer mask is shown in grey. **B:** A threshold is applied so that only voxels that are within the cells are considered to be positive.

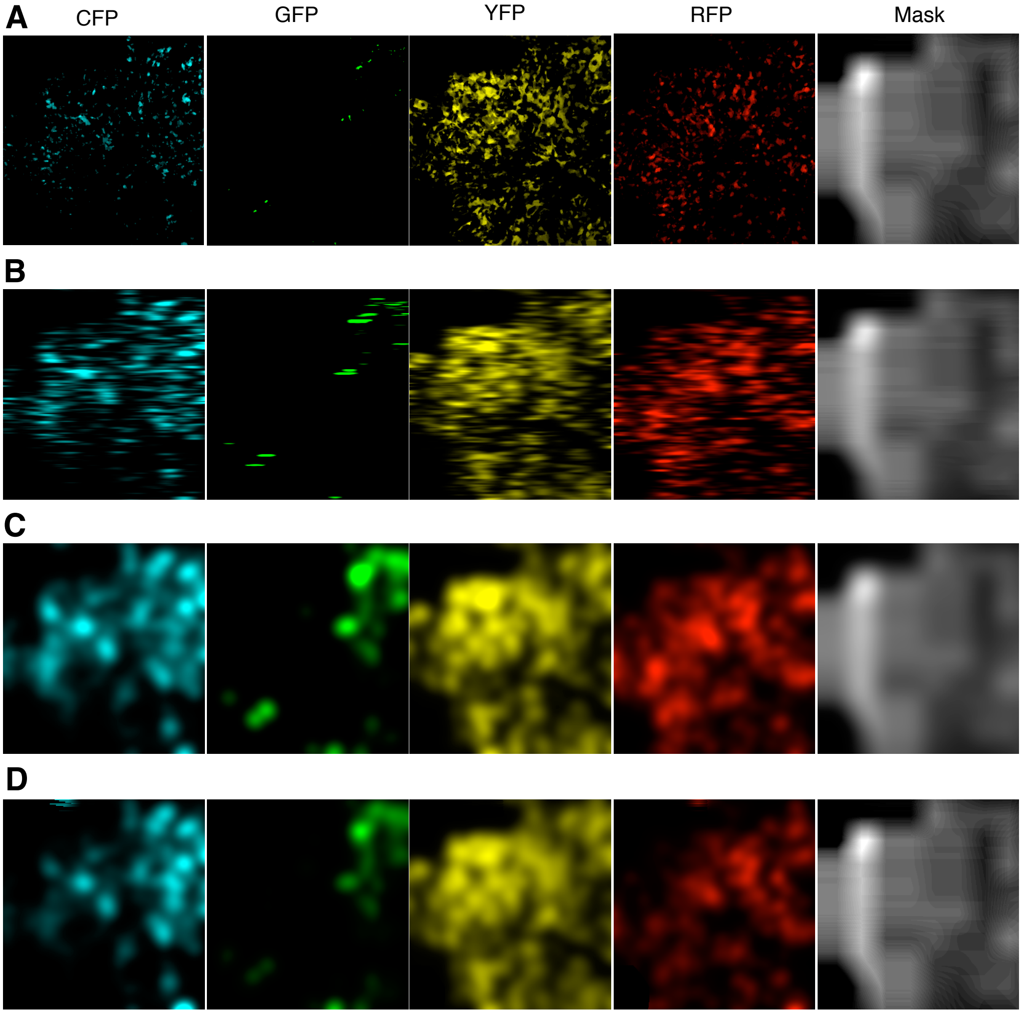

Figure A.4: Encoding of a 2D Colour Map (Continued from Figure A.3) In each image Brightness and Contrast have been set independently. **A:** The image represented in Figure A.3B is flattened in Z, counting the number of 'positive' voxels in each position in X and Y. **B:** The resulting image is blurred in one direction. **C:** The second direction is blurred, but only for pixels that lie within the original mask **D:** Each pixel in each fluorophore channel is divided by the corresponding pixel in the blurred mask channel to obtain the Colour Map, which is then normalised. The original summed mask is re-applied as the fifth channel.

A.8 Watershed analysis reveals single colour patches

The Watershed Analysis plugin for ImageJ by Daniel Sage [Sage, 2011] allows for the segregation of an image into discrete regions. This is accomplished by finding a 'catchment basin' around a local maxima. This is done progressively: the maxima are located and created as new basins. The next level of intensity is then analysed, and grouped into existing basins if adjacent, or created as new basins if not. The analogy of 'watershedding' is accurate, in that if image intensity were rendered as a landscape, basins represent the rainfall catchment basin or 'watershed' of individual valleys. The inverse operation may be performed, watershedding into local minima.

The Blur Maps described in Chapter 8 can be segregated through this watershed analysis. It can be assumed that regions of the greatest cell density represent either points of significant cell division, or a point of invasion. Lateral spread out from this point will dilute the density of a single colour of cells. As cell density is effectively encoded as colour intensity in a 22.6μm Colour Density map, we can use this approach to provide an impression of groups of single expanding clones. The more accurate 8-Connected Watershed Algorithm was used to accomplish this.

Reading of Patch Maps

The patch maps generated by the Watershed Analysis plugin are simply RGB images comprising of many islands of colour. In order to analyse these further, they must be interpreted by the software as polygonal regions of interest. Once the correct 'Patch Map' is selected by the user from the drop-down list, the 'Scan Basins' button will load the patches into memory as polygons. This is accomplished by exploiting the functionality of the 'magic wand' selection tool. This tool creates polygonal selections from contiguous regions of the same colour, and thus provides the outline of each patch. The polygonal regions of interest are stored as an extended version of the existing data structure of ImageJ which has additional functionality for the purposes of this study.

Mapping Patch Density

While cell density within patches is also discussed within this thesis, this should not be confused with the density of patches within space. This is easily calculated by moving a circle through the image and counting how many patches overlap with it. This was conducted for every channel, and a sum map produced to help with interpretation of patch density distribution. The circle used had an area of 1.79 mm^2.

A.8.1 Quantifying features within watershed patches

Once a patch map has been generated and read into memory as a collection of regions of interest, these areas can be examined and enumerated against several other factors. This is quite simply accomplished, as ImageJ contains many tools for examining both the geometric characteristics of a region of interest, and image characteristics within in.

Area, thickness and volume

Area quantification is accomplished simply, as this is already a feature of polygonal regions of interest within ImageJ that can be accessed through the 'measure' tool and associated API functions. A further 'Volume' extension is possible by examining a region of interest with reference to a thickness map, which is generated as the final channel of a Colour Density map. As this image represents the number of pixels in the now flattened Z dimension that were present in the original layer, the volume of the space represented by a basin can be easily calculated. As this pixel-by-pixel thickness is encoded in the image as an intensity, this is actually accomplished by taking the average intensity within a basin and multiplying by the area, as this is more efficient within the program.

The thickness of Layer 2 is a valuable characteristic, as it can be used as a proxy for the development of the bone. For this reason, the ability to tabulate the average thickness within a region of interest was added. This is set up such that the Thickness Map can be separate from the Colour Density Map, allowing for the evaluation of the thickness of Layer 2 underlying a patch that was drawn out in Layer 1. The standard deviation and standard error of the mean of thickness are also tabulated, which allows for characterisation of variation within basins.

Cell density can be estimated

A tool was developed for the estimation of the number of voxels occupied by a single cell. This relies upon the use of the segmented 3 dimensional image stacks, and the same thresholding pseudobinary approach as for Colour Density quantification is used. The user may select a volume occupied by cells and obtain a readout of the number of voxels occupied within that region. If a volume that contains a known number of complete cells is obtained, this total voxel count can be divided by the user-observed cell number to give an average number of voxels per cell. For this study, 40 cells were used, as this tended to give a reliable average. This process is repeated for each cell colour to account for the different cell compartment labelling and imaging differences, but not for each layer as the thresholding process should reduce bias between layers.

The Sum-Flattened Maps described in the previous chapter can then be used to estimate cells per basin. These maps contain the total number of counted voxels as an intensity, so by obtaining the sum intensity and dividing by the calculated voxels per cell, an estimate of cell number can be obtained. This can then be divided by the volume to obtain an estimate of cell density.

A.8.2 Tabulation and Plotting

The software allows for the tabulation of each patch and its associated features. The resulting table includes the following columns, enumerated in the manners described.

Channel The image channel from which the patch originated.

X/Y Position If new axes are provided, the patch centroid's position within that coordinate system. If no new axes are provided, the patch centroid's position within the image coordinate system.

Area The area of the patch, in pixels.

Average L2 Thickness The average intensity of the thickness map provided within the area of this patch, in slices.

StDev L2 Thickness The standard deviation of the above average

SEM L2 Thickness The standard error of the mean of the above average

Volume The volume of this patch in voxels. This is the sum of the pixel intensity within the patch in the thickness channel of the flattened cell map.

Cells or Pixels If cell volume estimates are provided, this represents an estimate of the number of cells within the patch. If no estimates are provided, this is a count of the number of voxels within the patch that contain part of a cell.

This is the sum of the pixel intensities within the patch in the corresponding colour channel of the flattened cell map.

Density The cell number divided by the patch volume.

The resulting tables were plotted within R [R Core Team, 2013] using the ggplot2 package [Wickham, 2009]. Patches with fewer than one cell were regarded as false positives and discarded. The black trend lines in the dot plots represent a generalised additive model as described in Wood [2011], with the default formula. The total number of cells of each colour was calculated by addition of all patches following filtering.

A.9 Comparing colours in multi-dimensional space

In order to explore differences between and across Blur Maps, it was necessary to develop a means of comparing two points and the populations they represent. This is achieved by using euclidian distance in a four dimensional space, where the abundance of each of the Confetti colours are used as the axes.

Pythagoras' Theorem can be extended to an arbitrary number of dimensions [Yeng et al., 1990], giving $\sum_{i=1}^{n}(a_1, a_2, a_3 ... \hat{a}_i ... a_n) = {C_d}^2$ where n is the number of dimensions, a_n is the difference between two points in the nth dimension, and C_d is the 'colour distance'. This allows us to evaluate the relative similarity of populations with respect to any number of fluorophores. For the four colour Confetti reporter, the sum for the 'colour distance' (C_d) between two populations is quite simple:

$$C_d = \sqrt{\Delta CFP^2 + \Delta GFP^2 + \Delta YFP^2 + \Delta RFP^2}$$

This will return a value of between 0.0 for perfect match and a maximum distance of $\sqrt{n}$, which in the Confetti case is 2.0. This process is similar to comparing points within principal component space, which again uses the concepts of relative distance in a multi-dimensional space. However there is no reorientation along new axes of highest variation, as the random assortment of cells nullifies any insight that technique can provide.

A.9.1 Elaborations upon the Colour Distance principle.

The direct comparison of the densities of cells from their values in the Blur Maps is termed ‘Value Mode’. An additional modification to this method is termed ‘Ratio Mode’. In Ratio Mode, the largest value of the four colour proportions for each population is scaled to 1, and the other proportions are scaled accordingly, maintaining their relative magnitudes. Then the Colour Distance is calculated as above. This approach is useful for comparing populations where the relative composition is the same, but the density is different. This was developed in order to explore the possibility of different dynamics within the polyclonal architecture.

In practice, it is more useful to invert the scale of colour distance, and to display the best matching pairs as greater numbers and the least matching pairs as lesser numbers. This is termed ‘Inverted Mode’ in subsequent descriptions. Furthermore, in some situations it is beneficial to further encode the intensity of the constituent colours which contributed to the distance metric: a match based on exact matching of extremely dense cells is far more informative than a match based upon a mutual absence of cells. To accomplish this, the sum of intensities of all colours used in the comparisons is calculated and divided by twice the number of colours. This gives a value between 0.0 (absence of cells) and 1.0 (maximum density across all colours in both points of comparison). This can be multiplied by the colour distance in ‘Inverted Mode’ to give a value that is a function not only of the degree of similarity but also the degree of label density. This is termed ‘Density Encoded Mode’. All of these elaborations are summarised in table A.2.

For the purposes of analysis, Inverted Density mode is clearly the most significant. This value represents the difference between two points, taking into account the confidence of that number relative to the amount of material that has informed it and excluding voxels that are identical based only on their mutual lack of cells. It is these maps which are used for all machine-read analysis. However, the Inverted Non-Density maps are slightly more accessible to a human observer, as while they share the same features as the density encoded maps, they are much more contrasted and distinct. These are used for diagrams within this thesis. Observable differences between the two, and associated caveats, are presented in this chapter.

Table A.2: Metrics for encoding colour similarity. Note that Value Mode and Ratio Mode represent different approaches to calculating the value C_d, which is then used to calculate ${C_d}^{inverted}$ or ${C_d}^{density}$ if desired.

Designation	Definition
Value Mode	$C_d = \sqrt{\sum_{i=1}^{n} (a_i - b_i)^2}$
Ratio Mode	$C_d = \sqrt{\sum_{i=1}^{n} (\frac{a_i}{max(a)} - \frac{b_i}{max(b)})^2}$
Inverted Mode	${C_d}^{inverted} = \sqrt{n} - C_d$
Density Encoded Mode	${C_d}^{density} = {C_d}^{inverted} \times \frac{\sum_{i=1}^{n} a_i + \sum_{i=1}^{n} b_i}{2n}$

C_d - ‘Colour Distance’ between two equally sized collections of colours termed a and b.
a_i, b_i - Value of the colour in channel i, within collections a and b.
n - number of colour channels
$max(a)$,$max(b)$ - the largest colour value in collections A and B respectively.

A.9.2 Summary and generation of invasion maps

The process described above gives an elegant means to compare colour matching, from which invasion and growth characteristics can be inferred. Software developed within ImageJ/FIJI implements this technique. For the maps presented in this thesis, a sigma of $22.75\mu m$ was used. This was chosen arbitrarily from a stepwise series of blurs as representing the best balance between integration of cells and maintenance of structural detail. Below this level, individual cells dominate blurs to a great degree. Above this level, fine detail is obscured. The software allows for a range of blurs to be created and colour matching maps generated from them.

A.9.3 Comparing Colour Similarity and Bone Thickness

The colour similarity map gives a value for layer matching to each pixel of the original image. These pixels also have their respective layer thickness values. As Layer 2 thickness is a sign of bone development, thickness was tabulated against layer matching. Density hexplots were generated within R for interpretation of this data [Wickham, 2009; R Core Team, 2013].

A.10 Solutions

A.10.1 Mowiol

- 6g Glycerol (Sigma)
- 2.4g Mowiol 4-99 (Calbiochem)
- 6mL dH2o
- 12mL 0.2M Tris Buffer pH 8.5
- 2.5% w/v DABCO (1,4-diazobicyclo-[2,2,2]-octane, Sigma)

A solution of glycerol, Mowiol and water is mixed for a period longer than 3 hours. 12mL 0.2M Tris Buffer pH8.5 is added and the mixture is stirred overnight on a warm plate. The solution is incubated for 10 min at 55°C and centrifuged at 5000g for 15 minutes. DABCO is added to the supernatant. Aliquots were stored frozen.

A.10.2 4% Paraformaldehyde

20 g of PFA powder (Sigma, UK) was dissolved in distilled water. 3-4 drops of 10N Sodium Hydroxide was added before the solution was heated to 65°C. The PFA solution was buffered with tablet form PBS (Sigma). pH was confirmed at 7.5 and aliquots frozen. For usage, aliquots were carefully thawed at room temperature.

Bibliography

Makoto Abe, Yoshihiro Tamamura, Hiroyuki Yamagishi, Takashi Maeda, Joji Kato, Makoto J Tabata, Deepak Srivastava, Satoshi Wakisaka, and Kojiro Kurisu. Tooth-type specific expression of dhand/hand2: possible involvement in murine lower incisor morphogenesis. *Cell and tissue research*, 310(2):201–212, 2002.

Arhat Abzhanov, Stephen J Rodda, Andrew P McMahon, and Clifford J Tabin. Regulation of skeletogenic differentiation in cranial dermal bone. *Development*, 134(17):3133–3144, 2007.

Francis Adams et al. *The genuine works of Hippocrates*, volume 17. Sydenham society, 1849.

Veerasathpurush Allareddy. Prevalence and impact of complications on hospitalization outcomes following surgical repair for craniosynostosis. *Journal of Oral and Maxillofacial Surgery*, 72(12):2522–2530, 2014.

Brooke A Armfield, Zhengui Zheng, Sunil Bajpai, Christopher J Vinyard, and JGM Thewissen. Development and evolution of the unique cetacean dentition. *PeerJ*, 1:e24, 2013.

WILLIAM R Atchley and BRIAN K Hall. A model for development and evolution of complex morphological structures. *Biol. Rev*, 66:101–157, 1991.

Melvyn Jerome Baer. Patterns of growth of the skull as revealed by vital staining. *Hum Biol*, 26:80–126, 1954.

Mehmet Bani, Ali Melih Tezkirecioglu, Nese Akal, and Tamer Tuzuner. Ectodermal dysplasia with anodontia: a report of two cases. *European journal of dentistry*, 4 (2):215, 2010.

Francie Barron, Crystal Woods, Katherine Kuhn, Jonathan Bishop, Marthe J Howard, and David E Clouthier. Downregulation of dlx5 and dlx6 expression by hand2 is essential for initiation of tongue morphogenesis. *Development*, 138 (11):2249–2259, 2011.

CA Berry and RJ Berry. Epigenetic variation in the human cranium. *Journal of anatomy*, 101(Pt 2):361, 1967.

Bhart-Anjan S Bhullar, Jesús Marugán-Lobón, Fernando Racimo, Gabe S Bever, Timothy B Rowe, Mark A Norell, and Arhat Abzhanov. Birds have paedomorphic dinosaur skulls. *Nature*, 487(7406):223–226, 2012.

Marianne Bronner-Fraser and Scott E Fraser. Cell lineage analysis reveals multipotency of some avian neural crest cells. *Nature*, 335(6186):161–4, September 1988.

JA Buckwalter, MJ Glimcher, RR Cooper, R Recker, et al. Bone biology. *J Bone Joint Surg Am*, 77(8):1256–1275, 1995.

Peter H Byers, Gregory S Barsh, and Karen A Holbrook. Molecular pathology in inherited disorders of collagen metabolism. *Human pathology*, 13(2):89–95, 1982.

Sebastian Cachero, Aaron D Ostrovsky, Y Yu Jai, Barry J Dickson, and Gregory SXE Jefferis. Sexual dimorphism in the fly brain. *Current Biology*, 20 (18):1589–1601, 2010.

Dawen Cai, Kimberly B Cohen, Tuanlian Luo, Jeff W Lichtman, and Joshua R Sanes. Improved tools for the brainbow toolbox. *Nature methods*, 10(6):540–547, 2013.

LM Calvi, GB Adams, KW Weibrecht, JM Weber, DP Olson, MC Knight, RP Martin, E Schipani, P Divieti, FR Bringhurst, et al. Osteoblastic cells regulate the haematopoietic stem cell niche. *Nature*, 425(6960):841–846, 2003.

Allison F Carey, Guirong Wang, Chih-Ying Su, Laurence J Zwiebel, and John R Carlson. Odorant reception in the malaria mosquito anopheles gambiae. *Nature*, 464(7285):66–71, 2010.

L Luca Cavalli-Sforza. Genes, peoples, and languages. *Proceedings of the National Academy of Sciences*, 94(15):7719–7724, 1997.

Robert Cerny, Peter Lwigale, Rolf Ericsson, Daniel Meulemans, Hans-Henning Epperlein, and Marianne Bronner-Fraser. Developmental origins and evolution of jaws: new interpretation of “maxillary” and “mandibular”. *Developmental biology*, 276(1):225–236, 2004.

Robert Cerny, Maria Cattell, Tatjana Sauka-Spengler, Marianne Bronner-Fraser, Feiqiao Yu, and Daniel Meulemans Medeiros. Evidence for the prepattern/cooption model of vertebrate jaw evolution. *Proceedings of the National Academy of Sciences*, 107(40):17262–17267, 2010.

Martin Chalfie, Yuan Tu, Ghia Euskirchen, William W Ward, and Douglas C Prasher. Green fluorescent protein as a marker for gene expression. *Science*, 263(5148):802–805, 1994.

A Charles and MD Parker. Wormian bones, 1905.

Kwanghun Chung, Jenelle Wallace, Sung-Yon Kim, Sandhiya Kalyanasundaram, Aaron S Andalman, Thomas J Davidson, Julie J Mirzabekov, Kelly A Zalocusky, Joanna Mattis, Aleksandra K Denisin, et al. Structural and molecular interrogation of intact biological systems. *Nature*, 497(7449):332–337, 2013.

Jennifer A Clack. *Gaining ground: the origin and evolution of tetrapods.* Indiana University Press, 2012.

Jonathan DW Clarke. Using fluorescent dyes for fate mapping, lineage analysis, and axon tracing in the chick embryo. In *Molecular Embryology*, pages 319–328. Springer, 1999.

M Michael Cohen. Editorial: perspectives on craniosynostosis. *American Journal of Medical Genetics Part A*, 136(4):313–326, 2005.

M Michael Cohen Jr. The new bone biology: pathologic, molecular, and clinical correlates. *American journal of medical genetics Part A*, 140(23):2646–2706, 2006.

Richard M Cripps and Eric N Olson. Control of cardiac development by an evolutionarily conserved transcriptional network. *Developmental biology*, 246(1):14–28, 2002.

E Roy Davies. *Machine vision: theory, algorithms, practicalities.* Elsevier, 2004.

Tiphaine Davit-Béal, Abigail S Tucker, and Jean-Yves Sire. Loss of teeth and enamel in tetrapods: fossil record, genetic data and morphological adaptations. *Journal of anatomy*, 214(4):477–501, 2009.

Gavin De Beer et al. *Homology, an unsolved problem.* Oxford University Press, 1971.

Johnny B Delashaw, John A Persing, William C Broaddus, and John A Jane. Cranial vault growth in craniosynostosis. *Journal of neurosurgery*, 70(2):159–165, 1989.

JA Dent, AG Polson, and MW Klymkowsky. A whole-mount immunocytochemical analysis of the expression of the intermediate filament protein vimentin in xenopus. *Development*, 105(1):61–74, 1989.

Philip CJ Donoghue and Ivan J Sansom. Origin and early evolution of vertebrate skeletonization. *Microscopy research and technique*, 59(5):352–372, 2002.

William E Duellman and Linda Trueb. *Biology of amphibians*. JHU Press, 1986.

Mostafa El Khashab, Farideh Nejat, Shahrooz Yazdani, and Nima Baradaran. Case report acquired craniomeningocele in an infant with craniosynostosis: a case report. *Journal of Medical Case Reports*, 2010.

Simone A Fietz, Iva Kelava, Johannes Vogt, Michaela Wilsch-Bräuninger, Denise Stenzel, Jennifer L Fish, Denis Corbeil, Axel Riehn, Wolfgang Distler, Robert Nitsch, et al. Osvz progenitors of human and ferret neocortex are epithelial-like and expand by integrin signaling. *Nature neuroscience*, 13(6):690–699, 2010.

DJ Finkel. Wormian bone formation in the skeletal population from lachish. *Journal of Human Evolution*, 5(3):291–295, 1976.

H Francillon-Vieillot, V De Buffrénil, J Castanet, J Géraudie, FJ Meunier, JY Sire, L Zylberberg, and A De Ricqlès. Microstructure and mineralization of vertebrate skeletal tissues. *Skeletal biomineralization: patterns, processes and evolutionary trends*, 1:471–530, 1990.

Gareth J Fraser and Moya Meredith Smith. Evolution of developmental pattern for vertebrate dentitions: an oro-pharyngeal specific mechanism. *Journal of Experimental Zoology Part B: Molecular and Developmental Evolution*, 316(2):99–112, 2011.

Gareth J Fraser, Robert Cerny, Vladimir Soukup, Marianne Bronner-Fraser, and J Todd Streelman. The odontode explosion: the origin of tooth-like structures in vertebrates. *Bioessays*, 32(9):808–817, 2010.

Noriko Funato, Shelby L Chapman, Marc D McKee, Hiromasa Funato, Jesse A Morris, John M Shelton, James A Richardson, and Hiromi Yanagisawa. Hand2 controls osteoblast differentiation in the branchial arch by inhibiting dna binding of runx2. *Development*, 136(4):615–625, 2009.

Walter Holbrook Gaskell. *The origin of vertebrates.* Longmans, Green, 1908.

Sam Giles, Matt Friedman, and Martin D Brazeau. Osteichthyan-like cranial conditions in an early devonian stem gnathostome. *Nature*, 520(7545):82–85, 2015.

J Andrew Gillis, Melinda S Modrell, and Clare VH Baker. Developmental evidence for serial homology of the vertebrate jaw and gill arch skeleton. *Nature communications*, 4:1436, 2013.

William K Gregory. The origin and evolution of the human dentition a palaeontological review. *Journal of Dental Research*, 2(1):89–183, 1920.

Ruth Griffin, Anne Sustar, Marianne Bonvin, Richard Binari, Alberto del Valle Rodriguez, Amber M Hohl, Jack R Bateman, Christians Villalta, Elleard Heffern, Didier Grunwald, et al. The twin spot generator for differential drosophila lineage analysis. *Nature methods*, 6(8):600–602, 2009.

H Grüneberg and GM Truslove. Two closely linked genes in the mouse. *Genetical Research*, 1(01):69–90, 1960.

Dafni Hadjieconomou, Shay Rotkopf, Cyrille Alexandre, Donald M Bell, Barry J Dickson, and Iris Salecker. Flybow: genetic multicolor cell labeling for neural circuit analysis in drosophila melanogaster. *Nature methods*, 8(3):260–266, 2011.

Hiroshi Hama, Hiroshi Kurokawa, Hiroyuki Kawano, Ryoko Ando, Tomomi Shimogori, Hisayori Noda, Kiyoko Fukami, Asako Sakaue-Sawano, and Atsushi Miyawaki. Scale: a chemical approach for fluorescence imaging and reconstruction of transparent mouse brain. *Nature neuroscience*, 14(11):1481–1488, 2011.

Stefanie Hampel, Phuong Chung, Claire E McKellar, Donald Hall, Loren L Looger, and Julie H Simpson. Drosophila brainbow: a recombinase-based fluorescence labeling technique to subdivide neural expression patterns. *nAture methods*, 8(3): 253–259, 2011.

Gregory R Handrigan and Joy M Richman. Autocrine and paracrine shh signaling are necessary for tooth morphogenesis, but not tooth replacement in snakes and lizards (squamata). *Developmental biology*, 337(1):171–186, 2010.

James Hanken. *The Skull, Volume 2: Patterns of Structural and Systematic Diversity*, volume 2. University of Chicago Press, 1993.

Enni Harjunmaa, Kerstin Seidel, Teemu Häkkinen, Elodie Renvoisé, Ian J Corfe, Aki Kallonen, Zhao-Qun Zhang, Alistair R Evans, Marja L Mikkola, Isaac Salazar-Ciudad, et al. Replaying evolutionary transitions from the dental fossil record. *Nature*, 512(7512):44–48, 2014.

Matthew P Harris, Sean M Hasso, Mark WJ Ferguson, and John F Fallon. The development of archosaurian first-generation teeth in a chicken mutant. *Current Biology*, 16(4):371–377, 2006.

Shigemi Hayashi and Andrew P McMahon. Efficient recombination in diverse tissues by a tamoxifen-inducible form of cre: a tool for temporally regulated gene activation/inactivation in the mouse. *Developmental biology*, 244(2):305–318, 2002.

Roger Heim, Andrew B Cubitt, and Roger Y Tsien. Improved green fluorescence. *Nature*, 373(6516):663–664, 1995.

Tyler J Hendershot, Hongbin Liu, Anjali A Sarkar, David R Giovannucci, David E Clouthier, Makoto Abe, and Marthe J Howard. Expression of hand2 is sufficient for neurogenesis and cell type–specific gene expression in the enteric nervous system. *Developmental Dynamics*, 236(1):93–105, 2007.

Tyler J Hendershot, Hongbin Liu, David E Clouthier, Iain T Shepherd, Eva Coppola, Michèle Studer, Anthony B Firulli, Douglas L Pittman, and Marthe J Howard. Conditional deletion of hand2 reveals critical functions in neurogenesis and cell type-specific gene expression for development of neural crest-derived noradrenergic sympathetic ganglion neurons. *Developmental biology*, 319(2):179–191, 2008.

J Hicklin, C Moler, P Webb, RF Boisvert, B Miller, R Pozo, and K Remington. Jama: A java matrix package (2012). *URL: http://math. nist. gov/javanumerics/jama*, 2012.

Harold Hotelling. Analysis of a complex of statistical variables into principal components. *Journal of educational psychology*, 24(6):417, 1933.

Ann Huysseune. Formation of a successional dental lamina in the zebrafish (danio rerio): support for a local control of replacement tooth initiation. *International Journal of Developmental Biology*, 50(7):637, 2006.

Jennifer M Iklé, Kristin B Artinger, and David E Clouthier. Identification and characterization of the zebrafish pharyngeal arch-specific enhancer for the basic helix-loop-helix transcription factor hand2. *Developmental biology*, 368(1):118–126, 2012.

Pervin Imirzalioglu, Sina Uckan, and Seda Gürsoy Haydar. Surgical and prosthodontic treatment alternatives for children and adolescents with ectodermal dysplasia: a clinical report. *The Journal of prosthetic dentistry*, 88(6):569–572, 2002.

Philippe Janvier. *Early vertebrates*, volume 33. Clarendon Press Oxford, 1996.

Jukka Jernvall and Irma Thesleff. Tooth shape formation and tooth renewal: evolving with the same signals. *Development*, 139(19):3487–3497, 2012.

Thomas M Jessell. Neuronal specification in the spinal cord: inductive signals and transcriptional codes. *Nature Reviews Genetics*, 1(1):20–29, 2000.

DR Johnson. The interfrontal bone and mutant genes in the mouse. *Journal of anatomy*, 121(Pt 3):507, 1976.

Ian Jolliffe. *Principal component analysis.* Wiley Online Library, 2002.

Kate Jordan. *Exploring the Generative Architecture of Intramembranous Ossification.* PhD thesis, University of Warwick, 2011.

Kate Weymouth-Crocker Jordan, Xintao Zhang, Hiromi Yanagisawa, Marthe J. Howard, David E. Clouthier, and Georgy Koentges. Dermal bone grows by cellular invasion and intercalary biomineralization. In preparation, 2015.

Gerard Karsenty, Henry M Kronenberg, and Carmine Settembre. Genetic control of bone formation. *Annual Review of Cell and Developmental*, 25:629–648, 2009.

Brian K Kay and H Benjamin Peng. *Xenopus laevis: practical uses in cell and molecular biology*, volume 36. Academic press, 1992.

Meng-Tsen Ke, Satoshi Fujimoto, and Takeshi Imai. Seedb: a simple and morphology-preserving optical clearing agent for neuronal circuit reconstruction. *Nature neuroscience*, 16(8):1154–1161, 2013.

Clyde E Keeler. Interfrontal—a heritable cranial variation of the house mouse. *Journal of Mammalogy*, 14(1):75–76, 1933.

Thomas Kleinteich, Alexander Haas, and Adam P Summers. Caecilian jaw-closing mechanics: integrating two muscle systems. *Journal of the Royal Society Interface*, 5(29):1491–1504, 2008.

Edward J Kollar and Grace R Baird. The influence of the dental papilla on the development of tooth shape in embryonic mouse tooth germs. *Journal of embryology and experimental morphology*, 21(1):131–148, 1969.

Toshihisa Komori. Runx2, a multifunctional transcription factor in skeletal development. *Journal of cellular biochemistry*, 87(1):1–8, 2002.

Georgy Kontges and Andrew Lumsden. Rhombencephalic neural crest segmentation is preserved throughout craniofacial ontogeny. *Development*, 122(10):3229–3242, 1996.

Gert-Jan Kremers, Sarah G Gilbert, Paula J Cranfill, Michael W Davidson, and David W Piston. Fluorescent proteins at a glance. *Journal of Cell Science*, 124 (2):157–160, 2011.

CD Kuglin. The phase correlation image alignment method. In *Proc. Int. Conf. Cybernetics and Society, Sept. 1975*, pages 163–165, 1975.

CYNTHIA C Lance-Jones and CARL F Lagenaur. A new marker for identifying quail cells in embryonic avian chimeras: a quail-specific antiserum. *Journal of Histochemistry & Cytochemistry*, 35(7):771–780, 1987.

Nicole M Le Douarin and FRANCINE V Jotereau. Tracing of cells of the avian thymus through embryonic life in interspecific chimeras. *The Journal of experimental medicine*, 142(1):17–40, 1975.

Nicole M Le Douarin and Marie-Aimée M Teillet. Experimental analysis of the migration and differentiation of neuroblasts of the autonomic nervous system and of neurectodermal mesenchymal derivatives, using a biological cell marking technique. *Developmental biology*, 41(1):162–184, 1974.

Aaron RH LeBlanc and Robert R Reisz. Periodontal ligament, cementum, and alveolar bone in the oldest herbivorous tetrapods, and their evolutionary significance. *PloS one*, 8(9), 2013.

Tzumin Lee and Liqun Luo. Mosaic analysis with a repressible cell marker (marcm) for drosophila neural development. *Trends in neurosciences*, 24(5):251–254, 2001.

Jay R Lieberman and Gary E Friedlaender. Bone regeneration and repair. In *Chapter 4, Biology of bone graft*, page 57. Springer, 2005.

Jean Livet, Tamily A Weissman, Hyuno Kang, Ryan W Draft, Ju Lu, Robyn A Bennis, Joshua R Sanes, and Jeff W Lichtman. Transgenic strategies for combinatorial expression of fluorescent proteins in the nervous system. *Nature*, 450 (7166):56–62, 2007.

John A Long. Arthrodire predation by onychodus (pisces, crossopterygii) from the late devonian gogo formation, western australia. *Rec West Aust Mus*, 15:503–516, 1991.

Antoine Louchart and Laurent Viriot. From snout to beak: the loss of teeth in birds. *Trends in ecology & evolution*, 26(12):663–673, 2011.

AG Lumsden. Pattern formation in the molar dentition of the mouse. *Journal de biologie buccale*, 7(1):77–103, 1979.

AGS Lumsden. Spatial organization of the epithelium and the role of neural crest cells in the initiation of the mammalian tooth germ. *Development*, 103 (Supplement):155–169, 1988.

Grant R MacGregor, Gamy P Nolan, Steven Fiering, Mario Roederer, and Leonard A Herzenberg. Use of escherichiu coli (e. coli) lacz (β-galactosidase) as a reporter gene. In *Gene transfer and expression protocols*, pages 217–235. Springer, 1991.

Tadanori Mammoto, Akiko Mammoto, Yu-suke Torisawa, Tracy Tat, Ashley Gibbs, Ratmir Derda, Robert Mannix, Marlieke de Bruijn, Chong Wing Yung, Dongeun Huh, et al. Mechanochemical control of mesenchymal condensation and embryonic tooth organ formation. *Developmental cell*, 21(4):758–769, 2011.

Miguel Maroto and Olivier Pourquié. A molecular clock involved in somite segmentation. *Current topics in developmental biology*, 51:221–248, 2001.

Toshiyuki Matsuoka, Per E Ahlberg, Nicoletta Kessaris, Palma Iannarelli, Ulla Dennehy, William D Richardson, Andrew P McMahon, and Georgy Koentges. Neural crest origins of the neck and shoulder. *Nature*, 436(7049):347–355, 2005.

Joseph G McCarthy, Scot B Glasberg, Fred J Epstein, Barry H Grayson, Gregg Ruff, Charles H Thorne, Jeffrey Wisoff, Barry M Zide, et al. Twenty-year experience with early surgery for craniosynostosis. *Plastic and reconstructive surgery*, 96(2): 272–295, 1995.

Melanie McCollum and Paul T Sharpe. Evolution and development of teeth. *Journal of anatomy*, 199(1&2):153–159, 2001.

Robert W Meredith, John Gatesy, and Mark S Springer. Molecular decay of enamel matrix protein genes in turtles and other edentulous amniotes. *BMC evolutionary biology*, 13(1):20, 2013.

JJ Mitala, JP Boardman, RA Carrano, and JD Iuliucci. Novel accessory skull bone in fetal rats after exposure to aspirin. *Teratology*, 30(1):95–98, 1984.

Gillian M Morriss-Kay and Andrew OM Wilkie. Growth of the normal skull vault and its alteration in craniosynostosis: insights from human genetics and experimental studies. *Journal of anatomy*, 207(5):637–653, 2005.

Tung Nguyen, Lucia Cevidanes, Beatriz Paniagua, Hongtu Zhu, Leonardo Koerich, and Hugo De Clerck. Use of shape correspondence analysis to quantify skeletal changes associated with bone-anchored class iii correction. *The Angle Orthodontist*, 84(2):329–336, 2013.

Sonja Nowotschin and Anna-Katerina Hadjantonakis. Use of kikgr a photoconvertible green-to-red fluorescent protein for cell labeling and lineage analysis in es cells and mouse embryos. *BMC developmental biology*, 9(1):49, 2009.

Ronald A Nussbaum and Michael E Pfrender. *Revision of the African caecilian genus Schistometopum Parker (Amphibia: Gymnophiona: Caeciliidae).* University of Michigan Museum of Zoology, 1998.

Valerie Dean O'Loughlin. Effects of different kinds of cranial deformation on the incidence of wormian bones. *American journal of physical anthropology*, 123(2): 146–155, 2004.

Lynne A Opperman. Cranial sutures as intramembranous bone growth sites. *Developmental dynamics*, 219(4):472–485, 2000.

David M Ornitz and Pierre J Marie. Fgf signaling pathways in endochondral and intramembranous bone development and human genetic disease. *Genes & development*, 16(12):1446–1465, 2002.

JW Osborn. Morphogenetic gradients: fields versus clones. *Development, function and evolution of teeth*, pages 171–201, 1978.

Karl Pearson. On lines and planes of closest fit to systems of points in space. *The London, Edinburgh, and Dublin Philosophical Magazine and Journal of Science*, 2(11):559–572, 1901.

Douglas C Prasher, Virginia K Eckenrode, William W Ward, Frank G Prendergast, and Milton J Cormier. Primary structure of the aequorea victoria green-fluorescent protein. *Gene*, 111(2):229–233, 1992.

Jitesh Pratap, Amjad Javed, Lucia R Languino, Andre J Van Wijnen, Janet L Stein, Gary S Stein, and Jane B Lian. The runx2 osteogenic transcription factor regulates matrix metalloproteinase 9 in bone metastatic cancer cells and controls cell invasion. *Molecular and cellular biology*, 25(19):8581–8591, 2005.

Stephan Preibisch, Stephan Saalfeld, and Pavel Tomancak. Globally optimal stitching of tiled 3d microscopic image acquisitions. *Bioinformatics*, 25(11):1463–1465, 2009.

Hector Mario Pucciarelli. The influence of experimental deformation on neurocranial wormian bones in rats. *American Journal of Physical Anthropology*, 41(1):29–37, 1974.

R Core Team. *R: A Language and Environment for Statistical Computing*. R Foundation for Statistical Computing, Vienna, Austria, 2013. URL `http://www.R-project.org/`. ISBN 3-900051-07-0.

Timothy Ragan, Lolahon R Kadiri, Kannan Umadevi Venkataraju, Karsten Bahlmann, Jason Sutin, Julian Taranda, Ignacio Arganda-Carreras, Yongsoo Kim, H Sebastian Seung, and Pavel Osten. Serial two-photon tomography for automated ex vivo mouse brain imaging. *Nature methods*, 9(3):255–258, 2012.

Sohini Ramachandran, Omkar Deshpande, Charles C Roseman, Noah A Rosenberg, Marcus W Feldman, and L Luca Cavalli-Sforza. Support from the relationship of genetic and geographic distance in human populations for a serial founder effect originating in africa. *Proceedings of the National Academy of Sciences of the United States of America*, 102(44):15942–15947, 2005.

Mary E Rawles. Origin of pigment cells from the neural crest in the mouse embryo. *Physiological zoology*, pages 248–266, 1947.

DP Rice, T Aberg, Y Chan, Zequn Tang, Päivi J Kettunen, Leila Pakarinen, RE Maxson, and Irma Thesleff. Integration of fgf and twist in calvarial bone and suture development. *Development*, 127(9):1845–1855, 2000.

Yuval Rinkevich, Paul Lindau, Hiroo Ueno, Michael T Longaker, and Irving L Weissman. Germ-layer and lineage-restricted stem/progenitors regenerate the mouse digit tip. *Nature*, 476(7361):409–413, 2011.

Ariel Rinon, Shlomi Lazar, Heather Marshall, Stine Büchmann-Møller, Adi Neufeld, Hadas Elhanany-Tamir, Makoto M Taketo, Lukas Sommer, Robb Krumlauf, and Eldad Tzahor. Cranial neural crest cells regulate head muscle patterning and differentiation during vertebrate embryogenesis. *Development*, 134(17):3065–3075, 2007.

CE Rio, LE Pinckney, and LA Kennedy. Craniolacunia without associated anomalies. *Neuroradiology*, 22(3):155–157, 1981.

Charles H Rodeck and Martin J Whittle. *Fetal medicine: basic science and clinical practice*. Elsevier Health Sciences, 2009.

Louis-Bruno Ruest, Marcus Dager, Hiromi Yanagisawa, Jeroen Charité, Robert E Hammer, Eric N Olson, Masashi Yanagisawa, and David E Clouthier. dhand-cre transgenic mice reveal specific potential functions of dhand during craniofacial development. *Developmental biology*, 257(2):263–277, 2003.

B Ryll. *The role of Hand2 in branchial arch and head-shoulder patterning*. PhD thesis, UCL (University College London), 2010.

Daniel Sage. Graylevel watershed - an imagej plugin to apply watershed segmentation on graylevel images. *URL: http://bigwww.epfl.ch/sage/soft/watershed/*, September 2011.

Isaac Salazar-Ciudad, Jukka Jernvall, et al. A computational model of teeth and the developmental origins of morphological variation. *Nature*, 464(7288):583–586, 2010.

Brian Sauer and Nancy Henderson. Site-specific dna recombination in mammalian cells by the cre recombinase of bacteriophage p1. *Proceedings of the National Academy of Sciences*, 85(14):5166–5170, 1988.

Arnout G Schepers, Hugo J Snippert, Daniel E Stange, Maaike van den Born, Johan H van Es, Marc van de Wetering, and Hans Clevers. Lineage tracing reveals lgr5+ stem cell activity in mouse intestinal adenomas. *Science*, 337(6095): 730–735, 2012.

Johannes Schindelin, Ignacio Arganda-Carreras, Erwin Frise, Verena Kaynig, Mark Longair, Tobias Pietzsch, Stephan Preibisch, Curtis Rueden, Stephan Saalfeld, Benjamin Schmid, et al. Fiji: an open-source platform for biological-image analysis. *Nature methods*, 9(7):676–682, 2012.

RÉGINE Schmitt, HERVÉ Lesot, JL Vonesch, and JEAN-VICTOR Ruch. Mouse odontogenesis in vitro: the cap-stage mesenchyme controls individual molar crown morphogenesis. *International Journal of Developmental Biology*, 43:255–260, 1999.

Dalit Sela-Donenfeld and Chaya Kalcheim. Regulation of the onset of neural crest migration by coordinated activity of bmp4 and noggin in the dorsal neural tube. *Development*, 126(21):4749–4762, 1999.

MA Selleck and Marianne Bronner-Fraser. Origins of the avian neural crest: the role of neural plate-epidermal interactions. *Development*, 121(2):525–538, 1995.

Oliver Semler, Moira S Cheung, Francis H Glorieux, and Frank Rauch. Wormian bones in osteogenesis imperfecta: correlation to clinical findings and genotype. *American Journal of Medical Genetics Part A*, 152(7):1681–1687, 2010.

Osamu Shimomura, Frank H Johnson, and Yo Saiga. Extraction, purification and properties of aequorin, a bioluminescent protein from the luminous hydromedusan, aequorea. *Journal of cellular and comparative physiology*, 59(3):223–239, 1962.

David M Shotton. Confocal scanning optical microscopy and its applications for biological specimens. *Journal of Cell Science*, 94(2):175–206, 1989.

SV Smirnov. Postmetamorphic skull development in bombina orientalis (amphibia, discoglossidae), with comments on neoteny. *Zoologischer Anzeiger*, 223(1-2):91–99, 1989.

Kathleen K Smith. Sequence heterochrony and the evolution of development. *Journal of morphology*, 252(1):82–97, 2002.

Moya M Smith and Michael I Coates. Evolutionary origins of the vertebrate dentition: phylogenetic patterns and developmental evolution. *European Journal of Oral Sciences*, 106(S1):482–500, 1998.

Moya M Smith and Mike I Coates. The evolution of vertebrate dentitions: phylogenetic pattern and developmental models. *Major events in early vertebrate evolution*, 61:223–240, 2001.

Hugo J Snippert, Laurens G Van Der Flier, Toshiro Sato, Johan H Van Es, Maaike Van Den Born, Carla Kroon-Veenboer, Nick Barker, Allon M Klein, Jacco Van Rheenen, Benjamin D Simons, et al. Intestinal crypt homeostasis results from neutral competition between symmetrically dividing lgr5 stem cells. *Cell*, 143(1): 134–144, 2010.

Claudio D Stern, Flora De Pablo, and Alberto Ferrús. *Cellular and Molecular Procedures in Developmental Biology.* Academic Press, 1998.

Nat Sternberg and Daniel Hamilton. Bacteriophage p1 site-specific recombination: I. recombination between loxp sites. *Journal of molecular biology*, 150(4):467–486, 1981.

Stanley R Sternberg. Biomedical image processing. *Computer*, 16(1):22–34, 1983.

David W Stock, Kenneth M Weiss, and Zhiyong Zhao. Patterning of the mammalian dentition in development and evolution. *BioEssays*, 19(6):481–490, 1997.

Etsuo A Susaki, Kazuki Tainaka, Dimitri Perrin, Fumiaki Kishino, Takehiro Tawara, Tomonobu M Watanabe, Chihiro Yokoyama, Hirotaka Onoe, Megumi Eguchi, Shun Yamaguchi, et al. Whole-brain imaging with single-cell resolution using chemical cocktails and computational analysis. *Cell*, 157(3):726–739, 2014.

Yasuto Tanabe and Thomas M Jessell. Diversity and pattern in the developing spinal cord. *Science*, 274(5290):1115, 1996.

Tiffani Thomas, Hiroki Kurihara, Hiroyuki Yamagishi, Yukiko Kurihara, Yoshio Yazaki, Eric N Olson, and Deepak Srivastava. A signaling cascade involving endothelin-1, dhand and msx1 regulates development of neural-crest-derived branchial arch mesenchyme. *Development*, 125(16):3005–3014, 1998.

Jean-Philippe Tissier-Seta, Marie-Laurence Mucchielli, Manuel Mark, Marie-Geneviève Mattei, Christo Goridis, and Jean-François Brunet. Barx1, a new mouse homeodomain transcription factor expressed in cranio-facial ectomesenchyme and the stomach. *Mechanisms of development*, 51(1):3–15, 1995.

Grant Townsend, Edward F Harris, Herve Lesot, Francois Clauss, and Alan Brook. Morphogenetic fields within the human dentition: a new, clinically relevant synthesis of an old concept. *Archives of oral biology*, 54:S34–S44, 2009.

Gillian M Truslove. Genetical studies on the skeleton of the mouse. *Journal of Genetics*, 51(1):115–122, 1952.

Abigail Tucker and Paul Sharpe. The cutting-edge of mammalian development; how the embryo makes teeth. *Nature Reviews Genetics*, 5(7):499–508, 2004.

Abigail S Tucker, Karen L Matthews, and Paul T Sharpe. Transformation of tooth type induced by inhibition of bmp signaling. *Science*, 282(5391):1136–1138, 1998.

Michael Umorin, 2006. URL `http://rsb.info.nih.gov/ij/plugins/stack-focuser.html`.

Seppo Vainio, Irina Karavanova, Adrian Jowett, and Irma Thesleff. Identification of bmp-4 as a signal mediating secondary induction between epithelial and mesenchymal tissues during early tooth development. *Cell*, 75(1):45–58, 1993.

Willem Vrolik. *Tabulae ad illustrandam embryogenesin hominis et mammalium, tam naturalem quam abnormem: De Vrucht van den Menschen en van de Zoogdieren.* Londonck, 1849.

Hadley Wickham. *ggplot2: elegant graphics for data analysis.* Springer New York, 2009. ISBN 978-0-387-98140-6. URL `http://had.co.nz/ggplot2/book`.

GE Wise, S Frazier-Bowers, and RN D'souza. Cellular, molecular, and genetic determinants of tooth eruption. *Critical Reviews in Oral Biology & Medicine*, 13 (4):323–335, 2002.

Lewis Wolpert, Cheryll Tickle, and Alfonso Martinez Arias. *Principles of development.* Oxford university press, 2015.

Simon N Wood. Fast stable restricted maximum likelihood and marginal likelihood estimation of semiparametric generalized linear models. *Journal of the Royal Statistical Society: Series B (Statistical Methodology)*, 73(1):3–36, 2011.

Manuela Wuelling and Andrea Vortkamp. Transcriptional networks controlling chondrocyte proliferation and differentiation during endochondral ossification. *Pediatric Nephrology*, 25(4):625–631, 2010.

T Yamada, M Placzek, H Tanaka, J Dodd, and TM Jessell. Control of cell pattern in the developing nervous system: polarizing activity of the floor plate and notochord. *Cell*, 64(3):635–647, 1991.

Hiroyuki Yamagishi, Chihiro Yamagishi, Osamu Nakagawa, Richard P Harvey, Eric N Olson, and Deepak Srivastava. The combinatorial activities of nkx2. 5 and dhand are essential for cardiac ventricle formation. *Developmental biology*, 239(2):190–203, 2001.

Hirotsugu Yanai, Toshihiro Tanaka, and Hiroo Ueno. Multicolor lineage tracing methods and intestinal tumors. *Journal of gastroenterology*, 48(4):423–433, 2013.

Shwu Yeng, T Lin, and You-Feng Lin. The n-dimensional pythagorean theorem. *Linear and multilinear algebra*, 26(1-2):9–13, 1990.

Hu Zhao, Jifan Feng, Thach-Vu Ho, Weston Grimes, Mark Urata, and Yang Chai. The suture provides a niche for mesenchymal stem cells of craniofacial bones. *Nature cell biology*, 2015.

Min Zhu, Xiaobo Yu, Per Erik Ahlberg, Brian Choo, Jing Lu, Tuo Qiao, Qingming Qu, Wenjin Zhao, Liantao Jia, Henning Blom, et al. A silurian placoderm with osteichthyan-like marginal jaw bones. *Nature*, 502(7470):188–193, 2013.

Hui Zong, J Sebastian Espinosa, Helen Hong Su, Mandar D Muzumdar, and Liqun Luo. Mosaic analysis with double markers in mice. *Cell*, 121(3):479–492, 2005.

Robert M Zucker and Owen Price. Evaluation of confocal microscopy system performance. *Cytometry*, 44(4):273–294, 2001.